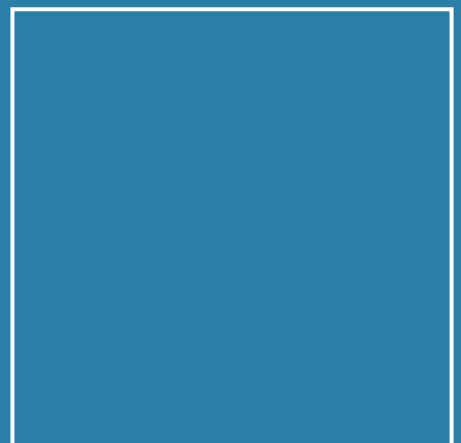
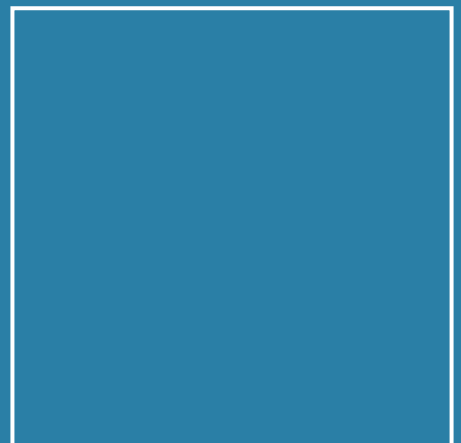




Dissertation

Fabian Plag

Integral methods of measurement for photovoltaics



ISSN 0341-6712
ISBN 978-3-95606-497-5

Die Serien der PTB-Berichte:

Dosimetrie	PTB-Dos
Elektrizität	PTB-E
Elektronische Entwicklung	PTB-EW
Fertigungsmesstechnik	PTB-F
Informationstechnik	PTB-IT
Mechanik und Akustik	PTB-MA
Medizinische Messtechnik	PTB-MM
Neutronenphysik	PTB-N
Optik	PTB-Opt
Physikalische Grundlagen	PTB-PG
Radioaktivität	PTB-Ra
Thermodynamik	PTB-Th
Explosionsschutz	PTB-Ex
Chemische Physik	PTB-CP

Eingestellte Serien:

Akustik	(bis 1985)	PTB-Ak
Forschungs- und Meßreaktor Braunschweig	(bis 1988)	PTB-FMRB
Institut Berlin	(bis 1985)	PTB-IB
Mechanik	(bis 1985)	PTB-Me
Neutronendosimetrie	(bis 1988)	PTB-ND
Sicherstellung und Endlagerung radioaktiver Abfälle	(bis 1989)	PTB-SE
Wärme	(bis 3/97)	PTB-W
Literaturzusammenstellungen und Veröffentlichungshinweise	(bis 2001)	PTB-L
Akkreditierung, Qualitätsmanagement, Zertifizierung	(bis 2003)	PTB-AQZ
Atomphysik	(bis 2003)	PTB-APh
Internationale Organisation für Gesetzliches Messwesen	(bis 2003)	PTB-OIML
Thermodynamik und Explosionsschutz	(bis 2003)	PTB-ThEx
Technisch-Wissenschaftliche Dienste	(bis 2003)	PTB-TWD

Physikalisch-Technische Bundesanstalt

Optik

PTB-Opt-87

Braunschweig, Dezember 2019

Fabian Plag

Integral methods of measurement for photovoltaics

Development and application of a multidimensional model
for the improvement of solar energy metrology

ISSN 0341-6712

ISBN 978-3-95606-497-5

Herausgeber:

Physikalisch-Technische Bundesanstalt

ISNI: 0000 0001 2186 1887

Presse und Öffentlichkeitsarbeit

Bundesallee 100

38116 Braunschweig

Telefon: (05 31) 592-93 21

Telefax: (05 31) 592-92 92

www.ptb.de

Integral methods of measurement for photovoltaics
-
Development and application of a multidimensional
model for the improvement of solar energy
metrology

Von der Fakultät für Elektrotechnik, Informationstechnik, Physik
der Technischen Universität Carolo-Wilhelmina zu Braunschweig

zur Erlangung des Grades eines Doktors
der Naturwissenschaften (Dr. rer. nat.)
genehmigte Dissertation

von Fabian Plag
aus Frankfurt am Main
eingereicht am: 01.04.2019
Disputation am: 05.11.2019
1. Referent: Hon.-Prof. Dr. rer. nat. Stefan Kück
2. Referent: Prof. Dr. rer. nat. habil. Andreas Waag

Druckjahr: 2019

Dissertation an der Technischen Universität Braunschweig,
Fakultät für Elektrotechnik, Informationstechnik, Physik

Abstract

In the domain of solar irradiance measurements, a wide range of irradiation conditions exist. While the primary calibration of reference solar irradiance detectors is usually performed using only direct irradiance, secondary calibrations are conducted with a diffuse incident irradiance component. If the optical properties vary between the reference and the device under test, spectral and angular dependencies of the incident irradiance and the detectors' responsivities may result in a mismatch when referring to defined reference conditions. This becomes particularly significant when photovoltaic (PV) devices short-circuit currents are measured under global natural sunlight.

In this thesis a new multidimensional model is presented. It introduces *spectral-angular* effects to the field of photovoltaic metrology, with a focus on quantifying their impact on high-accuracy device calibrations.

A novel measurement technique has been developed in this thesis. It allows the characterization of the angle of incidence (AOI) and polarization dependence of the spectral responsivity of solar cells. As a consequence of a thorough validation and an uncertainty analysis, a novel metrological service is offered to customers of the Physikalisch-Technische Bundesanstalt.

The enhanced modeling approach, developed in this thesis, considers the anisotropic solar spectral radiance for arbitrary device orientation, including spectrally resolved ground reflections. To account for these effects, both the spectral radiance of the source and the angular-dependent spectral responsivities of the detectors are considered. Angular mismatches of more than 1 % are identified for the investigated examples in this thesis. The proposed model allows the spectral and angular effects to be determined and corrected. The knowledge of this correction factors allows their consideration for establishing measurement uncertainty budgets of high-accuracy outdoor measurements. In addition to global natural sunlight measurements, the approach can be also utilized for the evaluation of indoor laboratory measurements with solar simulators containing diffuse light.

Additionally, a study on the impact of simplifications in the model is shown. One important result is that the neglect of the radiance's anisotropy leads to systematic errors in the range of the angular mismatch itself, when the simplified approach is compared against the multidimensional model.

A separate section treats the determination of AOI dependent optical losses with regard to PV module energy rating procedures. This study on angular losses includes a discussion on the procedure's uncertainties. The impact of the mathematical model proposed in the international standard IEC 61853-3 is identified to be the most crucial contribution to the uncertainty of the angular loss.

This thesis includes an exemplary energy rating scenario that focusses on the determination of the generated electricity of PV devices under reference climate profiles. This comparison considers three different models. The energy loss differences at one exemplary clear sky day are ranging from 0.3 % to 2.7 %, solely for spectral and angular effects. Finally, the results are discussed and an outlook for subjects of future research is presented. Meanwhile, the findings presented in this work are discussed in a standardization committee of the IEC and an interlaboratory comparison on AOI dependent measurements has been completed successfully.

Keywords: photovoltaic metrology, calibration, angle of incidence, spectral responsivity, diffuse irradiance, optical losses, energy rating.

Kurzzusammenfassung

Im Bereich der solaren Bestrahlungsstärkemessungen existieren unterschiedlichste Einstrahlungsbedingungen. Während die primäre Kalibrierung von Referenzbestrahlungsstärkedetektoren in der Regel unter Verwendung von direkter Bestrahlungsstärke durchgeführt wird, werden sekundäre Kalibrierungen häufig mit einer diffus einfallenden Strahlungskomponente durchgeführt. Wenn die optischen Eigenschaften zwischen der Referenz und dem zu testenden Detektor variieren, können spektrale und winkelabhängige Eigenschaften der einfallenden Strahlung, sowie die der Empfindlichkeit der Detektoren zu einer Fehlanpassung führen, wenn auf definierte Referenzbedingungen Bezug genommen wird. Dies ist besonders dann wichtig, wenn der Kurzschlussstrom von photovoltaischen (PV) Generatoren unter globalem natürlichem Sonnenlicht gemessen wird.

In der vorliegenden Arbeit wird ein neues multidimensionales Modell vorgestellt. Es führt spektral- und winkelabhängige Effekte in das Gebiet der Photovoltaik-Messtechnik ein, wobei der Schwerpunkt auf der Quantifizierung ihrer Auswirkungen auf präzise Kalibrierungen von PV Generatoren liegt. Im Rahmen dieser Arbeit wurde eine neuartige Messtechnik entwickelt. Diese ermöglicht die Charakterisierung von Einfallswinkel- und Polarisationsabhängigkeiten der spektralen Empfindlichkeit von Solarzellen. Als Ergebnis einer gründlichen Validierung und einer Unsicherheitsanalyse wird Kunden der Physikalisch-Technischen Bundesanstalt eine neue metrologische Dienstleistung angeboten. Der erweiterte Modellierungsansatz, der in dieser Arbeit entwickelt wurde, berücksichtigt die anisotrope spektrale Strahldichte einschließlich spektral aufgelöster Bodenreflexionen, sowie eine beliebige Ausrichtung der PV Generatoren. Um diesen Einflüssen Rechnung zu tragen, werden sowohl die spektrale Strahldichte der Strahlungsquelle als auch die winkelabhängigen spektralen Empfindlichkeiten der Detektoren berücksichtigt. In dieser Arbeit wurden Winkelfehlanpassungen von mehr als 1% identifiziert. Mit dem vorgeschlagenen Modell können die spektral- und winkelabhängigen Effekte, die bei der Strommessung an PV Generatoren auftreten können, bestimmt und korrigiert werden. Die Kenntnis dieser Korrekturfaktoren ermöglicht ihre Berücksichtigung bei der Bestimmung von Messunsicherheitsbudgets für Freifeldmessungen. Neben globalen Messungen der natürlichen Sonneneinstrahlung kann der hier vorgestellte Ansatz auch zur Korrektur von Labormessungen mit Solarsimulatoren unter diffuser Einstrahlung verwendet werden. Darüber hinaus wird eine Studie über die Auswirkungen von Vereinfachungen im Modell präsentiert. Ein wichtiges Ergebnis zeigt, dass die Vernachlässigung der Anisotropie der Strahldichte zu systematischen Fehlern in der Größenordnung der Winkelfehlanpassung selbst führt, wenn der vereinfachte Ansatz mit dem mehrdimensionalen Modell verglichen wird. Eine Analyse über die winkelabhängigen Verluste bei Ertragsbewertungsverfahren von PV Modulen beinhaltet eine Diskussion über die Unsicherheiten verschiedener eingesetzter Verfahren. Die Auswirkung der Verwendung des mathematischen Modells aus der internationalen Norm IEC 61853-3 wurde hierbei als einer der dominantesten Beiträge zur Unsicherheit von winkelabhängigen Verlusten identifiziert.

Diese Thesis enthält ein exemplarisches Szenario für die Energiebewertung untersuchter PV Generatoren, das die Bestimmung der erzeugten Elektrizität unter Referenzklimabedingungen ermöglicht. Dieser Vergleich berücksichtigt drei verschiedene Modelle. Die Differenzen der drei ermittelten Energieverluste unter klarem Himmel reichen von 0,3 % bis 2,7 %. Inzwischen werden Teile der in dieser Arbeit vorgestellten Ergebnisse in einem Normungsausschuss der IEC diskutiert und ein Ringvergleich mit winkelabhängigen Messungen wurde erfolgreich abgeschlossen. **Schlagworte:** Photovoltaik-Messtechnik, Kalibrierung, Einfallswinkel, spektrale Empfindlichkeit, diffuse Einstrahlung, optische Verluste, Energiebewertung

Table of contents

Abstract	3
Kurzzusammenfassung	4
Table of contents	5
1. Introduction.....	7
2. Fundamentals.....	11
2.1. Solar radiation.....	11
2.2. Radiative transfer simulation – <i>uvspec</i> as a tool.....	15
2.3. Principle of operation of conventional silicon solar cells.....	16
2.4. Calibration of PV devices.....	22
2.5. The concept of PV module energy rating	23
2.6. The f_2 model for the determination of angular-dependent optical losses.....	28
2.7. Measurement uncertainty.....	28
3. New multidimensional metric for the relation between solar radiation and solar cell.....	37
3.1. State of development.....	37
3.2. Problem definition.....	39
3.3. Definition of the angular distribution of the reference irradiation condition.....	39
3.4. Multidimensional model	40
3.5. Spectral and directional properties of the sky.....	45
3.6. Numerical approach.....	50
3.7. Summary	53
4. Experimental methodology and realization	55
4.1. Characterization of the solar cells' optical properties.....	55
4.2. Measurement uncertainty of the angular-dependent responsivity	71
4.3. Summary	87

5.	Impact: From Standard Test Conditions to the real world	89
5.1.	Spectral-angular mismatch for PV device calibration under global natural sunlight.....	89
5.2.	Effect of the angle of incidence on optical losses of solar cells.....	107
5.3.	Effect of diurnal variations of the irradiation conditions on the spectral-angular mismatch.....	123
6.	Discussion and Outlook	135
7.	Summary	141
	Data availability.....	143
	List of publications	145
	References	149
	Acknowledgement/Danksagung.....	159

1. Introduction

As of 2018, the cumulative world-wide installed capacity of solar photovoltaic (PV) amounts to a total of 402.5 GW_p (IEA, International Energy Agency, 2018), 70 times larger than in 2006. In 2017 alone, an additional capacity of nearly 100 GW_p was installed. Assuming a price of approximately \$2/W_p, the costs of these newly installed systems amount to \$200 billion (Barbose & Darghouth, 2018). The increasing growth of solar PV power in the past decade was driven by a decrease in the costs of the technology, enabled by significant improvements in industrial production processes. The total costs of a PV installation in the commercial sector consists of the costs of the system and installation as well as the maintenance, but also of the costs of finance. Commercial PV powerplants are commonly financed by loans. The yield from the harvested solar energy is used to cover the repayment of the loan. However, measurement uncertainties of the PV device performance at standard test conditions (STC) can lead to large energy yield uncertainties. This increased uncertainty can lead to a higher risk and thus to increasing costs of finance.

As a single performance parameter is not sufficient for energy yield predictions of PV devices at certain locations, a new energy rating standard series has been developed in the past years. The idea behind energy rating is to provide more than the power parameter in kW_p. The standard series IEC 61853 (IEC 61853-1 Edition 2, 2011; IEC 61853-2, 2016; IEC 61853-3, 2018; IEC 61853-4, 2018) provides a description on procedures to determine standardized energy yield parameters for individual PV modules on the market. These include energy-based values in kWh/year for a set of reference climate profiles to account for conditions at characteristic locations in the world. The availability of these parameters allows to select the PV module type and technology with the maximum yield at defined locations from the beginning of the planning phase of a PV installation project.

Energy rating parameters are traceable to primary calibrated reference solar cells. The uncertainty of primary calibrations and subsequent secondary calibrations contribute to the uncertainty of the energy rating parameters. Within the scope of this thesis a method to improve the accuracy of PV device measurements was developed, enabling further reductions of the uncertainty of the performance and the energy rating parameters.

In this context, an important aspect is the angle of incidence (AOI) of the incident solar radiation onto the PV device. A new international standard on the consideration of AOI dependent effects for energy rating parameters has been published recently (IEC 61853-3, 2018). To ease its applicability for energy rating purposes, a number of assumptions and simplifications were made. These simplifications can lead to an increase in the uncertainties of the energy rating parameters. Thus, in this work, the investigation of influences such as polarization-, spectral- and AOI dependent effects of solar cells and PV modules and their quantum efficiency (spectral responsivity) is performed. Additionally, their impact on measurements taken under global sunlight is studied.

Studies published previously on the spectral and angular dependencies of PV devices were focused on the physical processes inside the device, including light trapping effects in thin film solar cells (Ulbrich, 2011), the measurement of these effects on PV modules (Al Husna, 2018), and the measurement as well as the analytical and numerical simulation of AOI effects (Reiners, 2018). In this work, a novel modelling approach is proposed. It combines traceable laboratory measurements of the AOI dependent spectral responsivity of PV devices with the irradiation conditions under diffuse sunlight allowing to obtain information on the performance of PV devices under real world conditions. It will be compared to state-of-the-art models, including a comprehensive discussion of the associated uncertainty.

At Germany's national metrology institute Physikalisch-Technische Bundesanstalt (PTB) a laser-based differential spectral responsivity facility (Laser-DSR) was installed. It provides high-accuracy primary calibrations of the absolute spectral responsivity of reference solar cells at various irradiance levels and temperatures (Winter, et al., 2014). An important parameter for the PV device performance is the short-circuit current of the device. This quantity is primary calibrated under normal incidence. In this work, the facility has been upgraded to measure the AOI and polarization dependent spectral responsivity of reference solar cells and PV devices.

The experimental characterization of the detector's responsivity as well as the properties of the diffuse light source (i.e. the sky) requires considerable efforts. Within the scope of this thesis the primary calibration facility at PTB has been thoroughly characterized to perform AOI dependent measurements of PV devices with associated uncertainties. With this multidimensional data, AOI dependent effects on the device performance under diffuse light (e.g. global natural sunlight) can be studied and the short-circuit current under any spectral and directional distribution of the incident irradiation can be computed. While the computation of angular-dependent optical losses is straightforward for direct irradiance, the computation of the diffuse irradiance components requires information on the directional distribution, termed as radiance. Therefore, in this work the impact of angular-dependent effects on PV device calibration measurements under consideration of both the angular-dependent spectral responsivity and the anisotropic sky spectral radiance is studied. The proposed model additionally considers tilted device orientations and the spectral albedo of the ground surface.

The model proposed allows most possible uncertainty contributions to be quantified, whereas such contributions are neglected when using state-of-the-art models. By means of a sensitivity analysis possible sources of uncertainty of three different models that are compared in this work are identified. Advantages and shortcomings of these models and their accuracy are discussed. Beside a thorough analysis on exemplary ideal scenarios, an additional study on the impact of variable irradiation conditions is performed, including the diurnal variation of the irradiation conditions simulated for an entire day.

There are versatile studies onto this thematic. To the authors knowledge, no model has been published yet that allows to investigate the impact of simplifications on the uncertainty of primary calibrations and energy rating parameters. This thesis includes the required

methods and developments to perform these studies and discusses the results in the context of the simplifications made in the procedures of the new IEC energy rating standard.

A background on the fundamental physics that is relevant for high-accuracy PV performance measurements and calibrations is presented in Chapter 2. The concept of PV module energy rating is summarized, and an overview on the evaluation of the measurement uncertainty is given. Chapter 3 introduces the mathematical framework of the multidimensional model proposed and developed in this work. It is aimed at the determination of spectral-angular mismatch effects for high-accuracy measurements and calibrations of solar cells performed under diffuse natural sunlight and for the use with solar simulators. In Chapter 4, experimental results of AOI dependent measurements of several PV devices are presented. This is accompanied by a description of the measurement equipment and the facility that is used for polarization- and angular-dependent spectral responsivity measurements of PV devices. A comprehensive analysis of the measurement uncertainty is presented, including a thorough characterization of the AOI facilities and procedures developed in this work.

In Chapter 5 a computational study on the impact of spectral-angular mismatch on high-accuracy calibrations of the short-circuit current of PV devices taken under global natural sunlight is presented. A sensitivity analysis is performed and the impact of different assumptions that simplify the multidimensional approach is discussed. A comprehensive comparison on alternative angular mismatch correction approaches is presented, their measurement uncertainties are discussed. Using a scenario that exemplifies the impact of varying solar irradiation conditions on the spectral-angular losses for different PV devices compared to ideal detectors, the results of three different models are evaluated and compared. Chapter 6 includes a discussion on the presented results, putting them into the context of recent developments and standardization activities in this field. Also, possible subjects for further research on this topic are identified. Chapter 7 concludes this thesis with a summary.

2. Fundamentals

This chapter includes the fundamentals related to the thematic of this thesis. A first section treats the background of solar radiation in the context of terrestrial photovoltaic use. An introduction on the radiative transfer simulation software *uvspec* is summarized in Section 2.2. In the third section the principles of operation of crystalline silicon solar cells, such as the spectral responsivity and optical losses are shown. A separate section is dedicated to calibration methods for solar cells and PV modules. The concept of PV module energy rating that uses an energy-based parameter for the module performance under realistic operating conditions is treated subsequently. It includes angular and spectral mismatch correction procedures and an alternative approach for the AOI correction used in the field of photometry. Finally, methods for the determination on measurement uncertainty components are summarized.

2.1. Solar radiation

Thermal energy is generated by a thermonuclear reaction in the Sun which is mainly composed of hydrogen. The heat generated in the region called the core is transported by convection and radiation to the Sun's surface, the photosphere. The Sun's surface is the source of the mostly visible solar radiation received by the Earth. Due to its inhomogeneous nature the temperature of the photosphere ranges from 4000 K to 6000 K. For the terrestrial use of solar radiation as source of photovoltaic energy, a detailed understanding of the nuclear processes in the Sun is not important. Interesting is the amount of energy and its temporal and spectral variations. The average temperature of the Sun's surface is approximately equivalent to a black body temperature of 5760 K (Goswami, et al., 2000a). The extraterrestrial irradiance received by the Earth's atmosphere is also termed as solar constant with a value of 1367 Wm^{-2} (Iqbal, 1983). It represents an average value. More recent measurements show that the solar constant is not constant. It was determined seven years ago to be slightly lower with 1361 Wm^{-2} based on satellite measurements (Kopp & Lean, 2011). This value is confirmed by a recent reevaluation (Gueymard, 2018). The spectral distribution of the solar irradiance was experimentally determined by various measurements taken by space aircrafts, high-altitude flights, satellites and balloons. All spectral irradiances E_λ in this work are given in $\text{Wm}^{-2}\text{nm}^{-1}$.

The solar radiation arriving at the Earth's atmosphere interacts by absorption, scattering and reflection processes with its gases and particles. These processes have significant impact on the magnitude and the spectral and directional composition of the solar radiation incident on the Earth's surface. Subsection 2.1.1 gives a brief overview on the attenuation processes of solar radiation passing through the atmosphere. Subsection 2.1.2 includes information on the polarization of the skylight, that is dependent on observers viewing angle (direction).

A simple quantity that describes the pathlength of the light travelling through the atmosphere is the airmass AM that is defined in simplified Equation (2.1) that is accurate for

$\theta_{SZA} < 60^\circ$. The extraterrestrial solar irradiance is also termed as AM0 because no interaction with the atmosphere is present. AM1 means that the Sun's position is in the zenith, while larger AM values AMx with $x > 1$ represent scenarios with solar zenith angles θ_{SZA} larger than zero.

$$AM = \frac{1}{\cos \theta_{SZA}}. \quad (2.1)$$

The international standard (IEC 60904-3 Edition 2, 2008) used in the photovoltaic community defines a terrestrial reference solar spectral irradiance with AM1.5G. The letter G indicates a global irradiance, that includes direct, diffuse and albedo irradiation components. The reference spectrum is determined by a radiative transfer model called SMARTS (Gueymard, 1995; Gueymard, et al., 2002). The reference spectral irradiance is shown in Figure 2.1 (while details on it are discussed within a comparison made in Section 3.5). This spectrum is an important part of the STC that are used for a world-wide homogenized comparability of performance measurements of photovoltaic devices, such as solar cells or PV modules.

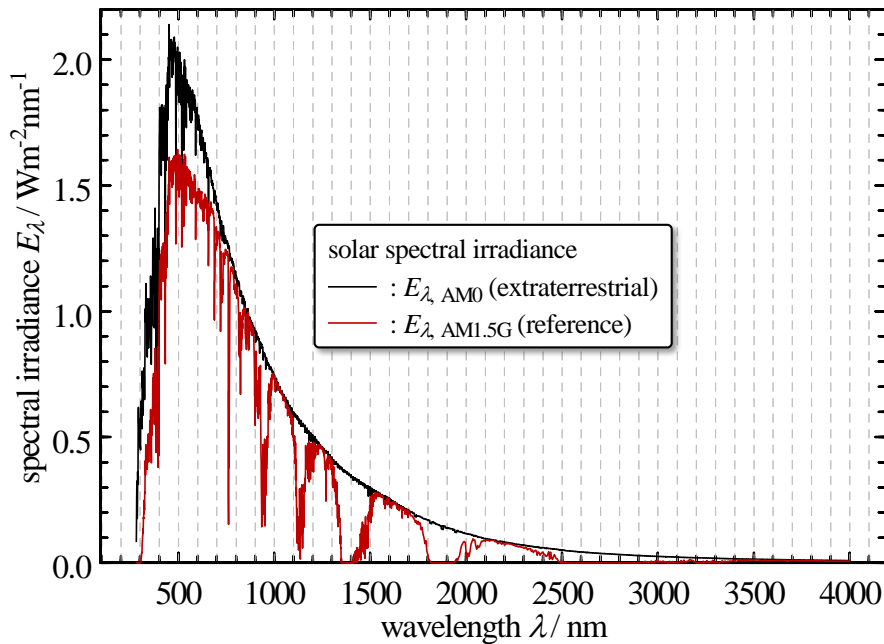


Figure 2.1: Extraterrestrial solar spectral irradiance with AM0 (black curve); and reference spectral irradiance AM1.5G (red curve) within a wavelength range from 280 nm to 4000 nm in accordance with (IEC 60904-3 Edition 2, 2008).

It means, that all calibration measurements taken under any spectral irradiance should be corrected by applying a spectral mismatch correction that compensates for the differences in the apparent spectrum, different from the reference spectrum and the different spectrally selective devices. The spectral mismatch correction in accordance with the standard (IEC 60904-7 Edition 3, 2008) is discussed in Section 3.4.

Note that this work mainly focusses on a computational study on high-precision measurements taken under clear sky conditions. Scenarios including overcast sky or broken cloud conditions introduce significant differences in the irradiation conditions. Previous studies observe that under broken cloud conditions an enhancement of the global horizontal irradiance relative to clear sky conditions appears, if the direct beam is not attenuated by surrounding cumulus clouds. (Gueymard, 2017a; Gueymard, 2017b; Zhang, et al., 2018). Irradiances of up to 1891 Wm^{-2} have been reported in these studies. Differently distributed water or ice clouds that are not stationary in the atmosphere introduce more absorption and scattering of the incident solar radiation. Beside fluctuations in the global irradiance, the directional distribution of the incident irradiation, the radiance, and the spectral irradiance may change. Because high-precision measurements on PV devices require very stable irradiation conditions, the investigation of more complex irradiation scenarios, including clouds, is not included this work.

More details on the impact of a changing airmass under clear sky conditions are presented and discussed in Subsection 5.3.1. by means of the average photon energy parameter (*APE*). This parameter is proposed by Jardine, et al. to describe the spectral distribution as a parameter that is independent from the technology of the photovoltaic device and the incident solar irradiance (Jardine, et al., 2002). Therefore, it is used to compare spectral irradiance measurements, e.g. taken at different locations (Norton, et al., 2015). The average photon energy in eV is defined as:

$$APE = \frac{1}{q_e} \left(\frac{\int E_\lambda d\lambda}{\int \Phi_\lambda d\lambda} \right), \quad (2.2)$$

where the spectral photon flux density

$$\Phi_\lambda = \frac{E_\lambda}{hc/\lambda}, \quad (2.3)$$

with the speed of light c and the Planck constant h , the elementary electric charge q_e , and the photon wavelength λ .

2.1.1. Direct solar irradiance and diffuse sky radiance

In the field of photovoltaic metrology, the incident solar irradiation is distinguished between direct and diffuse irradiance components. Both components are dependent from processes caused by the Earth's atmosphere. Parts of the extraterrestrial solar radiation is reflected back into space, while some parts are absorbed by water vapor and air, some get scattered by different molecules or dust particles. The molecules can be composed of water vapor, air and aerosols. The solar radiation that reaches the surface without a change in the direction is called the direct irradiance E_{dir} and is attenuated by the atmosphere. The scattered radiation that reaches the surface makes up the diffuse irradiance E_{diff} (Goswami, et al., 2000a). The diffuse irradiance includes also the part of radiation which is reflected multiple times between ground and atmosphere. The contribution of the direct sunlight is approximately 10 times higher than the diffuse component under clear sky conditions. Because of its rather small contribution to the global irradiance, and for simplicity, the

diffuse irradiance is often assumed to be isotropically distributed in the sky's hemisphere. This is not the case for realistic conditions. A circumsolar brightening around the solar disc and a horizon brightening are apparent at the sky. The brightening can be even seen by naked eye under clear sky conditions. To describe the directional dependence of the sky radiations anisotropy the radiometric quantity radiance L is used. In simple terms it indicates how bright a part of the sky appears. More details on the radiance L_{sky} are elaborated and presented in Chapter 3 of this work. The radiance anisotropy of the sky and its impact on the PV devices output short-circuit current plays an important role in this study. The short-circuit current is an electrical parameter that is proportional to the irradiance when the PV device is linear with the irradiance in the relevant range. Chapter 3 also includes a visualization on sky radiance patterns and their spectral distributions under clear sky conditions that are suitable for high-precision measurements of the performance of solar cells and PV modules, and for calibrations of their short-circuit currents.

2.1.2. Polarization of the sky

The extraterrestrial solar radiation that passes through the Earth's atmosphere is scattered resulting in diffuse radiation. The scattering is caused by absorption and re-emission processes in the atmospheric molecules. This process is termed as Rayleigh scattering, which also causes the blue color of the skylight due to its rather high wavelength-dependency. The electric field of the incident light interacts by coupling with the electric dipole of the gas molecules in the atmosphere. Molecules with much smaller diameters than the wavelength of the incident light scatter the light with the fourth power of its frequency. Consequently, the efficiency of molecular scattering for blue light is much higher than for red light (Goldstein, 2010). The following example easily illustrates the directional dependence of scattered polarized light from an observer's point of view located at the Earth's surface:

The molecular scattering is dependent on the direction and on the incident light polarization. When the observers viewing angle directs in the zenith while the sun is located at the horizon a molecule located at the zenith re-emits horizontally polarized light in the direction of the observer because of the dipole field of the molecule. Vertically polarized light is dominantly scattered in the forward direction of the incident light, so the observer doesn't see the light emitted by the molecule. Thus, the observer sees only the horizontally polarized light component at that specific viewing angle if it is assumed that the incident direct sunlight is unpolarized.

Note that the direct sunlight can be polarized dependent on the spectral emission of the Sun's surface and surrounding layers. Observation of the Sun's disk show that the polarization is not uniform and that it depends on the solar magnetic fields (Goldstein, 2010). In this work the direct sunlight is assumed to be unpolarized in a first approach. The interested reader will find further details on measurements and images of the sky's polarization patterns in (Gál, et al., 2001) and on a simulation study in (Emde, et al., 2010).

2.2. Radiative transfer simulation – *uvspec* as a tool

To perform computational studies with simulated solar irradiation conditions the freely available software package libRadtran version 2.0 is used in this work. The central program *uvspec* included in libRadtran is a radiative transfer model that calculates the radiance field in the Earth’s atmosphere (Mayer & Kylling, 2005). It computes the solar irradiance as well as the solar radiance (the directional distribution of the solar irradiation) on the Earth’s surface.

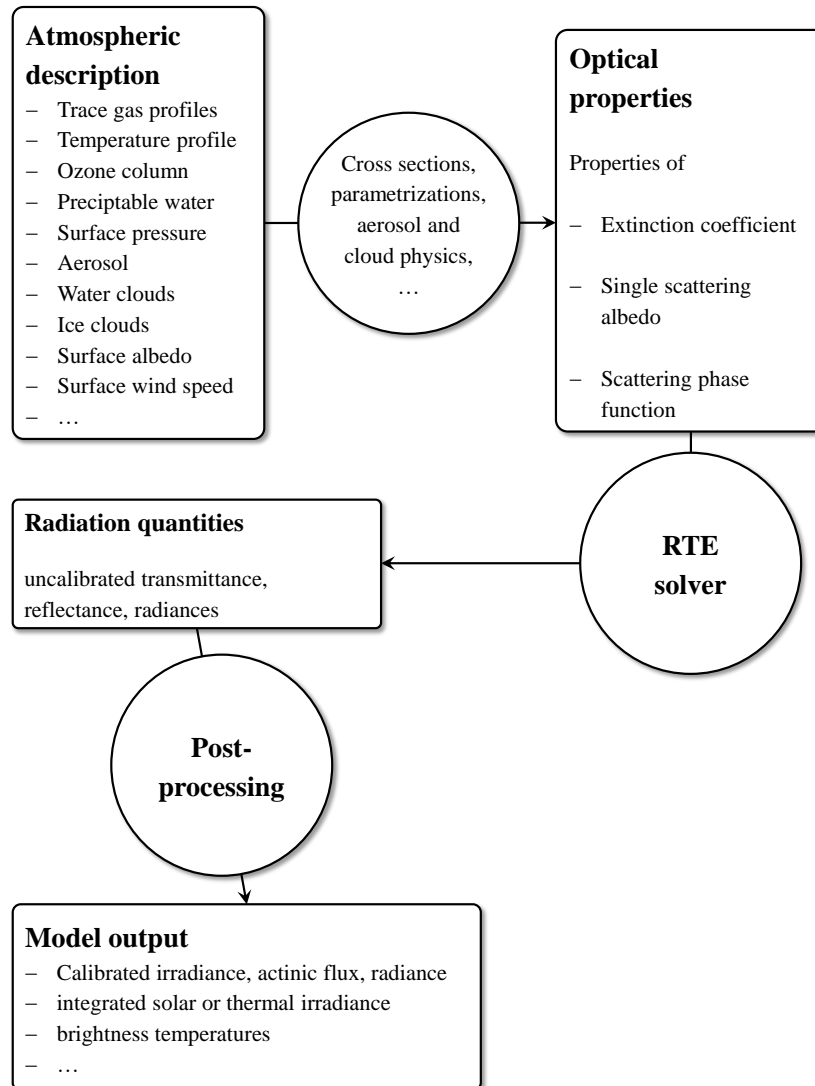


Figure 2.2: Structure of the *uvspec* model. This scheme is originally published in (Mayer & Kylling, 2005) and used here to summarize the radiative transfer model used in this work as a tool for the calculation of solar irradiances and radiances.

To perform studies with the terrestrial solar spectrum, a large variety of input parameters can be selected, including trace gas profiles, temperature profiles of different atmospheric layers, ozone column, water, aerosol properties, clouds, surface albedo (reflection), and more. A radiative transfer equation solver calculates then the radiances and irradiances

under consideration of the given optical properties for each wavelength. The post-processing includes corrections of the Sun to Earth distance, dependent on the day of the year and a multiplication with the extraterrestrial solar spectrum. The schematic shown in Figure 2.2 gives an overview on the structure of the radiative transfer model *uvspec*. More detailed information on the radiative transfer software can be found in (Mayer & Kylling, 2005; Mayer, et al., 2015; Emde, et al., 2016).

2.3. Principle of operation of conventional silicon solar cells

This section provides a description of the basic physics of silicon solar cells. Most of its content summarizes fundamental chapters of textbooks (McEvoy, et al., 2012; Goswami, et al., 2000b) and lecture material (Glunz & Würfel, 2014). The following lines include the background to comprehend the investigated quantities and relationships in this work, such as the short-circuit current, the spectral responsivity and optical losses of solar cells.

The photovoltaic conversion is the direct conversion of sunlight (electromagnetic radiation) into electrical energy. This conversion principle works without an intervening heat engine. Photons are absorbed by valence electrons of atoms when the photon energy is equal or larger than the band gap of a semiconductor. The photons excite electrons from the valence band into the conduction band. In case of an absorbed photon with lower energy than the band gap, the excess energy will be dissipated as heat by a conversion to kinetic energy of the electron to the lattice of the material (crystalline silicon) and the electron remains in the valence band. A photon with higher energy than the band gap excites an electron in the conduction band and the excess energy increases its kinetic energy transferred to the lattice. It is important to know that from a single photon only one electron can be excited. Thus, only one electron-hole pair can be generated per photon within the material. In the conduction band the electron can move freely before it recombines with a hole.

Conventional solar cells, i.e. silicon-based solar cells, consist of a *p-n*-junction that is realized by doping of the silicon. The pure bulk material, the base, is therefore doped with trivalent atoms (e.g. boron) creating a *p*-type semiconductor with excess holes as the majority charge carriers. A second layer, the emitter, is doped with pentavalent atoms to create a *n*-type semiconductor (e.g. phosphorus) with excess electrons as the majority charge carriers. The region between base and emitter forms the *p-n*-junction where almost no mobile charge carriers are apparent due to an electric field between the two junctions. The voltage observed due to the electric field between the two differently charged ion cores is termed as the built-in voltage. If light is absorbed by the solar cell and an electron-hole pair is generated, transport mechanisms can move the free carriers across the *p-n*-junction within their respective diffusion lengths, generating a current. There are two different mechanisms that cause a charge carrier separation within the solar cell and thus generating a current across the junction: drift and diffusion.

The drift driving source is the electric field in the material that causes a net transport of electrons in the opposed direction of the electric field from the *p*-region to the *n*-region and vice versa for holes. Diffusion is transporting charge carriers from the region with high concentration to the region with low concentration. Both transport mechanisms cause a net

current termed as the dark current density (or diode saturation current density) J_0 that is also apparent without illumination of the device. An additional light induced recombination current J_r acts against the dark current, so that the current density across the junction J_j is defined as:

$$J_j = J_r - J_0, \quad (2.4)$$

while J_r is proportional to J_0 and is dependent on the temperature T and on the voltage V , applied at the junction terminals

$$J_r = J_0 e^{\frac{-q_e V}{kT}}, \quad (2.5)$$

with the Boltzmann constant k , so that the junction current density is

$$J_j = J_0 \left(e^{\frac{-q_e V}{kT}} - 1 \right). \quad (2.6)$$

The solar cells area is A and, for simplicity, it is assumed that no parasitic losses are apparent. Under illumination of the solar cell the currents in the electrical circuit follow two parallel paths, one through the junction I_j and another through the terminals I . The current I that can be extracted through an external load (i.e. a resistance) is then defined as:

$$I = I_{SC} - I_j = I_{SC} - I_0 \left(e^{\frac{-q_e V}{kT}} - 1 \right), \quad (2.7)$$

with I_{SC} the short-circuit current of the solar cell that is generated by the available photons. Equation (2.7) describes the ideal characteristic I - V -curve, assuming a high-quality solar cell with no parasitic losses, that is used to determine the solar cells conversion efficiency under standard test conditions. It is important to know that the generated I_{SC} is dependent on the energy of incident photons, resulting in a wavelength-dependent quantum efficiency or spectral responsivity. The spectral responsivity of conventional silicon solar cells is explained in the next subsection.

Note that Equations (2.4) to (2.7) represent an idealized solar cell by using a one diode approach including a number of approximations. For a deeper understanding of parasitic resistance effects and charge carrier recombination effects (described by a second diode) that are dependent on the region in the solar cell the author refers to relevant textbooks such as (McEvoy, et al., 2012). Common procedures on PV performance measurements are described in the textbook (Emery, 2005) and in the international standard (IEC 60904-1 Edition 2, 2006).

2.3.1. Spectral responsivity

The relation between the generated short-circuit current of a solar cell and the incident irradiation is the quantum efficiency. Thereof, the spectral responsivity can be derived. Both are dependent on the wavelength and on the material properties of the solar cell. This subsection is based on the content of the online learning platform PVEducation.org

(Honsberg & Bowden, 2018a). To ease the understanding of this relation one needs to know that the absorption of photons in materials is a function of the wavelength and penetration depth. Thus, the spectral photon flux Φ_λ at a distinct wavelength is a function of the penetration depth x in the material:

$$\Phi_\lambda(x) = \Phi_\lambda(x = 0)e^{-\alpha x}, \quad (2.8)$$

while $x = 0$ defines the depth at solar cells surface. The absorption α is a function of the photon wavelength λ and dependent on the extinction coefficient κ , a property related to the refractive index n :

$$\alpha(\lambda) = \frac{4\pi\kappa}{\lambda}. \quad (2.9)$$

The penetration depth increases with increasing wavelength. It is assumed that the generation rate of electron-hole pairs $G(x)$ in the solar cell is proportional to $\Phi_\lambda(x)$. The collection probability $CP(x)$ that describes the contribution of the charge carrier to the generated short-circuit current density J_{SC} at a defined depth x within the material is multiplied by the generation rate $G(x)$. Thus, the generated current density is

$$\begin{aligned} J_{SC} &= q_e \int_{x=0}^{x=l} G(x) \cdot CP(x) dx \\ &= q_e \int_{x=0}^{x=l} \left(\int_{\lambda} \alpha(\lambda) \Phi_\lambda(x = 0) e^{-\alpha x} d\lambda \right) \cdot CP(x) dx \end{aligned} \quad (2.10)$$

Figure 2.3 shows the generation rate and the collection probability as schematic functions of the absorption depth x in the device with a thickness l . The quantum efficiency can be calculated or simulated when a variety of parameters including the collection probability $CP(x)$ are known. The collection probability $CP(x)$ depends on the charge carrier life times, surface recombination velocities and diffusion lengths of the electrons and holes in the material. This is not presented in this work, which focusses on the experimental determination of the quantum efficiency.

Usually the external quantum efficiency EQE is determined experimentally. It defines the ratio between the incident photons on the solar cells surface and the usable charge carriers contributing to the generated output short-circuit current J_{SC} .

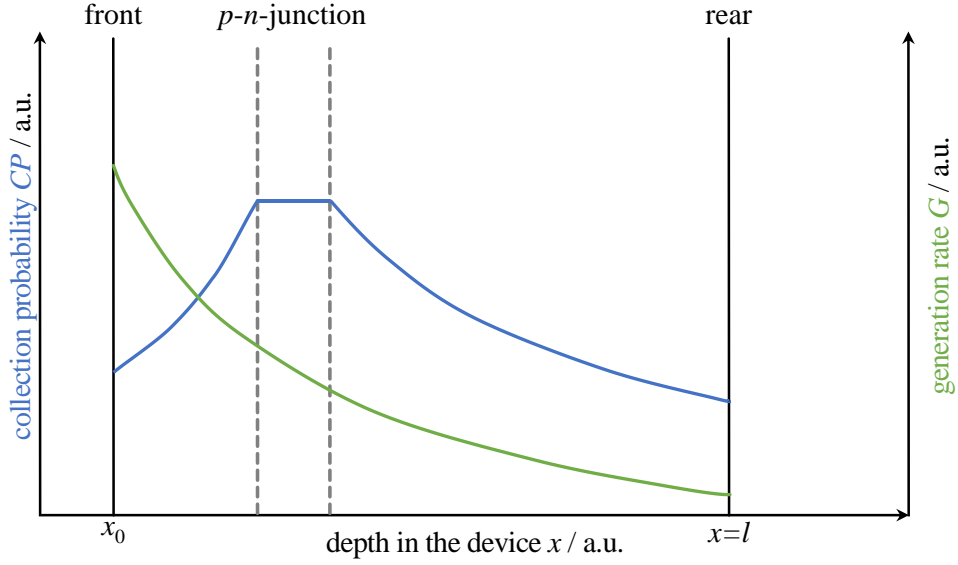


Figure 2.3: Generation rate G and the collection probability as simplified schematic functions of the absorption depth in the device (x_0 is located at $x = 0$). The schematic is based on the figures of the educational website PVEducation.org and is modified for this work (Honsberg & Bowden, 2018b).

If the reflectance r of the solar cells surface is known, the internal quantum efficiency $IQE(\lambda)$ is used to determine the short-circuit current density

$$J_{SC} = q_e \int_{\lambda} \Phi_{\lambda}(\lambda) (1 - r(\lambda)) IQE(\lambda) d\lambda, \quad (2.11)$$

while

$$EQE(\lambda) = (1 - r(\lambda)) IQE(\lambda). \quad (2.12)$$

In practice, the $IQE(\lambda)$ is determined from measurements of the $EQE(\lambda)$ and of the reflectance $r(\lambda)$. The $EQE(\lambda)$ is often expressed as the spectral responsivity of solar cells $s(\lambda)$ which is directly linked to the energy content of the incident photons. The spectral responsivity is computed in accordance with Equation (2.13)

$$s(\lambda) = \frac{q_e \lambda}{hc} EQE(\lambda). \quad (2.13)$$

Note that the spectral responsivity can be non-linear regarding the incident irradiance. Non-linearities can lead to an increase of the responsivity for rising irradiances towards 1000 Wm^{-2} or vice versa. Good reference solar cells that are used as irradiance sensors are therefore designed to provide high linearity in the range of their operating irradiance. This is achieved by producing the reference solar cells from a high-quality material (low impurities) and a suitable passivation. More details on the determination of the linearity of the spectral responsivity are presented in (Winter, 2003) and details on the determination

of the linearity of the short-circuit current of PV reference devices are included in the standard (IEC 60904-10 Edition 2, 2009).

2.3.2. Optical losses at surfaces

Optical losses of solar cell materials at surfaces occur due to reflection of the incident irradiation at the interface between the materials. To give a brief overview of the physical background of the angular-dependence of the reflectance, the most essential equations, Snell's law and the Fresnel equations are presented here.

Snell's law for planar surfaces with an interface from one material with the refractive index n_1 to another material with the refractive index n_2 is defined as

$$n_1 \sin \theta_i = n_2 \sin \theta_t, \quad (2.14)$$

with the AOI of the incident light θ_i and the AOI of the transmitted light θ_t , both relative to the surface normal of the interface.

The ratio of reflected light to the incident light is termed as the reflectance r when light is transmitted from one to another medium. The Fresnel equations describe the reflectance for linear polarized light with s- and p-polarization. Thereby is

$$r_s = \left| \frac{n_1 \cos \theta_i - n_2 \cos \theta_t}{n_1 \cos \theta_i + n_2 \cos \theta_t} \right|^2, \quad (2.15)$$

the reflectance of the s-polarized light, and

$$r_p = \left| \frac{n_1 \cos \theta_t - n_2 \cos \theta_i}{n_1 \cos \theta_t + n_2 \cos \theta_i} \right|^2, \quad (2.16)$$

the reflectance of the p-polarized light. If the θ_t is unknown, the reflectance's can be also calculated with the refractive indices and by rearranging the Equations (2.15) and (2.16) with Snell's law (Equation (2.14)):

$$r_s = \left| \frac{n_1 \cos \theta_i - n_2 \sqrt{1 - \left(\frac{n_1}{n_2} \sin \theta_i\right)^2}}{n_1 \cos \theta_i + n_2 \sqrt{1 - \left(\frac{n_1}{n_2} \sin \theta_i\right)^2}} \right|^2, \quad (2.17)$$

and

$$r_p = \left| \frac{n_1 \sqrt{1 - \left(\frac{n_1}{n_2} \sin \theta_i\right)^2} - n_2 \cos \theta_i}{n_1 \sqrt{1 - \left(\frac{n_1}{n_2} \sin \theta_i\right)^2} + n_2 \cos \theta_i} \right|^2. \quad (2.18)$$

Thus, the reflectance at a material interface for unpolarized light is

$$r = \frac{r_s + r_p}{2}. \quad (2.19)$$

In the following examples the angular-dependent reflectance's are presented for two different material interface combinations. Figure 2.4 shows the reflectance of an air to glass interface for s-, p- and unpolarized light as a function of θ_i in the top graph (solid lines). The bottom graph indicates the reflectance's for an air to silicon interface (dashed lines). Both graphs provide additional information on the relative angular-dependent transmittance τ on the scale located on right-hand side. The relative transmittance is normalized to its absolute value at an AOI perpendicular to the surface between both media $\theta_i = 0^\circ$.

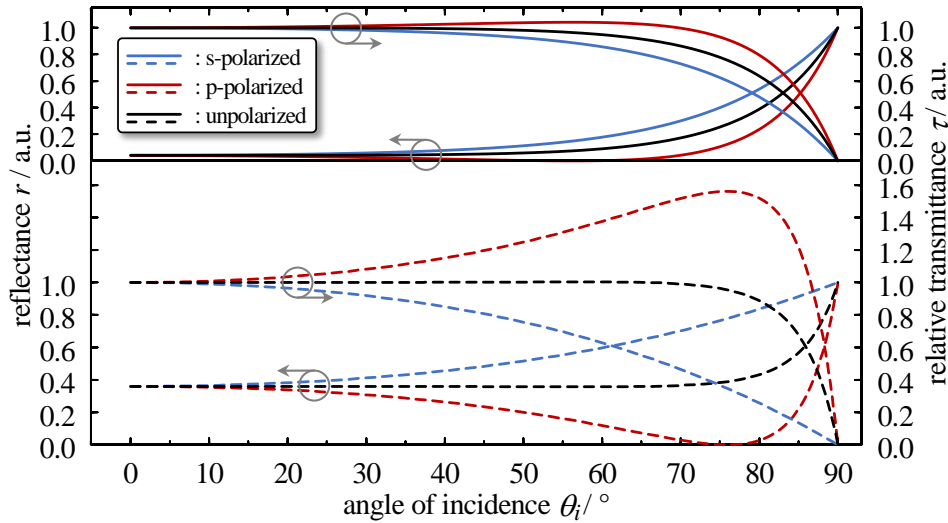


Figure 2.4: (Top graph and solid lines) Angular-dependent reflectance of differently polarized light calculated in accordance with the Fresnel Equations (2.17) and (2.18) for a planar air to glass interface with $n_1 = 1$ and $n_2 = 1.5$; and (Bottom graph and dashed lines) angular-dependent reflectance for a planar air to silicon interface with $n_1 = 1$ and $n_2 = 4$. Normalized angular-dependent transmissions with $\tau(\theta = 0^\circ) = 1$ are scaled on the axes at the right hand side. The black lines show the reflectance's and relative transmissions for unpolarized light while the blue lines represent the curves for s-polarized light and the red curves those for p-polarized light.

Note that the refractive index of a medium is dependent on the wavelength. Accordingly, the angular-dependent reflectance is also wavelength-dependent.

The Equations (2.14) to (2.19) represent the simplified case of a single planar interface. Modern crystalline silicon solar cells provide textured surfaces, light trapping mechanisms, and antireflective coatings. Additionally, they are encapsulated as PV modules so that a textured front glass and an ethylene vinyl acetate layer (EVA) are apparent in the optical path which makes it difficult to determine the reflectance solely by using the Equations (2.14) to (2.19). Because several interfaces are apparent, multiple reflections need to be considered by more complex models. Commonly ray tracing software is used to optimize solar cells and PV modules by reducing optical losses of the entire material system (Schinke, et al., 2018).

It is worth to mention that soiling of PV modules surfaces during their outdoor operation forms an additional layer in the optical path resulting in additional optical losses affecting

the energy yield (John, et al., 2014). The effects of soiling and degradation through aging are not investigated in this work. Optical losses due to absorption of encapsulant materials are neglected and thus not discussed in the theoretical part of this work.

2.4. Calibration of PV devices

Calibrated PV devices are usually used as irradiance sensors in various measurement environments. The main goal of utilizing calibrated PV reference devices is to ensure world-wide traceability and comparability of PV performance measurements. The calibrated quantity relevant for this work is the short-circuit current of the device under STC or in some cases a voltage proportional to it, that is traceable to the International System of Units SI. The definition of the STC is defined in the international standard (IEC 60891 Edition 2, 2009) and requires beside the AM1.5G reference spectral irradiance presented in Section 2.1 $E_{\lambda, \text{AM1.5G}}$ (or $E_{\lambda, \text{ref}}$ in this work), a device temperature T of 25°C and an irradiance E of 1000 Wm⁻². Two categories of calibrations are distinguished: primary and secondary calibration methods.

2.4.1. Primary calibration methods

Primary calibration methods are tracing the electrical output quantity of the PV device directly to radiometric standard detectors such as thermoelectric cavity radiometers (electrical substitution radiometers working at room temperature) and reference photodiodes, calibrated against a cryogenic radiometer (IEC 60904-4, 2009). Alternatively, traceability can be achieved by the calibration of the PV devices against radiometric sources such as standard lamps or high temperature black body radiators. Primary calibration methods achieve low uncertainties while the experimental effort is immense. Only a few laboratories world-wide offer primary calibrations of reference solar cells. The most renowned laboratories are the National Institute of Advanced Industrial Science and Technology AIST in Japan (Hishikawa, et al., 2003), the National Renewable Energy Laboratory NREL in the United States (Emery & Osterwald, 1989), the European Commission's Joint Research Centre JRC in Italy (Müllejans, et al., 2005a), and the Physikalisch-Technische Bundesanstalt PTB in Germany (Winter, et al., 2000). These four laboratories maintain the World Photovoltaic Scale WPVS. *"The WPVS provides a scale for PV performance measurements that has been established through round-robin calibration of a group of primary monocrystalline Si reference cells and is traceable to Système International (SI) units."* (Osterwald, et al., 1999). While the most laboratories practice **integral** (or broadband) **methods** of measurement with solar simulators or natural sunlight, the PTB applies a **spectral method** with monochromatic irradiation (Metzdorf, 1987), see Chapter 4.

2.4.2. Secondary calibration methods

Secondary calibration methods are tracing the electrical output quantity of the PV device to (primary) calibrated reference solar cells (IEC 60904-2 Edition 2, 2007). Therefore, solar simulators or natural sunlight are used, both represent irradiation sources for integral methods of measurement. Secondary calibrated solar cells and PV modules are commonly

used in the production environment for the quality assurance and testing. The experimental effort is lower than for the primary calibration method which causes a tradeoff in the accuracy. The reduced measurement uncertainty can be attributed to larger deviations of the apparent conditions to the STC and corrections therefore. When it comes to larger device areas that are relevant in the (industrial) application of PV, difficulties with the temperature control and uniformity of irradiation introduce larger sources of uncertainty. One of the most unattended sources of uncertainty in secondary PV device calibrations is the diffuse content of the incident irradiation as already illustrated in the introduction. The focus of this work is to emphasize the impact of systematic effects introduced by spectral and directional effects of the diffuse irradiance onto the PV device. Chapter 3 includes a novel correction technique based on a multidimensional model.

2.5. The concept of PV module energy rating

Performance measurements of PV devices output power under STC do not necessarily reflect the energy yield that can be expected under varying irradiation and temperature conditions when PV modules are used for its designated purpose under realistic outdoor conditions: As generators for electrical energy.

The international standard series “Photovoltaic (PV) module performance testing and energy rating” parts 1 to 4 describes a methodology to determine the maximum power output of PV modules over a range of irradiances and temperatures. In addition to the output power vs. temperature and irradiance characterization defined in the first part of the standard (IEC 61853-1, 2011), part 2 of the series includes a description of measurement procedures to determine the spectral responsivity, the AOI dependence and a methodology to determine the operating temperature of PV modules in dependence of ambient and for predefined mounting conditions (IEC 61853-2, 2016). The characteristic set of parameters defined in part 1 and 2 are then used for energy prediction purposes, that are defined in part 3 of the series (IEC 61853-3, 2018). It describes the determination of standardized PV module energy rating values. A first value characterizes the PV module energy output $W_{\text{mod,year}}$ in kWh for a complete year at maximum power output operation at differently defined reference climate profiles. A second parameter gives information about a normalized energy value, i.e. the climate specific energy rating *CSE*R of a PV module. The dimensionless *CSE*R value of a PV module for a reference climatic profile describes the ratio of the actual energy collection to that which would have been accumulated if the PV module operates with the efficiency measured under STC. The standard reference climatic profiles are defined in part 4 of the series (IEC 61853-4, 2018) that includes different irradiation, ambient temperature T_{amb} and wind speed v conditions for six different locations. Figure 2.5 illustrates the calculation procedure of the energy rating values for PV modules as a flow chart for a given climatic profile.

This work focusses on the correction of spectral- and angular-dependent effects that influences the power output of the individual PV device. Hence, the author will only give a brief description of the energy rating procedure defined in the standard series. The two Subsections 2.5.1 and 2.5.2 summarize the most important information for the theoretic background related to this work and includes the steps of the energy rating procedure

marked with a red dashed box in Figure 2.5. Further details on an alternative outdoor characterization method and the determination of the spectral responsivity of PV devices are described in the standards (IEC 61853-2, 2016) and (IEC 60904-8 Edition 3, 2014).

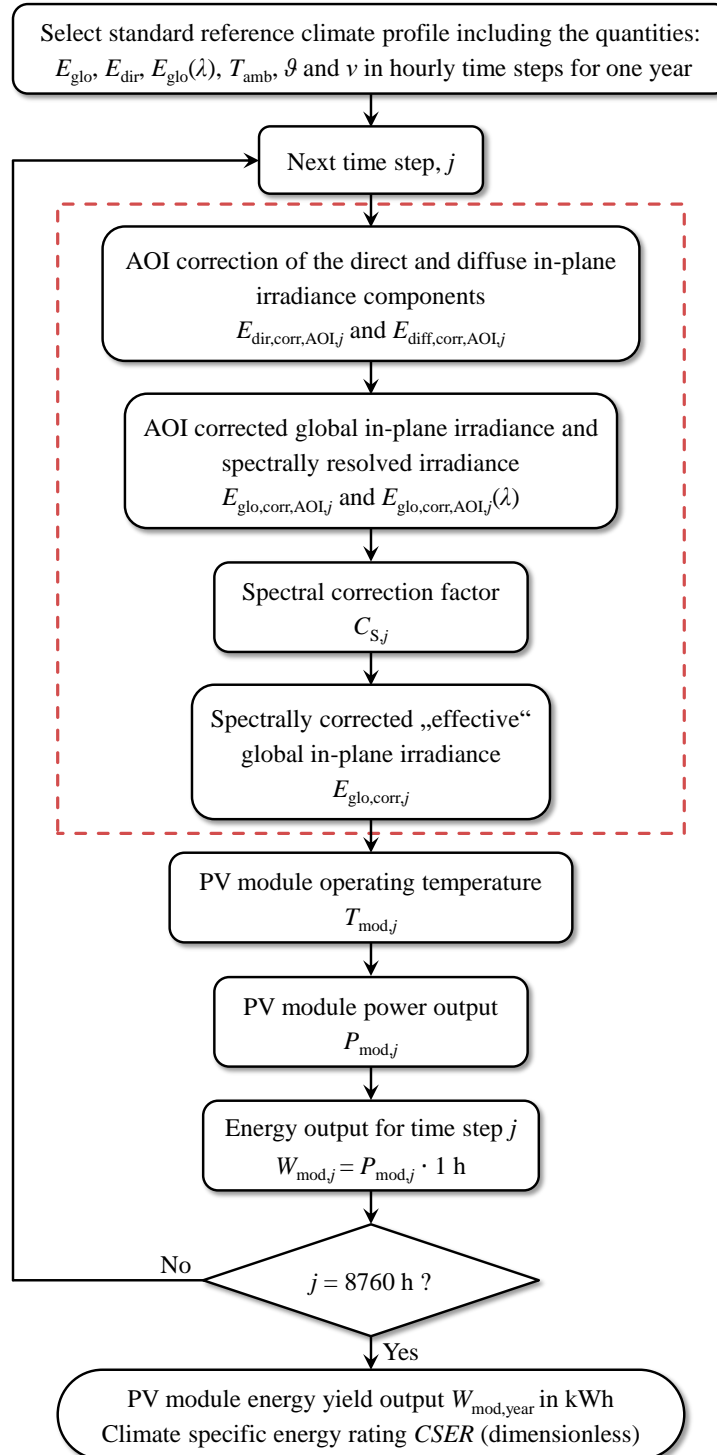


Figure 2.5: Flow chart of calculation procedure based on the figure included in (IEC 61853-3, 2018). The red dashed line marks the steps relevant for this work.

The AOI of the incident irradiation modifies the amount of reflected optical losses and thus the effective amount of solar energy that can be converted into electrical energy by a PV device. The losses are dependent on the material of the solar cell and encapsulation system of the PV module (i.e. front glass, encapsulant, and back sheet). Because conventional crystalline silicon modules commonly provide textured front surfaces for both layers, the front glass element and the solar cells, the Fresnel equation are not sufficient for modeling the angular-dependent reflectance and transmissions of the layer system. Therefore, the standard recommends in any case to measure the angular transmission.

2.5.1. Indoor measurement procedure for the determination of angle of incidence effects

This subsection briefly summarizes a solar simulator-based angular-dependent responsivity measurement procedure for PV modules in accordance with the standard (IEC 61853-2, 2016).

The measured quantity here is the short-circuit current I_{SC} of the PV device in dependence of the AOI within a uniform and stable light field. Details on the requirements of the instrumentation are listed in the standard. The most important requirements are:

- A reference PV device for the measurement of the solar simulators irradiance that is linear with the incident irradiance of the solar simulator in accordance with the standards (IEC 60904-2 Edition 2, 2007; IEC 60904-10 Edition 2, 2009).
- A solar simulator that provides a Class B irradiance uniformity of the light field and a Class C temporal stability in accordance with (IEC 60904-9 Edition 2, 2007). The solar simulator should provide a minimum of collimated irradiation which means that 95 % of the irradiance should be within an angle of radiation of 10° . The irradiance uniformity of the light field within the rotation volume of the device should be within the requirements of Class C.
- The rotation stage for the device under test should provide a positioning accuracy of better than $\pm 1^\circ$ for the AOI.

The measurement of the temperature and irradiance corrected short-circuit currents of the device under test should be taken among two orthogonal azimuthal directions in case if the symmetrical properties of the device are unknown. The rotational symmetry is verified by comparing the I_{SC} measured at the AOI's $\theta = -80^\circ$ and 80° . The measured ratios $[I_{SC}(80^\circ)/I_{SC}(0^\circ)]/\cos 80^\circ$ should be within a deviation of less than 2%. [Comment of the author: Note that an error of $\pm 1^\circ$ leads to larger deviations (see Figure 4.23 and the discussion on measurement uncertainty in Subsection 4.2.7).]

The relative angular transmission τ of the PV module in accordance with (IEC 61853-2, 2016) is defined as:

$$\tau(\theta) = \frac{I_{SC}(\theta)}{\cos \theta I_{SC}(0^\circ)}. \quad (2.20)$$

Because the angular transmission is measured with a discrete AOI step-width a fitting procedure is used in the standard to describe τ as follows:

$$\tau(\theta) = \frac{1 - e^{-\frac{\cos \theta}{a_r}}}{1 - e^{-\frac{1}{a_r}}}. \quad (2.21)$$

The angular loss coefficient a_r should be determined by using an appropriate fitting algorithm that determines a_r with at least three decimal places and an estimate of the measurement uncertainty. An explanatory note in the standard points out that this procedure implies that the angular-dependent responsivity of the device under test is equal for both spectral irradiances, this under direct sunlight and this under diffuse sunlight.

This simplification is questioned in this work by performing a sensitivity analysis shown in Subsection 5.1.5. that is focused on the impact of this assumption on the accuracy of the procedure.

2.5.2. Angle of incidence and spectral correction procedures in accordance with IEC 61853-3

To determine the standardized PV module energy output, one should follow the procedure defined in (IEC 61853-3, 2018) that is summarized by a flow chart shown in Figure 2.5. The relevant steps that are used in this work are marked with a red dashed box in the flow chart and include the AOI correction of the direct solar irradiance and diffuse irradiance components, and thus the AOI corrected global in-plane irradiance, the spectral correction factor, and the spectrally corrected “effective” irradiance. The procedure is applied repetitively for each hour of the climate profile to finally obtain an AOI and spectral corrected energy output that effectively remains for the conversion of solar energy into electrical energy under the specific standard reference climate profile.

The hourly global in-plane irradiance $E_{\text{glo,corr,AOI},j}$ that is corrected for the AOI is given by the components of the AOI corrected direct irradiance $E_{\text{dir,corr,AOI},j}$ and the diffuse irradiance $E_{\text{diff,corr,AOI},j}$ as defined in (IEC 61853-3, 2018):

$$E_{\text{dir,corr,AOI},j} = E_{\text{dir},j} \left[\frac{1 - e^{-\frac{\cos \vartheta_j}{a_r}}}{1 - e^{-\frac{1}{a_r}}} \right], \quad (2.22)$$

with $E_{\text{dir},j}$ the uncorrected in-plane direct irradiance at the j^{th} hour, and ϑ_j is the angle between sun and the normal of the PV module.

$$\begin{aligned}
 & E_{\text{diff,corr,AOI},j} \\
 &= E_{\text{diff},j} \left[1 - e^{-\frac{1}{a_r} \left(\frac{4}{3\pi} \left(\sin \beta + \frac{\pi - \beta - \sin \beta}{1 + \cos \beta} \right) + \left(\frac{1}{2} a_r - 0.154 \right) \left(\sin \beta + \frac{\pi - \beta - \sin \beta}{1 + \cos \beta} \right)^2 \right)} \right], \quad (2.23)
 \end{aligned}$$

with $E_{\text{diff},j} = E_{\text{glo},j} - E_{\text{dir},j}$ the uncorrected in-plane diffuse irradiance at the j^{th} hour and β the tilt angle of the PV module in radians that has a fixed orientation. Consequently,

$$E_{\text{glo,corr,AOI},j} = E_{\text{dir,corr,AOI},j} + E_{\text{diff,corr,AOI},j}. \quad (2.24)$$

The Equations (2.22) and (2.23) are based on a model introduced by Martin and Ruiz (2001; 2002) and are simplified by the assumption that no ground-reflected irradiance is apparent. Therefore, in this work it is further termed as simplified MR model. Moreover, the MR model assumes that the diffuse irradiance is distributed isotopically over the hemisphere within the field of view of the PV device.

Because the standard reference climate datasets are not providing spectrally resolved data for both, the direct and the diffuse irradiance separately, but datasets with a discrete bandwidth for the global irradiance $E_{\text{glo},j}(\lambda)$ in Wm^{-2} ; the AOI correction of the global spectrum is applied as follows:

$$E_{\text{glo,corr,AOI},j}(\lambda) = \frac{E_{\text{glo,corr,AOI},j}}{E_{\text{glo},j}} \cdot E_{\text{glo},j}(\lambda). \quad (2.25)$$

Since the PV modules performance changes when different spectra are apparent a spectrally corrected or “effective” global in-plane irradiance $E_{\text{glo,corr},j}$ needs to be calculated for each hour. It accounts for the spectral mismatch effect. In a first step, a spectral correction factor $C_{S,j}$ at the hour j is determined by using the relative spectral responsivity $s_{\text{rel}}(\lambda)$ of the PV module as defined in the procedures written in (IEC 61853-3, 2018) and in Equation (2.26). $s_{\text{rel}}(\lambda)$ is measured as prescribed in the standards (IEC 61853-2, 2016) and (IEC 60904-8 Edition 3, 2014).

$$C_{S,j} = \frac{1000 \frac{\text{W}}{\text{m}^2} \int_{300 \text{ nm}}^{4000 \text{ nm}} E_{\lambda,\text{glo,corr,AOI},j}(\lambda) \cdot s_{\text{rel}}(\lambda) d\lambda}{E_{\text{glo,corr,AOI},j} \int_{300 \text{ nm}}^{4000 \text{ nm}} E_{\lambda,\text{ref,bands}}(\lambda) \cdot s_{\text{rel}}(\lambda) d\lambda}, \quad (2.26)$$

with the in-plane spectral irradiance (in $\text{Wm}^{-2}\text{nm}^{-1}$) that are calculated as the ratios of $E_{\text{glo,corr,AOI},j}(\lambda)$ and the width of the discrete spectral bands, in nm. Accordingly, $E_{\lambda,\text{ref,bands}}(\lambda)$ is the equivalent spectral irradiance within discrete spectral bands for the spectral irradiance $E_{\lambda,\text{ref}}(\lambda)$ under AM1.5G STC in accordance with the standard (IEC 60904-3 Edition 2, 2008). Consequently, the effective in-plane irradiance that is corrected for AOI and spectral effects is given as

$$E_{\text{glo,corr},j} = C_{S,j} \cdot E_{\text{glo,corr,AOI},j}. \quad (2.27)$$

2.6. The f_2 model for the determination of angular-dependent optical losses

The international standard (ISO/CIE 19476, 2014) which addresses the research field of photometry includes a procedure for the characterization of the directional “*response*” of planar illuminance meters. This instrument characteristic is described by a directional response function $f_2(\theta, \varphi)$ and an index f_2 . The index f_2 characterizes the deviation of an illuminance meter relative to an instrument following the cosine law as both would be illuminated by an isotropic luminance distribution. Thus, f_2 represents a measure of the instrument’s relative optical loss.

In accordance with the standard, $f_2(\theta, \varphi)$ should be determined experimentally for varying AOI’s θ ranging from 0° to 80° at four different orthogonal azimuth orientations φ ($0, \pi/2, \pi, 3\pi/2$) by measuring the angular-dependent output signal Y of the illuminance meter:

$$f_2(\theta, \varphi) = \frac{Y(\theta, \varphi)}{Y(0, \varphi) \cdot \cos \theta} - 1. \quad (2.28)$$

The index f_2 is calculated as:

$$f_2 = \frac{1}{4} \sum_{i=0}^3 f_2(\varphi = i \frac{\pi}{2}), \quad (2.29)$$

$$\text{with} \quad f_2(\varphi) = \int_0^{80^\circ \cdot \frac{\pi}{180^\circ}} |f_2(\theta, \varphi)| \cdot \sin 2\theta \, d\theta. \quad (2.30)$$

Note that the angles used in Equations (2.28)-(2.30) are in radian.

In Chapter 5 of this work the f_2 model is used in a modified version, based on the CIE standard, to determine and correct angular-dependent losses of solar cells and to compare the results with other models.

2.7. Measurement uncertainty

The following section includes a summary on basic definitions and formulations in the context of the thematic: determination of the uncertainty in measurements. It summarizes the content elaborated in a previous work of the author (Plag, 2013), and from a more recently published thesis (Mihaylov, 2016). Both theses represent comprehensive studies of measurement uncertainty propagation in the thematic field of solar cell calibration and the estimation of PV module energy rating. A first subsection includes the classical approach for the determination on measurement uncertainty, while a second subsection focusses on the determination on uncertainties using a Monte Carlo method to overcome limitations of the classical approach when multidimensional or correlated quantities needs to be considered. The content of this section should facilitate the uncertainty analysis performed for the measurements of the angular-dependent spectral responsivity of solar cells, presented in

Chapter 4, and the evaluation of uncertainties discussed in the Sections 5.2 and 5.3, rather than being a comprehensive guide.

2.7.1. Measurement uncertainty: Definitions in accordance with the GUM

Several guides exist that describe procedures for the evaluation or estimation of uncertainty. An internationally accepted guide in the metrology community is the ISO standard (JCGM 100, 2008) entitled “Guide to the Expression of Uncertainty in Measurement” (GUM). The International Vocabulary of Metrology (VIM) (JCGM 200 Edition 3, 2012) contributes a valuable reference book for scientists and engineers involved in performing measurements. It includes a comprehensive vocabulary essential for the global harmonization of the terminology used in the field of metrology. In this section the most important definitions are marked as bold letters. According to the VIM the definition of the **uncertainty of a measurement** is a “*non-negative parameter characterizing the dispersion of the quantity values being attributed to a measurand, based on the information used*”, while the **measurand** is the “*quantity intended to be measured*” (JCGM 200 Edition 3, 2012).

The aim of the determination of the uncertainty in a measurement is to assign a quantitative measure of quality to the result of a measurement. It gives an interval wherein the true value of the measurement exists within a defined probability and is therefore a measure of confidence.

The fact that the result of a measurement cannot be reflected solely by a single value without an uncertainty results from phenomena called **sources of uncertainty**. Possible sources of uncertainty are defined in the GUM (JCGM 100, 2008):

“... ”

- a) *incomplete definition of the measurand;*
- b) *imperfect realization of the definition of the measurand;*
- c) *nonrepresentative sampling – the sample measured may not represent the defined measurand;*
- d) *inadequate knowledge of the effects of environmental conditions on the measurement or imperfect measurement of environmental conditions;*
- e) *personal bias in reading analogue instruments;*
- f) *finite instrument resolution or discrimination threshold;*
- g) *inexact values of measurement standards and reference materials;*
- h) *inexact values of constants and other parameters obtained from external sources and used in the data-reduction algorithm;*
- i) *approximations and assumptions incorporated in the measurement method and procedure;*
- j) *variations in repeated observations of the measurand under apparently identical conditions.”*

The sources of uncertainty listed above can also occur in combination, so that they are not necessarily independent. If a source of uncertainty remains unrecognized or unconsidered the systematic effect contributes to the **error of the measurement**. The remaining

(unknown) error should not be confused with the uncertainty of a measurement. Note that nominal quantities, e.g. natural or mathematical constants such as π , as well as reference values defined by standards, do not have a measurement uncertainty.

The **measurand** is the physical quantity Y that is measured. Y is termed as the **output quantity**. Because in most cases Y is not measured directly it needs to be determined from a number of N **input quantities** X_1, X_2, \dots, X_N through the functional relationship g which is called **mathematical model** that describes the measurand.

$$Y = g(X_1, X_2, \dots, X_N). \quad (2.31)$$

The input quantities X_i , with $i = 1..N$ are distinguished in two categories: a) quantities that are directly determined by a measurement; and b) quantities that are not directly determined by a measurement. These are usually taken from datasheets, calibration certificates or reference data from handbooks. Both types of quantities are only complete if a measurement uncertainty of the individual input quantity is assigned.

An **estimate of the measurand** Y , is denoted by y , the result of a measurement. It is usually determined by using the estimates x_i of the input quantities X_i and by using the functional relationship in accordance with Equation (2.31):

$$y = g(x_1, x_2, \dots, x_N). \quad (2.32)$$

The estimates of the input quantities need to be corrected appropriately. The corrections are applied to compensate for systematic effects that influence the individual estimate. If the estimates of the input quantities are not corrected one by one, **correction factors** f need to be applied that compensate the effects on the estimate y of output quantity Y . The correction factors f represent input quantities themselves. Thus, individual uncertainties need to be associated. The physical quantities X_i are also termed as **random variables** because their estimates x_i vary within a distinct **probability distribution**.

The **variance** σ^2 is the distribution of a random variables estimate q that is repetitively measured n times ($j = 1..n$). The variance represents a measure of the dispersion of the estimate:

$$\sigma^2(q) = \frac{1}{n-1} \sum_{j=1}^n (q_j - \bar{q})^2, \quad (2.33)$$

with \bar{q} the arithmetic mean value of the independently observed values q_j .

The **standard deviation** is in metrology termed as the **standard measurement uncertainty** u . It has a positive value with the same units as the measurand:

$$u(x_i) = u(\bar{q}) = \sigma = +\sqrt{\sigma^2}. \quad (2.34)$$

This method for the determination of the standard uncertainty is a statistical approach that accounts for **Type A** standard uncertainty. It is rarely the case that a Type A evaluation of the standard uncertainty is satisfactory for a complete determination of the measurement uncertainty, because systematic influences on the measurand remain unconsidered when applying Equations (2.33) and (2.34).

The **Type B** method allows the determination of the standard measurement uncertainty u without a statistical analysis of the series of measurement. The method is based on the scientific judgement, also known as educated guess, and based on the available information on the variability of the measured input quantity X_i . The pool of information given in (JCGM 100, 2008) include:

- “...
 — *previous measurement data;*
 — *experience with or general knowledge of the behaviour and properties of relevant materials and instruments;*
 — *manufacturer’s specifications;*
 — *data provided in calibration and other certificates;*
 — *uncertainties assigned to reference data taken from handbooks.* “

The Type B evaluation of the standard measurement uncertainty is especially used when only a small number of statistical independent observations are available. Note that the standard measurement uncertainties evaluated in accordance with the GUM Type A and Type B methods result always a Gaussian probability distribution. If an uncertainty is only available given as a symmetrical probability distribution different than Gaussian, a conversion is required. Possible distributions and conversions therefore can be found in the GUM (JCGM 100, 2008).

For different estimates of input quantities x_i and x_k that are not independent from each other, a correlation needs to be considered when the standard measurement uncertainty is determined. This is expressed by the covariance $u(x_i, x_k)$ associated with x_i and x_k defined by the equation:

$$u(x_i, x_k) = u(x_i)u(x_k)r(x_i, x_k), \quad (2.35)$$

with the **correlation coefficient** r that indicates the degree of correlation between the estimates x_i and x_k . When $r = 1$ or $r = -1$, both estimates are linear dependent on each other ($|r| \leq 1$). The value of r can be determined empirically by evaluating the results of n observations of x_i and x_k . Then,

$$r(x_i, x_k) = \frac{1}{n(n-1)} \frac{\sum_{j=1}^n (x_{ij} - \bar{x}_i)(x_{kj} - \bar{x}_k)}{\sigma(x_i)\sigma(x_k)}, \quad (2.36)$$

where j stands for the j^{th} observation.

The contribution of the standard measurement uncertainty assigned to the estimate of a single input quantity x_i , is denoted by u_i . It indicates the dispersion of the estimate of the output quantity y caused solely by the standard uncertainty $u_i(x_i)$ by using the **sensitivity coefficient** c_i .

$$u_i(y) = c_i u_i(x_i), \quad (2.37)$$

$$\text{with } c_i = \left. \frac{\partial g}{\partial x_i} \right|_{x_1=x_1, \dots, x_N=x_N}.$$

The determination of the **combined standard uncertainty** $u(y)$ with correlated input quantities is performed in accordance with:

$$u^2(y) = \sum_{i=1}^N u_i^2(y) + 2 \sum_{i=1}^{N-1} \sum_{k=i+1}^N u_i(y) u_k(y) r(x_i, x_k). \quad (2.38)$$

Equation (2.38) is also known as the Gaussian law of error propagation. For the simplified case that all N input quantities are independent, Equation (2.38) can be reduced to the summation of the squared standard uncertainties. Then,

$$u^2(y) = \sum_{i=1}^N u_i^2(y). \quad (2.39)$$

In the international metrology community, it is common to indicate the measurement uncertainty as an **expanded uncertainty**. In IEC documents the expanded uncertainty is simply termed as the “uncertainty” (JCGM 200 Edition 3, 2012). It is defined by the multiplication of the combined standard uncertainty $u(y)$, which is Gaussian distributed, and a **coverage factor** k :

$$U(y) = k \cdot u(y). \quad (2.40)$$

The coverage factor for the expression of the expanded uncertainty is $k = 2$ when a Gaussian distribution is apparent. In that case the estimate is located with a **coverage probability** of approximately 95 % within a **confidence interval** of $\pm U$. Note that it cannot be assumed in general that the measurand is well described by a Gaussian distribution. The distribution is dependent on the number of observations made to determine the measurand. A thorough discussion on the minimum number of observations is presented in (Stant, et al., 2016).

Often relative uncertainties are stated by calibration or testing laboratories. The **relative uncertainty** indicates a value in relation to the value of the estimate y , that is often given as percentage value. It is recommended to indicate the coverage factor and/or the coverage probability with the relative uncertainty, e.g. $k = 2 ; 95 \%$.

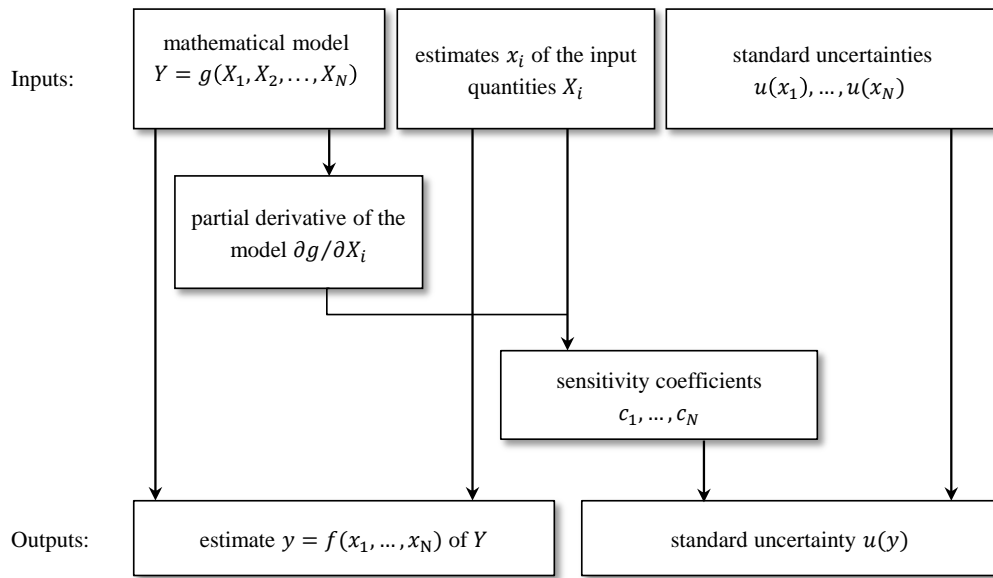


Figure 2.6: Simplified schematic of the classical GUM approach based on a figure included in (JCGM 104, 2009).

An introductory document gives a brief overview into the GUM Supplements and other documents released by the Joint Committee for Guides in Metrology JCGM (JCGM 104, 2009), in which a schematic shown in Figure 2.6 summarizes the classical GUM approach for the evaluation of measurement uncertainties.

The method recommended by the GUM (JCGM 100, 2008) is not always feasible for the practical use when: many input quantities are apparent, the mathematical model function is non-linear, and the probability distribution of an input quantity is asymmetric. Often it is challenging to determine all partial derivatives of the model g , as required in Equation (2.37); particularly when the input quantities are correlated. In the next subsection an approach is presented that overcomes some of these difficulties and limitations.

2.7.2. Measurement uncertainty: The Monte Carlo method

The Monte Carlo method is a numerical technique that uses pseudo-random numbers to perform an error propagation (Cox & Siebert, 2006). The Supplement 1 to the GUM “Propagation of distributions using a Monte Carlo method” includes details on this procedure (JCGM 101, 2008). The random estimates x_i are therefore generated within their corresponding probability distribution for each Monte Carlo trial accordingly. M is the number of Monte Carlo trials. Every kind of probability distribution for the input quantities can be utilized by this method (see Figure 2.7) To determine a number of estimates of the output quantity y , the function values of g are calculated M times by using the drawn input quantities. If M is sufficiently large (based on experience $M > 10,000$ trials are often sufficient), a probability distribution can be derived from the dispersion of the y values. This distribution is not necessary Gaussian or symmetric, but it contains information on the combined standard uncertainty $u(y)$.

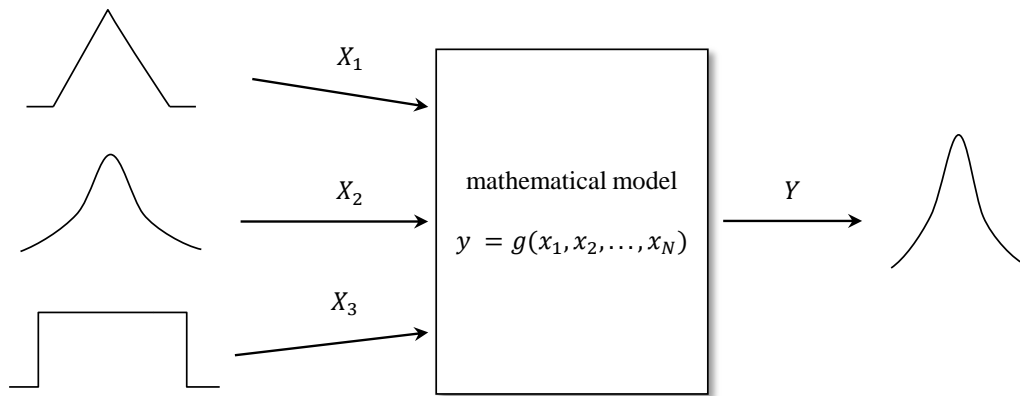


Figure 2.7: Illustration of the propagation of distributions for $N=3$ input quantities based on a figure in the supplementary GUM document (JCGM 101, 2008).

A major advantage of the Monte Carlo method is that the partial derivatives of the model g are not required. This leads to a significantly reduced effort for the evaluation of uncertainties. Additionally, it is possible to consider non-linear models and asymmetric probability distributions. It is also possible to consider correlations of dependent input quantities with the Monte Carlo method by choosing the random numbers to be correlated for the related input quantities. The simplified schematic illustrated in Figure 2.8 summarizes the method proposed by the Supplement 1 of the GUM.

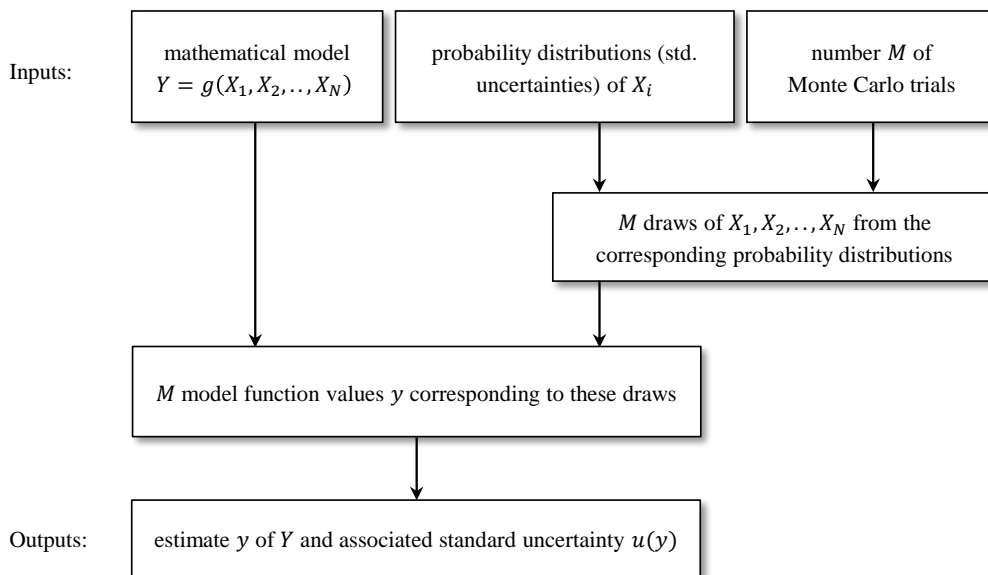


Figure 2.8: Simplified schematic of the Monte Carlo method described in the supplementary GUM document (JCGM 101, 2008) and based on a figure included in (JCGM 104, 2009).

The sensitivity coefficients are not determined directly by using the Monte Carlo method described above. It is often required to establish an uncertainty budget to specify how the uncertainties of individual input quantities contribute to the combined standard uncertainty $u(y)$. The determination of the sensitivity coefficients can be achieved by using the Monte Carlo method as described in the Annex B of Supplement 1 (JCGM 101, 2008). The probability distribution of the output quantities estimate is therefore determined for each input quantity

individually by setting all other input quantities uncertainties to zero, but not the investigated one. The resulting standard uncertainty u_i is then divided by the combined standard uncertainty to obtain the absolute value of the sensitivity coefficient. With all individually determined sensitivity coefficients, a tabular uncertainty budget can be established that should be used as qualitative tool for the identification of the dominant terms contributing to $u(y)$.

3. New multidimensional metric for the relation between solar radiation and solar cell

The following chapter introduces a novel multidimensional model that brings spectral angular effects into the field of PV metrology with focus on quantifying their impact on high-accuracy performance measurements. Before introducing many equations and detailed derivations of the metric, a summary of the current state of development is presented and a brief description of the problem is shown to motivate the need for a comprehensive modeling covering the spectral-angular mismatch. A separate section is dedicated to a proposal on an important additional definition: The directional properties of a reference irradiation condition. This enables a reduction of the measurement uncertainty by homogenization of worldwide PV device measurements and calibrations under diffuse irradiance conditions. Since measurements of the spectral sky radiance and datasets of the ground-reflected radiance covering the relevant spectral range from 300 nm – 1200 nm are not available to the author, simulations are used in this work. Parts of this chapter including a description of the multidimensional model, the spectral and directional properties of the sky, and a numerical calculation procedure are published in (Plag, et al., 2018a). The majority of the text included in this chapter is content of this article. Figures that are used from the original article, are labeled with a citation. The last section concludes this chapter with a summary.

3.1. State of development

Secondary calibrations and performance measurements of PV devices are commonly performed under global natural sunlight or artificial broadband light sources such as solar simulators. Also, spectral and angular effects can have a significant influence on the measurement uncertainty during the calibration of irradiance sensors. To correct measurements taken under natural or artificial sunlight with respect to STC, numerous measures need to be applied (IEC 60891 Edition 2, 2009; IEC 60904-7 Edition 3, 2008). In addition to temperature and irradiance compensation, a spectral mismatch correction must be carried out, as the spectral irradiance conditions of the measurement differ from the reference solar spectrum defined in (IEC 60904-3 Edition 2, 2008). The international standard series IEC 60904 - including amongst others (IEC 60904-7 Edition 3, 2008; IEC 60904-3 Edition 2, 2008; IEC 60904-1 Edition 2, 2006; IEC 60904-4, 2009) - does not consider under- or overestimation of the incident irradiance arising from diffuse light, which irradiates detectors that have different angular-dependent responsivities, despite this effect being known in the research community for many years. This problem was identified as early as the first performance measurements of solar cells, which used a horizontal global sunlight method (Treble, 1965). Today, this difference is known as an angular mismatch.

The output of PV devices depends on the AOI of the incident light; this dependency has been studied previously (Heinämäki & Guekos, 1987; Mialhe, et al., 1991; Parretta, et al., 1999; Michalsky, et al., 1995; Balenzategui & Chenlo, 2005; Winter, et al., 2010; Driesse, et al.,

2015). In the 1930s, earlier research had focused on spectral and angular dependencies in light metering (Barnard, 1936; 1939). Furthermore, angular-dependent optical losses of PV devices under global solar irradiance have been investigated under simplified conditions such as isotropic sky spectral radiance (Winter, et al., 2010; Martin & Ruiz, 2001; 2002; 2005; King, et al., 1997; 2004). Models using an isotropic approach cannot properly consider sky spectral radiance properties, which may be noticeably anisotropic under real world conditions (Hay & McKay, 1985; Gueymard, 1987; Perez, et al., 1990).

Investigations of the angular-dependent spectral responsivities of solar cells under anisotropic global horizontal irradiance with azimuthal symmetry were carried out by (Shimokawa, et al., 1986) using a global radiation model proposed by (Miyake, et al., 1987). Angular losses ranging from 1.23 % and 3.52 % in the total output current of several solar cells were observed in a computational study where the Sun was at its zenith. The radiation model of Miyake, et al. (1987) considers the global horizontal spectral radiance in 50-nm wavelength bands while also considering a spectrally independent albedo. However, the spectral influence of ground reflectance for a tilted device orientation was not elaborated in Shimokawa, et al. (1986). Later studies showed that spectral albedo effects can have a significant effect on PV device performance, particularly for bifacial PV devices (Andrews & Pearce, 2013; Brennan, et al., 2014). Differences of 1 % to 4 % between indoor and outdoor measurements using the same chain of traceability performed at the same laboratory were observed (Shimokawa, et al., 1987), which confirms the observations made in the computational study of Shimokawa, et al. (1986). At that time, the measurement uncertainties using the global (normal) sunlight method were typically in the range of 2.5 % to 3.7 % for the short-circuit current (Emery & Osterwald, 1989). Indoor laboratory calibrations of reference solar cells using only direct normal incidence irradiation provide uncertainties of 0.4 % ($k = 2$, expanded uncertainty 95 %) (Winter, et al., 2014). Since the indoor primary calibrated reference cells are often used as irradiance sensors for secondary calibrations of other PV devices such as modules using global outdoor irradiation conditions or simulated sunlight, the relatively high impact of angular effects is not negligible.

This leads to the conclusion that the AOI effects have to be considered, as they affect significantly the measured value and thus contribute to the total measurement uncertainty budget for global sunlight methods. Furthermore, spectral dependencies of the sky radiance (Bullrich, et al., 1952) are only negligible for devices without differing angular-dependent spectral responsivities. Emery and Osterwald devised a generalized equation for this problem and incorporated it into the uncertainty budget of outdoor measurements under global sunlight (Emery & Osterwald, 1988). The dependence of the responsivity of PV devices on polarization, spectrum, reflection and absorption losses, as well as on light trapping effects, has been subject of several studies (Shimokawa, et al., 1986; Seibert, 1968; Dennler, et al., 2007; Gjessing & Marstein, 2014; Beal, et al., 2014; Potter, et al., 2015; Smeets, et al., 2015; Geisemeyer, et al., 2017; Plag, et al., 2017a; Reiners, 2018).

Müllejjans et al. (2005a) report reduced measurement uncertainties of 1 % ($k = 2$, expanded uncertainty 95 %) for measurements of the short-circuit current using the global sunlight method traceable to the world radiometric reference. Müllejjans et al. proposed the

application of the global sunlight method for the primary calibration of reference solar cells. Their analysis of measurement uncertainties assumes an “ideal cosine response” (Müllejans, et al., 2005b). The differences from the cosine responsivity observed in a previously published article of the author Plag, et al. (2017b) and also in Geisemeyer, et al. (2017) for different solar cell types encourages to perform a computational study and a sensitivity analysis on different approaches to investigate the effect of diffuse light on solar cells in depth for a number of scenarios and assumptions.

3.2. Problem definition

For primary calibrations of the short-circuit current of reference solar cells commonly direct normal irradiance (DNI) is used in the experimental procedures to achieve the lowest measurement uncertainties (Emery & Osterwald, 1989; Hishikawa, et al., 2003; Winter, et al., 2014; Ahn, et al., 2014). For those primary measurements, irradiation with a direct or collimated beam perpendicular to the devices surface is used. Following the path of traceability towards the application, primary calibrated reference solar cells are used as irradiance reference devices for the secondary calibration of solar cells. Regularly secondary calibrations and routinely calibrations of working references are performed under simulated or natural sunlight, where directional properties of the irradiance often differ to those of primary calibrations. In Chapter 4 it is shown that solar cells provide differences in their angular responsivity characteristics. Analogous to the requirements of a spectral mismatch correction procedures defined in the international standard (IEC 60904-7 Edition 3, 2008), angular-dependent spectral responsivity and spectral radiance needs to be considered for measurements taken under diffuse conditions. This leads to a multidimensional problem, which must be solved in order to compensate differences in measurements between PV devices providing different angular-dependent spectral responsivities. Under conditions differing to those of the primary calibration measurement situation, a spectral-angular mismatch needs to be elaborated and studied.

3.3. Definition of the angular distribution of the reference irradiation condition

When performing measurements of solar cells’ electrical performance characteristics, deviations to standard testing conditions are always apparent to a certain extent. Therefore, effects of spectral mismatch, temporal irradiance fluctuation and temperature are compensated by procedures in accordance with a series of international standards (IEC 60891 Edition 2, 2009; IEC 60904-1 Edition 2, 2006; IEC 60904-4, 2009; IEC 60904-7 Edition 3, 2008; IEC 60904-3 Edition 2, 2008) which not include any kind of angular distribution of the reference irradiance. At least the newer version of the standard (IEC 60904-3 Edition 3, 2016) distinguishes between direct and global spectral irradiance contributions to the reference spectrum. While edition 3 of this standard still lacks in a complete description of the angular irradiance distribution, a recent draft of a future fourth edition includes such a definition (IEC draft 60904-3 Edition 4, 2018):

“The reference angular distribution is defined for both, the direct and the global spectral distribution, so that the complete radiation hits the solar device perpendicularly under normal incidence.”

Albeit the reference spectral irradiance datasets calculated with SMARTS (Gueymard, 1995) are based on an anisotropic sky radiance model, they are not providing datasets including the sky spectral radiances anisotropy (Gueymard, et al., 2002).

Sophisticated primary calibrations of PV solar reference devices are performed using direct normal irradiance only (i.e., by using the direct sunlight method and the differential spectral responsivity method (IEC 60904-4, 2009)). For a better comparability, the author suggests that for secondary calibrations including diffuse irradiance, a reasonable reference angular distribution should be defined as direct beam only, parallel to the surface normal of the device. This definition holds the advantage of a lower computational effort on the mismatch calculations, compared to reference conditions which provide diffuse spectral radiance contributions.

3.4. Multidimensional model

The following section presents the radiometric background necessary to understand the relationship between the electrical output current of a linear PV device under short-circuit condition and the incident irradiation that depends on the solar spectrum and its angular distribution. A detailed elaboration of the current equations and of the spectral-angular mismatch correction factor is shown.

For the development of a modeling equation describing the angular mismatch in PV metrology, the relationship between the directional radiometric quantity radiance L and the irradiance E , is fundamental:

$$E = \int_{\varphi} \int_{\theta} L(\theta, \varphi) \cdot \cos \theta \sin \theta \, d\theta \, d\varphi \quad (3.1)$$

To simplify the concept of angular mismatch, an elaboration for a simplified wavelength-independent case is presented in the first step. In the second step, the model is enhanced by spectral dependencies; later, the special case of tilted PV devices under consideration of ground reflectance is discussed.

To describe the output signal of a detector when it is receiving optical power from different directions (θ and φ), knowledge of the detector’s responsivity s is required. An ideal detector with a flat surface accumulates incident radiance L over all infinitesimal solid angles $d\Omega = \sin \theta \, d\theta \, d\varphi$ within its active field of view, following the cosine with the angle of incidence (see Figure 3.1 and Equation (3.1)). Due to optical losses, such as reflection and absorption, real detectors provide angular-dependent responsivities that differ from those of the cosine. The difference is known as the cosine error of a device.

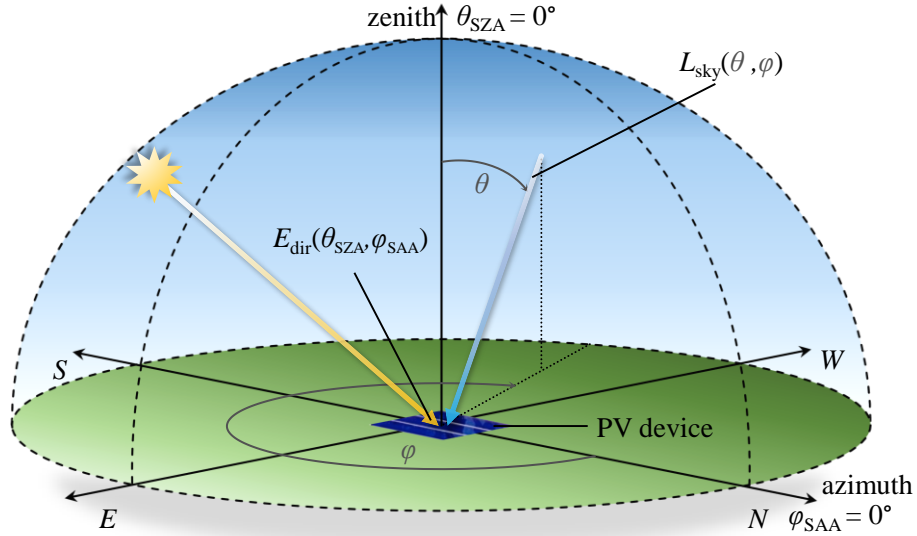


Figure 3.1: Simplified schematic view of a PV device measurement under global sunlight with horizontal orientation. The PV device accumulates the direct irradiance E_{dir} on a horizontal surface from the direction of the solar zenith angle θ_{SZA} and the solar azimuth angle φ_{SAA} . θ and φ represent the zenith and azimuth angles in a stationary spherical coordinate system. The sky radiance L_{sky} is accumulated additionally from all directions of the hemisphere. Spectral quantities are not included in this figure for reasons of clarity. This figure is also published in (Plag, et al., 2018a).

The output short-circuit current I_{SC} of a linear PV device that has an individual angular-dependent irradiance responsivity $s(\theta, \varphi)$ in $A\ m^2\ W^{-1}$ exposed to a solar radiance field consisting of the direct normal irradiance E_{DNI} in $W\ m^{-2}$ and the diffuse radiance L_{sky} in $W\ m^{-2}\ sr^{-1}$ can be described as:

$$I_{SC} = E_{DNI}(\theta_{SZA}, \varphi_{SAA}) \cdot s(\theta_{SZA}, \varphi_{SAA}) + \int_{\varphi} \int_{\theta} L_{sky}(\theta, \varphi) \cdot s(\theta, \varphi) \sin \theta\ d\theta\ d\varphi, \quad (3.2)$$

where θ_{SZA} is the solar zenith angle and φ_{SAA} the solar azimuth angle (see Figure 3.1). $L_{sky} \cdot s(\theta, \varphi)$ is integrated over the zenith angles θ and azimuth angles φ of the sky, while E_{DNI} is the direct normal irradiance on a surface orthogonal to the direct beam. The direct irradiance is not expressed as radiance here, because it is considered being a point source and thus difficult to integrate on a defined grid with finite resolution.

Exposing two PV devices or detectors with the same orientation and with different angular responsivities $s(\theta, \varphi)$ to the same solar radiance field, results in a systematic deviation of the measured output signals. If the responsivities of both devices - for example, a PV reference device s_{ref} and a device under test s_{DUT} - are normalized to their values at normal incidence with $\theta = 0^\circ$, a ratio Dev_{Ω} expresses the deviation of the output short-circuit current due to angular effects:

$$\text{Dev}_\Omega = \frac{E_{\text{DNI}}(\theta_{\text{SZA}}, \varphi_{\text{SAA}}) \cdot s_{\text{ref,norm}}(\theta_{\text{SZA}}, \varphi_{\text{SAA}})}{E_{\text{DNI}}(\theta_{\text{SZA}}, \varphi_{\text{SAA}}) \cdot s_{\text{DUT,norm}}(\theta_{\text{SZA}}, \varphi_{\text{SAA}})} \dots \quad (3.3)$$

$$\dots \frac{+ \int_\varphi \int_\theta L_{\text{sky}}(\theta, \varphi) \cdot s_{\text{ref,norm}}(\theta, \varphi) \sin \theta \, d\theta \, d\varphi}{+ \int_\varphi \int_\theta L_{\text{sky}}(\theta, \varphi) \cdot s_{\text{DUT,norm}}(\theta, \varphi) \sin \theta \, d\theta \, d\varphi}$$

where $s_{\text{ref,norm}}$ and $s_{\text{DUT,norm}}$ are the responsivities normalized to their values at an angle of incidence of $\theta = 0^\circ$. The device used as reference irradiance detector is indicated with the index (ref) and the device under test is indicated as index (DUT).

The deviation described by Equation (3.3) describes the (relative) difference between two detectors under one specific angular distribution. However, to obtain measurements that are comparable with each other independently from the apparent condition, a definition of a reference angular distribution, as proposed in Section 3.3, is required. To elaborate a factor that corrects the angular mismatch in the same way as to the spectral mismatch *SMM* defined in the standard (IEC 60904-7 Edition 3, 2008) (see Equation (3.4)), a reference radiance distribution must be defined.

$$\text{SMM} = \frac{\int_\lambda E_{\lambda,\text{ref}}(\lambda) s_{\text{ref}}(\lambda) d\lambda \int_\lambda E_{\lambda,\text{meas}}(\lambda) s_{\text{DUT}}(\lambda) d\lambda}{\int_\lambda E_{\lambda,\text{meas}}(\lambda) s_{\text{ref}}(\lambda) d\lambda \int_\lambda E_{\lambda,\text{ref}}(\lambda) s_{\text{DUT}}(\lambda) d\lambda}, \quad (3.4)$$

where $E_{\lambda,\text{ref}}(\lambda)$ is the solar reference spectral irradiance, $s_{\text{ref}}(\lambda)$ is the spectral responsivity of the device used as a reference detector, $E_{\lambda,\text{meas}}(\lambda)$ is the measured spectral irradiance and $s_{\text{DUT}}(\lambda)$ is the spectral responsivity of the DUT PV device.

The angular mismatch *AMM* between two devices with different angular responsivities $s(\theta, \varphi)$ is defined as the product of their two output current relationships, each of which is under unique irradiation conditions - primary (ref, with direct beam only) and secondary (measurement (meas) with diffuse radiance and direct irradiance apparent). The *AMM* is expressed as:

$$\text{AMM} = \frac{I_{\text{ref,ref}} I_{\text{meas,DUT}}}{I_{\text{meas,ref}} I_{\text{ref,DUT}}}$$

$$= \frac{E_{\text{ref}} \cdot s_{\text{ref}}(\theta = 0^\circ, \varphi = 0^\circ)}{E_{\text{DNI}}(\theta_{\text{SZA}}, \varphi_{\text{SAA}}) \cdot s_{\text{ref}}(\theta_{\text{SZA}}, \varphi_{\text{SAA}}) + \int_\varphi \int_\theta L_{\text{sky}}(\theta, \varphi) \cdot s_{\text{ref}}(\theta, \varphi) \sin \theta \, d\theta \, d\varphi} \quad (3.5)$$

$$\cdot \frac{E_{\text{DNI}}(\theta_{\text{SZA}}, \varphi_{\text{SAA}}) \cdot s_{\text{DUT}}(\theta_{\text{SZA}}, \varphi_{\text{SAA}}) + \int_\varphi \int_\theta L_{\text{sky}}(\theta, \varphi) \cdot s_{\text{DUT}}(\theta, \varphi) \sin \theta \, d\theta \, d\varphi}{E_{\text{ref}} \cdot s_{\text{DUT}}(\theta = 0^\circ, \varphi = 0^\circ)},$$

where $I_{\text{ref,ref}}$ is the current of the PV reference device (ref) exposed to the reference irradiance E_{ref} , $I_{\text{ref,DUT}}$ is the current of the device under test (DUT) exposed to the reference radiance E_{ref} , $I_{\text{meas,DUT}}$ is the current of the DUT exposed to the diffuse radiance L_{sky} and the direct normal irradiance E_{DNI} , and $I_{\text{meas,ref}}$ is the current of the PV reference device exposed to L_{sky} and E_{DNI} . $s_{\text{ref}}(\theta = 0^\circ, \varphi = 0^\circ)$ is the spectral responsivity of the reference device under normal incidence, whereas $s_{\text{ref}}(\theta, \varphi)$ at other zenith and azimuth angles represents the responsivity of the reference device as a function of the incidence angles. $s_{\text{DUT}}(\theta, \varphi)$ is defined accordingly.

The angular mismatch for the measured DUT current $I_{\text{meas,DUT}}$ under global irradiance can be corrected when multiplying $I_{\text{meas,DUT}}$ with a correction factor f_{AMM} :

$$f_{\text{AMM}} = \frac{1}{\text{AMM}} \quad (3.6)$$

The simplified Equations (3.2)-(3.3) and (3.5)-(3.6) neglect the spectral responsivity $s(\lambda)$ of the solar cells and the spectral distribution of the broadband solar irradiance. If the angular-dependent responsivity of the PV device being investigated is also spectrally dependent, separated computations of the spectral mismatch in accordance with Equation (3.4) and angular mismatch in accordance with Equation (3.5) are no longer applicable.

For comprehensive modeling, the spectral radiance $L_{\lambda,\text{sky}}(\lambda, \theta, \varphi)$ and the direct normal spectral irradiance $E_{\lambda,\text{DNI}}(\lambda)$ have to be included as source properties, as do the angular-dependent spectral responsivities $s(\lambda, \theta, \varphi)$ as detector properties. The output short-circuit current I_{SC} of a PV device is then defined as:

$$I_{\text{SC}} = \int_{\lambda} E_{\lambda,\text{DNI}}(\lambda) \cdot s(\lambda, \theta_{\text{SZA}}, \varphi_{\text{SAA}}) d\lambda + \int_{\lambda} \int_{\varphi} \int_{\theta} L_{\lambda,\text{sky}}(\lambda, \theta, \varphi) \cdot s(\lambda, \theta, \varphi) \sin \theta d\theta d\varphi d\lambda \quad (3.7)$$

A more generalized expression for the AMM can be found when including the device orientation into the multidimensional model. A simplified coordinate transformation was performed by applying an Euler coordinate transformation in Cartesian coordinates in two steps (see Figure 3.2). The device's angular-dependent spectral responsivities $s(\lambda, \theta, \varphi)$ are tilted and rotated relative to the spherical coordinate system by a tilt angle θ' and a rotation angle φ' , respectively. In the first step, the tilt towards the horizon by an angle θ' took place in Cartesian coordinates to obtain $\overrightarrow{s_{\text{tilt},\theta'}}$:

$$\overrightarrow{s_{\text{tilt},\theta'}} = \begin{pmatrix} 1 & 0 & 0 \\ 0 & \cos \theta' & -\sin \theta' \\ 0 & \sin \theta' & \cos \theta' \end{pmatrix} \begin{pmatrix} s_x \\ s_y \\ s_z \end{pmatrix} \quad (3.8)$$

After transforming back into spherical coordinates, a rotation φ' around the zenith axis was performed:

$$s_{\text{tilt}}(\lambda, \theta, \varphi) = s_{\text{tilt},\theta'}(\lambda, \theta, \varphi + \varphi') \quad (3.9)$$

A rotation around the surface normal of the PV device was neglected in this first approach. A more generalized form of the transformation can be found in (Goldstein, 1980).

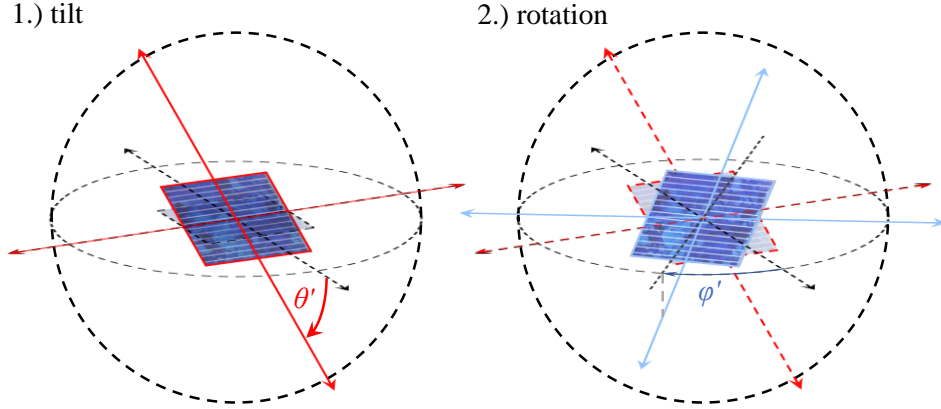


Figure 3.2: Schematic of the coordinate transformation that needs to be applied to consider any given device orientation using the proposed model. Left-hand side: a zenithal tilt θ' of the solar cell's responsivity dataset towards the horizon is performed in Cartesian coordinates as the first step in accordance with Equation (3.8). Right hand side: The dataset is rotated in the second step by φ' around the zenith axis in spherical coordinates in accordance with Equation (3.9). This figure is also published in (Plag, et al., 2018a).

The tilted angular dependent spectral responsivities $s_{\text{tilt}}(\lambda, \theta, \varphi)$ receive additional ground-reflected irradiance if $\theta' \neq 0^\circ$. This contributes in the following way to the short-circuit current generated I_{SC} :

$$\begin{aligned}
 I_{\text{SC}} = & \int_{\lambda} E_{\lambda, \text{DNI}}(\lambda) \cdot s_{\text{tilt}}(\lambda, \theta_{\text{SZA}}, \varphi_{\text{SAA}}) d\lambda \\
 & + \int_{\lambda} \int_{\varphi} \int_{\theta} [L_{\lambda, \text{sky}}(\lambda, \theta, \varphi) + L_{\lambda, \text{ground}}(\lambda, \theta, \varphi)] \\
 & \cdot s_{\text{tilt}}(\lambda, \theta, \varphi) \sin \theta d\theta d\varphi d\lambda,
 \end{aligned} \tag{3.10}$$

with the ground-reflected spectral radiance $L_{\lambda, \text{ground}}(\lambda)$ under the assumption that the ground is a spatially uniform Lambertian reflector with a spectrally dependent albedo $a(\lambda)$,

$$\begin{aligned}
 L_{\lambda, \text{ground}}(\lambda) = & \\
 & \frac{a(\lambda)}{\pi} \cdot \left(E_{\lambda, \text{DNI}}(\lambda) \cdot \cos \theta_{\text{SZA}} + \int_0^{2\pi} \int_{\frac{\pi}{2}}^{\pi} L_{\lambda, \text{sky}}(\lambda, \theta, \varphi) \cdot \cos \theta \sin \theta d\theta d\varphi \right) \\
 & = \frac{a(\lambda)}{\pi} \cdot E_{\lambda, \text{glo}}(\lambda),
 \end{aligned} \tag{3.11}$$

where $E_{\lambda, \text{glo}}(\lambda)$ is the global spectral irradiance on the Earth's horizontal surface.

Thus, the spectral-angular mismatch that accounts for the coupled quantities (spectral and directional) and tilted devices is then defined as:

$$\begin{aligned}
S_{AMM} = & \frac{\int_{\lambda} E_{\lambda,ref}(\lambda) \cdot s_{ref}(\lambda, \theta = 0^{\circ}, \varphi = 0^{\circ}) d\lambda}{\int_{\lambda} E_{\lambda,DNI}(\lambda) \cdot s_{ref,tilt}(\lambda, \theta_{SZA}, \varphi_{SAA}) d\lambda + \dots} \dots \\
& \dots \frac{\dots + \int_{\lambda} \int_{\varphi} \int_{\theta} [L_{\lambda,sky}(\lambda, \theta, \varphi) + L_{\lambda,ground}(\lambda, \theta, \varphi)] \cdot s_{ref,tilt}(\lambda, \theta, \varphi) \sin \theta d\theta d\varphi d\lambda}{\dots} \\
& \dots \frac{\int_{\lambda} E_{\lambda,DNI}(\lambda) \cdot s_{DUT,tilt}(\lambda, \theta_{SZA}, \varphi_{SAA}) d\lambda + \dots}{\int_{\lambda} E_{\lambda,ref}(\lambda) \cdot s_{DUT}(\lambda, \theta = 0^{\circ}, \varphi = 0^{\circ}) d\lambda} \dots \\
& \dots \frac{\dots + \int_{\lambda} \int_{\varphi} \int_{\theta} [L_{\lambda,sky}(\lambda, \theta, \varphi) + L_{\lambda,ground}(\lambda, \theta, \varphi)] \cdot s_{DUT,tilt}(\lambda, \theta, \varphi) \sin \theta d\theta d\varphi d\lambda}{\dots},
\end{aligned} \tag{3.12}$$

with the solar reference spectral irradiance $E_{\lambda,ref}(\lambda)$ defined in (IEC 60904-3 Edition 2, 2008).

S_{AMM} can be applied as an inverse correction factor $f_{S_{AMM}}$, similar to the factor f_{AMM} expressed in Equation (3.6), to compensate for spectral and angular influences that differ from the reference conditions proposed, solely with direct normal irradiance.

Once the spectral-angular mismatch correction factor $f_{S_{AMM}}$ is known, the derivation of an approximate pure angular mismatch correction factor f_{AMM} for a generalized case can be determined as:

$$\begin{aligned}
f_{AMM} & \approx \frac{f_{S_{AMM}}}{f_{SMM}} = f_{S_{AMM}} \cdot SMM \\
& = f_{S_{AMM}} \frac{\int_{\lambda} E_{\lambda,ref}(\lambda) \cdot s_{ref}(\lambda) d\lambda}{\int_{\lambda} E_{\lambda,meas}(\lambda) \cdot s_{ref}(\lambda) d\lambda} \frac{\int_{\lambda} E_{\lambda,meas}(\lambda) \cdot s_{DUT}(\lambda) d\lambda}{\int_{\lambda} E_{\lambda,ref}(\lambda) \cdot s_{DUT}(\lambda) d\lambda},
\end{aligned} \tag{3.13}$$

where f_{SMM} stands for the inverse spectral mismatch factor SMM in accordance with Equation (3.4), with $E_{\lambda,meas}(\lambda)$ standing for the spectral irradiance inclined perpendicular on the tilted detector with a spectral responsivity $s(\lambda, \theta = 0^{\circ}, \varphi = 0^{\circ})$.

3.5. Spectral and directional properties of the sky

In this section, simulations of the outdoor spectral radiance conditions performed using a radiative transfer model are presented. Additionally, the global spectral irradiance on a tilted surface is computed with the simulated spectral radiance field to show differences between the resulting spectrum and the reference solar spectrum defined in (IEC 60904-3 Edition 2, 2008).

To generate data that includes directional information on the radiation conditions as an input quantity for the model elaborated in the section above, version 2.0 of the libRadtran software package is used for radiative transfer calculations (Mayer & Kylling, 2005; Emde, et al., 2016). LibRadtran's main program, *uvspec*, computes the sky spectral radiance distribution on the Earth's surface for defined atmospheric conditions under consideration of multiple extinction and scattering events. DISORT (Discrete-Ordinate-Method Radiative Transfer) (Stamnes, et al., 1988), a radiative transfer equation (RTE) solver that accounts

for pseudospherical atmospheric layering is used for the computations performed in this work.

The following output parameters are analyzed: the sky's anisotropic diffuse spectral radiance $L_{\lambda,\text{sky}}(\lambda, \theta, \varphi)$ together with the ground-reflected spectral radiance $L_{\lambda,\text{ground}}(\lambda, \theta, \varphi)$ and the direct spectral irradiance of the Sun $E_{\lambda,\text{dir}}(\lambda)$.

The input parameters for the radiative transfer calculations are selected carefully. To generate a spectral radiance distribution comparable to the irradiation conditions defined in the standard IEC 60904-3 Edition 2, which is calculated by using SMARTS (Gueymard, 1995), the spectrally dependent albedo (light soil), standard U.S. atmosphere profile (Anderson, et al., 1986) and extraterrestrial solar spectrum (Gueymard, et al., 2002) contained in this standard are selected as input quantities for the simulation program *uvspec*. A rural aerosol-type profile (Shettle, 1989) that includes information about the different layers and aerosol-types in the atmosphere, an aerosol asymmetry factor of 0.65 that characterizes the scattering angle and a (horizontal) visibility of 50 km are used. The reference publication by Gueymard, et al. that proposes a reference spectral irradiance includes the assumption of an aerosol optical depth of 0.084 at 500 nm, which corresponds approximately to a visibility of 100 km. However, for this work, a visibility of 50 km is chosen, which seems to be more representative of clear-sky at conditions in Central Europe. Note that the visibility impacts the sky radiance calculated (i.e., the circumsolar radiance may increase compared to conditions with exceptionally high visibility). In the example given, the position of the Sun is located at a zenith angle of $\theta_{\text{SZA}} = 48.2^\circ$ (air mass 1.5) and at an azimuth angle of $\varphi_{\text{SAA}} = 180^\circ$ (southern orientation), as defined in the standard. In the approach presented here, the sky radiance is assumed to be unpolarized and an ideal Lambertian and spectrally dependent ground reflection process is assumed. This study focuses on the mismatch related to spectral and angular effects, as found under "typical" clear sky conditions, recommended for high-accuracy solar cell calibration. To this end, both spectral and angular information is required. The latter is not provided by SMARTS output datasets.

The spectral resolution used in this study is 1 nm and ranges from 300 nm to 1200 nm, which turns out to be a suitable resolution and range for the computation of the spectral mismatch between two silicon PV devices. To limit the enormous computational effort, an angular resolution of 1 degree is chosen, resulting in a spherical radiance field (including ground reflection) with a size of approximately 65,000 data points per wavelength. Including the spectral dimension, a single spectral radiance field contains up to 60 million data points. The simulated diffuse clear-sky radiance L_{sky} is visually represented as a contour plot in Figure 3.3 for the hemisphere above the horizon. The radiance values indicated are obtained by integrating the spectral radiance calculated $L_{\lambda,\text{sky}}(\lambda, \theta, \varphi)$ over the wavelength range of interest, separately for each direction.

Figure 3.3 shows an example of an anisotropic clear-sky radiance condition. The color contour of the diffuse sky radiance forms a clear visual representation of a brightening of the horizon and a strong increase of sky radiance in the circumsolar region. Rayleigh

scattering of the direct solar radiation results in a minimum radiance in northern azimuthal orientation at zenith angles θ between 10° and 50° .

The isotropic and Lambertian ground-reflected radiance $L_{\text{ground}}(\theta, \varphi)$ is not included in Figure 3.3 due to the fact that no additional directional information can be obtained. Based on the ground-reflected direct and diffuse sunlight, the ground-reflected spectral radiance $L_{\lambda, \text{ground}}(\lambda, \theta, \varphi)$ is integrated over the wavelength range investigated to form a ground-reflected radiance $L_{\text{ground}}(\theta, \varphi)$ of $53 \text{ W m}^{-2} \text{ sr}^{-1}$ for angles below a defined horizon line. The ground-reflected radiance is integrated over the downward-facing hemisphere which results in a reflected hemispheric irradiance E_{ground} of 166.6 W m^{-2} within 300 nm to 1200 nm. The reflected hemispheric irradiance E_{ground} is also termed upwelling global irradiance in atmospheric sciences.

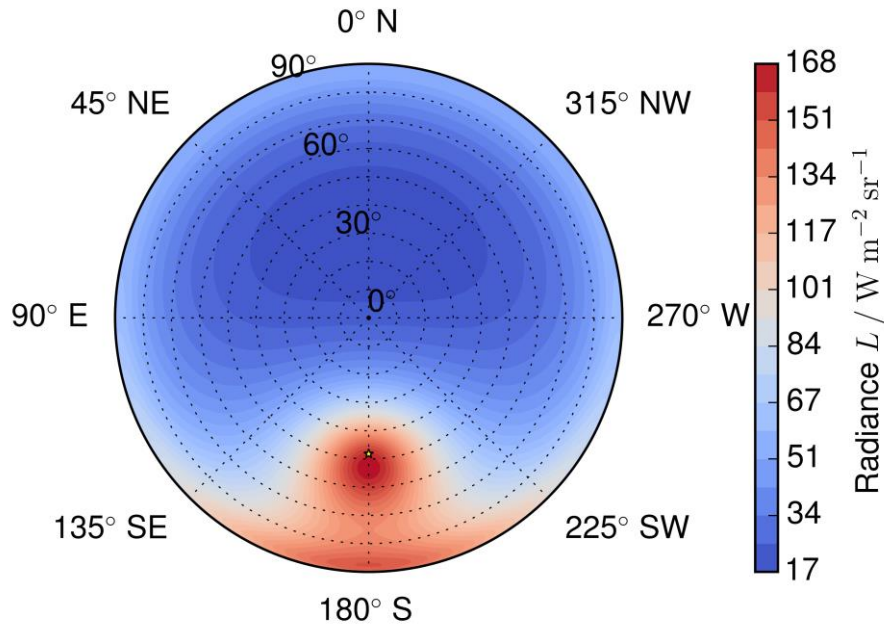


Figure 3.3: Diffuse sky radiance L_{sky} calculated using libRadtran for defined atmospheric parameters within a waveband ranging from 300 nm to 1200 nm. The Sun's position at $\theta_{\text{SZA}} = 48.2^\circ$ and southern azimuthal orientation is indicated as a yellow star. The direct beam is not included in this contour. This figure is also published in (Plag, et al., 2018a).

To visually represent spectral dependencies in the sky radiance, a solar principal plane cut is performed representing the meridian from north to south along the position of the Sun, including the ground. The spectral radiance $L_\lambda(\lambda, \theta, \varphi = 180^\circ)$ at each orientation is rendered into RGB colors (Walker, 1996) for each solar zenith angle θ across the solar principal plane. These colors are plotted in Figure 3.4 as the filled-in colors below the black line, which indicates the integral radiance L within the spectral range investigated. It is found that the maximum radiance is located at a zenith angle that is slightly higher than the Sun's position θ_{SZA} . A second local radiance maximum can be identified at $\theta = 90^\circ$ close to the southern horizon; this is almost three times larger than the local radiance maximum at the northern horizon; $\theta = 90^\circ, \varphi = 0^\circ$. Below the horizon ($\theta > 90^\circ$ and $\theta < -90^\circ$), the flat line indicates

the isotropic radiance with Lambertian reflectance in a light brown color calculated for the spectrum reflected from light soil.

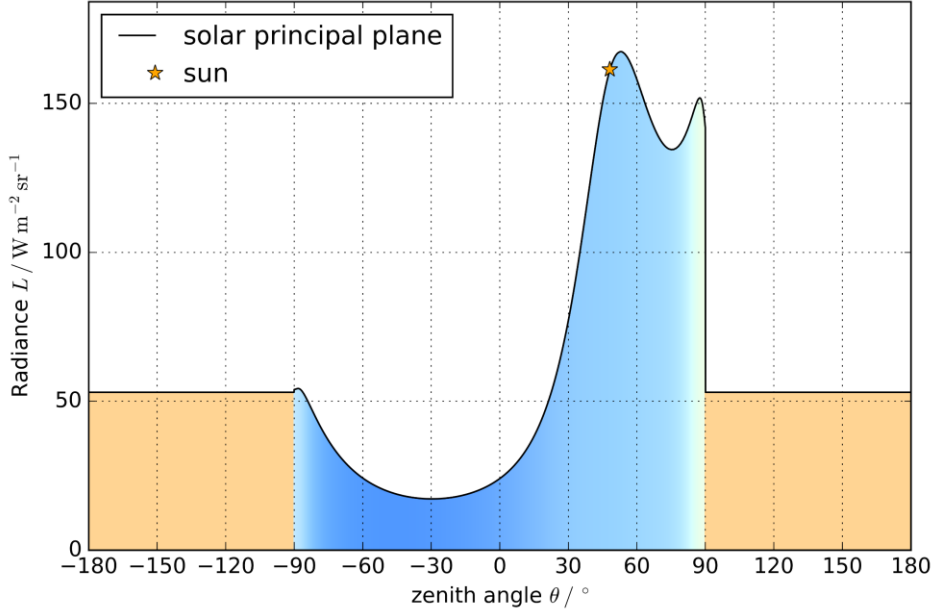


Figure 3.4: Sky radiance across the solar principal plane, showing a slice of the radiance field cut along a meridian from north to south $\varphi = 180^\circ$. The spectra at each zenith angle θ are converted into RGB colors, indicating a bluish-white coloration of the sky and a light brown ground-reflected radiance of light soil (ideal Lambertian reflectance assumed). The Sun's position at $\theta_{\text{SZA}} = 48.2^\circ$ is indicated by a yellow star. This figure is also published in (Plag, et al., 2018a).

The impact of the anisotropic radiance distribution on the output signal of an ideal detector can be easily determined by multiplying it by the cosine of the angle of incidence within its field of view. In Figure 3.5, cosine-weighted radiances are plotted, representing the responsivities of ideal spectrally-independent detectors. In addition, the radiance on a solar principal plane taken from Figure 3.4 is shown.

Two cases are considered in this example: a horizontal (black dashed line) and a tilted detector orientation (red dashed line). When considering all azimuthal orientations enclosing a sphere, the diffuse spectral irradiance $E_{\lambda, \text{diff}}$ can be obtained with a numerical calculation based on Equation (3.1) wavelength by wavelength. For tilted detector orientations, the Euler coordinate transformation in accordance with the Equations (3.8) and (3.9) should be applied; an interpolation onto the original spherical grid also needs to be performed. Subsequently, $E_{\lambda, \text{diff}}(\lambda)$ obtained for the tilted plane is added to the direct normal spectral irradiance $E_{\lambda, \text{DNI}}(\lambda)$, resulting in the global spectral irradiance $E_{\lambda, \text{glo}}(\lambda)$. The simulated global spectral irradiance $E_{\lambda, \text{glo}}(\lambda)$ inclined on a 37° tilted surface facing south (azimuth rotation $\varphi' = 180^\circ$) obtained with libRadtran is slightly higher in the spectral range observed than the corresponding values calculated by SMARTS 2.9.2. The global irradiance E_{glo} integrates to 845.57 W m^{-2} within 300 nm and 1200 nm when using libRadtran, while with SMARTS, a lower value of 833.66 W m^{-2} is obtained within the corresponding spectral range.

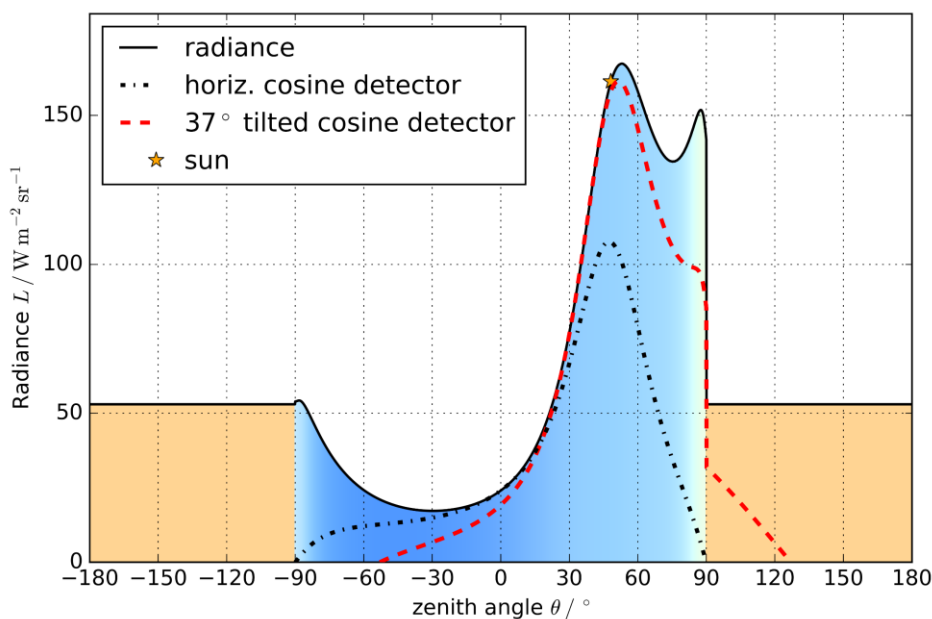


Figure 3.5: Solar principal plane of the radiance (black solid line) at $\varphi = 180^\circ$, and the cosine weighted radiances of ideal horizontal (black dashed dotted line) and tilted (red dashed line) detectors following the cosine law. The surface normal of the tilted detector is inclined by $\theta' = 37^\circ$ at 180° azimuthal orientation. The Sun's position at $\theta_{\text{SZA}} = 48.2^\circ$ is indicated by a yellow star. This figure is also published in (Plag, et al., 2018a).

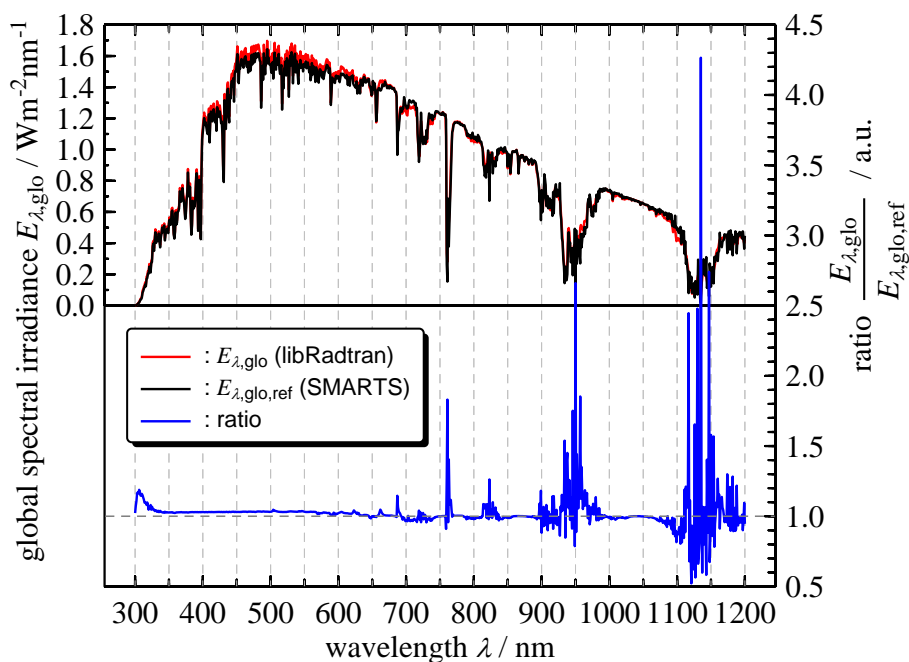


Figure 3.6: Comparison between global reference spectral irradiance on absolute scale calculated by SMARTS $E_{\lambda,\text{glo,ref}}(\lambda)$ (black line), and global spectrum calculated by libRadtran (red line) using the same input parameters, where possible. Both spectra are related to a tilted detector surface with $\theta' = 37^\circ$ at 180° azimuthal orientation and are calculated within a wavelength range from 300 nm to 1200 nm. To indicate differences in the spectra calculated, the quotient is taken (blue line). This figure is also published in (Plag, et al., 2018a).

A possible reason for this can be found by comparing the computed global spectral irradiances resulting from both models (see Figure 3.6). Slight differences in the absorption bands can be identified. The libRadtran spectrum also provides a small blue shift. The UV and visible wavelength range of the libRadtran spectrum provides approximately 3 % more irradiance on average, whereas both spectra agree within differences smaller than 1 % in the near infrared region (except the absorption bands). To demonstrate that the simulated libRadtran spectrum is in close match with the SMARTS solar reference spectrum under consideration of significantly different spectral responsivities of two c-Si solar cells $s_{\text{ref}}(\lambda)$ and $s_{\text{DUT}}(\lambda)$, the spectral mismatch correction factor $f_{\text{SMM}} = 1/\text{SMM}$ is calculated in accordance with Equation (3.4). In case that the measured spectral responsivity datasets presented in the next chapter are used (the encapsulated solar cell used as reference device and the non-encapsulated used as DUT), the correction factor $f_{\text{SMM}} = 1.0005$ and is very close to 1 when the libRadtran spectrum shown in Figure 3.6 is used as $E_{\lambda, \text{meas}}(\lambda)$. Further evaluation of the differences of resulting spectral irradiances calculated by SMARTS and libRadtran is outside the scope of this study.

The simulated, spectrally resolved radiance data makes it possible to investigate coupled spectral- and angular-dependent mismatch effects; these effects are examined in Chapter 5.

3.6. Numerical approach

This section includes a description of the data pre-conditioning and processing to ensure the compatibility of both datasets, the detector responsivities and the source's radiance field, for computing the spectral-angular mismatch numerically.

To incorporate the simulated radiance field together with the experimentally-obtained detector responsivities in the multidimensional model elaborated in the sections above, careful pre-conditioning of the data is required to avoid errors in the mismatch computation. The angular-dependent spectral responsivity characterization of different solar cells is shown in Chapter 4. To merge the high spectral and angular resolution of the simulated dataset with the measured spectral and angular detector data three mandatory steps must be performed, in order to proceed with the computation of spectral-angular mismatch. The three preconditioning steps are schematically illustrated in Figure 3.7 and described below:

- 1) Interpolation of the spectral responsivity $s(\lambda, \theta = 0^\circ)$ onto the same wavelength resolution than the spectral radiance field $L_\lambda(\lambda, \theta, \varphi)$.
- 2) Weighting (step 2a) of the normalized angular-dependent spectral responsivity $s_{\text{rel}}(\lambda, \theta, \varphi)$ with the absolute spectral responsivity at the normal angle of incidence $s(\lambda, \theta = 0^\circ)$; interpolation (step 2b) of the angular-dependent spectral responsivity dataset $s(\lambda, \theta, \varphi)$ onto the high-resolution wavelength grid as in step 1).
- 3) Interpolation of the absolute angular-dependent spectral responsivity $s(\lambda, \theta, \varphi)$ from low to high angular resolution (step 3a) under consideration of a coordinate

transformation (step 3b) when the devices are tilted and rotated by θ' and φ' . Afterwards re-gridding of the data onto the original spherical grid (step 3c) matching with $L_\lambda(\lambda, \theta, \varphi)$ is required.

The interpolations performed in steps 1) to 3) are carried out by cubic splines. The interpolation of the measured spectral responsivity onto a high-resolution wavelength grid was carried out without overshooting of the datasets investigated in this work. To avoid overshooting of function values of the interpolated responsivity datasets onto a high-resolution angular grid, particularly the regions with large zenith angles ($\theta > 85^\circ$ and close to 90°) are carefully checked and precautionary interpolated using a nearest neighbor approach.

Pre-conditioning the datasets facilitates the spectral-angular mismatch calculation procedure derived in Section 3.4. The integrals in Equation (3.12) are solved, using a discretization approach with the corresponding grids for λ , θ and φ based on (Schrempf, 2018). To compute the pure spectral mismatch correction factor $f_{SMM} = 1/SMM$, the required global spectrum is used by incorporating the spectral radiance field $L_\lambda(\lambda, \theta, \varphi)$ into a spectral irradiance $E_\lambda(\lambda)$ separately for each individual wavelength λ_i within the wavelength range of interest.

To investigate the influence of the pure angular mismatch an approach in accordance with Equation (3.13) is used. The inverse of the obtained mismatches is then used as correction factors (e.g. $f_{SAMM} = 1/SAMM$) to compensate for spectral-angular effects under the diffuse irradiance conditions. The results presented in Chapter 5 of this work are expressed as a percentage of deviation from an ideal case without any mismatch ($f_{SAMM} = 1$).

The routine demonstrated here is an important part of this work to determine the spectral angular mismatch between two detectors under global irradiation conditions and angular losses of single detectors compared to ideal detectors following the cosine law. Therefore, the open source-based programming language python is used, which provides a variety of scientific programming packages.

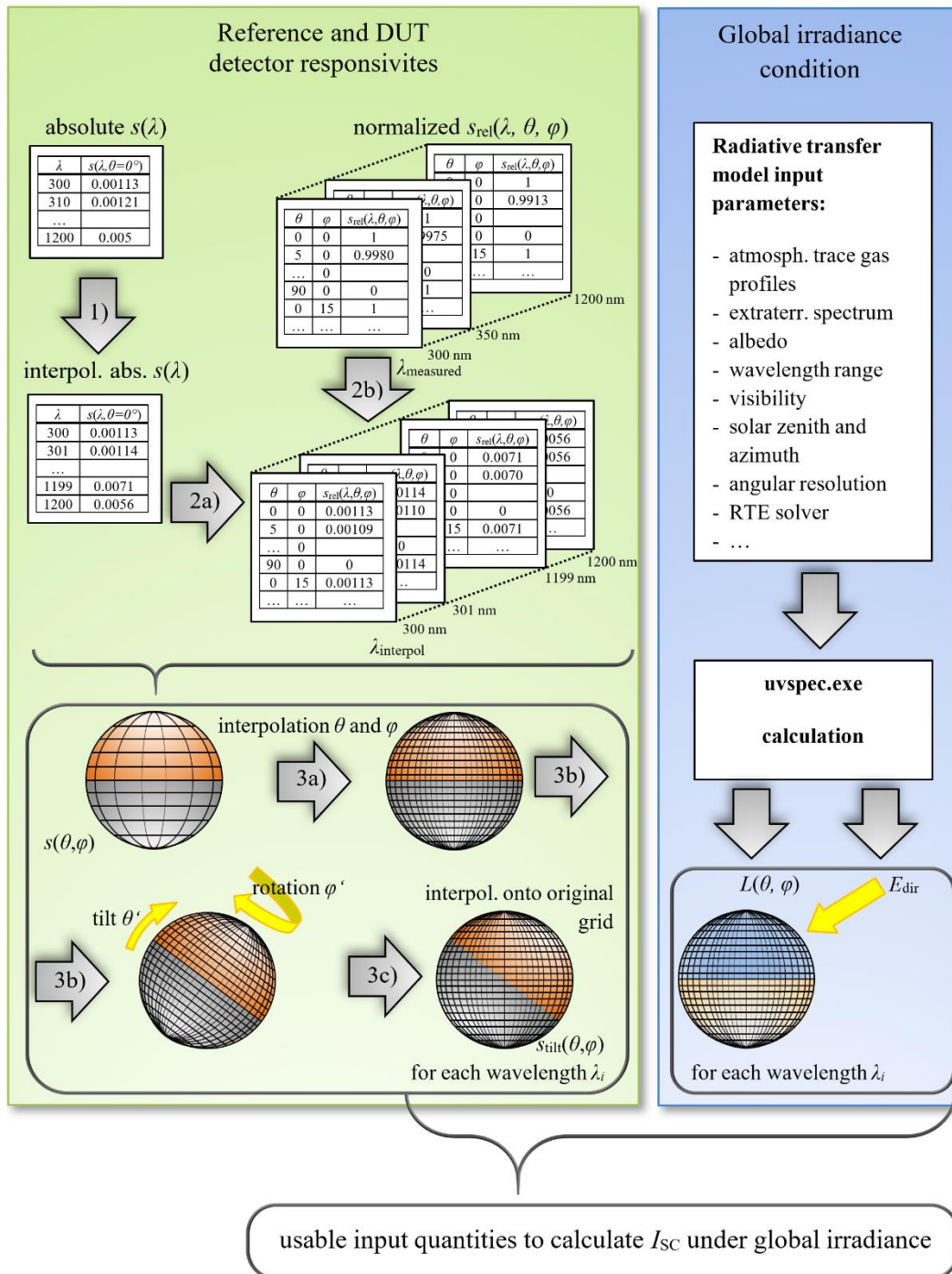


Figure 3.7: Data processing of the detector and source properties. On the left-hand side, a schematic description provides details on interpolation and coordinate transformation procedures of the measured device responsivity datasets with limited angular and spectral resolution used in order to obtain device responsivity datasets on a high resolution grid (green column); these datasets, in turn, can be used for the calculation of short-circuit currents under global irradiance conditions calculated by the radiative transfer model shown on the right-hand side (blue column). By using the ratios of the different short-circuit currents, the mismatch can be derived (see Equation (3.12)). This schematic figure is also published in (Plag, et al., 2018a).

3.7. Summary

The need of a novel method to consider and compensate errors introduced by diffuse irradiance during secondary high-accuracy PV device calibrations referring to reference conditions is presented. In this work the author proposes to define a directional property in addition to the reference conditions existing in international standards: All measurements taken under diffuse irradiation should be corrected to reference conditions containing a direct beam perpendicular to the device surface only. Based on a fundamental radiometric background, this chapter elaborates how to derive a beyond-the-state-of-the-art model that is used to determine the spectral-angular mismatch correction factor. The current reference spectrum based on simulations performed with SMARTS does not include information on the radiance or spectral radiance. To study the new multidimensional metric, the open source software package libRadtran is used to simulate a spectral- and angular-resolved sky radiance field for typical outdoor measurement conditions under clear sky. Therefore, conditions are chosen which are very close to those defined in the international standard IEC 60904-3 Edition 2, where SMARTS is used. Because the simulated spectral radiance dataset obtained by using libRadtran has a higher resolution than the later experimentally-obtained responsivity datasets, a detailed scheme about the data pre-conditioning procedure of the measured responsivity datasets is reported to convert them onto the same resolution and coordinate system as the simulated radiance field. Beside several interpolations in the spectral and the angular dimension, a coordinate transformation needs to be performed to account for the non-horizontal device orientation. The simulated spectrally resolved radiance data makes it possible to investigate coupled spectral- and angular-dependent mismatch effects, which are treated in Chapter 5.

4. Experimental methodology and realization

The following chapter outlines the most important experiments performed in this work. It is focused on a multidimensional solar cell characterization method and includes experimental results of a variety of investigated solar cells. To the authors knowledge, the detector characterization setup and procedure presented here are novelties. It includes a complete method that performs measurements of the angular-dependent responsivity for different wavelengths, device orientations covering the entire hemisphere, and two different polarization states, while it is possible to consider irradiance non-linearities of the devices. Thereby, the measurement of the absolute spectral responsivity is a primary calibration method, directly traceable to the international system of units (SI). None of the prior developed methods included in the literature review presented in Section 3.1 account for the listed features altogether in a single setup. The large variety of the datasets that are achieved by the new method allow systematic studies on the impact of diffuse irradiation on PV devices. Consequently, and most important, the availability of high-accuracy datasets of the spectral responsivity allows the examination of spectral-angular mismatch effects. In a second section, a thorough evaluation on the measurement uncertainty of the measured data in accordance to the standard “Guide to the expression of uncertainty in measurement” is conducted by using a Monte Carlo method (JCGM 100, 2008). The procedure including details on individual contributions to the uncertainty can act as best practice guide for the characterization of other angle of incidence facilities and is therefore published in advance as separate article (Plag, et al., 2017b). The results are then discussed to emphasize the need of case-by-case-based uncertainty analysis’. Finally, the most important findings of this chapter are summarized.

4.1. Characterization of the solar cells’ optical properties

This section of the present work is focused on the experimental characterization of directional, polarization and spectral dependent losses on solar cells photocurrent generation. All experiments performed for this work examine effects on the current at short-circuit condition. This quantity significantly contributes to the total electrical power of a PV device. It is beyond the scope of this work to study the physical origin of the losses. However, more of interest is to study the impact of the losses in dependence of specific irradiation conditions. The majority of this section and of the Section 4.2 is published in (Plag, et al., 2017b). The following text cites parts of this article. Additional information and other wording are added to the original content of the journal article, to facilitate the comprehensibility of this extensive approach.

The experimental work performed for this section is conducted at the Physikalisch-Technische Bundesanstalt in the laboratories of the applied radiometry group 4.52 “Solar Cells”. The improvements of the existing laser-based DSR facility are achieved within the EMRP project “Photoclass – Towards an energy-based parameter for photovoltaic

classification” with the support of Dr. Thomas Fey, Dr. Ingo Kröger and Dr. Florian Witt. DSR stands for differential spectral responsivity (Metzdorf, 1987).

The first subsection includes a detailed description of the experimental setup and elaborates the mathematical model used for the determination of the measurand: the angular-dependent responsivity. The second subsection shows the resulting datasets of three different silicon reference solar cells and two silicon solar cells providing a large area that is of industrial relevance. The third subsection demonstrates the importance of measurements considering more than one azimuthal orientation with an example showing the azimuthal asymmetry in the angular-dependent responsivity measured for a non-encapsulated device. Subsequently, a validation of the angular-dependent responsivity measurements between two different characterization approaches is presented. A discussion on the impact of the spectral mismatch originating from broadband irradiation on measured broadband angular-dependent responsivity datasets is presented in the last subsection.

4.1.1. Experimental setup

To perform angle of incidence (AOI) dependent measurements on solar cells, a laser-based DSR facility (Winter, et al., 2014) equipped with a fully automated goniometer that realizes any AOI in the full hemisphere within the solar cells field of view ($0^\circ \leq \theta \leq 90^\circ$, $-180^\circ \leq \varphi \leq 180^\circ$) was upgraded (see Figure 4.1).

A three-axis translation stage (x -, y -, and z -direction) allows AOI measurements even for the case that devices are mounted off-axial relative to the optical axis. For angular-dependent measurements, the solar cell is tilted and rotated relative to the light source. Both axes, tilt and rotation, are in the center of the PV device on the optical axis between solar cell and light source for φ -rotation (azimuth). Figure 4.2 shows the side and front view schematics on a mounted PV device at the laser-DSR facility in relation to the motor axes. A motor axis tilt in θ -direction results in a y - and z -offset. The position of the correct tilt axis θ on the device’s front surface, shown in red in Figure 4.2 (left hand side), is then conserved by moving the translation stage. The same procedure is applied to maintain the rotational axis φ in the center of the beam by performing x - and y -translations (see Figure 4.2 right hand side). The linear translation stage provides a positioning precision of better than 0.1 mm while covering a translation range of several meters.

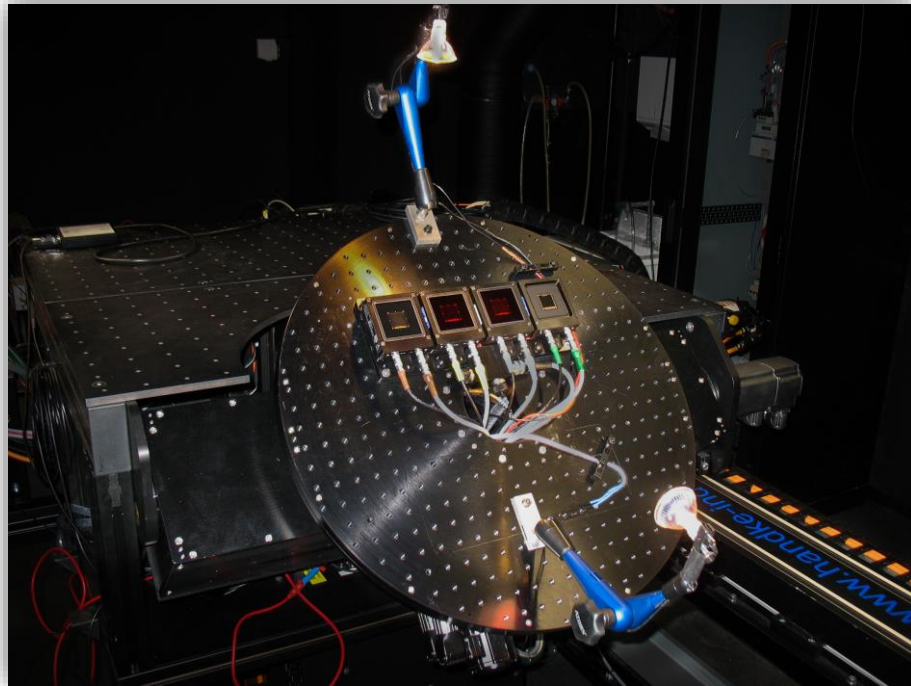


Figure 4.1: Photograph of the angle of incidence setup: An automated two-axis goniometer table is mounted on a x - y - z -translation stage. The liquid cooled round shaped mounting plate is equipped with a peltier controlled sample holder supporting up to four reference solar cells of different type. Two bias lamps are mounted stationary on the mounting plate.

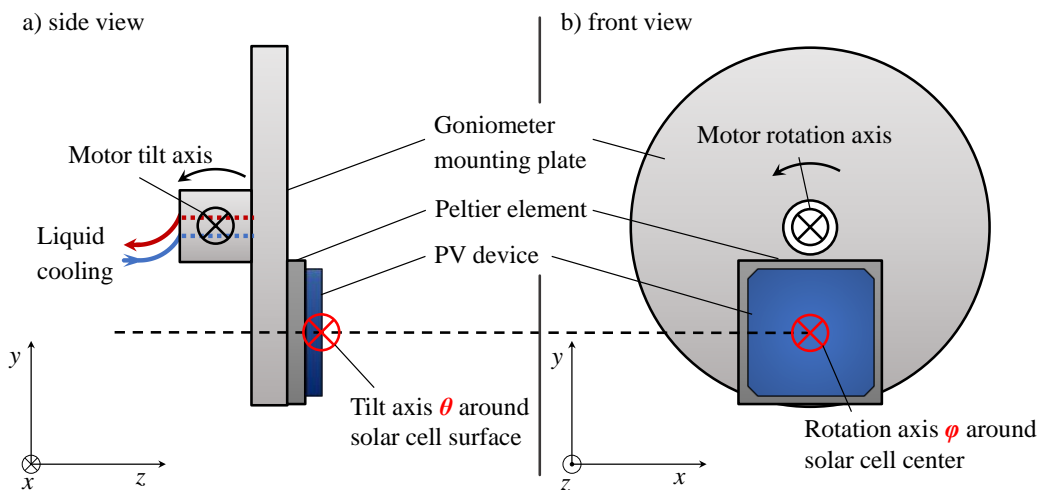


Figure 4.2: Mounted and thermoelectrically cooled PV device at the laser-DSR facility with off-axis position related to the solar cells front surface and center. a) shows a side view schematic with the position of the motor tilt axis (black) and the correct tilt axis (red) to visualize the need for a compensation by y - and z -translation. b) shows a front view schematic with the position of the motor rotation axis (black) and the correct rotation axis (red) to visualize the need for a compensation by x - and y -translation.

The solar cell mounting plate provides Peltier-controlled sample holders for sample thermostatzation and for investigation of the device's temperature dependencies. A variety of sample holders were developed to provide flexibility for mounting different PV device geometries ranging from reference solar cells in WPVS design over bare industrial crystalline silicon solar cells to encapsulated large area solar cells and mini modules. Bias lamps, providing a broadband spectral irradiance to set the samples in a steady working point, are mounted on the rotation stage for the AOI measurements. This arrangement is used to keep the bias irradiance steady during rotation (see Figure 4.3). Hence, irradiance non-linearity effects of PV devices under test are negligible. To measure the relative angular-dependent spectral responsivity $s(\lambda, \theta, \varphi)$, the solar cell is tilted and rotated in the monochromatic light field of the laser-DSR facility.

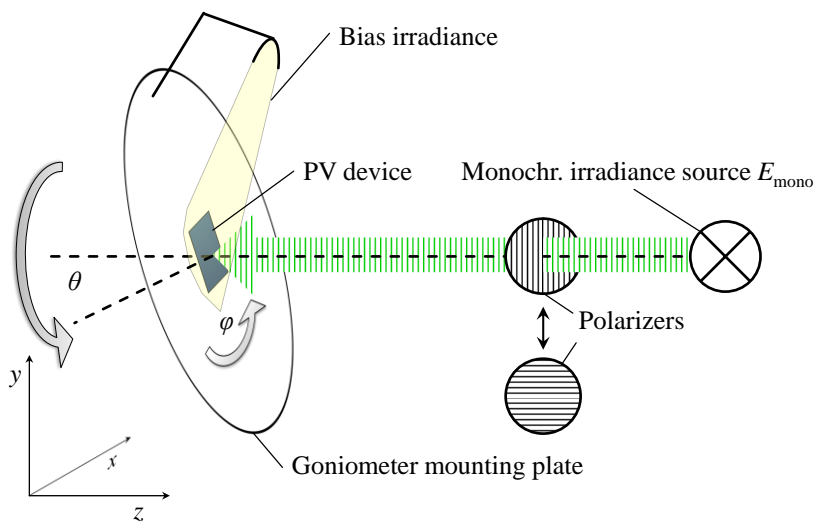


Figure 4.3: Schematic of the angular dependent spectral responsivity measurements using modulated monochromatic light and broadband bias light. To consider polarization effects two polarization filters in an automated filter wheel were aligned in the monochromatic optical path. The original figure is published in (Plag, et al., 2017b) and is modified for this work.

The usable spectrum of the laser-DSR ranges from 250 nm to 1600 nm. Because the AOI dependence of solar cells is dependent on the polarization of the incident light, the angular-dependent responsivity is determined subsequently for two orthogonal polarization states. In addition to the measurements of the angular-dependent responsivity relative to the value measured at normal incidence, a complete calibration of the absolute spectral responsivity $s(\lambda)$ at normal incidence with $\theta = 0^\circ$ is performed with the DSR method within the desired wavelength range. Finally, the AM1.5G-weighted angular-dependent responsivity $s_{\text{AM1.5G}}(\theta, \varphi)$ is derived by averaging the angular-dependent spectral responsivity curves weighted by their corresponding spectral responsivity $s(\lambda)$ and the AM1.5G reference solar spectral irradiance $E_{\lambda, \text{AM1.5G}}(\lambda)$.

In order to validate the AOI-dependent measurements two different setups are used to characterize different PV devices. In a first approach, the setup described above and illustrated in Figure 4.3 is used for the device characterization. In a second step, a tungsten halogen lamp (1000 W FEL) is used as a broadband light source with a known spectrum

$E_{\lambda,\text{lamp}}(\lambda)$, to obtain results with an alternative method at a given broadband spectrum (see Figure 4.4). Both optical setups are located side by side on the same optical table, that allows the use of the same goniometer system, when the sample is attached to the mounting plate.

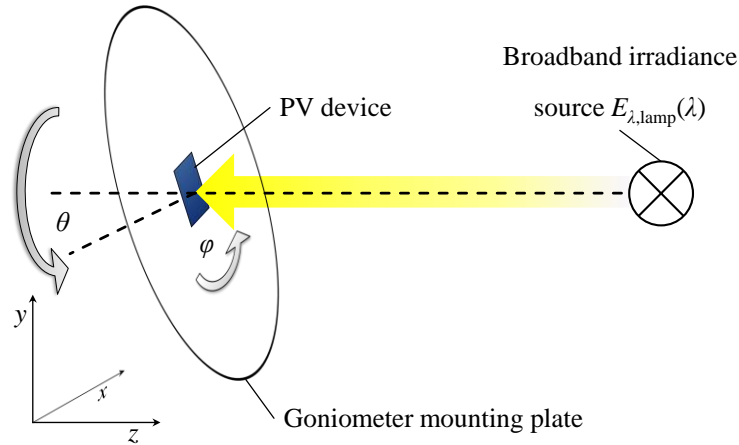


Figure 4.4: Schematic of the angular responsivity measurements using a broadband irradiance source. Between the measurements using two different light sources, the PV devices were kept attached on the same mounting plate as shown in Figure 4.3, while the tungsten halogen lamp is located on the same optical table next to the monochromatic setup. This setup was used to investigate the disadvantages of using an AOI facility with a given lamp spectrum $E_{\lambda,\text{lamp}}(\lambda)$. This figure is published in (Plag, et al., 2017b) and is modified for this work.

As reference plane for the tilt-axis θ , the thickness d_{real} is considered which is not necessarily matching with the geometrical location of the active front surface relative to the backside of the housing of the device, in case if the device is encapsulated (Witt, et al., 2013).

To measure the short-circuit current of the solar cell I_{SC} , a transimpedance amplifier (current to voltage converter with a resistance R_{SC}) and a voltmeter is used while the solar cell is actively kept at short-circuit condition. To consider fluctuations in the incident irradiance a photodiode, for the monochromatic radiation, and a solar cell, for the broadband radiation, are used as monitor detectors. By using a beam splitter, the monitor photodiode is positioned steady in the monochromatic beam, while the solar cell is tilted and rotated for the characterization sequence. A corresponding irradiance monitoring photocurrent I_{MD} is measured by means of the resistance R_{MD} of a second transimpedance amplifier. The alternating I_{SC} generated by the contribution of the modulated monochromatic radiation (AC) is separated from the steady direct current (DC) contribution by using a lock-in amplifier. A simplified circuit diagram of the electrical setup for the monochromator-based setup is schematically illustrated in Figure 4.5.

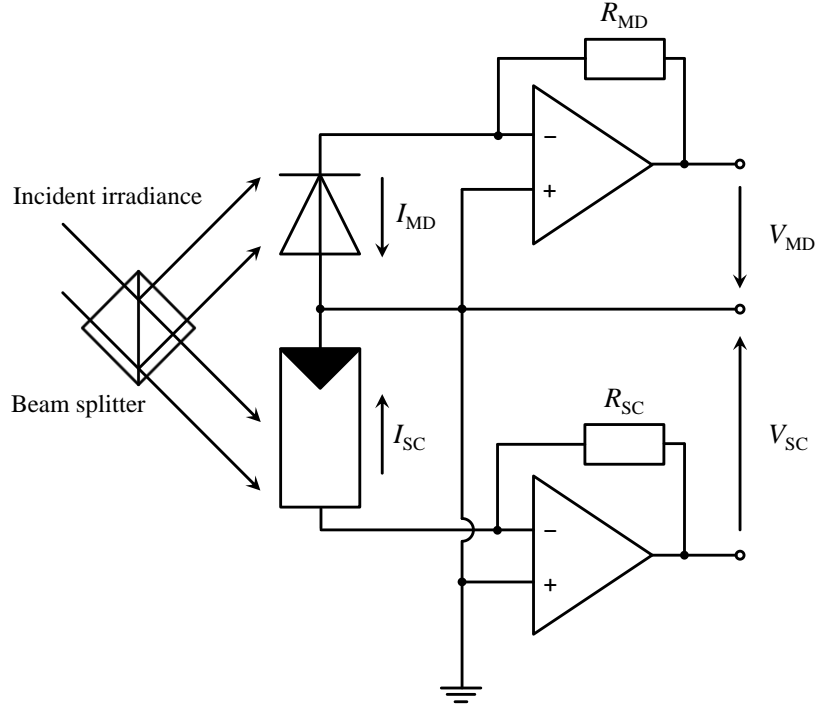


Figure 4.5: Simplified circuit diagram of the monochromatic setup for measurements of the angular-dependent responsivity $s(\theta, \varphi)$. The short-circuit currents of monitor photodiode I_{MD} and of the solar cell I_{SC} are converted into corresponding voltages V_{MD} and V_{SC} through the resistances R_{MD} and R_{SC} of two separate transimpedance amplifiers. By using a beam splitter, the monitor photodiode is positioned steady in the monochromatic beam, while the solar cell is tilted and rotated.

For angular-dependent measurements, the measured current $I_{SC}(\theta, \varphi)$ is normalized to the value at normal incidence $I_{SC}(\theta = 0^\circ, \varphi = 0^\circ)$. Hence, the mathematical model for the device under test AOI dependence, which corresponds to the relative angular responsivity $s(\theta, \varphi)$ is then:

$$s(\theta, \varphi) = \frac{\frac{I_{SC}(\theta, \varphi)}{I_{MD}(\theta, \varphi)}}{\frac{I_{SC}(\theta = 0^\circ, \varphi = 0^\circ)}{I_{MD}(\theta = 0^\circ, \varphi = 0^\circ)}} = \frac{\frac{V_{SC}(\theta, \varphi)/R_{SC}}{V_{MD}(\theta, \varphi)/R_{MD}}}{\frac{V_{SC}(0^\circ, 0^\circ)/R_{SC}}{V_{MD}(0^\circ, 0^\circ)/R_{MD}}} \quad (4.1)$$

$$= \frac{\frac{V_{SC}(\theta, \varphi)}{V_{MD}(\theta, \varphi)}}{\frac{V_{SC}(0^\circ, 0^\circ)}{V_{MD}(0^\circ, 0^\circ)}} = \frac{Q_{SC}(\theta, \varphi)}{Q_{SC}(0^\circ, 0^\circ)}$$

with Q_{SC} , representing the monitor corrected signals.

In case of angular-dependent spectral responsivity measurements, where modulated quasimonochromatic light is used, the voltages are determined using the lock-in technique by measuring the X - and Y -component (i.e. the real and imaginary part) of the voltages, both referred to a fixed phase ϕ_0 . In order to compensate stray light effects as well as amplifier offsets, the dark signals VX_{dark} and VY_{dark} are subtracted for each AOI measurement and for each detector, respectively. Hence, the individual voltages are:

$$V = \cos(\phi - \phi_0) \sqrt{(VX - VX_{\text{dark}})^2 + (VY - VY_{\text{dark}})^2} \quad (4.2)$$

with $\phi = \arctan\left(\frac{VY - VY_{\text{dark}}}{VX - VX_{\text{dark}}}\right)$.

To account for the polarization-dependent reflectance at the surface of the solar cell, the angular-dependent measurement sequence is performed at two orthogonal polarization states of the monochromatic irradiance using broadband polarization filters. Both normalized measurements are averaged to obtain an angular-dependent responsivity for unpolarized light. Thus, the expression for the unpolarized relative angular responsivity $s(\theta, \varphi)$ enhances to

$$s(\theta, \varphi) = \frac{\frac{\overline{Q_{\text{sc}}}(\theta, \varphi)}{Q_{\text{sc}}(0^\circ, 0^\circ)} \Big|_{\text{polarization} \rightarrow 0^\circ} + \frac{\overline{Q_{\text{sc}}}(\theta, \varphi)}{Q_{\text{sc}}(0^\circ, 0^\circ)} \Big|_{\text{polarization} \rightarrow 90^\circ}}{2}. \quad (4.3)$$

To allow a direct comparison of the measured angular-dependent responsivity against an ideal detector following the cosine with the AOI θ , the angular transmission $\tau(\theta)$ is used at every azimuthal orientation φ and for the corresponding monochromatic wavelength:

$$\tau(\theta) = \frac{s(\theta, \varphi)}{\cos \theta}. \quad (4.4)$$

A relative comparison in percent seems to be more tangible for the most readers. Therefore, in this work the deviation from cosine is used (see Equation (4.5)), which is also the negative angular loss in % compared to an ideal detector for incident irradiance originating from a distinct direction.

$$\text{deviation from cosine } (\theta) = (\tau(\theta) - 1) \cdot 100\%. \quad (4.5)$$

The determination of a large number of angular transmissions containing azimuthal and spectral information for a single PV device is a novel technique that leads to challenges when results are compared against state-of-the-art measured broadband angular transmissions under a defined spectral irradiance $E_{\lambda, \text{lamp}}(\lambda)$. To convert the spectrally resolved datasets into broadband datasets, the knowledge about the spectral responsivity at normal incidence and the spectral irradiance condition $E_{\lambda, \text{lamp}}(\lambda)$ is required. A major advantage of measuring spectrally resolved datasets is that they can be converted into broadband datasets for every

desired spectrum. This allows to perform a comparison between state-of-the-art measurement techniques that are based on broadband light sources with the novel approach, which is presented in Subsection 4.1.4.

4.1.2. Results of the angular dependent measurements

In the following section, exemplary results of the polarization- and angular-dependent spectral responsivities of different types of solar cells are shown in order to demonstrate the significant differences in the measured datasets. In a first step, three different reference solar cells are selected for characterization: An encapsulated, a non-encapsulated and an IR-filtered cell, all manufactured from monocrystalline silicon. Pictures of the samples are shown in Figure 4.6. Parts of this section are published in the journal articles (Plag, et al., 2017b; 2018a)

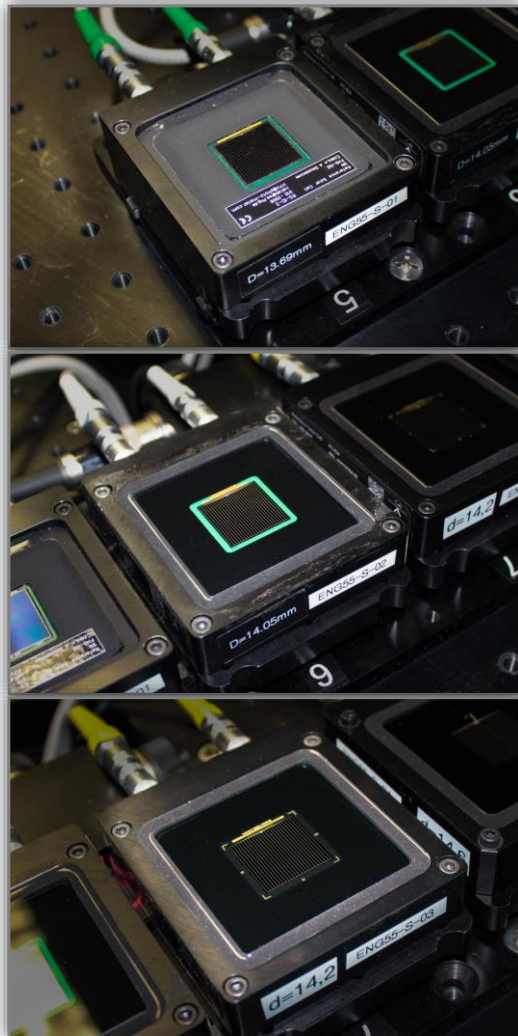


Figure 4.6: Photographs of the investigated reference solar cells in WPVS design with an area of $20 \times 20 \text{ mm}^2$. The solar cells are made of monocrystalline silicon. The housings contain PT100 temperature sensors and electrical connectors allowing four-wire measurements of the electrical cell characteristics at defined temperatures. (top) shows a non-encapsulated solar cell, (middle) shows an encapsulated solar cell and (bottom) shows an IR-filtered solar cell.

The samples are manufactured in a reference solar cell package design of the World Photovoltaic Scale (WPVS) (Osterwald, et al., 1999). The IR-filtered solar cell is covered by an infrared absorptive KG5 filter manufactured by Schott. Additionally, the absolute spectral responsivities $s(\lambda)$ of the devices are measured by means of the DSR-method at normal incidence against a reference photodiode.

Results on the calibration of the device's spectral responsivity at normal incidence with a wavelength step width of 5 nm are shown in Figure 4.7. The angular-dependent characterization of the device's relative spectral responsivity is carried out using different wavelengths ranging from

300 nm to 1150 nm for the encapsulated and non-encapsulated devices and from 350 nm to 800 nm for the IR-filtered device. A step width of 50 nm is chosen for the experiment. The angular resolution is set to 5° in zenithal (θ) direction. After each zenithal variation for a

single wavelength, the azimuthal (φ) orientation is increased by 15° and the sequence is continued.

To limit the experimental effort, the directional characterization is performed for seven different azimuths ranging from 0° to 90° covering a quarter of the hemisphere within the field of view of the solar cells. When the spectral- and polarization-dependence are both included, this sums up to 4788 data points per device for a non-filtered crystalline silicon (c-Si) solar cell, excluding the absolute spectral responsivity characterization at normal incidence. Hence, the azimuthal symmetry of the crystalline cell structure is only considered within an azimuthal range (φ) from 0° to 90° for the monochromator-based measurements.

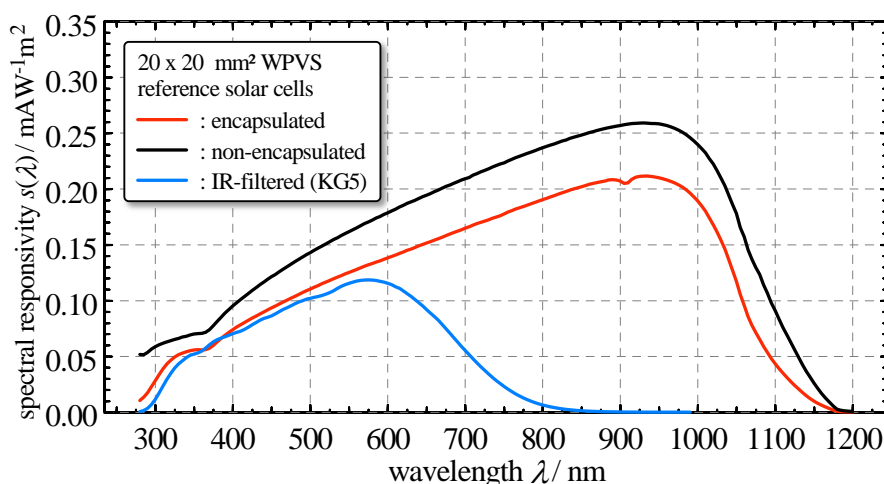


Figure 4.7: Absolute spectral responsivities $s(\lambda)$ of three investigated reference solar cells. The $s(\lambda)$ is measured at normal incidence ($\theta = 0^\circ$). The encapsulated solar cell is shown in red, the non-encapsulated solar cell in black and the IR-filtered solar cell in blue colored lines. The dataset shown in this figure is published in the journal article (Plag, et al., 2018a).

Figure 4.8 shows the angular-dependent responsivities at different wavelengths of a non-encapsulated c-Si reference solar cell (top), an encapsulated c-Si reference solar cell (middle) and an IR-filtered c-Si reference (bottom) that is typically used as a reference for calibration of amorphous Si solar cells. The graphs show the results of one azimuthal measurement sequence at $\varphi = 0^\circ$ for each solar cell. In the graphs on the left-hand side, the angular-dependent responsivity for different wavelengths is shown together with the cosine (black dashed line). In the graphs on the right-hand side, the relative deviation from cosine according to Equation (4.5) is shown. All datasets presented in Figure 4.8 include responsivities evaluated for unpolarized irradiation.

From these graphs, significant differences in the angular-dependent spectral responsivity are observed. The non-encapsulated reference solar cell has a strong deviation from cosine at incidence angles larger than 25° . This deviation enhances with decreasing wavelength. The encapsulated device also shows a spectral variation of the deviation from cosine. However, it is less pronounced. Most interestingly, the encapsulated solar cell significantly overperforms the cosine for wavelengths $\lambda > 900$ nm. This effect originates most likely from interreflections between the cover glass, the solar cell and the device housing. The IR-filtered

reference solar cell shows an opposed spectral characteristic of the angular-dependent responsivity. The deviation from cosine increases with increasing wavelength. Note that a differing color scale is used in Figure 4.8 (bottom). Due to the absorptive filter, the spectral responsivity reduces to zero for wavelengths $\lambda > 900$ nm (see Figure 4.7).

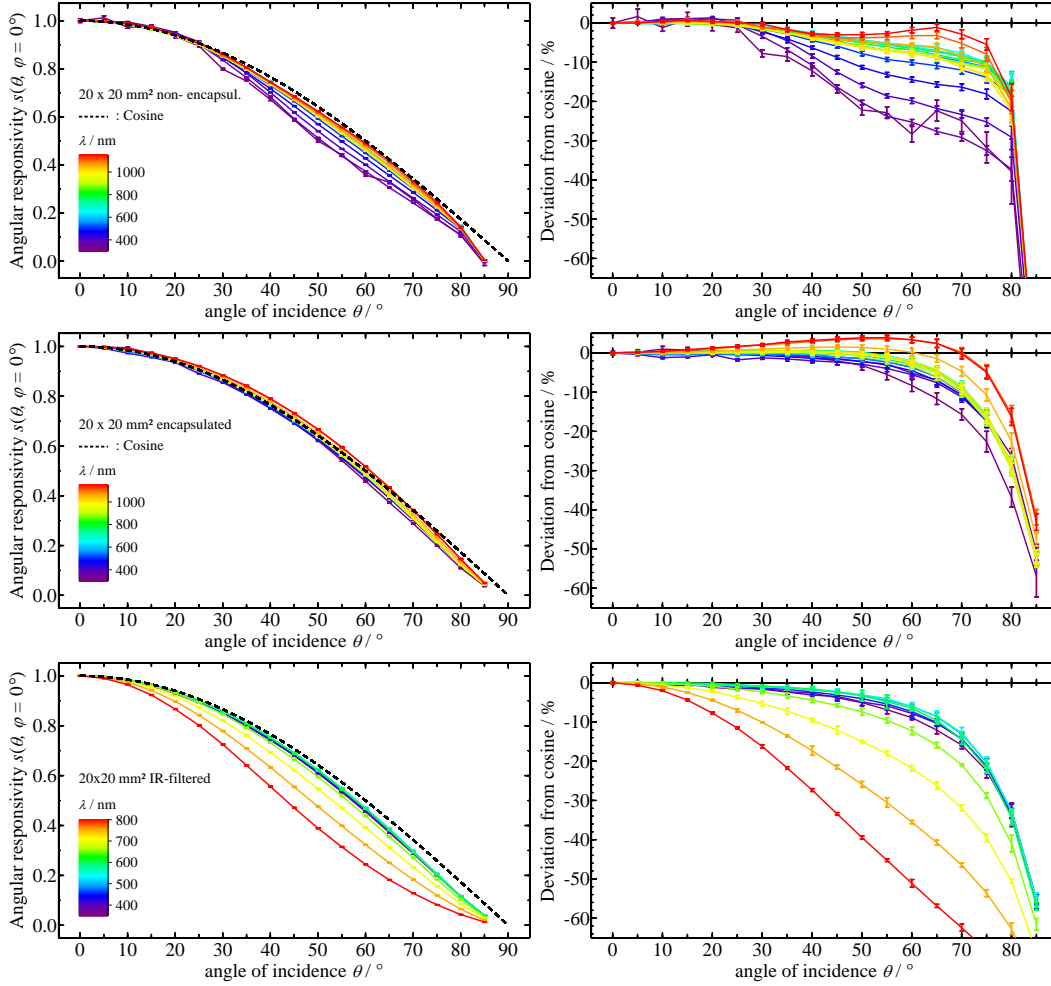


Figure 4.8: Angular-dependent responsivity (left-hand side) and deviation from cosine (right-hand side) of three different types of WPVS reference solar cells dependent on wavelength: a non-encapsulated c-Si reference solar cell (top), an encapsulated c-Si reference solar cell (middle) and an encapsulated c-Si reference with an IR-filter as cover glass (bottom). In the left-hand sided graphs, the angular responsivity is shown together with the cosine of the AOI (black dotted line). In the right-hand sided graphs, the deviation from cosine is shown. The results shown in this figure are published in (Plag, et al., 2017b).

In conclusion, these three different types of reference solar cells show strongly different angular-dependent spectral responsivities. Their generated short-circuit current under diffuse irradiance condition would be significantly different compared to the generated current under direct normal incidence only. This is of vital importance when reference devices are used in calibration facilities with a substantial contribution of diffuse light, i.e. using global natural sunlight or non-collimated solar simulators. Exemplary calculations of the spectral-angular mismatch effect for natural sunlight conditions for exactly these three reference devices are presented in Section 5.1.

With focus on the application of PV as generators for electricity, further experiments are performed to study the angle of incidence dependence of large area industrial c-Si solar cells ($125 \times 125 \text{ mm}^2$) with and without encapsulation (mini PV module and bare solar cell).

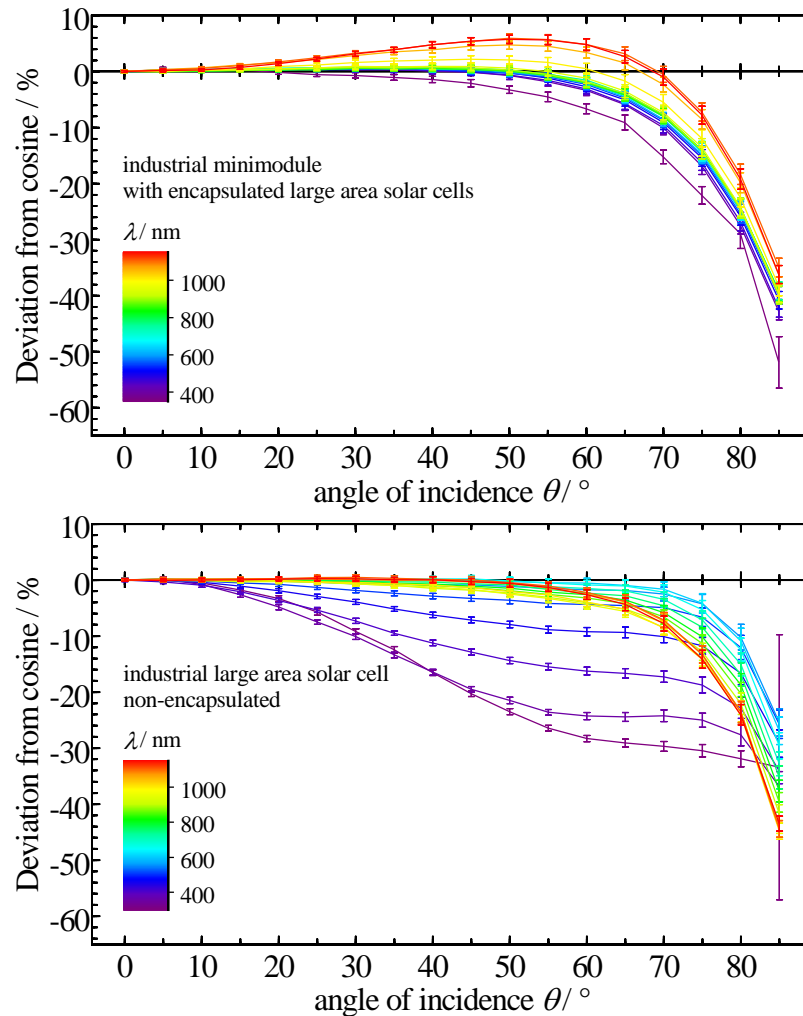


Figure 4.9: Effect of encapsulation on an industrial large area c-Si solar cell: Deviation from cosine of an industrial large area c-Si solar cell and a mini PV module made from the same type of solar cell. The relative angular-dependent responsivity significantly improves due to the encapsulation, leading even to a relative overperformance in the infrared wavelength region. This figure is published in (Plag, et al., 2017b).

The encapsulation material of the investigated mini PV module consists of a textured cover glass and white colored ethylene-vinyl acetate (EVA) back sheet, which are widely used in commercial PV module production. Due to a non-disclosure agreement with the manufacturing companies a presentation of further details and photographs showing these devices is omitted in this work.

Figure 4.9, bottom, shows the deviation from cosine for a typical industrial large area solar cell, and on the top, for an encapsulated mini PV module made of the same type of solar cell. The direct comparison demonstrates similarly to the described WPVS reference solar cells

the effect of encapsulation on the angular-dependence of the spectral responsivity. Similar observations are described in a previous study by (Geisemeyer, et al., 2017). For the bare solar cell, the deviation from cosine is large even at small angles of incidence for short wavelengths below 500 nm. In the VIS-NIR region from 500 nm – 1200 nm the deviation from cosine is very low even for increasing angles of incidence up to 60°. After encapsulation of this solar cell in an encapsulant, the spectral- and angular-dependent characteristics significantly change. The relative angular-dependent responsivity noticeably improves for all wavelengths and even overperforms the cosine for the infrared region at angles of incidence below 65°. Hence, it can be concluded that the spectral responsivity of typical photovoltaic devices significantly varies for different angles of incidence.

4.1.3. Azimuthal symmetry

Angle of incidence dependent measurements using monochromatic light or even a broadband light source are time-consuming procedures. Furthermore, the parameter space that should be covered (θ , φ , λ) results in very large measurement sequences. Hence, a complete characterization covering the full azimuthal range (φ) is often not feasible. For the determination of angular-dependent losses, the energy rating standard IEC 61853-2 demands measurements to be taken along two azimuthal directions with respect to the modules surface normal (IEC 61853-2, 2016). The rotational (azimuthal) symmetry should be verified at the two angles of incidence: $\theta = -80^\circ$ and $\theta = 80^\circ$. To evaluate the measurement uncertainty that occurs due to the azimuthal asymmetry of the device if measurements are taken along only two orthogonal azimuthal directions, a systematic comparison is performed. Hence, the measurements taken in accordance with the energy-rating standard are compared to the measurements taken in the full hemisphere by using the previously described broadband light source facility.

Figure 4.10 shows the result of this comparison for the non-encapsulated reference solar cell. This example provides the largest azimuthal asymmetry within the investigated sample set. Therefore, it represents a worst-case scenario in order to underline the possible magnitude of this effect. The blue and red dashed lines correspond to the measurements taken along the two orthogonal azimuthal directions both covering zenith angles ranging from $\theta = -80^\circ$ to $\theta = 80^\circ$. The grey area shows the maximum deviation observed for all other azimuthal orientations investigated here.

For this example, the asymmetry expressed by the difference of the deviation from cosine at two zenith angles $\theta = 80^\circ$ and $\theta = -80^\circ$ along the azimuth axis $\varphi = 0^\circ$ is 3.4 % (blue dashed line). The asymmetry between the measurements taken along the azimuth axis $\varphi = 90^\circ$ is 5.6 % (red dashed line). Hence, this non-encapsulated WPVS reference solar cell must be considered to be non-symmetrical according to the standards criterium.

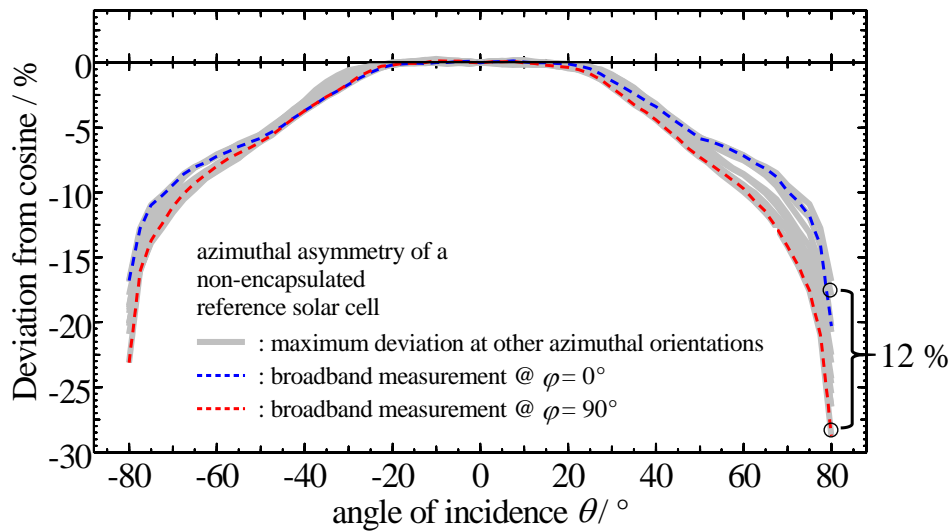


Figure 4.10: Measurement of the angular-dependent responsivity of a non-encapsulated WPVS reference solar cell using a halogen lamp measured at 24 different azimuthal orientations ranging from -180° to 180° in steps of $\Delta\varphi = 15^\circ$. This figure is published in (Plag, et al., 2017b)

However, the maximum observed azimuthal deviation indicated as black circles in Figure 4.10 is 12 %. A conclusion of this experiment is that the assumption of azimuthal symmetry in the studied reference PV device is not fulfilled. In this case, the procedure defined in the energy rating standard (IEC 61853-2, 2016) cannot be applied properly by reporting only one angular transmission. Note that a measurement error related to a systematic offset of the angle of incidence θ leads to asymmetric measurement results. A systematic offset of only 1° leads to an apparently measured asymmetry of 22 % at 80° angle of incidence. This observation emphasizes the high sensitivity on the accuracy of the instrumentation and alignment required to achieve a low measurement uncertainty of the angular-dependent responsivity.

All expanded measurement uncertainties shown in the Figures 4.8 and 4.9 are individually computed on case-by-case-based uncertainty analysis' in accordance with the GUM. The comprehensive characterization procedures required for the analysis and the derivation of an exemplary uncertainty budget is presented in Section 4.2.

4.1.4. Validation of the angular-dependent responsivity measurements

For validation of the measurements and their corresponding measurement uncertainties the two previously described methods for angular-dependent measurements are compared. Therefore, the angular-dependent responsivity of the previously described IR-filtered reference solar cell is measured using a broadband light source, a 1000 W FEL tungsten halogen lamp, and the spectral monochromator-based facility. From the spectral data, a broadband dataset is derived by weighting the angular-dependent spectral responsivity dataset with the measured absolute spectral responsivity of the device at normal incidence and the spectral irradiance of the 1000 W FEL tungsten halogen lamp. The results of this comparison are shown in Figure 4.11. The blue curve indicates the deviation from cosine of θ for the data determined with the spectrally resolved method which is converted to a

broadband dataset. The red curve indicates the deviation from cosine measured with the broadband tungsten halogen light source. Error bars indicate the expanded measurement uncertainties respectively.

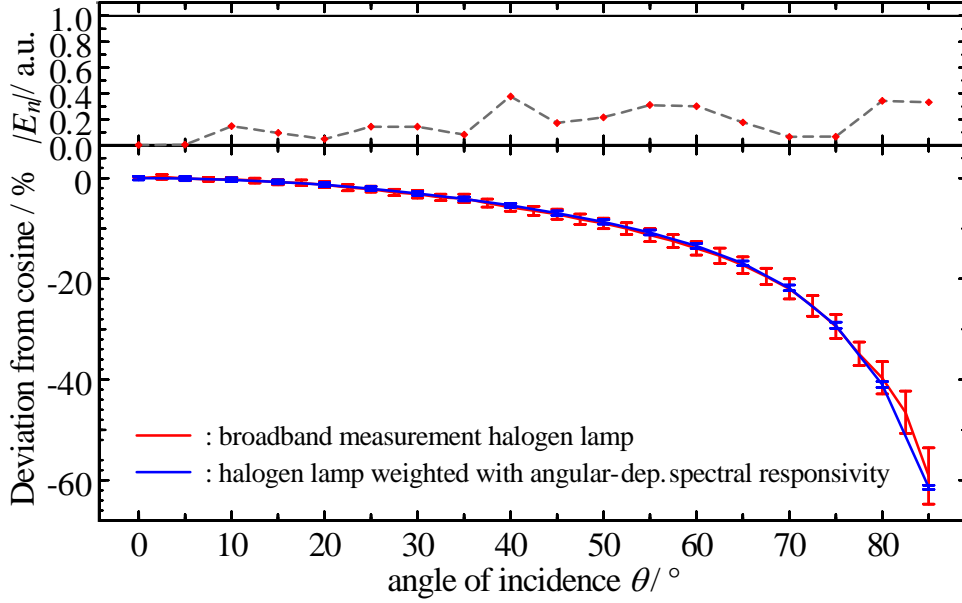


Figure 4.11: Comparison of the angular-dependent responsivity measurements of the IR-filtered reference device using the broadband light source (tungsten halogen lamp, red line) and the monochromatic light source (blue line). From the spectrally resolved data shown in Figure 4.8 (top) the weighted average is calculated using the measured spectral responsivity of the device at normal incidence and the spectral irradiance of the halogen lamp as weighting functions. The upper graph (grey dashed line) shows the absolute values of the E_n number in accordance with the standard (ISO/IEC 17043, 2010). The dataset shown in this figure is published in (Plag, et al., 2017b).

It is worth to mention that some uncertainty contributions of both methods included in this comparison are correlated. However, the most significant uncertainty contributions, explained in detail in Section 4.2, f_{anu} , f_{pol} , f_{θ} and f_E are different for both methods. For validation purposes, the E_n number in accordance with the ISO standard 17043 is commonly used (ISO/IEC 17043, 2010).

$$E_n = \frac{x_1 - x_2}{\sqrt{U_1(x_1)^2 + U_2(x_2)^2}}, \quad (4.6)$$

with x_1 and x_2 the measurands determined with method 1 and method 2, and the corresponding expanded measurement uncertainties $U_1(x_1)$ and $U_2(x_2)$.

The E_n number indicates whether two measurements agree within their reported expanded uncertainties or not. If $|E_n| \leq 1$, the measurements are consistent within their reported uncertainties. The E_n number for this comparison measurement is shown in the upper graph of Figure 4.11 for each angle of incidence. Hence, both angle of incidence dependent measurement methods taken for this study are consistent. Furthermore, it can be concluded that the angular-dependent responsivity for any spectral irradiance can be derived from the

measured angular-dependent spectral responsivity data by calculating the weighted average using the spectral responsivity at normal incidence and the spectral irradiance of any light source.

4.1.5. Discussion of the mismatch effect on AOI-dependent measurements

One conclusion of the previous Section 4.1.4 is that the measurement of the angular-dependent spectral responsivity allows the analysis of spectral and angular effects under any given spectrum including individual diffuse irradiance components. Due to the relative change in the spectral responsivity as a function of AOI θ , spectral mismatch errors can be neglected for monochromator based AOI measurements, but they have to be considered for measurements taken with broadband setups providing a fixed spectrum. To illustrate this problem, the angular-dependent spectral mismatch factor $SMM(\theta)$ due to the spectral irradiance of the broadband light source $E_{\lambda,\text{lamp}}(\lambda)$ and due to the angular-dependent spectral responsivity $s(\lambda, \theta)$ of the individual PV device can be expressed based on the definition of the spectral mismatch given in (IEC 60904-7 Edition 3, 2008):

$$SMM(\theta) = \frac{\int_{\lambda} E_{\lambda}(\lambda) \cdot s(\lambda, \theta = 0^{\circ}) d\lambda}{\int_{\lambda} E_{\lambda}(\lambda) \cdot s(\lambda, \theta) d\lambda} \frac{\int_{\lambda} E_{\lambda,\text{lamp}}(\lambda) \cdot s(\lambda, \theta) d\lambda}{\int_{\lambda} E_{\lambda,\text{lamp}}(\lambda) \cdot s(\lambda, \theta = 0^{\circ}) d\lambda} \quad (4.7)$$

As a reference spectral responsivity for this calculation, the device's spectral responsivity under normal incidence ($\theta = 0^{\circ}$) is used with a step width of 50 nm. A linear interpolation is used in this qualitative attempt to bring the low-resolution spectral responsivities onto the same high resolution as the spectral irradiance $E_{\lambda}(\lambda)$, which represents the spectral irradiance of the condition on that the spectral mismatch refers to (i.e. a reference spectrum). When the spectral responsivity of a PV device is AOI-dependent, and it is measured with a broadband source $E_{\lambda,\text{lamp}}(\lambda)$, the spectral mismatch affects the determination of an angular-dependent responsivity measurement results under a given (different) spectrum $E_{\lambda}(\lambda)$, as it is the case for the state-of-the-art procedures defined in the energy rating standard.

The spectral mismatch factors in dependence of the AOI θ are computed for three different PV devices (see Figure 4.12). In this example, the mismatch refers to the global solar reference spectrum under AM1.5G defined in the standard (IEC 60904-3 Edition 2, 2008) by using it in Equation (4.7) for $E_{\lambda}(\lambda)$ and the spectral irradiance of a 1000 W tungsten halogen lamp $E_{\lambda,\text{lamp}}(\lambda)$ used in the previously described broadband AOI-facility.

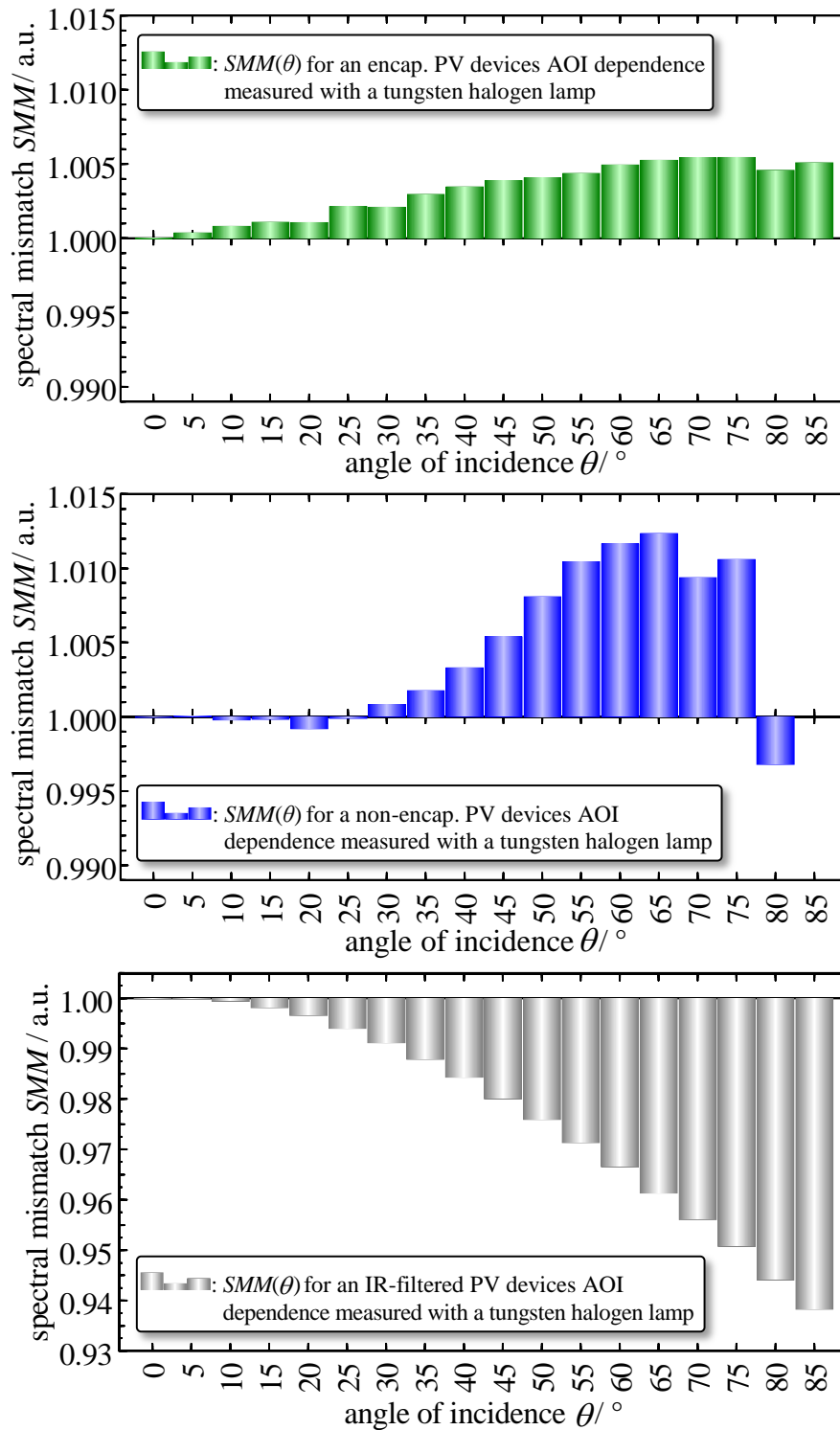


Figure 4.12: Angular-dependent spectral mismatch factors for three different reference solar cells in WPVS design ($20 \times 20 \text{ mm}^2$) measured with a tungsten halogen lamp. (top) Spectral mismatch factor for an encapsulated device; (middle) Spectral mismatch factor for a non-encapsulated device and (bottom) Spectral mismatch factor for an IR-filtered encapsulated device. The exemplary spectral mismatch calculations in this figure are published in (Plag, et al., 2017b).

These results show the need for a spectral mismatch correction of AOI-dependent measurements, when broadband light sources are used. In this study, the spectral irradiance of the halogen lamp differs significantly and is considered to be a solar simulator with a poor spectral match and represents a worst-case scenario. For the encapsulated device, the angular-dependent change of spectral responsivity (shown in Figure 4.8, middle) is less pronounced. Hence, the spectral mismatch correction is less than 0.5 %, even at larger AOI. For the non-encapsulated device, the angular-dependent change of the spectral responsivity (shown in Figure 4.8, top) is more pronounced, especially in the UV-VIS region and for AOI's larger than 30°. This leads to a spectral mismatch of up to 1.2 %. The most pronounced angular-dependent change of the spectral responsivity is observed for the IR-filtered reference device (shown in Figure 4.8, bottom). The resulting spectral mismatch correction is more than 6 %.

It can be concluded, that an angular-dependent spectral mismatch is of major importance and should be included in any uncertainty budget for broadband light source AOI-facilities. If the angular-dependent spectral responsivity is not known, it should be conservatively estimated and considered as contribution to the uncertainty.

4.2.Measurement uncertainty of the angular-dependent responsivity

The derivation of a measurement uncertainty budget for the angular-dependent responsivity measurements is of vital importance in this work. In this section, a novel and thorough characterization of the AOI-facilities is presented to finally determine a measurement uncertainty budget. A number of correction factors f_i with individual uncertainties contributing to the combined standard uncertainty $u(s(\theta, \varphi))$ of the measurand $s(\theta, \varphi)$ need to be multiplied with Equation (4.3) to compensate for systematic effects related to the individual experimental approach. The following discussion of the correction factors f_i in this section, is part of the uncertainty analysis published in the article (Plag, et al., 2017b) and is quoted and supplemented here.

Contributing influences on the measurement uncertainty are:

- Type A uncertainty, due to statistical fluctuation in the corrected signals Q_{sc} ,
- Electrical non-linearities of the current measurement,
- Irradiance non-uniformity onto the device during the rotation,
- Positioning of the device under test relative to the rotational axis,
- Thickness of the PV device,
- Polarization,
- Uncertainty of the tilt angle (AOI) θ ,
- Irradiance non-linearity of the PV device,
- Uncertainty of the temperature measurement,
- and wavelength uncertainty.

4.2.1. Type A uncertainty

To consider Type A uncertainties the voltage measurements at a given angle of incidence are repeated typically $n = 20 \dots 40$ times (see Figure 4.13).

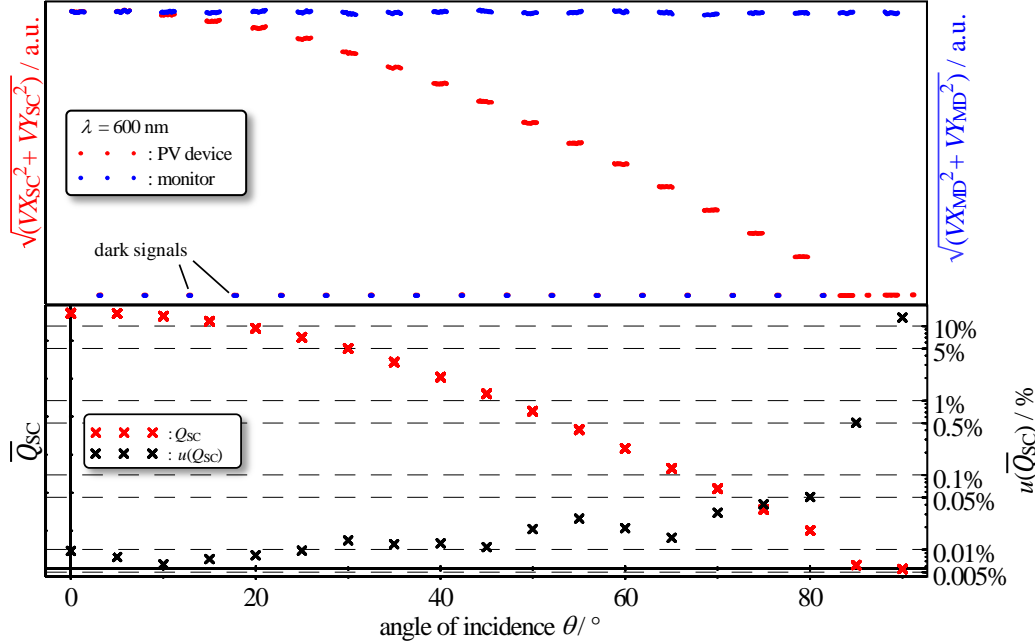


Figure 4.13: (top) Measured voltages against the angle of incidence ranging from $\theta = 0^\circ$ to $\theta = 90^\circ$. The voltages are proportional to the generated photocurrent of the solar cell. Each angular measurement is repeated 20 times; (bottom) monitor corrected and averaged signal \bar{Q}_{SC} against the AOI θ and assigned relative standard uncertainties. The dataset presented in this figure is published in (Plag, et al., 2017b).

Type A uncertainties are individually calculated by the variance of the monitor corrected average signal \bar{Q}_{SC} :

$$u(\bar{Q}_{SC}) = \sqrt{\text{Var}(Q_{SC})}. \quad (4.8)$$

4.2.2. Non-linearity of the current measurement

While the absolute values of the internal resistances of the current-to-voltage converters cancel out in the mathematical model given in Equation (4.1), the linearity of the amplifiers is of major importance. When the solar cell is tilted, the signal reduces approximately with the $\cos(\theta)$ from 1 (at 0°) to 0.09 (at 85°), roughly one order of magnitude. The non-linearity of the transimpedance amplifier is determined to be $< 0.1 \%$ (Type B, rectangular). Additionally, typical nonlinearities of similar lock-in amplifiers or digital voltmeter are $< 0.1 \%$ (Type B, rectangular) (Theocharous, 2008). Thus, the uncertainty related to electrical components is smaller than 0.15% . Consequently, f_{el} is estimated to be:

$$f_{el} = 1 \pm 0.0015. \quad (4.9)$$

4.2.3. Irradiance non-uniformity onto the device during the rotation

For laboratory measurements, a change of the irradiance spatial non-uniformity (nu) inclined on a device surface with a given tilt angle is expected. The reason is the inverse-square law, which provides a $1/z^2$ dependence for the irradiance in case if a divergent point light source is used. The surface integral for determining the generated short-circuit current of the solar cell I_{nu} at distinct wavelengths λ_{mono} includes the superposition of the spatial distribution of the spectral responsivity of a solar cell $s(\lambda_{\text{mono}}, x, y)$ at a designated monochromator wavelength λ_{mono} and the (non-uniform) monochromatic irradiance distribution of the corresponding light field $E_{\text{mono}}(\lambda_{\text{mono}}, x, y)$. It is expressed as:

$$I_{\text{nu}}(\lambda_{\text{mono}}) = \iint s(\lambda_{\text{mono}}, x, y) \cdot E_{\text{mono}}(\lambda_{\text{mono}}, x, y) \, dx dy. \quad (4.10)$$

For a perfect uniform (uni) light field, Equation (4.10) reduces to

$$\begin{aligned} I_{\text{uni}}(\lambda_{\text{mono}}) &= \iint s(\lambda_{\text{mono}}, x, y) \cdot E_{\text{mono}} \, dx dy \\ &= E_{\text{mono}} \iint s(\lambda_{\text{mono}}, x, y) \, dx dy = E_{\text{mono}} \cdot s. \end{aligned} \quad (4.11)$$

Hence, a non-uniformity correction factor f_{nu} for a wavelength λ_{mono} can be derived:

$$f_{\text{nu}}(\lambda_{\text{mono}}) = \frac{I_{\text{uni}}(\lambda_{\text{mono}})}{I_{\text{nu}}(\lambda_{\text{mono}})} = \frac{E_{\text{mono}} \iint s(\lambda_{\text{mono}}, x, y) \, dx dy}{\iint s(\lambda_{\text{mono}}, x, y) \cdot E_{\text{mono}}(\lambda_{\text{mono}}, x, y) \, dx dy}. \quad (4.12)$$

However, the non-uniformity factor itself is not an uncertainty contribution for angular-dependent measurements. For these measurements, only the relative change of the non-uniformity correction factor with respect to normal incidence is important. Accordingly, an approximation of the uncertainty of the angular-dependent non-uniformity $u(f_{\text{anu}}(\theta, \lambda_{\text{mono}}))$ as the relative deviation of the previously determined correction factors $f_{\text{nu}}(\theta, \lambda_{\text{mono}})$ to $f_{\text{nu}}(0^\circ, \lambda_{\text{mono}})$ is determined by

$$u(f_{\text{anu}}(\theta, \lambda_{\text{mono}})) = \frac{f_{\text{nu}}(\theta, \lambda_{\text{mono}})}{f_{\text{nu}}(0^\circ, \lambda_{\text{mono}})} - 1. \quad (4.13)$$

Because $f_{\text{anu}}(\theta, \lambda_{\text{mono}})$ of a device is strongly related to the non-uniformity of the solar cells lateral responsivity $s(\lambda_{\text{mono}}, x, y)$, and the lateral non-uniformity of the irradiance distribution at the given angle θ within the volume that is enveloped by the tilted surface of that device during the rotation, an extensive characterization would be required to obtain the individual correction parameters. This is not possible within reasonable time and effort for every measurement. For the estimation of a representative uncertainty related to the setup used in this work, an exemplary extensive characterization is shown. Thus, the quantification of these individual correction parameters is shown here for a general case of typical industrial c-Si solar cells and c-Si reference solar cells that are characterized in this work.

The spatial spectral responsivity $s(\lambda_{\text{mono}}, x, y)$ of a silicon solar cell ($156 \times 156 \text{ mm}^2$) is measured by using a light beam induced current mapping method, scanning across the surface of the detector using monochromatic light. A square shaped beam size with a cross-section of $5 \times 5 \text{ mm}^2$ allows mappings of $s(x, y)$. This measurement is performed for wavelengths ranging from 350 nm – 1150 nm in steps of 50 nm. Figure 4.14 (left-hand side) shows the measured non-uniformity of the spectral responsivity of a c-Si solar cell ($156 \times 156 \text{ mm}^2$) scanned with a monochromatic beam at a wavelength of $\lambda_{\text{mono}} = 800 \text{ nm}$.

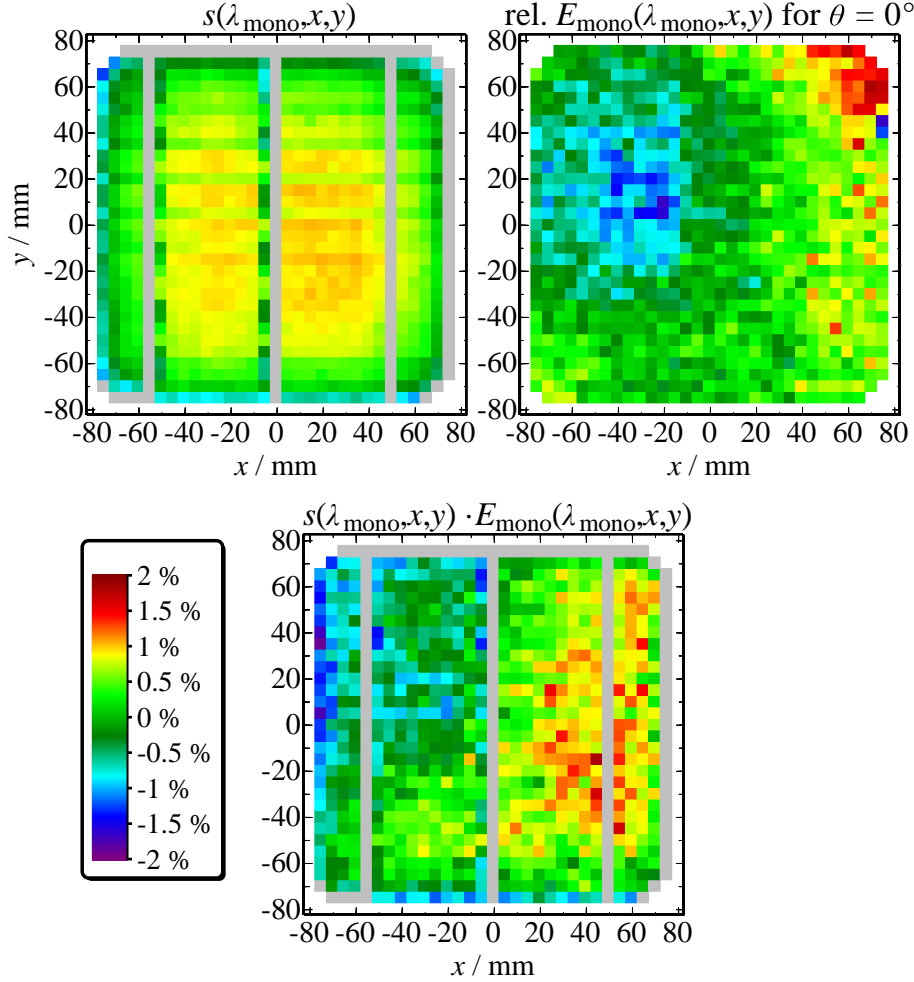


Figure 4.14: Measured non-uniformity of a c-Si solar cell ($156 \times 156 \text{ mm}^2$) with a laser-spot size of $5 \times 5 \text{ mm}^2$ and a step width of 5 mm (left-hand side); irradiance map of the monochromatic light field of the laser-DSR facility in a distance of $z_0 = 2500 \text{ mm}$ performed with a detector area of $5 \times 5 \text{ mm}^2$ and a step width of 5 mm (right-hand side) and superposition of both datasets at 800 nm (bottom). This figure is published in (Plag, et al., 2017b).

Figure 4.14 (right-hand side) shows the measured irradiance non-uniformity $E_{\text{mono}}(\lambda_{\text{mono}}, x, y, z_0)$ of the monochromatic light field at 800 nm in the measurement plane in a distance $z_0 = 2500 \text{ mm}$ from the light source. The irradiance map is measured by using a step width of 5 mm with a photodiode providing an active area of $5 \times 5 \text{ mm}^2$ limited by a precision aperture. The superposition of both in one map is shown in Figure 4.14 (bottom).

The non-uniformity of the irradiance within the volume of the device that is enveloped by the device's surface during the rotation, $E_{\text{mono}}(\lambda_{\text{mono}}, x, y, z)$ is calculated from the measured $E_{\text{mono}}(\lambda_{\text{mono}}, x, y, z_0)$ at a distance z_0 normal incidence using the $E \sim 1/z^2$ law. The irradiances $E_{\text{mono}}(\lambda_{\text{mono}}, x', y')$ for varying AOI corresponding to the surface of the tilted device located at new coordinates x' and y' in a new distance z are obtained by applying an interpolation procedure at the designated intersection points illustrated in Figure 4.15.

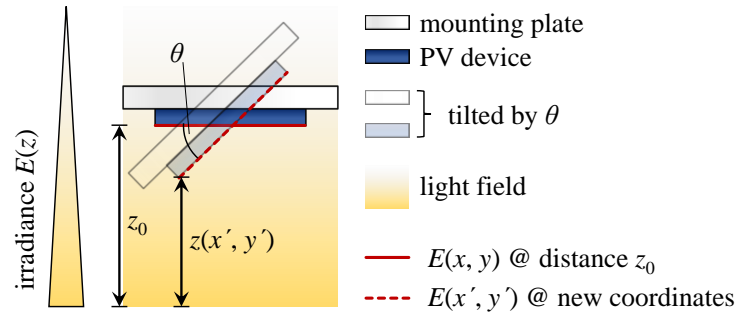


Figure 4.15: Schematic of the irradiance non-uniformity dependence at different AOI onto the PV device under test. By scanning the designated test area at a distance z_0 a lateral irradiance distribution is determined for $\theta = 0^\circ$. For larger AOI's, the irradiance on the inclined surface at a differing distance $z(x', y')$ is determined at new coordinates by using the inverse-square law and an interpolation procedure.

As an example, the dependence of the irradiance non-uniformity $E_{\text{mono}}(\lambda_{\text{mono}}, x', y')$ during a tilt of a large area device for a light field at $\lambda_{\text{mono}} = 800 \text{ nm}$ and $z_0 = 2500 \text{ mm}$ is shown in Figure 4.16. In this case the irradiance non-uniformity in the designated test plane calculated analog to a procedure defined in (IEC 60904-9 Edition 2, 2007) increases from 1.74 % at $\theta = 0^\circ$ to 7.07 % at $\theta = 80^\circ$ for a $156 \times 156 \text{ mm}^2$ sized field. In the case of a $20 \times 20 \text{ mm}^2$ sized monochromatic field the non-uniformity increases from 0.25 % at $\theta = 0^\circ$ to 0.9 % at $\theta = 80^\circ$.

These maps are determined for the wavelengths ranging from 350 nm - 1150 nm in steps of 50 nm and in addition for the broadband light field of a tungsten halogen lamp. Based on these datasets of $s(\lambda_{\text{mono}}, x, y)$ and $E_{\text{mono}}(\lambda_{\text{mono}}, x', y')$, $u(f_{\text{anu}}(\theta, \lambda_{\text{mono}}))$ is determined for a large area solar cell ($156 \times 156 \text{ mm}^2$) and different wavelengths. The result is shown in Figure 4.17 as colored curves in the graph shown on the top. It is observed, that this uncertainty strongly depends on the wavelengths which is a direct consequence of the wavelength-dependent non-uniformity of the device and the irradiance distribution. The black dotted line is then estimated as the worst-case assumption for a device of $156 \times 156 \text{ mm}^2$. The same analysis is performed for WPVS reference solar cells with an area of $20 \times 20 \text{ mm}^2$ and for both types of devices for the irradiance distribution of the broadband light source.

Analog, the worst-case uncertainties are shown in Figure 4.17 (bottom). The uncertainties for the broadband light source are conservatively estimated to be larger, because the non-uniformity of the irradiance distribution is higher within the volume enveloped by the device's surface during the rotation.

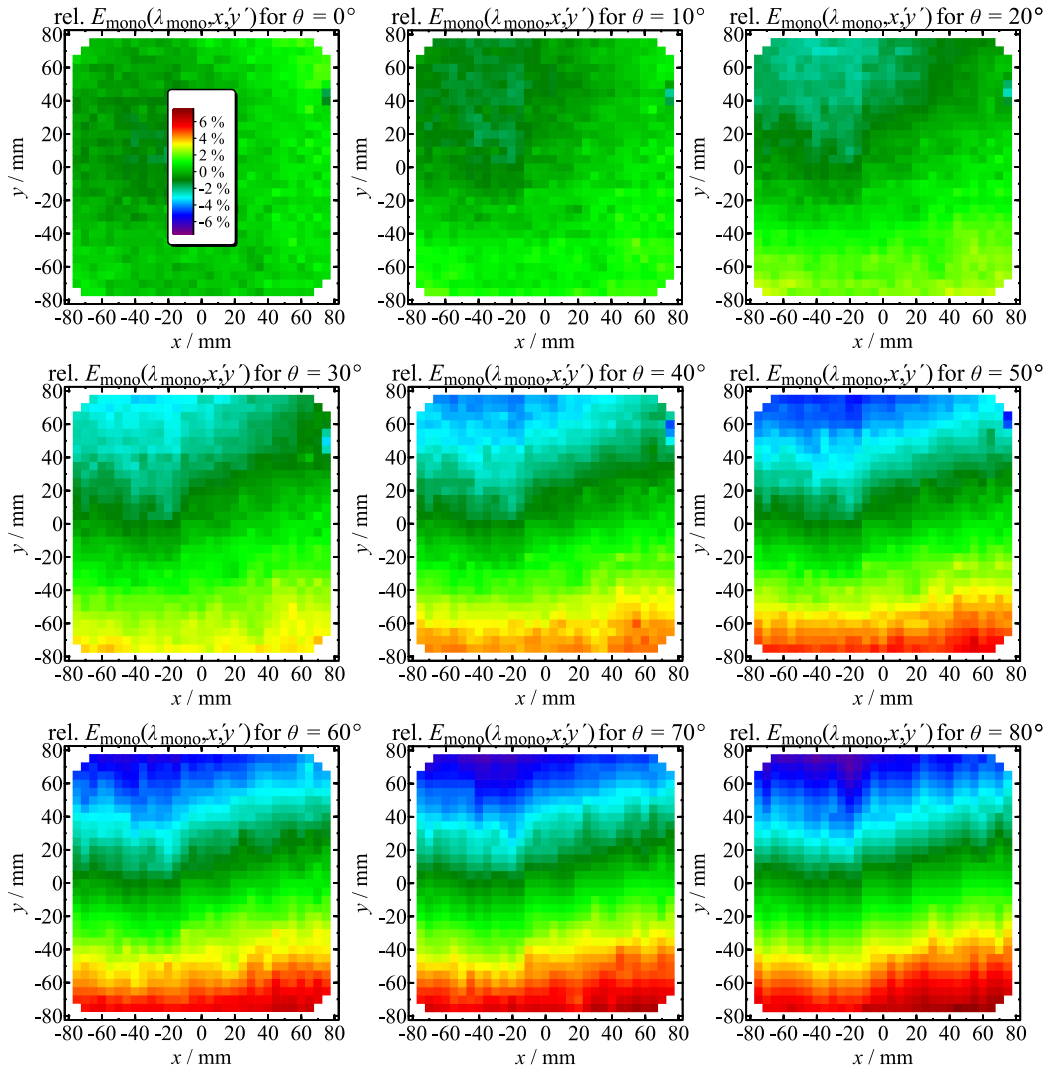


Figure 4.16: Irradiance maps with lateral cuts through the volume of the monochromatic light field ($\lambda = 800 \text{ nm}$) at different angles of incidence. Reason for the non-uniformity: The part of the rotated solar cell that has the largest distance from the monochromatic light source obtains a lower irradiance. This non-uniformity is received by the solar cell under test (here for a size of $156 \times 156 \text{ mm}^2$) and leads to systematic deviations. The dataset shown in this figure is published in (Plag, et al., 2017b).

Such a thorough analysis is not feasible for each single measurement within a reasonable time and effort. Therefore, the worst-case assumptions for the uncertainty of f_{anu} shown in Figure 4.17 are taken as generally assumed uncertainties for the given combination of device size and light source. Accordingly,

$$f_{\text{anu}}(\theta, \lambda_{\text{mono}}) \approx 1 \pm u(f_{\text{anu}}(\theta, \lambda_{\text{mono}})). \quad (4.14)$$

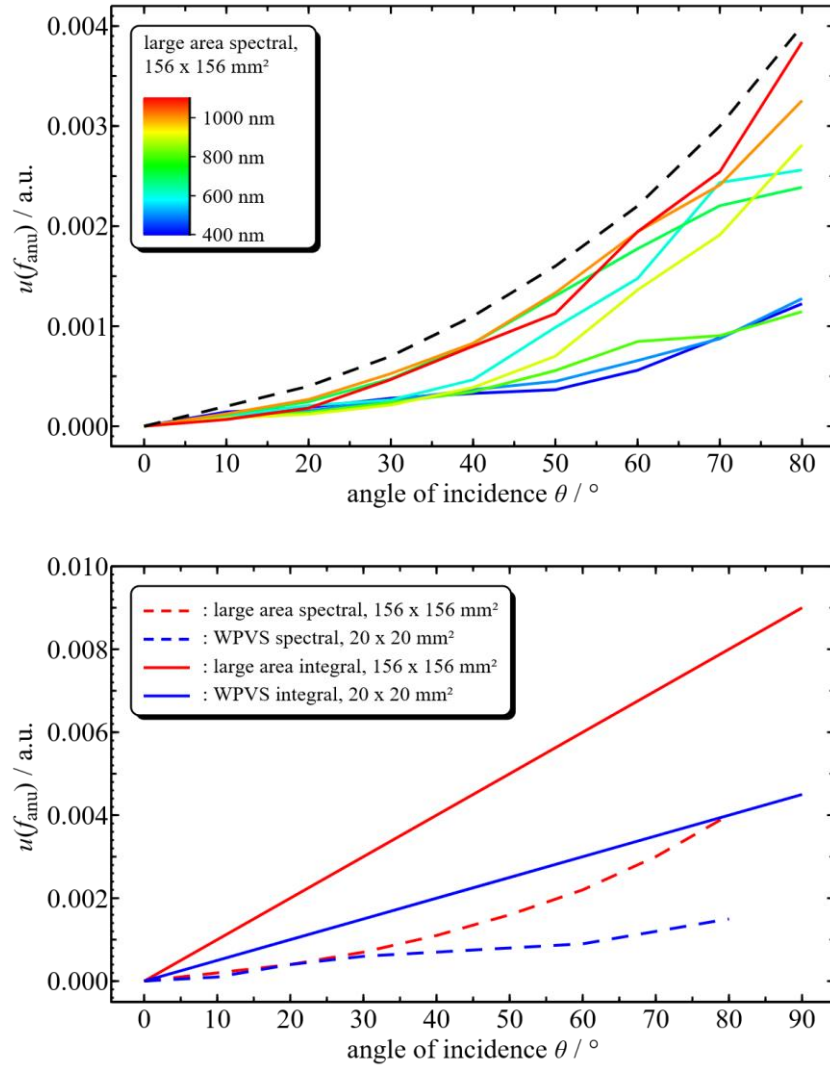


Figure 4.17: (top) Uncertainty of the angular-dependent non-uniformity of monochromatic irradiance on the measurement of the short-circuit current of $156 \times 156 \text{ mm}^2$ sized PV devices. The black dotted line shows the worst-case assumption of all measurements that is taken as an assumed uncertainty for the individual devices. (bottom) The blue curves represent the uncertainties for $20 \times 20 \text{ mm}^2$ sized devices while the red curves stand for $156 \times 156 \text{ mm}^2$ sized devices. The continuous lines represent the uncertainties for the broadband (integral) measurement and the dashed lines for the monochromator-based (spectral) measurement, respectively. This figure is published in (Plag, et al., 2017b).

4.2.4. Positioning of the PV device

The lateral positioning of the sample relative to the φ -rotation axis and optical axis (x - and y -direction) is carried out individually for each device using an accurate laser-alignment procedure. Accordingly, the exact position of the device center relative to the rotation axes is estimated to have an accuracy better than $\pm 0.1 \text{ mm}$. This is assumed for both, the monochromator-based and broadband-based setups because the same goniometer and alignment procedure is used. Hence, positioning uncertainties in x - and y -direction are negligibly small.

4.2.5. Thickness of the solar cell

The thickness d_{real} , i.e. the exact location of the active surface of the PV device in z -direction relative to the motor tilt axis is a more critical parameter compared to the positioning uncertainty in x - and y -direction. For encapsulated devices, the location of the active area relative to the backside of the housing is usually unknown (Witt, et al., 2013). This distance is defined as the thickness with an estimated uncertainty of ± 0.5 mm. The exact location of the θ -axis relative to the mounting plate of the solar cells has an uncertainty of $d \pm 0.5$ mm. Hence, the conservatively estimated uncertainty of the real relative position of the active device surface to the tilt axis has a maximum value of $u(d_{\text{real}}) \pm 1$ mm. Figure 4.18 illustrates the effect of an inaccurate thickness d on the angular-dependent measurements. In case of smaller thickness values (b) the device is tilted towards the light source resulting in an overestimation of the measured signal at increasing AOI. In case of larger thickness values (c) the solar cell is tilted away from the light source resulting in an underestimation of the measured signal.

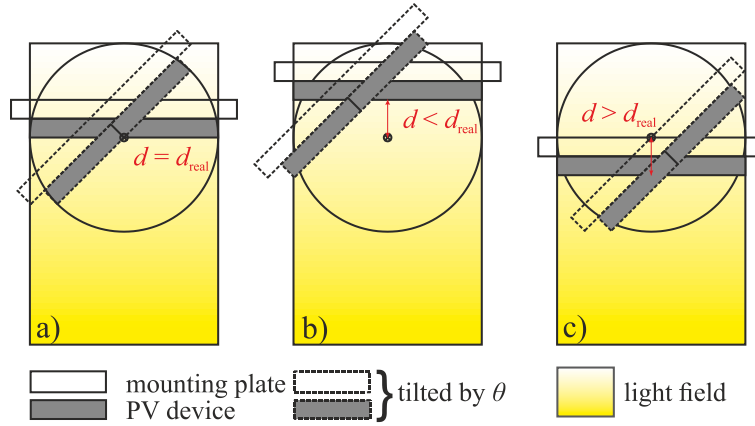


Figure 4.18: Impact of thickness on the angular dependent measurement. a) shows the exact consideration of the device thickness d_{real} relative to the position of the tilt axis θ . b) and c) show the over- and underestimation effects under consideration of an inaccurate thickness. This figure is published in (Plag, et al., 2017b).

A sensitivity analysis is performed to quantify the impact of this effect for $20 \times 20 \text{ mm}^2$ and $156 \times 156 \text{ mm}^2$ sized PV devices. Angular-dependent measurements are performed with different values for the thickness. Therefore, angular-dependent measurements with both device sizes are performed with thicknesses d ranging from -4 mm to $+4$ mm with an increment of 1 mm. The results on this sensitivity analysis are shown in Figure 4.19 for a WPVS reference solar cell and in Figure 4.20 for an industrial large area c-Si solar cell.

The sensitivity of the angular-dependent responsivity $c_d(\theta)$ per mm offset is then determined for each device size to obtain a combined uncertainty for the thickness correction factor f_d :

$$f_d(\theta) = 1 \pm u_d(\theta) = 1 \pm c_d(\theta) \cdot u(d_{\text{real}}) \quad (4.15)$$

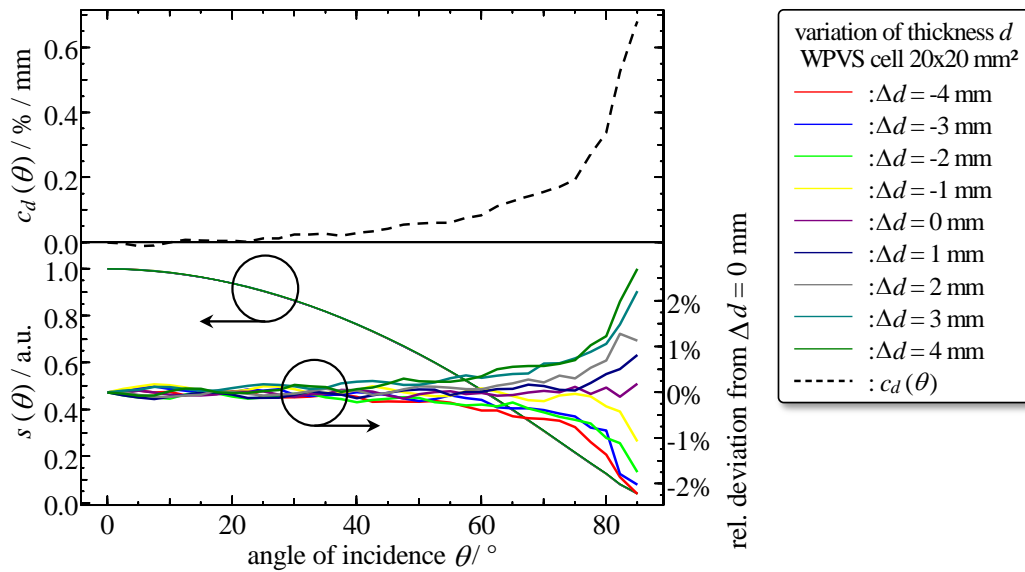


Figure 4.19: Determination of the sensitivity coefficient c_d of the thickness d for a WPVS solar cell with $20 \times 20 \text{ mm}^2$ size measured at AOI's ranging from 0° to 85° .

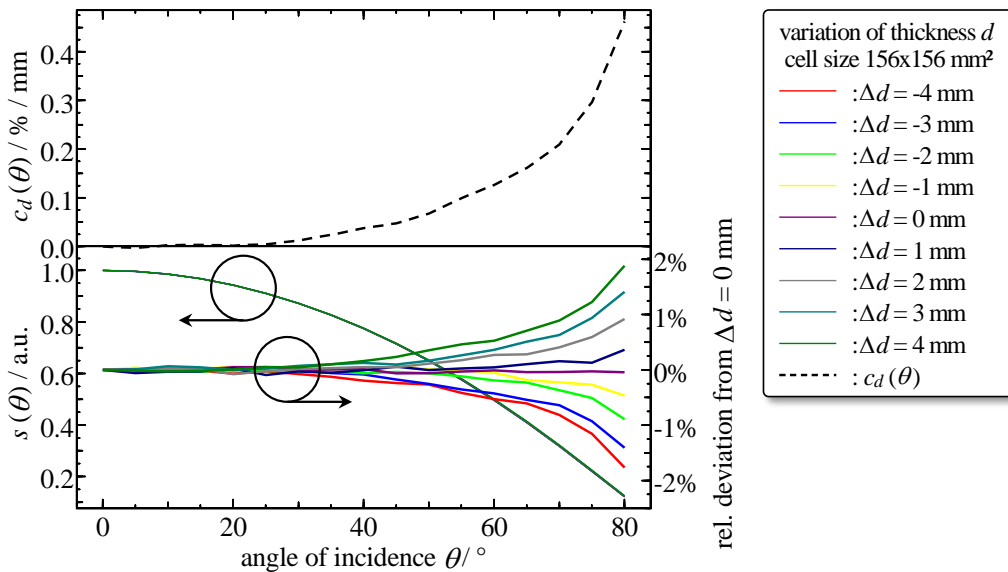


Figure 4.20: Determination of the sensitivity coefficient c_d of the thickness d for an industrial c-Si solar cell with $156 \times 156 \text{ mm}^2$ size measured at AOI's ranging from 0° to 80° .

4.2.6. Polarization

The monochromatic irradiance of the laser-DSR facility is polarized and the polarization changes with wavelength. To consider polarization effects on the angular-dependent spectral responsivity measurements, two broadband (250 nm - 4000 nm) polarization filters are positioned in a filter wheel within the optical path between the monochromator and the device under test. Hence, two polarization states are realized on the designated test area by placing either the 0° polarizer or the 90° polarizer into the beam. A full angular-dependent measurement cycle is then performed with 0° and with 90° polarization subsequently and

each cycle is evaluated independently. Normalized angular-dependent responsivities of the 0° and 90° polarized measurements are then averaged to obtain the responsivity for unpolarized light (see Equation (4.3)).

Uncertainties related to the polarization originate from the extinction ratio of the polarizer, the purity of the polarization state, and the alignment uncertainty of the perpendicular orientation of the two polarizers which would lead to unequal averaging. The relative orientation of the mounted polarizers is evaluated by using a third polarizer which is mounted in front of a photodiode in the measurement plane and then rotated by φ_{pol} around the optical axis. The relative orientation of the two polarizers is adjusted so that the shift between the polarization measurements curves equals to 90° . The uncertainty of the orientation is estimated to be $u_{\varphi, \text{pol}} \leq 1^\circ$. If the 90° polarizer is rotated by the maximum $u_{\varphi, \text{pol}} = 1^\circ$, overestimation and underestimation of the respective signals for polarization states 0° and 90° are slightly affecting the averaged angular-dependent responsivity for unpolarized light. The extinction ratio of the polarizers used in this work is in the range of larger than 1000:1. Hence, the related contribution the polarization uncertainty is $< 0.1\%$.

However, the uncertainty of the polarization is proportional to the individual polarization dependence of the PV device under test. If the device's angular-dependent responsivity is independent from polarization related effects the polarization uncertainty reduces to zero. If the device's angular-dependent responsivity shows strong polarization related effects the polarization uncertainty increases proportionally.

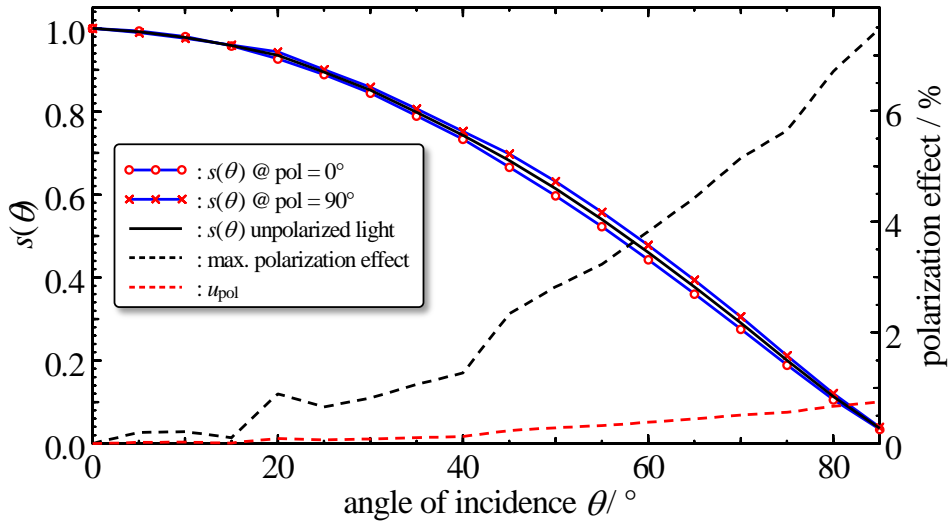


Figure 4.21: Angular-dependent responsivity of a reference solar cell at $\lambda_{\text{mono}} = 400 \text{ nm}$ for the two different polarization states 0° and 90° and the average of both. The black dashed line shows the deviation of as a percentage value. A conservative estimation of 10 % of this deviation is taken as uncertainty (rectangular) $u_{\text{pol}}(\theta, \lambda_{\text{mono}})$ for the polarization correction factor f_{pol} (red dashed line). This figure is published in (Plag, et al., 2017b).

Figure 4.21 shows an estimation of the determination of the polarization uncertainty that affects the output quantity. For a complete measurement sequence of the angular-dependent responsivity, the maximum deviation of the two polarization state measurements is taken.

This is illustrated as dashed lines in Figure 4.21. A conservative estimation of 10 % of this maximum deviation is taken as uncertainty $u_{\text{pol}}(\theta, \lambda_{\text{mono}})$ (rectangular) for the polarization correction factor f_{pol} :

$$f_{\text{pol}} = 1 \pm u_{\text{pol}}(\theta, \lambda_{\text{mono}}). \quad (4.16)$$

4.2.7. Uncertainty of the tilt angle θ due to an extended light source

In the experimental setup, the light source for the angular-dependent measurements are considered as an extended radiant area with an aperture diameter A . In this analysis, the aperture area is approximated to represent an equally distributed ensemble of point sources that irradiates the solar cell with a diagonal dimension L (see Figure 4.22).

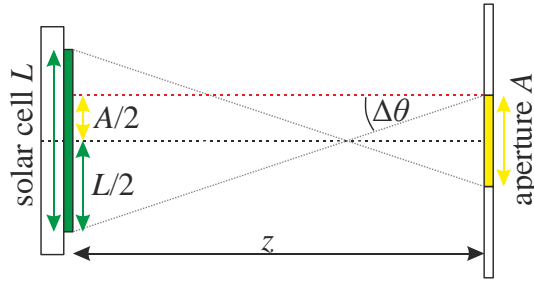


Figure 4.22: Influence of an extended light source on the uncertainty of the AOI θ . In this figure the AOI $\theta = 0^\circ$ (angle between surface normal of the solar cell and the black dashed line). A variety of AOI's are irradiating the sample at an adjusted tilt angle θ with a maximum deviation of $\Delta\theta$. This figure is published in (Plag, et al., 2017b).

Under the assumption of a Lambertian source surface, a rectangular distribution of deviating AOI's can be found within an interval of $-\Delta\theta$ and $+\Delta\theta$. By applying a simple trigonometric law (see also Figure 4.22), the maximum deviation is found to be dependent of θ and the distance z :

$$\Delta\theta = \arctan\left(\frac{\frac{A}{2} \cos(\theta) + \frac{L}{2}}{z}\right). \quad (4.17)$$

Additionally, a systematic offset θ_0 is present if the measurement plane is not exactly aligned perpendicular to the z -axis (i.e. the optical axis). Figure 4.23 illustrates the impact of a misalignment and its corresponding offset θ_0 for an ideal detector following the cosine of the AOI. An offset θ_0 of only 1° results in 10 % difference in the measured angular-dependent responsivity at $\theta = 80^\circ$ and an offset of 0.1° results in 1 % difference.

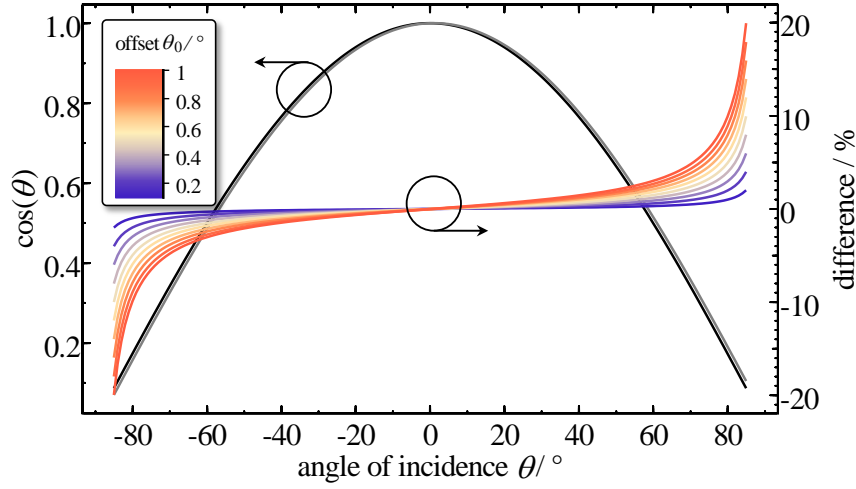


Figure 4.23: Impact of an offset θ_0 due to a misalignment between optical axis of the facility and the surface normal of the PV device. The black curve shows the cosine of θ and the grey curve is phase shifted by $\theta = 1^\circ$. The relative difference between both cosines originating from an offset θ_0 is shown on a colored scale as a set of curves on the right axis.

This offset θ_0 is experimentally determined to be $< 0.1^\circ$ for the setup used in this work. The angular-dependent responsivity $s(\theta)$ is an asymmetric function within a given interval $[-\Delta\theta + \theta_0, +\Delta\theta + \theta_0] = \{\theta \mid -\Delta\theta + \theta_0 \leq \theta_i \leq +\Delta\theta + \theta_0\}$. The average angular-dependent responsivity $s([-\Delta\theta + \theta_0, +\Delta\theta + \theta_0])$, would lead to a systematic deviation $\Delta s(\theta_i)$ from $s(\theta_i)$ at each AOI θ_i :

$$\Delta s(\theta_i) = s([-\Delta\theta + \theta_0, +\Delta\theta + \theta_0]) - s(\theta_i) \quad (4.18)$$

The impact of this systematic deviation for an aperture of 10 mm is shown in Figure 4.24. The error bars in the horizontal direction indicate the rectangular θ -interval $[-\Delta\theta + \theta_0, +\Delta\theta + \theta_0]$. For the angular-dependent responsivity within this interval $s([-\Delta\theta + \theta_0, +\Delta\theta + \theta_0])$ it is assumed that an averaged constant slope between incremental angular steps is apparent. The systematic deviation $\Delta s(\theta_i)$ is then the difference of this average spectral responsivity and the spectral responsivity at the given angle θ_i . This systematic deviation $\Delta s(\theta_i)$ is taken as the uncertainty for the AOI $u_\theta(\theta)$ (rectangular distributed):

$$f_\theta = 1 \pm \left(\frac{\Delta s(\theta)}{s(\theta)} - 1 \right) = 1 \pm u_\theta(\theta) \quad (4.19)$$

These uncertainty contributions are individually calculated for each device visualized as dashed blue curves. Note that the uncertainty is considered to be higher for smaller devices, because the effect of the systematic offset out weights the effect of the angular distribution.

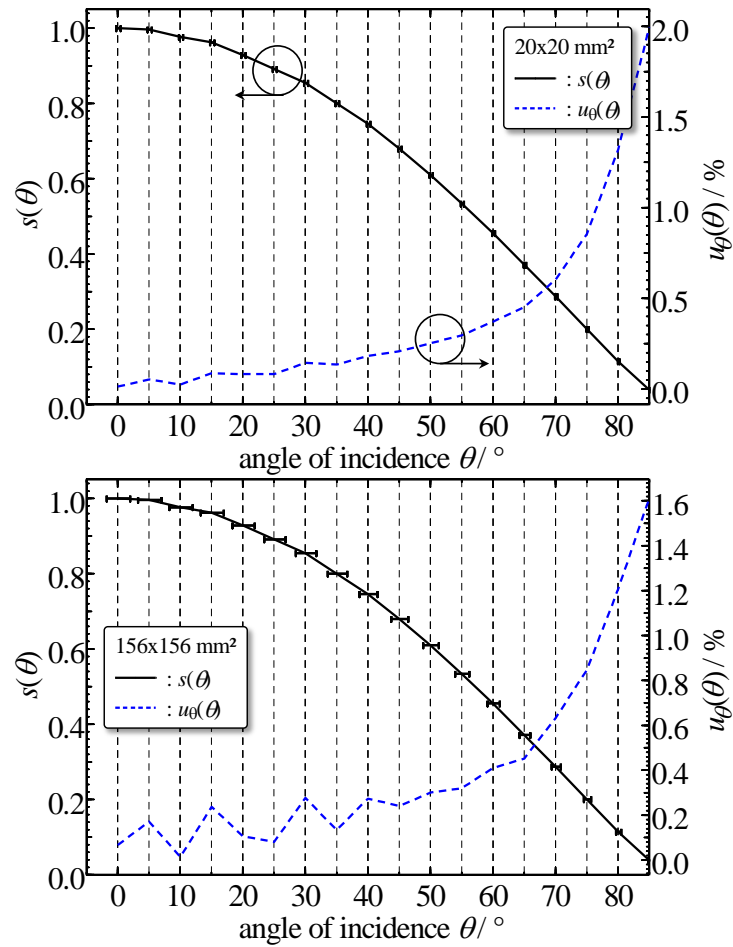


Figure 4.24: Impact of the θ -distribution ($\Delta\theta$) due to an extended light source and a systematic θ_0 offset on the measured angular-dependent responsivity $s(\theta)$. On the top, the impact is shown for a $20 \times 20 \text{ mm}^2$ sized solar cell, and on the bottom, it is shown for a $156 \times 156 \text{ mm}^2$ sized solar cell. This figure is published in (Plag, et al., 2017b).

4.2.8. Irradiance non-linearity of the PV device

The irradiance non-linearity of the PV device leads to systematic deviations with a changing AOI and hence a changing irradiance. These can either be corrected, when the non-linearity of the individual device is known or otherwise an uncertainty has to be assigned. In the case of the monochromatic AOI-facility, the angular-dependent spectral responsivity is measured with constant bias irradiance E . This is realized using bias lamps mounted on the rotation stage (see Figure 4.3). Hence, the non-linearity of the PV device due to the changing monochromatic irradiance is neglected because the dominating bias irradiance remains constant, independent of the AOI.

The situation changes for the broadband AOI-facility, used for the validation of this work (see Figure 4.11). In this case the irradiance changes upon rotation by one order of magnitude. In the present case of a 1000 W tungsten halogen lamp, set at a distance of 2500 mm to the PV device, the irradiance is lower than 10 Wm^{-2} when no additional bias lamps are used (see Figure 4.4). For AOI's larger than 80° , irradiance decreases to values below

1 Wm^{-2} . Because the uncertainty due to the irradiance non-linearity is device dependent, it should be investigated and corrected individually for each device and each AOI θ . However, for the broadband AOI setup, the uncertainty due to non-linearities $u_E(\theta)$ is assumed to be a function of θ and of the maximum influence of the individual irradiance non-linearity. The maximum influence is previously determined with the DSR method.

$$f_E = 1 \pm u_E(\theta) = 1 \pm (1 - \cos \theta) \cdot u(E) \quad (4.20)$$

4.2.9. Uncertainties due to the device temperature

The spectral responsivity of the solar cell is temperature-dependent. It is assumed that the temperature coefficient is not influenced by the angular-dependent excitation. Hence, only temperature fluctuations during the measurement remain as a source for uncertainties. The Peltierelement-based temperature control keeps the device temperature constant at 25°C with insignificant fluctuations around $\pm 0.05 \text{ K}$. In case of the monochromatic setup, steady state bias lamps are used, which are kept in fixed position related to the PV device during rotation (see Figure 4.3). The bias irradiance represents the dominant heat load. Therefore, the heat load on the solar cell doesn't change during rotation. Accordingly, the uncertainties introduced by temperature effects are assumed to be negligible for the angular-dependent spectral responsivity measurements.

In case of a broadband setup without additional bias irradiance, the heat load changes up to 15 % across the volume enveloped by the rotated surface of a $156 \times 156 \text{ mm}^2$ solar cell at a distance $z_0 = 2500 \text{ mm}$, if the $1/z^2$ distance law is assumed. The serially connected Peltier elements, used for temperature control of the large area solar cell, provide theoretically uniform cooling for a given uniform heat load. A non-uniform heat load can affect the device temperatures non-uniformity, resulting in differences in the temperature $\Delta T(x, y)$ for varying AOI. However, it can be assumed that at distances $> 2 \text{ m}$ the effect of the positive temperature difference in the surface area with a higher heat load is compensated by the effect of the negative temperature difference in the surface area with lower heat load for tilted devices. Asymmetries in the device temperature non-uniformity $\Delta T(x, y)$ seem to be negligible for larger distances. Consequently, uncertainties due to temperature effects are assumed to be negligible also for the investigated broadband AOI facility.

4.2.10. Wavelength uncertainties

The light source is a laser-based setup generating the desired wavelength by using a tunable Titan:Sapphire laser and different non-linear optics (Winter, et al., 2014). Furthermore, a monochromator reduces the spectral bandwidth. The wavelength uncertainty of this facility is determined to be smaller than 0.3 nm by using a Fourier Transform Spectroradiometer (Kröger, et al., 2014, Winter, et al., 2014). Hence, it is negligible in this study.

4.2.11. Calculation of a combined uncertainty for the angular-dependent measurements

All relevant uncertainty contributions described above are incorporated into the basic mathematical model (Equation (4.3)) resulting in the final equation for the angular-dependent spectral responsivity:

$$s(\theta, \varphi) = \frac{\frac{\overline{Q_{SC}}(\theta, \varphi)}{Q_{SC}(0^\circ, 0^\circ)} \Big|_{\text{pol} \rightarrow 0^\circ} + \frac{\overline{Q_{SC}}(\theta, \varphi)}{Q_{SC}(0^\circ, 0^\circ)} \Big|_{\text{pol} \rightarrow 90^\circ}}{2} \cdot f_{el} \cdot f_{anu} \cdot f_d \cdot f_{pol} \cdot f_\theta. \quad (4.21)$$

In analogy, the equation for the integral angular-dependent responsivity using a broadband light source can be written as:

$$s(\theta, \varphi) = \frac{\overline{Q_{SC}}(\theta, \varphi)}{Q_{SC}(0^\circ, 0^\circ)} \cdot f_{el} \cdot f_{anu} \cdot f_d \cdot f_\theta \cdot f_E. \quad (4.22)$$

The calculation of the uncertainty of the angular-dependent spectral responsivity $u(s(\theta, \varphi))$ is performed using Monte Carlo methods. The calculation is performed for each individual measurement, because the uncertainty contributions are partly dependent on the measurement result itself (i.e. Type A, f_{pol} , f_θ). Furthermore, the most uncertainty contributions are functions of the AOI. Therefore, the uncertainty budget changes dependent on the device, device size, wavelength and AOI. Since the evaluation of a classical tabulated uncertainty budget cannot cover all these dependencies, a selected example is shown in Figure 4.25 to visualize the magnitude of the individual standard uncertainty contributing to the combined standard uncertainty of the angular-dependent spectral responsivity $u(s(\theta, \varphi, \lambda_{mono}))$. In the upper graph, the relative standard uncertainties of the individual uncertainty contributions are shown for an angular-dependent measurement of the spectral responsivity at 450 nm of an encapsulated solar cell. The black curve indicates the combined standard uncertainty. It shows that the uncertainty increases with increasing AOI. This is related to the uncertainty contribution from the non-uniformity and the AOI θ . In the lower graph, the contributions of the individual uncertainty components to the combined standard uncertainty are shown as percentage values. This graph visualizes the dominating uncertainty components for the respective AOI for this specific example.

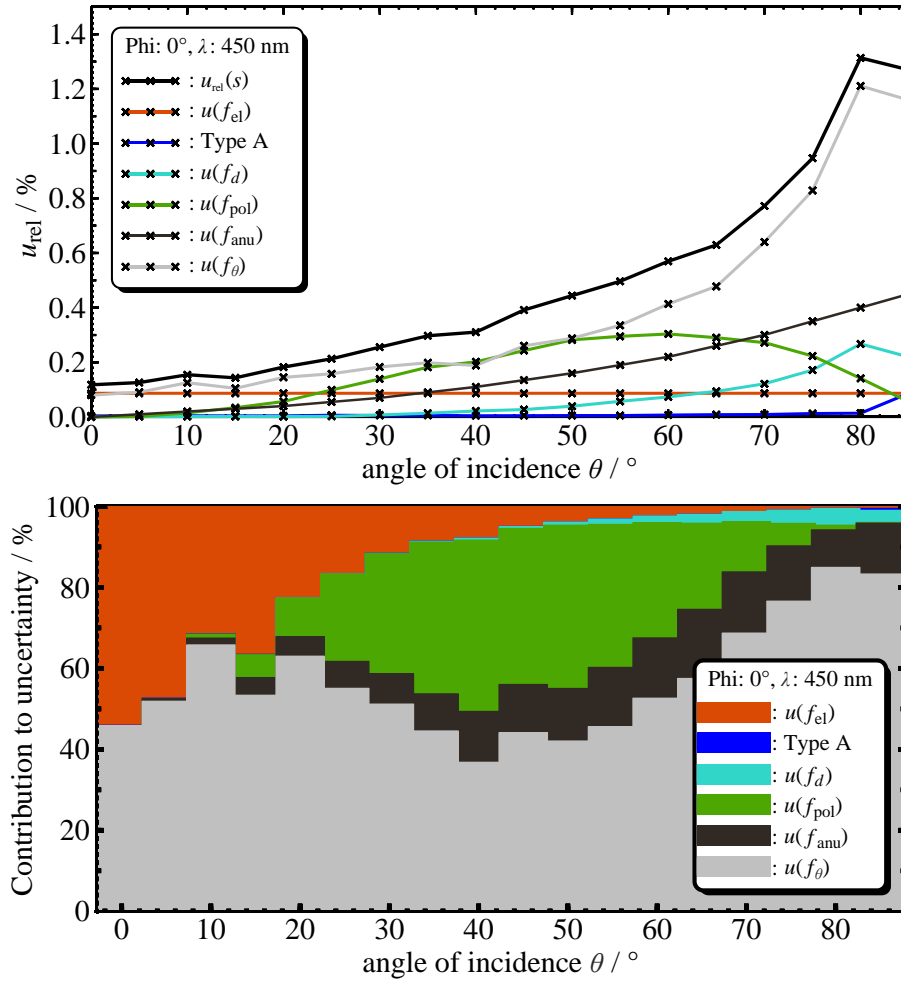


Figure 4.25: (top) Exemplary standard uncertainties of the discussed uncertainty contributions for the measurement of the angular-dependent spectral responsivity of an encapsulated reference solar cell at $\lambda_{\text{mono}} = 450 \text{ nm}$. The black curve shows the resulting combined relative standard uncertainty $u_{rel}(s(\theta, \varphi, \lambda_{\text{mono}}))$. (bottom) Percentage contribution of the individual uncertainty components contributing to the resulting combined standard uncertainty. The exemplary uncertainty budget is published in (Plag, et al., 2017b).

4.2.12. Correlations

It is important to note that correlated uncertainty components contributing to the combined standard uncertainty of the measurand need to be propagated through the entire mathematical model. This is necessary for the determination of the uncertainty of a PV device's angular loss under any AOI. Correlated uncertainties cannot be treated independently, otherwise this may affect the resulting combined standard uncertainty. In this work uncertainty contributions of the solar cells AOI characterization related to the non-linearity of the electrical current measurement (f_{el}), the angular non-uniformity of the volume enveloped by the rotated surface of the device (f_{anu}), the thickness of the solar cell (f_d) and an alignment offset of AOI θ to the optical axis of the facility (θ_o) are treated as correlated quantities. The correlations are considered for the uncertainty calculation based on a Monte Carlo method by using the software Hypradata 6.5, developed by Dr. Stefan Winter (Scientific Software Development, 2016).

4.3. Summary

The laser-DSR facility at Germanys National Metrology Institute PTB for the primary calibration of reference solar cells has been improved. It covers now the determination of the polarization- and angular-dependent spectral responsivity of solar cells and mini-modules with active areas of up to 156 x 156 mm². Results of the angular-dependent spectral responsivity are shown for a diversity of different PV devices. Dependent on the device, strong differences in the responsivities particularly in the UV and IR wavelength regions for varying AOI and polarization are observed. The measurement results obtained with the setup for primary calibration of reference solar cells are validated by a comparison against a broadband facility, providing a fixed lamp spectrum. The impact of an angular-dependent spectral mismatch problem is outlined: Measurements of the angular-dependent spectral responsivity performed with a broadband light source do not reveal differences in the spectral responsivity that are apparent for all investigated samples. The investigation shows also significant differences of PV devices' azimuthal symmetry for some of the investigated samples.

A comprehensive characterization of the experimental setup is presented. It includes a thorough evaluation of the measurement uncertainty. Not solely the setup contributes to the uncertainty; it is additionally dependent on the investigated samples' properties. For an exemplary case, the dominant contributions to the combined uncertainty $u(s(\theta, \varphi, \lambda_{\text{mono}}))$ are the uncertainty of the tilt angle, the uncertainty of the polarization and the uncertainty of the non-uniformity. The investigated sources of uncertainty are discussed in detail to provide a best practice guide that encourages other international laboratories to establish their own uncertainty evaluations for their individual facilities.

The most important finding of this investigation is that for calibrations of PV devices under diffuse light a mismatch needs to be considered between the device under test and the reference device when they provide different angular-dependent spectral responsivities. These scenarios are studied in the following chapter that is dedicated to computational studies on the impact of diffuse light on PV performance measurements.

The technique developed and presented in this work covering measurements under monochromatic and also under broadband irradiation is now available as new metrological service for PTB's customers (PTB Working Group 4.52 - Website, 2018). Meanwhile, an international intercomparison (round robin) of AOI dependent measurements on solar cells has been completed. Eight participating European PV laboratories (Riedel, et al., 2018) are involved in this activity.

5. Impact: From Standard Test Conditions to the real world

This chapter is focused on the investigation on mismatch effects and angular losses under global irradiation conditions, which occur because of the previously characterized device properties. In a first section, the impact of the spectral-angular mismatch between several PV devices on short-circuit current calibration scenarios under global sunlight is presented by means of a computational study. This study was previously published in parts in (Plag, et al., 2018a). In a second section different isotropic approaches for the determination of angular losses under global sunlight are compared. The first approach is a simplified version of the well-established Martin and Ruiz (MR) model proposed in a recently released energy rating standard for the computation of angular losses. The second approach for the determination of angular losses comes from the field of photometry. The two approaches are then compared against each other and against the new model proposed in this work. To highlight the significance of simplifications, such as the assumption of an isotropic sky radiance, the impact of anisotropic sky radiance conditions on the angular losses is investigated systematically and by using the new model that overcomes these shortcomings. Parts of the results included in the second section are published in a conference proceeding (Plag, et al., 2017a). A thorough discussion on uncertainties for both simplified models is presented to compare their accuracy. In a third section, the effect of diurnal variations in the irradiation conditions on fixed installed PV devices is shown with emphasis on spectral and angular losses on the possible energy yield. Each section concludes with a separate summary.

5.1. Spectral-angular mismatch for PV device calibration under global natural sunlight

To demonstrate the impact of spectral-angular mismatch, a computational study is performed in which a secondary outdoor calibration using the global sunlight method (GSM) at clear-sky conditions is simulated. This study covers the investigation of two different device combinations (calibration of a non-encapsulated device against an encapsulated device and calibration of an IR-filtered device against an encapsulated device) under four different global irradiance situations. The encapsulated reference solar cell is used as the irradiance reference device for all investigated conditions in this section. The results of the first two conditions in this study are published in the article (Plag, et al., 2018a). Parts of the study (Plag, et al., 2018a) are presented and supplemented in the text of this section and where a citation at tables and figures refers to this article.

For these situations, the spectral radiances $L_{\lambda,\text{sky}}(\lambda, \theta, \varphi)$ and $L_{\lambda,\text{ground}}(\lambda, \theta, \varphi)$ and the direct normal spectral irradiance $E_{\lambda,\text{DNI}}(\lambda)$ are simulated by libRadtran (as described in Chapter 3). LibRadtran provides the required directional information at a desirable angular resolution on each irradiation condition, respectively. With that, the datasets are used as input quantities to perform calculations in accordance with Equation (3.12). In combination with

the datasets for $s(\lambda, \theta, \varphi)$ of the reference and the DUT solar cells obtained by the measurements, which are shown in Chapter 4, the spectral-angular mismatch correction factors f_{SAMM} are calculated for each specific condition.

This section includes a variation of different parameters for the investigation on the change of the spectral-angular mismatch under different solar cell calibration situations at clear sky conditions:

- 1) A global natural sunlight condition which is close to that defined in (IEC 60904-3 Edition 2, 2008) and under consideration of an anisotropic diffuse spectral radiance field and the fact that this definition implies a device tilt of $\theta' = 37^\circ$ without normal incidence of the direct sunlight.
- 2) The same condition than in 1), but with a device tilt of $\theta' = \theta_{SZA} = 48.2^\circ$ with normal incidence of the direct sunlight. This condition represents an actual calibration using the GSM method, but it differs from the condition 1 that is defined in the IEC standard.
- 3) A global natural sunlight condition with AM2 and a larger device tilt of $\theta' = 60^\circ$ with normal incidence of the direct sunlight and with same spectral albedo of the ground than in 1) and 2) (light soil).
- 4) An AM2G condition with normal incidence of the direct sunlight but with different spectral albedo of the ground than in 1), 2) and 3). Green grass is used instead of light soil to investigate the influence of different spectral ground reflectance.

The conditions 3) and 4) are also in accordance with the standard (IEC 60904-4, 2009), wherein the procedures require a series of measurements between AM1.5 and AM3. The results of the proposed approach are presented in Tables 5.1 to 5.4 in the next subsections as a percentage contribution of spectral-angular mismatch. To follow the idea on how the results are presented in detail, a stepwise description is given by following bullet points:

- First, each irradiation condition is briefly described including the orientation of the devices, the solar position and the spectral albedo used as individual parameter.
- The second column of each table (labeled as global contribution) includes the computed mismatches between two devices under global irradiance with respect to reference conditions (written in bold letters).
 - For an ideal case, that the proposed reference conditions include only direct normal spectral irradiance, the spectral-angular mismatch f_{SAMM} as a percentage value is calculated relative to the ideal case, where the factor equals to 1.
 - The spectral mismatch f_{SMM} , which is a state-of-the-art approach that neglects directional dependencies, is calculated in accordance with Equation (3.4) and then given as a percentage value.

- To illustrate the pure influence of the angular mismatch f_{AMM} on the DUT current measured under this specific condition, the mismatch for angular effects only. f_{AMM} is then obtained by inserting f_{SAMM} and f_{SMM} in Equation (3.13).
- To study the mismatch effects in depth, the total short-circuit current generated from (Equation (3.10)) is subdivided into individual terms originating from the irradiation contributions (direct, sky and ground) and their assigned coefficients i , j and k (see Equation (5.1)). This allows the impact of diffuse irradiation on the mismatch to be investigated. This impact is particularly significant for tilted and bifacial PV devices. To compare the individual contributions of the spectral-angular mismatch in relation to the global mismatch, a weighting procedure is applied. The weighting factor w^{ijk} is determined by calculating the individual fraction of the short-circuit current of the device under test relative to the total current generated by the global irradiation accumulated by the device (see Equation (5.1)).
 - The spectral-angular mismatch corresponding to the direct irradiance is calculated using Equation (5.2), and by setting the radiance coefficients j and k to zero. Finally, the result is multiplied by w^{100} to determine f_{SAMM}^{100} to account for the actual current fraction generated by the direct irradiance.
 - The spectral-angular mismatch corresponding to the diffuse radiance accumulated by the DUT is calculated using Equation (5.2), and by setting the direct irradiance coefficient i to zero. Finally, the result is multiplied by w^{011} to determine f_{SAMM}^{011} to account for the actual current fraction generated by the diffuse irradiance.
 - The spectral-angular mismatch corresponding to the sky radiance is calculated using Equation (5.2), and by setting the direct irradiance coefficient i and the ground-reflected radiance coefficient k to zero. The result is then multiplied by w^{010} to determine f_{SAMM}^{010} to account for the actual current fraction generated by the sky radiance.
 - The spectral-angular mismatch corresponding to the ground-reflected radiance f_{SAMM}^{001} is obtained similarly to the previous steps using w^{001} .
- The weighted spectral mismatch f_{SMM}^{ijk} is calculated similarly to the weighted spectral-angular mismatch. Instead of spectral radiances L_λ spectral irradiances E_λ are used by computing Equation (3.1), wavelength by wavelength, for each specific condition.

$$w^{ijk} = \frac{i \cdot \int_\lambda E_{\lambda,DNI}(\lambda) \cdot s_{DUT,tilt}(\lambda, \theta_{SZA}, \varphi_{SAA}) d\lambda + j \cdot \iiint_{\lambda\varphi\theta} L_{\lambda,sky}(\lambda, \theta, \varphi) \cdot s_{DUT,tilt}(\lambda, \theta, \varphi) \sin \theta d\theta d\varphi d\lambda}{1 \cdot \int_\lambda E_{\lambda,DNI}(\lambda) \cdot s_{DUT,tilt}(\lambda, \theta_{SZA}, \varphi_{SAA}) d\lambda + 1 \cdot \iiint_{\lambda\varphi\theta} L_{\lambda,sky}(\lambda, \theta, \varphi) \cdot s_{DUT,tilt}(\lambda, \theta, \varphi) \sin \theta d\theta d\varphi d\lambda + k \cdot \iiint_{\lambda\varphi\theta} L_{\lambda,ground}(\lambda, \theta, \varphi) \cdot s_{DUT,tilt}(\lambda, \theta, \varphi) \sin \theta d\theta d\varphi d\lambda + 1 \cdot \iiint_{\lambda\varphi\theta} L_{\lambda,ground}(\lambda, \theta, \varphi) \cdot s_{DUT,tilt}(\lambda, \theta, \varphi) \sin \theta d\theta d\varphi d\lambda} \quad (5.1)$$

whereas $ijk = 100$ represents the direct normal irradiance component, $ijk = 011$ stands for the diffuse radiance and consists of sky and ground component, $ijk = 010$ denotes the sky radiance and $ijk = 001$ indicates the ground-reflected radiance.

The individual spectral-angular mismatch contributions originating from the respective irradiation contribution i , j or k (or combinations of all) is then determined by using the following expression:

$$f_{SMM}^{ijk} = \frac{i \cdot \int_{\lambda} E_{\lambda,DNI}(\lambda) \cdot s_{ref,tilt}(\lambda, \theta_{SZA}, \varphi_{SAA}) d\lambda + j \cdot \iiint_{\lambda\varphi\theta} L_{\lambda,sky}(\lambda, \theta, \varphi) \cdot s_{ref,tilt}(\lambda, \theta, \varphi) \sin \theta d\theta d\varphi d\lambda}{\int_{\lambda} E_{\lambda,ref}(\lambda) \cdot s_{ref}(\lambda, \theta = 0^{\circ}, \varphi = 0^{\circ}) d\lambda} \dots$$

$$+ k \cdot \iiint_{\lambda\varphi\theta} L_{\lambda,ground}(\lambda, \theta, \varphi) \cdot s_{ref,tilt}(\lambda, \theta, \varphi) \sin \theta d\theta d\varphi d\lambda \dots$$

$$(5.2)$$

$$\cdot \frac{\int_{\lambda} E_{\lambda,ref}(\lambda) \cdot s_{DUT}(\lambda, \theta = 0^{\circ}, \varphi = 0^{\circ}) d\lambda}{i \cdot \int_{\lambda} E_{\lambda,DNI}(\lambda) \cdot s_{DUT,tilt}(\lambda, \theta_{SZA}, \varphi_{SAA}) d\lambda + j \cdot \iiint_{\lambda\varphi\theta} L_{\lambda,sky}(\lambda, \theta, \varphi) \cdot s_{DUT,tilt}(\lambda, \theta, \varphi) \sin \theta d\theta d\varphi d\lambda} \dots$$

$$\dots \frac{\dots}{\dots + k \cdot \iiint_{\lambda\varphi\theta} L_{\lambda,ground}(\lambda, \theta, \varphi) \cdot s_{DUT,tilt}(\lambda, \theta, \varphi) \sin \theta d\theta d\varphi d\lambda} \dots$$

A separation into partial short-circuit currents is only valid under the assumption that the PV device current is linear with the incident irradiance. The separation is used here as a tool to investigate the origins of mismatch qualitatively, but not for the correction of the mismatch effects in parts.

5.1.1. Condition 1 (irradiance close to the definition of standard test conditions)

The standard (IEC 60904-3 Edition 2, 2008) defines a south-facing PV device with a 37° tilt angle θ , which is equal to a deviation of $\Delta\theta = 11.2^{\circ}$ from the incidence angle of the direct irradiance (see Figure 5.1). Under this configuration an angular mismatch between two different PV devices is expected, even if only the direct beam of the sunlight would be considered.

The global contributions of the spectral-angular mismatch in the first two example calculations are 0.71 % and 0.34 % (second columns of Table 5.1). In the investigated examples, the DUT's are the non-encapsulated (Table 5.1, top) and the IR-filtered solar cells (Table 5.1, bottom), which are calibrated against the reference device (encapsulated cell) under the Condition 1. The measured short-circuit currents of the DUT's is lower compared to the currents measured under reference condition with defined spectrum and direction due to the spectral-angular mismatch effect by the value of f_{SMM} in percent.

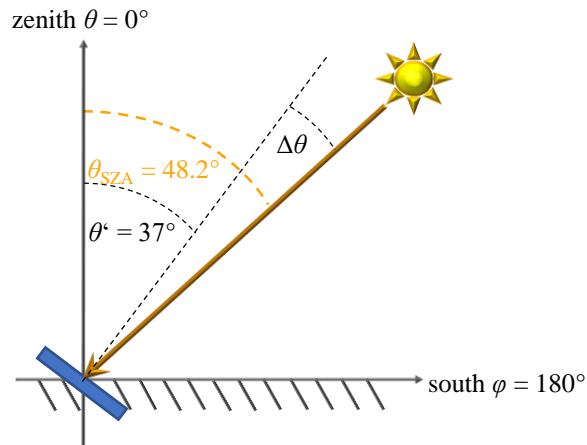


Figure 5.1: Orientation of the device's surface under an AM1.5G irradiance as defined in IEC 60904-3. The angle of incidence of the direct sunlight $\Delta\theta$ is 11.2° with respect to the device's surface normal (dashed line). This figure is also published in (Plag, et al., 2018a).

Whereas for the first calculation in Table 5.1, top, the spectral and the angular mismatch are both positive, the second example in Table 5.1, bottom, shows opposite effects, resulting in a smaller global contribution of the spectral-angular mismatch f_{SAMM} . In Table 5.1, top, the (conventional) spectral mismatch is almost not apparent, because the relative spectral responsivities of the solar cells are in close match (see Figure 4.7, black, and red curves, respectively). The angular mismatch is the dominating effect here. It can be attributed to the differences in the angular-dependent responsivities of both devices (Figure 4.8, top, and middle) and to the anisotropic shape of the diffuse radiance composed by the sky radiance and the ground reflected radiance within the device's field of view.

While the scenario shown in Table 5.1, top, provides mismatches corresponding to the contribution of the direct irradiance (third column) that are rather negligible, in the scenario shown in Table 5.1, bottom, this is not the case. A spectral-angular mismatch of 5.45 % can be assigned to the current generated by the direct irradiance component for this specific case. It is mainly composed of the (conventional) spectral mismatch of 5.13 %, caused by the large difference in the relative spectral responsivities of the DUT and the reference device (see Figure 4.7, red, and blue curve) and the fact, that the spectral irradiance of the direct irradiance is different from that of the reference spectrum. An approximate angular mismatch of 0.31 % is determined for the contribution of the direct irradiance.

This difference originates from the combination of both devices' angular-dependent responsivities at an angle of incidence of 11.2° which are shown in Figure 4.8, middle, and bottom. Interestingly, the spectral-angular mismatch related to the diffuse radiance (fourth column) has an opposing effect on the calibration of the IR-filtered device against the encapsulated device than the contribution of the direct irradiance under this specific irradiation condition.

Table 5.1: Example computation of the spectral-angular mismatch under global natural sunlight with tilted devices given as a percentage deviation from the ideal case with the factor equals to 1. The AM1.5G spectral radiance field for this case is calculated by using libRadtran considering the input parameters described in Section 3.5. Both devices are oriented towards the south ($\varphi' = 180^\circ$) with a tilt of $\theta' = 37^\circ$ as defined in (IEC 60904-3 Edition 2, 2008). The angle of incidence of the direct beam $\Delta\theta$ is 11.2° in this case. The global contribution to the mismatch consists of the mismatch corresponding to the individual irradiation contribution $E_{\lambda, \text{DNI}}(\lambda)$ and $L_{\lambda, \text{diff}}(\lambda, \theta, \varphi)$ (which is composed of $L_{\lambda, \text{sky}}(\lambda, \theta, \varphi)$ and $L_{\lambda, \text{ground}}(\lambda, \theta, \varphi)$). The top part of this table shows the mismatch results of an example computation using the angular-dependent spectral responsivity of an encapsulated c-Si device that is used as a reference; the angular-dependent spectral responsivity of a non-encapsulated c-Si device is used as a DUT. The bottom part of this table shows mismatch results for a scenario using an encapsulated c-Si device as a reference and an IR-filtered c-Si device as DUT. The dataset presented in this table is also published in (Plag, et al., 2018a).

mismatch parameter ↓	global contribution	weighted by contribution of i, j, k			
		direct irradiance	diffuse radiance (sky+ground)	sky radiance	ground reflected radiance
	$ijk = 111$	$ijk = 100$	$ijk = 011$	$ijk = 010$	$ijk = 001$
Global tilted: non-encapsulated DUT against encapsulated reference					
spectral-angular mismatch f_{SAMM} in %	0.71	0.03	0.68	0.57	0.11
spectral mismatch f_{SMM} in %	0.05	0.06	-0.01	-0.01	0.00
only <u>angular</u> mismatch f_{AMM} in % (approx.)	0.66	-0.03	0.69	0.58	0.11
IR-filtered DUT against encapsulated reference					
spectral-angular mismatch f_{SAMM} in %	0.34	5.45	-5.11	-5.77	0.65
spectral mismatch f_{SMM} in %	-0.81	5.13	-5.91	-6.47	0.56
only <u>angular</u> mismatch f_{AMM} in % (approx.)	1.01	0.31	0.85	0.75	0.10

The individual direct and diffuse contributions (third and fourth column) sum up to the global contributions of the spectral-angular mismatch and of the spectral mismatch (second column). The weighting approach becomes inconsistent for the sum of direct and diffuse

contribution of the pure angular mismatch. Under the investigated conditions, the maximum discrepancy can be found in Table 5.1, bottom. It is 0.15 % for the angular mismatch of the IR-Filtered device (the difference between the sum of the direct and diffuse angular mismatch compared to the global contribution of the angular mismatch). In Table 5.1, top, this discrepancy cannot be displayed within the two positions after the decimal point. Anyhow, a reason for this is a difference in the weighting factors determined for the combined spectral-angular mismatch and the pure spectral mismatch. On the other hand, this inconsistency appears because the spectral and angular characteristics of the light source and the detectors are coupled quantities, and because Equation (3.13) implies only an approximate approach that decouples these two quantities. Therefore, the validity of a separate treatment of the spectral and angular mismatch computations should be checked thoroughly for individual cases, especially if the spectrum shows large discrepancies to the reference condition.

5.1.2. Condition 2 (global normal irradiance AM1.5G)

Sophisticated calibrations of PV devices are commonly performed under global normal irradiance conditions with $\Delta\theta = 0^\circ$. To study the dependency of the mismatch on the device orientation independently of an angular mismatch contribution of the direct irradiance, the mismatches in this subsection are determined under global normal conditions using the same sky spectral radiance dataset (see Figure 5.2), but with the direct sunlight perpendicular to the device's surface ($\Delta\theta = 0^\circ$). With this orientation the impact of angular losses that originates from direct sunlight on the angular mismatch is expected to be negligible.

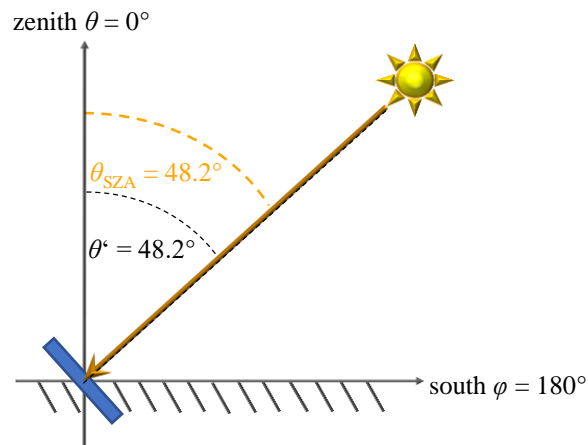


Figure 5.2: Direct normal orientation of the device's surface under an AM1.5G irradiance condition. The angle of incidence of the direct sunlight $\Delta\theta$ is 0° with respect to the device's surface normal (dashed line). This figure is also published in (Plag, et al., 2018a).

Compared to Condition 1 (irradiance close to the definition of standard test conditions) Condition 2 includes a larger tilt towards the horizon ($\theta' = 48.2^\circ$). Consequently, on the one hand, an increase of the ground reflected radiance accumulated by the PV devices is expected, and thus a larger resulting weighting factor w^{001} . On the other hand, the

accumulated sky radiance is reduced and with that the corresponding weighting factor w^{010} decreases.

The evaluation of the results for this specific irradiation condition (see Table 5.2, top and bottom) shows that the angular mismatch decreases in both cases compared to the two cases investigated under Condition 1 (irradiance close to the definition of standard test conditions). The absent contribution of angular mismatch assigned to the direct irradiance for this orientation is most likely the reason. While the decrease of the spectral-angular mismatch is negligibly small for the situation presented in Table 5.1, top, and Table 5.2, top (from 0.66 % to 0.65 %), it is more significant for the IR-filtered device calibration shown between Table 5.1, bottom and Table 5.2, bottom, (from 1.01 % to 0.84 %). Due to fact that the device tilt towards the horizon is larger here compared to Condition 1, an increase of the spectral-angular mismatch is originating from a higher ground-reflected spectral radiance contribution.

In the case of the IR-filtered device, the spectral-angular mismatch assigned to the ground reflected contribution increases from 0.65 % to 1.06 %. A second effect of the larger tilt becomes apparent, when observing the spectral mismatch effect for the ground-reflected contribution. For the IR-filtered device calibration scenarios treated in Table 5.1, bottom and Table 5.2, bottom, the ground-reflected contribution to the spectral mismatch increases by 0.34 % to a value of 0.90 %. The reason here is the larger discrepancy between the ground-reflected spectrum and the reference spectrum and the fact, that the ground-reflected radiance contributes more to the generated short-circuit current under Condition 2, than under Condition 1.

Table 5.2: Example computation of the spectral-angular mismatch for a global normal sunlight measurement given as a percentage deviation from the ideal case with the factor equals to 1. The AM1.5G spectral radiance field for this case is calculated by using libRadtran considering the input parameters described in Section 3.5. The direct beam is perpendicular to the surface of the devices ($\theta' = 48.2^\circ$ and $\varphi' = 180^\circ$). The global contribution to the mismatch consists of the mismatch corresponding to the individual irradiation contribution $E_{\lambda, \text{DNI}}(\lambda)$ and $L_{\lambda, \text{diff}}(\lambda, \theta, \varphi)$ (which is composed of $L_{\lambda, \text{sky}}(\lambda, \theta, \varphi)$ and $L_{\lambda, \text{ground}}(\lambda, \theta, \varphi)$). The top part of this table shows the mismatch results of an example computation using a non-encapsulated device that is calibrated against an encapsulated device. The bottom part of this table shows mismatch results for a scenario using an encapsulated c-Si device as a reference and an IR-filtered c-Si device as DUT. The dataset presented in this table is also published in (Plag, et al., 2018a).

mismatch parameter ↓	global contribution	weighted by contribution of i, j, k			
		direct irradiance	diffuse radiance (sky+ground)	sky radiance	ground reflected radiance
		$ijk = 111$	$ijk = 100$	$ijk = 011$	$ijk = 010$
Global <u>normal</u> AM1.5: non-encapsulated DUT against encapsulated reference					
spectral-angular mismatch f_{SAMM} in %	0.70	0.06	0.64	0.46	0.19
spectral mismatch f_{SMM} in %	0.05	0.06	-0.01	-0.01	0.01
only <u>angular</u> mismatch f_{AMM} in % (approx.)	0.65	0.00	0.65	0.47	0.18
Global <u>normal</u> AM1.5: IR-filtered DUT against encapsulated reference					
spectral-angular mismatch f_{SAMM} in %	0.58	5.13	-4.55	-5.62	1.06
spectral mismatch f_{SMM} in %	-0.26	5.06	-5.32	-6.22	0.90
only <u>angular</u> mismatch f_{AMM} in % (approx.)	0.84	0.07	0.81	0.65	0.16

5.1.3. Condition 3 (global normal irradiance AM2G)

The following two Conditions 3 and 4 are selected to further study mismatch effects under varying spectral radiance conditions. For Condition 3, the air mass is increased to AM2, which corresponds to a solar zenith angle θ_{SZA} of 60° (see Figure 5.3).

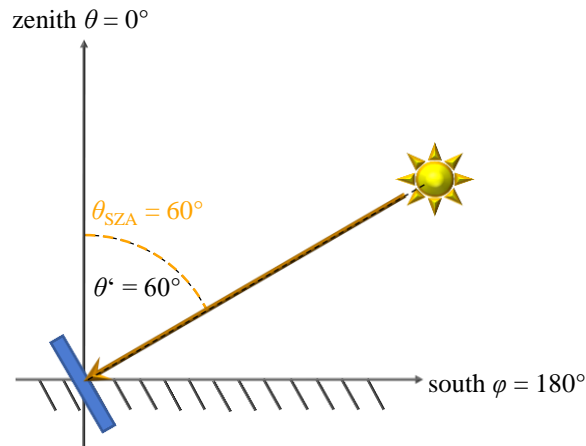


Figure 5.3: Direct normal orientation of the device's surface under an AM2G irradiance condition. The angle of incidence of the direct sunlight $\Delta\theta$ is 0° with respect to the device's surface normal (dashed line).

The spectral radiance field and direct spectral irradiance for this condition are simulated by using libRadtran. No other parameters than the solar zenith angle are changed in the radiative transfer calculation compared to the simulated data of Condition 2. It is expected that a change in the spectral and directional irradiation conditions causes differences in the spectral-angular mismatch for each individual measurement scenario. Table 5.3 shows the results of a computational study on global sunlight calibrations of a non-encapsulated device and an IR-filtered device, both used as a DUT, respectively, that are calibrated against an encapsulated reference device.

It becomes apparent that the changes of the mismatch values for the calibration scenario of a non-encapsulated device under AM2G condition (Table 5.3, top) are rather low compared to these under Condition 2 with AM1.5G (Table 5.2, top). The increase of the spectral mismatch is only 0.03 % and thus negligible. The angular mismatch decreases slightly which has a reason: The dominant portions of the sky radiance are in the circumsolar and horizontal regions. For this specific condition, these directions are mostly within a field of view with angles of incidence smaller than 30° related to the device surface normal. In these regions, the angular losses of both devices (DUT and reference) are below 2 % for these AOI's (see Figure 4.8, top right, and middle right). The rather small difference in the angular losses of both solar cells leads to a reduced angular mismatch compared to conditions where larger angles of incidence are more dominant.

The calibration scenario of the IR-filtered device under AM2 condition shows a significant impact on the spectral-angular mismatch compared to Condition 2 (AM1.5G). An underestimation due to the spectral-angular mismatch of 4.15 % is apparent compared to a primary calibration under a reference spectral irradiance with direct normal incidence only.

With a value of 3.28 %, most of this underestimation can be attributed to the spectral mismatch, but approximately 0.84 % of the mismatch originates from a larger difference in the angular losses of both devices under this condition.

Table 5.3: Example computation of the spectral-angular mismatch for a global normal sunlight measurement given as a percentage deviation from the ideal case with the factor equals to 1. The AM2G spectral radiance field for this case is calculated by using libRadtran considering the input parameters described in Section 3.5, but with $\theta_{\text{SZA}} = 60^\circ$. The direct beam is perpendicular to the surface of both devices ($\theta' = 60^\circ$ and $\varphi' = 180^\circ$). The global contribution to the mismatch consists of the mismatch corresponding to the individual irradiation contribution $E_{\lambda, \text{DNI}}(\lambda)$ and $L_{\lambda, \text{diff}}(\lambda, \theta, \varphi)$ (which is composed of $L_{\lambda, \text{sky}}(\lambda, \theta, \varphi)$ and $L_{\lambda, \text{ground}}(\lambda, \theta, \varphi)$). Mismatch results of an example computation using a non-encapsulated device that is calibrated against an encapsulated device are shown in the top part of this table, while the mismatch results for a scenario using an IR-filtered device that is calibrated against an encapsulated device are shown in the bottom part.

mismatch parameter ↓	global contribution	weighted by contribution of i, j, k			
		direct irradiance	diffuse radiance (sky+ground)	sky radiance	ground reflected radiance
		$ijk = 111$	$ijk = 100$	$ijk = 011$	$ijk = 010$
Global <u>normal</u> AM2: non-encapsulated DUT against encapsulated reference					
spectral-angular mismatch f_{SAMM} in %	0.67	0.08	0.60	0.39	0.21
spectral mismatch f_{SMM} in %	0.08	0.08	0.01	0.00	0.01
only <u>angular</u> mismatch f_{AMM} in % (approx.)	0.59	0.00	0.59	0.39	0.20
Global <u>normal</u> AM2: IR-filtered DUT against encapsulated reference					
spectral-angular mismatch f_{SAMM} in %	4.15	8.23	-4.08	-5.39	1.31
spectral mismatch f_{SMM} in %	3.28	8.12	-4.84	-5.96	1.12
only <u>angular</u> mismatch f_{AMM} in % (approx.)	0.84	0.10	0.80	0.61	0.19

As expected, the contribution of the ground-reflected radiance to the angular mismatch increases slightly with larger tilt angles of the devices. With 0.19 %, it contributes to one quarter of the angular mismatch related to diffuse spectral radiance, which represents the dominant source of angular mismatch in that case. Again, as already explained in Condition 1 (irradiance close to the definition of standard test conditions), a discrepancy between the sum of the direct and diffuse contributions to angular mismatch (third and fourth columns) and the global contribution (second column) becomes apparent for this specific situation. This is because the pure angular mismatch is calculated by assuming that the spectral and the directional dependencies are treated as decoupled quantities. Thus, this assumption leads to different weighting factors w^{ijk} between spectral-angular mismatch and spectral mismatch in Table 5.3, bottom.

5.1.4. Condition 4 (global normal irradiance AM2G and with green grass spectral albedo)

To examine the influence of probable reflective conditions of the ground considering a measurement site vegetation in Central Europe, the calibration scenarios under Condition 4 consider the spectral albedo of green grass provided by the software package SMARTS 2.9.2 (Gueymard, et al., 2002). For the Conditions 1 to 3 the spectral albedo of light soil is used (see Figure 5.4). Mismatch effects that can be attributed to the ground-reflected spectral radiance are expected to change compared to the example scenario shown in Condition 3. For this comparison the device orientation, the solar position and the atmospheric conditions are similar than those used for the simulation in Condition 3. The resulting mismatch values are summarized in Table 5.4, top, for a calibration of the non-encapsulated device against the encapsulated reference device and in Table 5.4, bottom, for a calibration of the IR-filtered device against the encapsulated reference device.

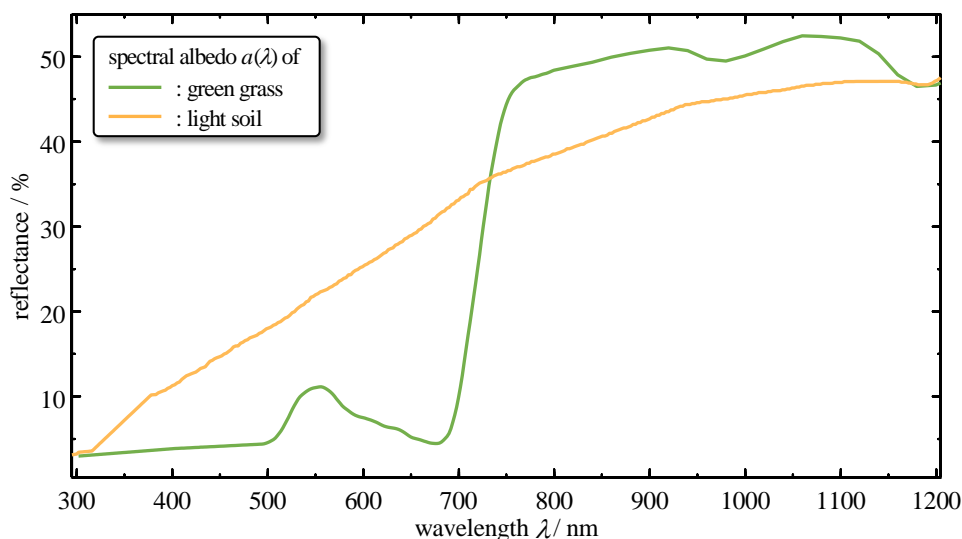


Figure 5.4: Spectral albedo of different ground materials within a spectral range between 300 nm and 1200 nm used by SMARTS (Gueymard, et al., 2002). The green curve represents the spectral albedo of green grass and the yellowish brown curve this of light soil.

The analysis of this scenario shows that the effect of different albedos on the mismatch is rather small, compared to the scenario shown in Table 5.3 under Condition 3 with a light soil spectral albedo. The low spectral mismatch correction f_{SMM} increases slightly when comparing the results shown in Tables 5.3 and 5.4, top, respectively.

Table 5.4: Example computation of the spectral-angular mismatch for a global normal sunlight measurement given as a percentage deviation from the ideal case with the factor equals to 1. The AM2G spectral radiance field for this case is calculated by using libRadtran considering the same input parameters described for Table 5.3 with one exception: the spectral albedo of green grass is used for the ground. The direct beam is perpendicular to the surface of both devices ($\theta' = 60^\circ$ and $\varphi' = 180^\circ$). The global contribution to the mismatch consists of the mismatch corresponding to the individual irradiation contribution. Mismatch results of an example computation using a non-encapsulated device that is calibrated against an encapsulated device are shown in the top part of this table, while the mismatch results for a scenario using an IR-filtered device that is calibrated against an encapsulated device are shown in the bottom part.

mismatch parameter ↓	global contribution	weighted by contribution of i, j, k			
		direct irradiance	diffuse radiance (sky+ground)	sky radiance	ground reflected radiance
		$ijk = 111$	$ijk = 100$	$ijk = 011$	$ijk = 010$
Global <u>normal</u> AM2: <u>green grass</u> spectral albedo; non-encapsulated DUT against encapsulated reference					
spectral-angular mismatch f_{SAMM} in %	0.66	0.08	0.58	0.39	0.19
spectral mismatch f_{SMM} in %	0.11	0.08	0.03	0.01	0.02
only <u>angular</u> mismatch f_{AMM} in % (approx.)	0.55	0.00	0.55	0.38	0.17
Global <u>normal</u> AM2: <u>green grass</u> spectral albedo; IR-filtered DUT against encapsulated reference					
spectral-angular mismatch f_{SAMM} in %	5.82	8.44	-2.63	-5.04	2.41
spectral mismatch f_{SMM} in %	5.15	8.36	-3.21	-5.60	2.40
only <u>angular</u> mismatch f_{AMM} in % (approx.)	0.64	0.08	0.60	0.60	0.02

The difference in the spectral-angular mismatch correction factor f_{SAMM} under the consideration of a light soil (Table 5.3, top) against this under the condition with a green grass spectral albedo (Table 5.4, top) is 0.01 % and thus negligible.

A significant change in the spectral-angular mismatch can be observed for the same computational example case, but with an IR-filtered device used as DUT which is calibrated against an encapsulated device. For the condition with green grass spectral albedo the resulting correction factor f_{SAMM} is 5.82 % (Table 5.4, bottom). In the case where light soil is surrounding the measurement site, a spectral-angular mismatch of 4.15 % between both devices is apparent (see Table 5.3, bottom). The f_{SAMM} difference of 1.67 % arises mainly from the change of the ground-reflected spectral irradiance resulting in a change of the spectral mismatch f_{SMM} . This changing f_{SMM} values are located in the sixth column and second last row of Table 5.3 and 5.4, bottom, respectively. The comparison of the results shown in Table 5.3 and 5.4 emphasizes the role of the directional and spectral coupling in the irradiation quantities and the device responsivities.

As aforesaid, the spectral mismatch values f_{SMM} presented in Tables 5.1 to 5.4 are calculated using the conventional approach in accordance with (IEC 60904-7 Edition 3, 2008) including an approximation that the entire incident irradiation takes effect on the devices spectral responsivity $s(\lambda)$ at normal incidence ($\theta = 0^\circ$). Directional dependencies of the incident spectrum, i.e. through different spectral ground reflectance's that may take effect on a spectral responsivity different from this at normal incidence can only properly considered by using the novel model proposed in this work. A sensitivity analysis on simplifications made to the model is presented in the next subsection to study the significance of the consideration of coupled spectral and angular source and detector properties.

5.1.5. Sensitivity analysis on simplified assumptions for the spectral-angular mismatch computation

Due to the fact, that the multidimensionality in the spectral-angular mismatch approach requires enormous experimental effort and computation time, it is worth to look at a tradeoff between accuracy and effort in the procedures. Therefore, important assumptions are changed in this subsection to study their influence on the spectral-angular mismatch correction factor f_{SAMM} . As common base for a comparison, the AM2 global normal sunlight condition (device tilt and solar zenith angle are both 60°) with a green grass spectral albedo are used. The following comparison considers angular-dependent spectral responsivities and an anisotropic spectral radiance field as a complex scenario and two simplified approaches:

1. The irradiation conditions are separated from directional and spectral properties into the integral quantities,
 - the diffuse radiance $L(\theta, \varphi)$,
 - and the direct normal irradiance E_{DNI} ,
and into the spectral quantities,
 - the diffuse spectral irradiance $E_{\lambda, \text{diff}}(\lambda)$,
 - and the direct normal spectral irradiance $E_{\lambda, \text{DNI}}(\lambda)$.

The corresponding experimental approach reflecting this simplification are the measurements of the anisotropic sky radiance and the direct normal irradiance both determined with ideal broadband detectors. To measure the sky radiance, a scanning or imaging method needs to be applied. The spectral quantities need to be measured by two spectroradiometers, accounting for the diffuse and the direct spectral irradiances separately. The entrance optics of the spectroradiometer measuring the diffuse component of the spectrum needs an ideal responsivity following the cosine. This simplification leads to a reduction of the spectral radiance L_λ field by one dimension and reduces the computational effort significantly when using the proposed model. The sky radiances anisotropy remains considered in this case.

2. A further simplification is made by assuming isotropy for the diffuse irradiance condition. Therefore, an isotropic radiance field $L_{\text{diff}}(\theta, \varphi)$ is determined by conserving the diffuse in-plane irradiance E_{diff} . An experimental approach reflecting this second simplification are global sunlight measurements using instrumentation without scanning the diffuse sky radiance. The diffuse irradiance is measured instead with an ideal global broadband detector, that is shaded from direct sunlight. Angular losses are considered in this simplified scenario. Note that the international standard (IEC 60904-4, 2009) neglects the angular losses of PV devices with the state-of-the-art calibration method using global sunlight (GSM).

Spectral and angular-dependent responsivities of the PV devices to determine spectral mismatch and angular deviation between both devices are treated separately in this investigation on simplifications. A separation of the devices directional and spectral properties enables the use of the proposed model with broadband responsivity datasets and limits the immense characterization effort, presented in Chapter 4 towards a reasonable time needed. This simplification requires a broadband light source only, i.e. a solar simulator or direct natural sunlight for the determination of the broadband angular-dependent responsivity with spectral irradiances close to reference conditions. State-of-the-art angle of incidence facilities for solar cell or PV module characterization usually not provide angular-dependent spectral responsivity datasets (a spectrally tunable light source is required), so that this first scenario of simplification is applicable for a broader range of users.

With focus on the applicability, the simplified cases studied in this subsection additionally assume that the broadband angular-dependent responsivity $s_{\text{AM1.5G}}(\theta, \varphi)$ of the PV devices are measured only for a single azimuthal orientation. Assuming further, that no polarization dependence is apparent for characterization under unpolarized broadband light sources, a reduction from 4788 to 19 data points can be achieved for each device. This enables faster measurements and data treatment procedures. The angular-dependent responsivity $s(\theta, \varphi = 0^\circ)$ at one azimuth angle for each device is normalized to one at the value at normal incidence $s(\theta = 0^\circ, \varphi = 0^\circ)$ and subsequently the dataset is extrapolated onto the complete hemisphere with the designated angular resolution, assuming azimuthal symmetry. Additionally, the spectral responsivity measurements at normal incidence of both devices are used for the calculation of individual spectral mismatch correction factors.

The angular deviation factors $\text{Dev}_{\Omega, i}$ between the reference solar cell and the DUT solar cell are determined individually for each of the two simplifications and irradiation conditions for each case, respectively, using Equation (3.3), with the index i representing either anisotropic (aniso) or isotropic (iso) conditions. Therefore, the required radiance values L_{diff} are obtained by integrating the simulated spectral radiance field $L_{\lambda, \text{sky}}(\lambda, \theta, \varphi)$ over the designated wavelength range from 300 nm to 1200 nm for each direction. The diffuse irradiance E_{diff} is then determined by using Equation (3.1).

The spectral-angular mismatch correction factors $f_{S\text{AMM}, i}$ are then obtained using Equation (5.3), while the individual spectral mismatch correction factors $f_{S\text{MM}, i}$ are calculated using effective global spectral irradiances $E_{\lambda, \text{glo}, \text{AOI}, i}(\lambda)$. This idea is related to the procedure described in the energy rating standard (IEC 61853-3, 2018) which is summarized in Chapter 2 with Equation (2.27). Whereas in Equation (2.26) the spectral correction factor C_S is determined, in this approach the consideration of two spectral responsivities (reference device and DUT) is necessary, because the device used as reference device provides also angular losses under diffuse irradiation conditions. The factors $f_{S\text{MM}, i}$ are obtained by using the following equation:

$$f_{S\text{MM}, i} = \frac{1}{S\text{MM}_i} \quad (5.3)$$

$$= \frac{\int_{\lambda} E_{\lambda, \text{glo}, \text{AOI}, i}(\lambda) \cdot s_{\text{ref}}(\lambda, \theta = 0^\circ) d\lambda}{\int_{\lambda} E_{\lambda, \text{ref}}(\lambda) \cdot s_{\text{ref}}(\lambda, \theta = 0^\circ) d\lambda} \cdot \frac{\int_{\lambda} E_{\lambda, \text{ref}}(\lambda) \cdot s_{\text{DUT}}(\lambda, \theta = 0^\circ) d\lambda}{\int_{\lambda} E_{\lambda, \text{glo}, \text{AOI}, i}(\lambda) \cdot s_{\text{DUT}}(\lambda, \theta = 0^\circ) d\lambda}$$

with the index i representing either anisotropic (aniso) or isotropic (iso) conditions and

$$E_{\lambda, \text{glo}, \text{AOI}, i}(\lambda) = \frac{E_{\lambda, \text{glo}, \text{AOI}}(\lambda)}{\text{Dev}_{\Omega, i}}. \quad (5.4)$$

Finally, for this comparison only, the spectral-angular mismatch correction factor $f_{S\text{AMM}, i}$ is given by following equation:

$$f_{S\text{AMM}, i} = f_{S\text{MM}, i} \cdot \text{Dev}_{\Omega, i}. \quad (5.5)$$

Table 5.5: Sensitivity analysis on different spectral-angular mismatch approaches for two different exemplary solar cell calibration scenarios. An AM2G spectral radiance for a global normal condition ($\theta_{SZA} = 60^\circ$) is simulated by using libRadtran under consideration of green grass spectral albedo. The second column shows the correction factors f_{SMM} by using the novel approach considering spectral and angular quantities to be coupled and with an anisotropic sky spectral radiance field. In the third column, the correction factors $f_{SMM,aniso}$ obtained by separating (decoupling) spectral and angular quantities are presented. The fourth column shows the differences between the second and third columns. The fifth column contains a major simplification: An isotropic sky radiance for the computation of angular mismatch and a separate treatment of spectral mismatch to compute $f_{SMM,iso}$. In the last column, the differences between second and fifth columns are shown. All values are given in percent.

Global <u>normal</u> AM2 ($\theta_{SZA} = 60^\circ$) with green grass spectral albedo:	<u>mismatch calculation approach:</u>				
	anisotropic model: spectral and angular coupled f_{SMM} in %	first simplification: anisotropic spectral and angular decoupled		second simplification: isotropic spectral and angular separated	
		$f_{SMM,aniso}$ in %	<u>difference</u>	$f_{SMM,iso}$ in %	<u>difference</u>
non-encapsulated DUT against encapsulated reference	0.66	0.59	<u>0.07</u>	0.85	<u>-0.19</u>
IR-filtered DUT against encapsulated reference	5.82	5.99	<u>-0.17</u>	6.46	<u>-0.64</u>

As shown in Table 5.5, the spectral-angular mismatch difference using an anisotropic separated approach compared to the more comprehensive multidimensional combined approach ($f_{SMM} - f_{SMM,aniso}$) is 0.07 % and thus rather small for the non-encapsulated device calibration. This difference becomes more significant with -0.17 % for the IR-filtered device calibration, when separating the (coupled) spectral and angular quantities. The largest difference is observed for the simplification that assumes isotropic diffuse radiance. Here, differences, between the mismatches calculated with the isotropic separated approach and calculated with the multidimensional combined approach, of -0.19 % for the non-encapsulated device calibration, and of -0.64 % for the IR-filtered device calibration are apparent.

An important conclusion of this sensitivity analysis is, that particularly the assumption of isotropic diffuse radiance yields to significant systematic deviations of the correction factors compared to a comprehensive model considering anisotropy and coupled spectral and directional quantities. In one specific case, the systematic deviation of -0.64 % is as large as the bare impact of angular mismatch itself (see Table 5.4, last row). But also, a deviation of -0.19 % for the other calibration scenario is particularly large compared to expanded measurement uncertainties of 0.4 % ($k=2$), that are achieved with primary high-accuracy

calibrations for the short-circuit current under normal incidence only. The author recommends taking the findings of this section into consideration when establishing measurement uncertainty budgets, especially for secondary high-accuracy calibrations of solar cells that are conducted under global natural sunlight or other light sources with a diffuse radiance contribution.

5.1.6. Summary

A comprehensive computational study of spectral-angular mismatches is performed to obtain an overview over the impact of four different outdoor calibration scenarios on the mismatch effect. The exemplary cases discussed in the subsections Condition 1 and 2 contain outdoor calibration scenarios close to the reference conditions defined in (IEC 60904-3 Edition 2, 2008). A comparison with the conventional spectral mismatch in accordance with IEC standard procedures (IEC 60904-7 Edition 3, 2008) shows that the pure angular mismatch f_{AMM} for these conditions can be larger than 1 %, depending on the individual case studied in this work. This becomes significant since expanded measurement uncertainties for primary outdoor calibrations of the short-circuit current of reference solar cells, using the global sunlight method (GSM) are reported to be lower than 0.7 % (IEC draft 60904-4 Edition 3, 2018). In the recent draft of the IEC standard that is currently under discussion in the standardization committee, AOI effects are still neglected for primary calibrations.

Interestingly, this study reveals opposite effects for spectral mismatches and angular mismatches in one example case. The model applied here allows individual irradiation contributions, such as ground-reflected radiance, sky radiance and direct irradiance to be separated; thus, each individual contribution to the mismatches are discussed. Additionally, examples under AM2G conditions and different spectral ground reflectance's are treated in the subsections Condition 3 and 4. A maximum spectral-angular mismatch value of 5.8 % is observed under these conditions. An important result is that the spectral composition of the ground surrounding the measurement site can significantly affect the spectral-angular mismatch for IR-filtered reference solar cells that provide an irregular angular-dependent spectral responsivity. The results of different computational studies show that the spectral-angular mismatch systematically affects measurements taken under diffuse irradiance. This depends on the PV device's angular-dependent spectral responsivities and on the shape of the spectral radiance field of each individual irradiation condition.

For the case of PV performance monitoring or energy rating purposes, the impact of the mismatch is expected to be even higher when the sky is dense overcast, due to the high contribution of the diffuse irradiance to the global irradiance under these conditions.

In a comprehensive sensitivity analysis, the irradiation conditions are simplified by separating the spectral and directional properties in a first step and by assuming an isotropic diffuse radiance in a second step. These simplifications are performed to investigate a tradeoff between accuracy of the model and the effort in the experimental characterization as well as the computational procedure. Deviations between the individual simplified approach to the comprehensive multidimensional model are ranging from 0.07 % to -0.64 %. While the first simplification reveals maximum absolute deviations of lower than

0.2 % the isotropic approach reveals deviations that are in the range of the bare angular mismatch itself. These high systematic deviations suggest using at least an anisotropic diffuse radiance field separated from the spectral distribution, when performing spectral-angular mismatch corrections to achieve more accurate results. With that first simplification the time consumption for the experimental and computational effort decreases by approximately two orders of magnitude and the procedure can be realized by laboratories without access to a laser-based AOI-facility.

This leads to the conclusion, that the spectral-angular mismatch correction factor should be individually applied for high-accuracy short-circuit current measurements on PV devices under global natural sunlight and that its impact on energy rating under realistic irradiation conditions should be further investigated.

5.2. Effect of the angle of incidence on optical losses of solar cells

In this section three different calculation approaches for the determination of solar cells' and PV modules' short-circuit current losses under global irradiance are investigated. These angular losses express the percentage short-circuit current decrease or gain (if its value is negative) of a real device compared to an ideal device whose short-circuit current follows the cosine with the angle of incidence. The investigation presented here neglects spectral effects to keep the focus on differences between the three approaches used for the determination of the angular losses. The first subsection includes the calculation of angular losses based on a simplified MR model (see Section 2.5.2), proposed by the IEC working group technical committee TC82 for energy rating purposes that is included in the recently released standard (IEC 61853-3, 2018). Two examples showing angular losses of two selected solar cells under global horizontal irradiance conditions are presented. Subsequently, in the second subsection the angular loss calculations are performed following an approach based on the f_2 index widely used in photometric applications (see Section 2.6) and which is included in the photometry standard (ISO/CIE 19476, 2014). The second approach based on the f_2 index was modified by the author for the calculation on angular losses under diffuse solar irradiance and to reflect the observed properties of solar cells, whose angular-dependent responsivities represent a "super cosine". Both state-of-the-art approaches use simplifications: They assume isotropic radiance conditions and azimuthal symmetry of the devices angular-dependent responsivities. Limitations and assumptions of the approaches are discussed in a separate subsection to emphasize their impact on the angular losses and their corresponding measurement uncertainty. Finally, a summary concludes the findings of this section.

5.2.1. Simplified MR models' angular losses

Major parts of this subsection are published in advance in the conference proceedings (Plag, et al., 2017a). The approach introduced by Martin and Ruiz (Martin & Ruiz, 2001) uses coefficients determined by a least square curve fitting routine (Levenberg-Marquardt algorithm). To calculate the angular losses of the generated short-circuit currents, the curves of angular transmissions $\tau(\theta)$ are determined from the measured datasets presented in Chapter 4 to further use them with the simplified MR model summarized in Chapter 2.

Therefore, the seven experimentally determined angular-dependent spectral responsivities for the measured azimuth angles ($\varphi = 0^\circ \dots 90^\circ$ in steps of 15°) are converted from spectrally resolved datasets to broadband datasets weighted with an AM1.5G spectrum. Angular loss coefficients a_r are derived from the AM1.5G-weighted broadband datasets for two different solar cells and are shown here for two selected azimuthal orientations (see photographs in Figures 5.5 and 5.6).

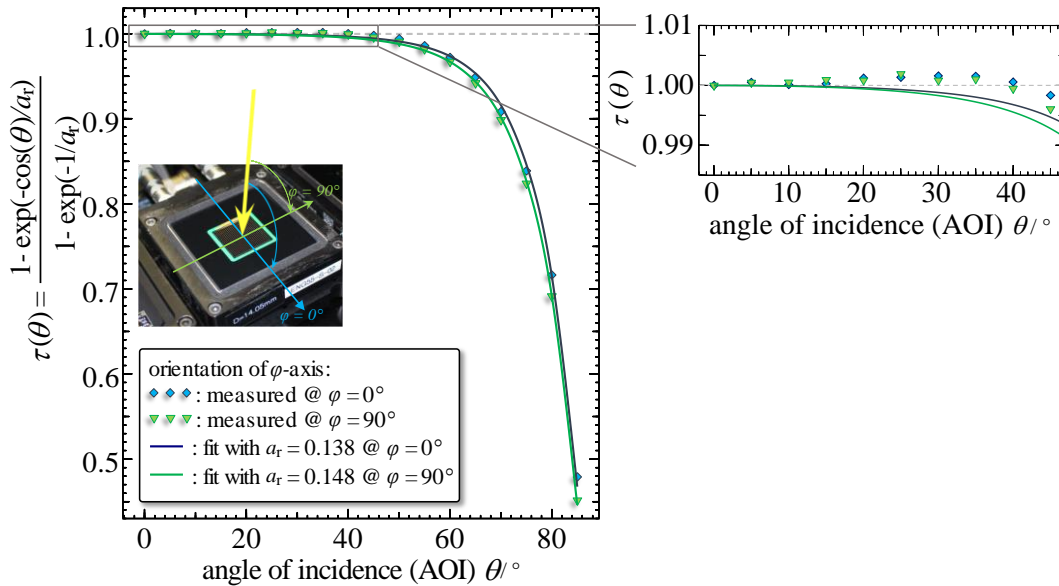


Figure 5.5: Angular loss coefficients a_r for an encapsulated reference solar cell, determined with a Levenberg–Marquardt algorithm. Left-hand side: Angular transmissions for an AM1.5G-weighted spectrum are shown for two different azimuthal orientations of the device (φ -axis). Blue diamonds indicate the measured values of the angular transmission $\tau(\theta)$ at $\varphi = 0^\circ$, green triangles indicate the measured values at $\varphi = 90^\circ$. Dark blue and dark green lines show the analytic expressions with corresponding a_r -values, respectively. Right-hand side: details on the magnified area highlighted in the diagram on the left-hand side as grey rectangle. A graph of this dataset (left-hand side) is also published in the conference proceeding (Plag, et al., 2017a).

The Figures 5.5 and 5.6 show only two of seven orthogonal azimuthal orientations for reasons of clarity. The determination of the fitting parameter a_r seems to work well for the measured and AM1.5G-weighted broadband angular transmission of the encapsulated reference solar cell at the first impression (Figure 5.5 left-hand side). The two calculated angular loss coefficients a_r shown in the graph are 0.138 and 0.148 for the azimuthal orientations 0° and 90° respectively. A detailed view at Figure 5.5 reveals deviations between the fitted curves and measured datasets in the zenithal range from 0° to 45° (detailed view at the right-hand side in Figure 5.5). It becomes apparent that most of the measured angles of incidences in this magnified graph exhibit a “super cosine” resulting as an increase in the solar cells short-circuit current compared to the cosine. The Levenberg-Marquardt fitting algorithm cannot represent those super cosine values by means of the analytical expression given in Equation (2.21), even though the coefficients of determination $R^2 = 1.000$ (for both

curves) suggest an optimal fit for the encapsulated solar cell dataset shown in Figure 5.5. The coefficient of determination R^2 is determined using the square sum of the residuals.

An underestimation of 0.5 % is apparent at $\theta = 35^\circ$ when using the fitted datasets compared to the measured ones. Between 60° and 75° angle of incidence, a slight overestimation is observed.

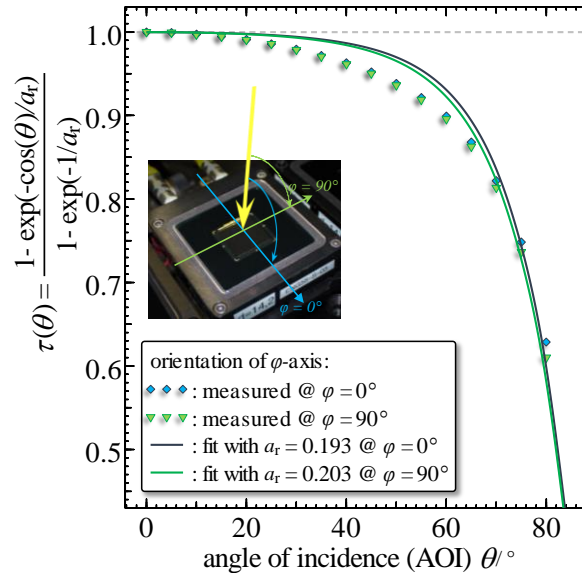


Figure 5.6: Angular loss coefficients a_r for an IR-filtered reference solar cell, determined with a Levenberg–Marquardt algorithm. Angular transmissions for an AM1.5G-weighted spectrum are shown for two different azimuthal orientations of the device (φ -axis). Blue diamonds indicate the measured values of the angular transmission $\tau(\theta)$ at $\varphi = 0^\circ$, green triangles indicate the measured values at $\varphi = 90^\circ$. Dark blue and dark green lines show the analytic expressions with corresponding a_r -values, respectively. This dataset is also published in the conference proceeding (Plag, et al., 2017a).

The evaluation of the measured IR-filtered reference solar cells angular loss coefficients a_r reveals a poor agreement between the analytical expression in Equation (2.21) and the measured datasets, even though the coefficients of determination R^2 are close to one. $R^2 = 0.993$ is determined for the dark blue curve and $R^2 = 0.995$ for the green curve in Figure 5.6. An explanation for that can be found in (Martin & Ruiz, 2001). The MR model neglects optical absorption properties of the encapsulation material within the air-to-cell path. This is most likely the reason for the large disagreement resulting between the fitted curves and the experimentally obtained datasets, because the IR-filtered reference solar cell includes an absorptive filter glass to adapt the spectral match of the monocrystalline silicon solar cell to that of amorphous silicon solar cells. The consequence is an underestimation of angular losses for the isotropic diffuse irradiance and for most of the incidence angles of the direct sunlight. One conclusion of this findings is that the coefficient of determination R^2 cannot be used as a quality parameter for the determination of a_r .

To consider the azimuthal symmetry assumption of the simplified MR model, the average a_r values (mean value averaged over seven separately treated azimuthal orientations) for the examined devices were determined to be 0.143 ± 0.003 and 0.198 ± 0.003 , respectively, for

the encapsulated and the IR-filtered solar cells, respectively. Both coefficients are given here with their assigned expanded uncertainty, determined by averaging. A more detailed discussion on measurement uncertainty of the measured angular transmission $u(\tau(\theta))$ propagating through the simplified MR model is shown in Subsection 5.2.4.

By using the a_r coefficients, the angular losses of both solar cells under direct and under diffuse sunlight is determined in a next step. The selected irradiation condition represents an exemplary clear sky scenario, where the solar zenith angle $\theta_{\text{SZA}} = 50^\circ$ and the solar cell is mounted horizontal. The percentage angular losses of direct sunlight are determined to be $1.029\% \pm 0.080\%$ for the encapsulated device and $3.28\% \pm 0.13\%$ for the IR-filtered device. The percentage angular losses under isotropic diffuse sunlight are $3.92\% \pm 0.14\%$ and $6.85\% \pm 0.14\%$ for the encapsulated and the IR-filtered device's, respectively. Both angular loss components are computed using the Equations (2.22) and (2.23).

5.2.2. Modified f_2 models' angular losses based on a CIE photometry standard

The Commission Internationale de l'Éclairage (CIE) international standard 19476 defines quality indices for the characterization of illuminance and luminance meters in the field of photometry (ISO/CIE 19476, 2014). The analogy in the description of the performance in lighting measurement situations can be also applied in the field of PV metrology. Among many other quality indices, a function called “*deviation in directional response to the incident radiation $f_2(\theta, \varphi)$* ” of planar illuminance meters and a corresponding index f_2 is defined in this standard.

The deviation in directional responsivity functions $f_2(\theta)$ are determined from the measured datasets presented in Chapter 4 to apply them with the procedure based on the definitions given in the CIE 19476 standard which is summarized in Section 2.6. The seven angular-dependent responsivities measured for different azimuthal orientations are used to determine $f_2(\theta, \varphi)$ using Equation (2.28). In a next step, the average over all azimuth directions φ is determined for $f_2(\theta)$. While for the calculation of direct irradiances angular losses the function $f_2(\theta)$ can be used directly at the Sun's position relative to the device, the index f_2 defined by the standard cannot be applied for a general case for the determination of the angular loss under diffuse irradiance, for the following reasons:

1. The standard proposes to proceed in the calculation of the index f_2 by using the absolute values of $f_2(\theta)$ (see Equation (2.29)). This approach includes the fact that $|f_2(\theta)|$ doesn't consider both, positive and negative values of the deviation in directional response. Figure 5.7 highlights this problem in a magnified view on the $f_2(\theta)$ function for one specific example. The area enveloped by the green line, representing the function values obtained by an interpolation, needs to be appropriately integrated over the θ -axis, under consideration of the correct algebraic sign, to obtain the angular loss under isotropic diffuse irradiance. Equation (2.30) sums up both enveloped areas, thus overestimating angular losses in this specific case, where an optical gain is apparent.

2. Additionally, angular loss calculations in accordance with Equation (2.30) are not considering incident irradiance contributions for angles of incidence larger than 80° . Consequently, approximately 1.5 % of the total isotropic diffuse irradiance remains unconsidered in the determination of angular losses when the procedure in accordance with the CIE standard is used.

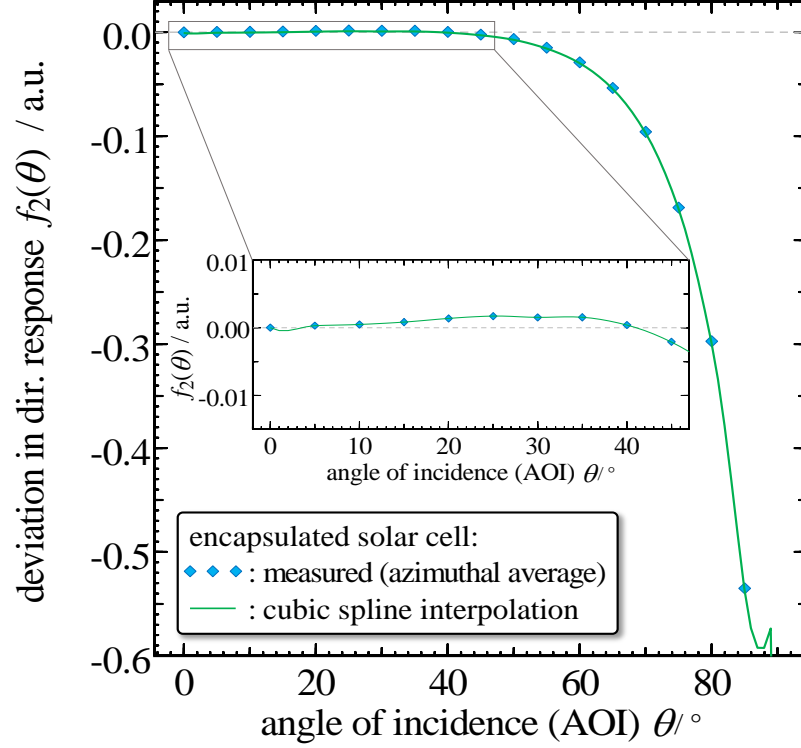


Figure 5.7: Deviation in the directional response function $f_2(\theta)$ of the encapsulated solar cell (analog to the angular transmission $\tau(\theta)$). The blue diamonds indicate the measured deviation in the directional response averaged over seven different azimuthal orientations. The green line shows the $f_2(\theta)$ function obtained using a cubic spline interpolation onto a high-resolution grid for θ between 0° and 90° in steps of 1 degree. A magnified view indicated by a grey box highlights the positive values, where this device provides an optical gain.

The measured optical gain of the encapsulated device at specific angles of incidence shown in Figure 5.7 and the observed high losses at AOI's $\theta > 80^\circ$ motivate an adaption of the CIE procedure for PV metrology purposes to avoid errors due to the abovementioned shortcomings. The diffuse angular loss $f_{2,\text{loss,diff}}$ (for isotropic diffuse irradiance) can be obtained by using the following equation:

$$f_{2,\text{loss,diff}}(\varphi) = 1 - \frac{\int_0^{\pi/2} s_{\text{AM1.5G}}(\theta, \varphi) \cdot \sin \theta \, d\theta}{\int_0^{\pi/2} s_{\text{AM1.5G}}(0^\circ, \varphi) \cdot \cos \theta \cdot \sin \theta \, d\theta}. \quad (5.6)$$

To numerically solve the integrals given in Equation (5.6), a cubic spline interpolation is applied on the measured angular-dependent responsivities $s_{\text{AM1.5G}}(\theta, \varphi)$ for each azimuthal

orientation to obtain a high-resolution grid for θ in steps of 1 degree (see green line in Figure 5.7). The angular losses corresponding to the direct irradiance $f_{2,\text{loss,dir}}$ for a horizontal device is obviously expressed by this equation:

$$f_{2,\text{loss,dir}}(\varphi) = -f_2(\theta_{\text{SZA}}, \varphi). \quad (5.7)$$

The angular losses in accordance with Equations (5.6) and (5.7) are determined separately for each azimuth direction φ . Subsequently, the average of each loss type is determined including its standard deviation which is expressed here as an expanded uncertainty ($k=2$). Percentage angular loss values are determined relative to the cases without angular losses. In the presented example, consistent of a clear sky condition considering a global horizontal irradiance with a solar zenith angle of $\theta_{\text{SZA}} = 50^\circ$, the diffuse angular losses are $3.76\% \pm 0.12\%$ for the encapsulated device and $8.48\% \pm 0.11\%$ for the IR-filtered device. The direct angular losses in this case are $0.65\% \pm 0.27\%$ for the encapsulated device, and $6.25\% \pm 0.22\%$ for the IR-filtered device.

5.2.3. Comparison of the simplified MR model (IEC), the modified f_2 model (based on CIE) and the proposed model

The two previously presented approaches are compared against the results on angular loss calculations using the model proposed in this work. To determine angular losses with the proposed model Equation (3.3) is used, but for the normalized reference angular responsivity $S_{\text{ref,norm}}(\theta, \varphi)$ the cosine of AOI is chosen to obtain Dev_Ω as deviation due to angular effects under global sunlight compared to an ideal detector. Additionally, the AM1.5G-weighted angular-dependent responsivities $S_{\text{DUT,norm}}(\theta, \varphi)$ are normalized to one at $\theta = 0^\circ$ for each of the seven different azimuth directions. Besides the consideration of azimuthal asymmetry, the metric introduced in Section 3.4 allows to consider diffuse anisotropic radiances, which can provide a shape significantly different from that of isotropic conditions. For this comparison, irradiation conditions are simulated using libRadtran with same input parameters as shown in Chapter 3 but using a solar position at $\theta_{\text{SZA}} = 50^\circ$ and $\varphi_{\text{SAA}} = 180^\circ$. The diffuse, direct and global in-plane irradiances are simulated within a wavelength from 300 nm to 1200 nm for a horizontal device orientation $\theta' = 0^\circ$ and $\varphi' = 0^\circ$. The contribution of the diffuse irradiance E_{diff} to the global in-plane irradiance E_{glo} is approximately 17.8 % for this situation. The direct irradiance E_{dir} contributes to 82.2 %.

The diagrams shown in Figures 5.8 and 5.9 illustrate the direct and diffuse angular losses determined for the encapsulated (Figure 5.8) and the IR-filtered (Figure 5.9) devices, respectively and bring them in relation to the losses obtained for the global irradiance scenario (see colored bars labeled as global). The datasets determined by using the state-of-the-art approaches are indicated as orange and green bars. They assume an isotropic sky radiance and an azimuthal averaged angular-dependent responsivity $S_{\text{AM1.5G}}(\theta, \bar{\varphi})$ of the corresponding device.

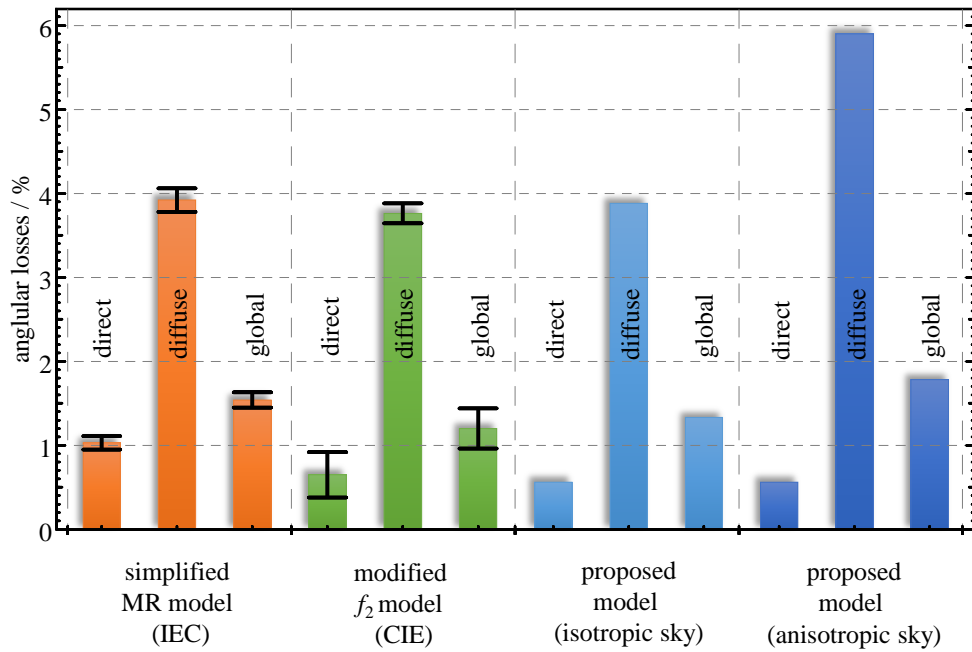


Figure 5.8: Angular losses for the encapsulated reference solar cell under global horizontal irradiance with $\theta_{\text{SZA}} = 50^\circ$. Direct and diffuse angular losses are determined by using three different models (a simplified MR model (IEC), a modified f_2 model (based on CIE), and the model proposed in this work). Additionally, to the results shown for isotropic sky radiance conditions, angular losses are presented using an anisotropic sky radiance situation simulated with libRadtran.

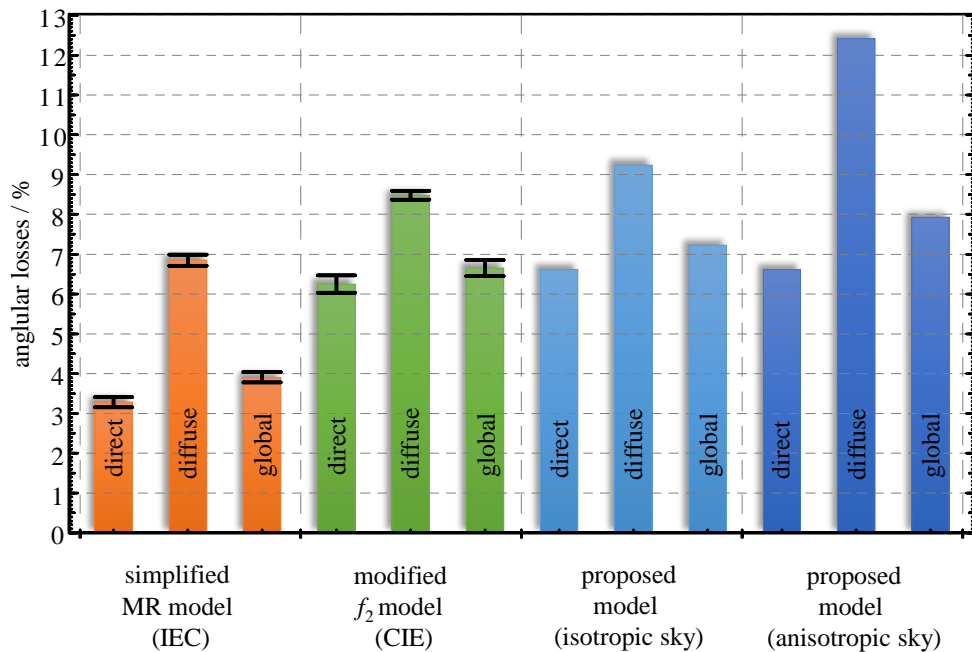


Figure 5.9: Angular losses for the IR-filtered reference solar cell under global horizontal irradiance with $\theta_{\text{SZA}} = 50^\circ$. Direct and diffuse angular losses were determined by using three different models (a simplified MR model (IEC), a modified f_2 model (based on CIE), and the model proposed in this work). Additionally, to the results shown for isotropic sky radiance conditions, angular losses are presented using an anisotropic sky radiance situation simulated with libRadtran.

The assigned expanded uncertainties, indicated as error bars, are determined by averaging over the variation of their angular-dependent responsivity for seven measured azimuthal orientations. The angular losses are then compared with results obtained by the proposed model. For reasons of comparability, the angular losses are determined initially with the assumption on an isotropic sky radiance condition shown as light blue bars in Figures 5.8 and 5.9. Secondly, the angular losses, shown in dark blue, are determined under the anisotropic global horizontal radiance conditions simulated with libRadtran. Both cases, using the proposed model consider asymmetric angular-dependent responsivity $s_{AM1.5G}(\theta, \varphi)$ without averaging over the azimuthal orientation of the devices. This is the reason for the missing errorbars at the results indicated for the proposed model shown in Figures 5.8 and 5.9 as blue bars. The encapsulated devices angular losses contributed by the direct irradiance under an angle of incidence of 50° are calculated by using a cubic spline interpolation, which is used by the proposed model and the modified f_2 model (based on CIE). Their differences of lower than 0.1 % are in agreement within the expanded uncertainty determined by averaging over the azimuth (see Figure 5.8). The angular loss assigned to the direct irradiance determined with the MR model results in a larger disagreement between the two other approaches. Obviously, the reason can be found in the procedure on the determination of a single angular loss coefficient a_r . The relationship described by Equation (2.21) is not in agreement with the experimental results (see Figure 5.5). The analysis of the results reveals, that expanded uncertainties of the direct irradiance losses obtained using Equation (2.22) are significantly smaller than those obtained by the cubic spline interpolation used by the modified f_2 model (based on CIE).

The encapsulated devices' angular losses assigned to the diffuse irradiance assuming an isotropic diffuse radiance are in close range for all models used in this comparison in Figure 5.8. It becomes apparent, that the calculated angular losses are approximately 2 % higher using the proposed model and when an anisotropic diffuse radiance is assumed. The reason here is, that the dominant radiance contribution originates from larger angles of incidence on the solar cells surface at those angles where higher losses are determined experimentally.

The global angular losses determined by the f_2 model and the proposed model using an isotropic approach agree within the expanded uncertainty of the azimuthal variation. However, the global angular losses obtained by using the simplified MR model (IEC) and the anisotropic version of the model proposed in this work are significantly higher for the reasons discussed before.

The results presented in Figure 5.9 provide larger differences in the calculated angular losses of the IR-filtered device. The angular losses assigned to the direct irradiance provide differences of more than 3 % between the simplified MR model (IEC) and the proposed model. The results obtained using the modified f_2 approach (based on CIE) and the proposed model are in close range with a difference of only 0.36 %, which is slightly larger than the expanded uncertainty of 0.22 % due to azimuthal averaging.

Another disagreement can be observed for the angular losses assigned to the diffuse irradiance shown in Figure 5.9. The modified f_2 model (based on CIE) results in a loss value which is more than 1.6 % higher than this obtained with the simplified MR model (IEC). The

results obtained with the proposed model assuming an isotropic diffuse radiance show a value which is 2.4 % larger than this obtained with the simplified MR model (IEC). The highest difference is apparent between the anisotropic novel approach and the simplified MR model (IEC). In this case, the angular loss difference is larger than 5.5 %. Thus, the angular loss assigned to the global irradiance determined with the proposed model and under anisotropic diffuse radiance (dark blue bars) is double than the value determined with the simplified MR model (IEC). The difference between the global angular losses obtained with the modified f_2 model (based on CIE) shown in green bars and the proposed model assuming isotropic diffuse radiance shown in light blue bars is rather low with less than 0.6 %.

5.2.4. Discussion on measurement uncertainties

In this subsection, the most important contributions to the measurement uncertainty of angular losses are discussed. The diversity of the investigated methods reveals distinct differences, originating partly from the approach and partly from some of the assumptions, so that a discussion on the dominant contributions to the uncertainty of angular losses depicts a larger benefit than the derivation of a comprehensive uncertainty budget in tabular form. Consequently, this part of the work does not include a complete measurement uncertainty analysis in accordance with the “Guide to the Expression of Uncertainty in Measurement” (JCGM 100, 2008). At this stage, it is more reasonable to localize systematic deviations, which can make up 100 % of the angular loss value itself. Furthermore, an uncertainty budget would only represent a specific exemplary scenario, so that the conclusions cannot be drawn for a general case. The discussion treats the most important effects leading to different results and shows their order of magnitude:

1. *Mathematical methods* leading to a lack of information and thus to systematic deviations
 2. *Simplifications* on the modeling equation, that cannot properly reflect reasonable physical conditions and properties
 3. Impact of the *angular resolution* selected for the computation of angular losses
 4. Impact of the *interpolation procedure* selected for the computation of angular losses with an appropriate angular resolution
 5. *Polarization* of the incident irradiation and its possible effect on the measurement uncertainty
 6. *Measurement uncertainty* $u(s(\theta))$ of the measured angular-dependent responsivity datasets propagating through the angular loss models
-
1. The experimentally determined characteristics of the angular-dependent responsivity of the encapsulated reference device are not properly represented by Equation (2.21), which describes an angular transmission function by using only one coefficient. Figure 5.5 shows the measured angular transmission and the angular transmission

represented by the a_r coefficient determined for the encapsulated device. Angular losses assigned to the direct irradiance are directly derived for both values. At an angle of incidence of $\theta_{SZA} = 50^\circ$, the function expressed by the angular loss coefficient a_r , which is determined using the Levenberg-Marquardt algorithm overestimates the angular loss by almost a factor of two compared to the measured value, although the coefficient of determination $R^2 = 1.000$. Thus, R^2 should be evaluated with special care, when rating the appropriateness of the approach. Even if a_r would match the angular transmission at values below one accurately, it is not able to describe values larger than one, which follow a “super cosine” with AOI. The derived functions shown in Figure 5.6 show also, that an over- or underestimation of the angular losses cannot be assigned to a systematic shortcoming in the simplified MR approach itself. Moreover, the deviations are dependent on the individual device characteristics. Thus, the angular loss of the direct irradiance at $\theta_{SZA} = 50^\circ$ determined with the MR model is underestimated for the IR-filtered device and overestimated for the encapsulated device.

2. The first simplification that takes effect on angular losses is the azimuthal averaging of the angular-dependent responsivity. This simplification can be appropriate for calculations of angular losses of the diffuse radiance in case if an isotropic diffuse radiance is apparent, but it is not suitable for the accurate determination of angular losses of the direct irradiance. The angular-dependent responsivity can vary significantly with the solar azimuth angle φ_{SAA} . The examples shown in Figure 5.8 and Figure 5.9 indicate systematic deviations in the angular losses assigned to the direct irradiance of approximately 0.1 % and 0.3 % (compare the green bars with the light blue bars indicating the angular losses for the direct irradiance), when using an azimuthal average angular responsivity instead of the individually measured responsivity at the position of the sun. This deviation can be significantly larger for devices with exceeding asymmetric angular-dependent responsivity which is shown as an example in Figure 4.10 for the non-encapsulated device.

The azimuthal average of the device characteristic is additionally smoothing the irradiation properties in case of an anisotropic diffuse radiance. Particularly the diffuse circumsolar radiance can be apparent at a distinct azimuth region. Thus, systematic deviations of angular losses assigned to the diffuse radiance can be also apparent when neglecting azimuthal asymmetry of the PV device’s angular-dependent responsivity.

The second simplification includes the assumption of an isotropic diffuse radiance. This is applicable for overcast skies, where no direct irradiance is apparent, and a horizontal PV device orientation without objects located at the horizon. But for situations reflecting realistic clear skies or broken clouds and site locations with PV device orientations towards the horizon, the assumption on an isotropic diffuse radiance leads to systematic deviations of the angular losses, compared to those determined by using an anisotropic model.

Differences of more than 2 % for the encapsulated device and more than 5.5 % for the IR-filtered device are observed.

Note that the original MR model is capable to consider the contribution of a ground reflected radiance separately to compute angular losses for tilted devices (Martin & Ruiz, 2001; 2002). The model developed in N. Martin's PhD thesis offers also a possibility to model a separate region describing a horizon brightening of the sky radiance (Martin, 1999). Both possibilities reflect meaningful simplifications of realistic conditions, by a discretization of the anisotropic diffuse radiance and thus, they should deserve consideration in a follow up comparison, which is out of scope in this work. However, in the proposed energy rating standard represented by the IEC 61853 series (IEC 61853-1, 2011; IEC 61853-2, 2016; IEC 61853-3, 2018; IEC 61853-4, 2018), the procedure developed in Martin's thesis is further simplified, most probably to ease the applicability for a broad range of users by making a major tradeoff in the accuracy.

3. A sensitivity analysis on the calculation of $f_{2,loss,diff}$ is performed here including different angular resolutions for the cubic spline interpolation. The comparison presented in Figure 5.10 includes two different cases shown as a difference to those diffuse angular losses computed at an angular resolution of 5° . The differences of angular losses determined for the encapsulated device are shown as orange bars, while those determined for the IR-filtered device are shown as green bars. It turns out, that a higher resolution selected for the procedure, results in an increase of $f_{2,loss,diff}$ for both examined cases. A large difference can be observed for the change from 5° to 2.5° resolution. A systematic deviation of almost 0.05 % is present. When increasing the angular resolution further to a step width of 1° , the deviation to the situation with 2.5° is in the lower range of 10^{-4} . A further increase of the angular resolution provides a change of the deviation in the region of 10^{-5} or lower. This leads to the conclusion, that an angular resolution of 1° would meet the requirements of a reasonable accuracy as a tradeoff with the computational effort.

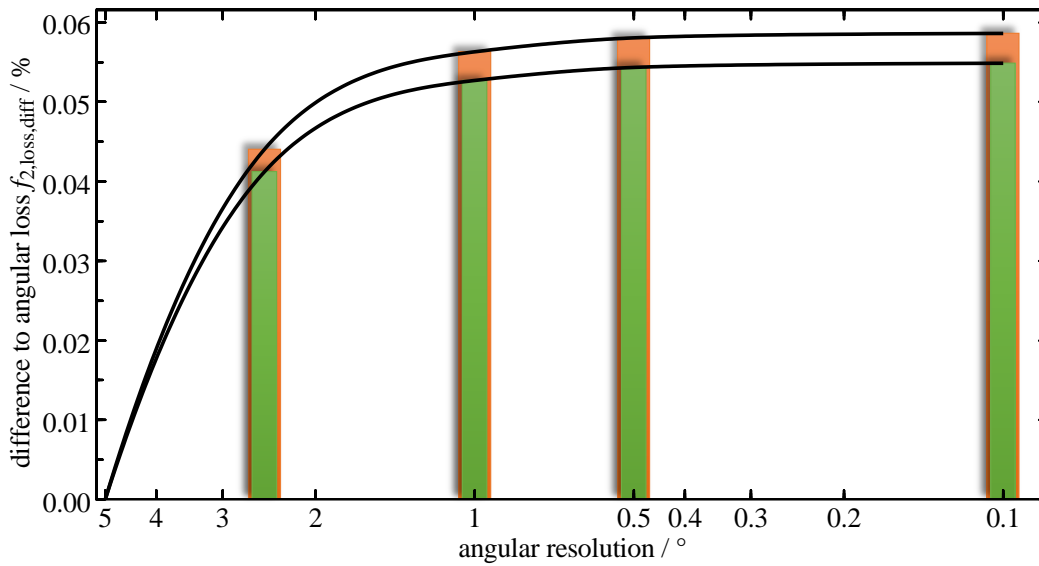


Figure 5.10: Sensitivity analysis of the impact of the selected angular resolution. The orange bars show the impact on the change of the angular resolution on the diffuse angular loss of the encapsulated device. The green bars show the corresponding impact on the diffuse angular loss for the IR-filtered device. All values are shown as differences to the angular losses assigned to an isotropic diffuse radiance determined with the modified f_2 model (based on CIE) using the measured 5° angular resolution.

4. When the measured datasets are interpolated onto an appropriate resolution, a detailed view onto the interpolation procedure is essential for the understanding of systematic deviations in the interpolated data, that are not directly linked with the measurement procedure. Therefore, two interpolation procedures are compared, to investigate the influence onto the calculation of $f_{2,loss,diff}$ and $f_{2,loss,dir}$ of a non-encapsulated device.

Figure 5.11 shows the azimuthal averaged deviation in the directional response $f_2(\theta)$, derived from the individually measured datasets indicated as blue diamonds. The measured angular-dependent responsivity dataset is interpolated onto a high-resolution grid with a step width of 0.1° . The deviation in the directional response is determined subsequently. The resulting functions are shown in Figure 5.11 indicated as green and orange colored lines for the cubic spline and the linear interpolation, respectively. Because no measurements were performed at angles of incidence $>85^\circ$, the values of the linear interpolation are replaced by a nearest neighbor approach. The deviation in the directional response $f_2(\theta = 90^\circ)$ is difficult to define and thus, a value of -1 is chosen for both procedures. A grey shaded area shows the most dominant differences between both approaches. Consequently, both interpolation methods lead to different angular loss values assigned to both, the direct irradiance and to the diffuse radiance. For the specific example of the non-encapsulated device, the cubic spline interpolation method overshoots at angles of incidence larger than 85° , resulting in a deviation of less than -1. A $f_2(\theta)$ value of lower than -1 is technically impossible, because it presumes a negative responsivity.

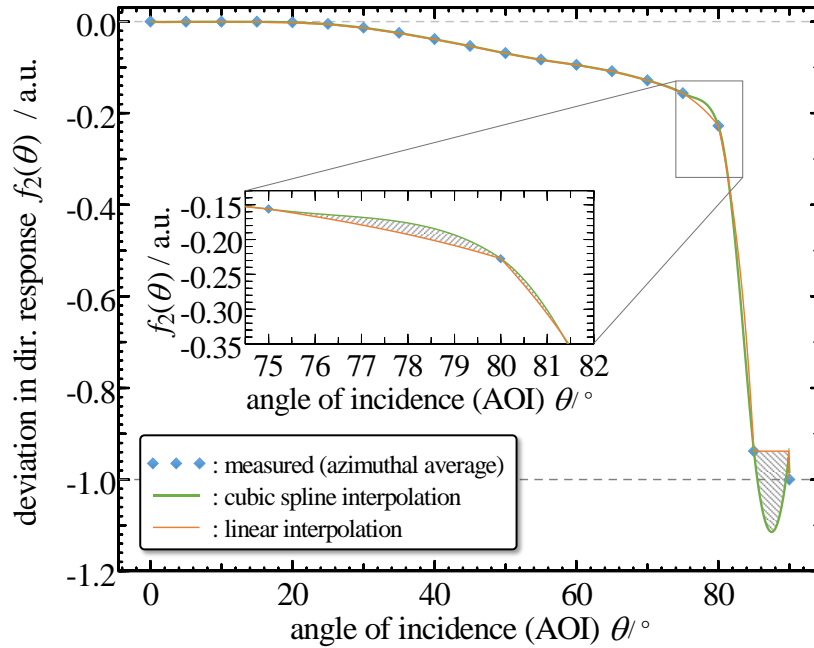


Figure 5.11: Comparison of two different interpolation methods selected to interpolate the measured angular-dependent responsivities onto a high angular resolution. This example shows the deviations in the directional response of a non-encapsulated solar cell. Both interpolation methods are applied on the angular-dependent responsivity dataset measured with an angular resolution of 5° . Their deviation in the directional response is indicated as blue diamonds. The cubic spline interpolation is shown as a green line, while the linear interpolation is shown as orange line. Grey shaded areas show the regions with the most dominant deviations between the two interpolation methods. Because no measurements were performed at angles of incidence larger than 85° , the values of the linear interpolation are performed using a nearest neighbor approach.

Nevertheless, when the curve determined by cubic spline interpolation is used for the computation of the angular loss, the resulting $f_{2,\text{loss,diff}}$ is 0.06 % smaller compared to the case where the linear interpolation method is used. This rather low difference occurs, because the two dominant differing regions between angles of incidence from 75° to 80° and from 85° to 90° counterbalance each other. If the diffuse radiance distribution is assumed to be anisotropic, they would balance another way, resulting in a larger difference of $f_{2,\text{loss,diff}}$. When comparing the direct contributions to the angular loss at an exemplary angle of incidence of $\theta_{\text{SZA}} = 78^\circ$, the $f_{2,\text{loss,dir}}$ is 1.64 % larger when using the linear interpolation method instead of the cubic spline interpolation.

5. The experimental characterization of solar cells angular-dependent spectral responsivity in Chapter 4 shows that polarization dependencies are apparent. All previous calculations to obtain spectral and angular losses or spectral-angular mismatch correction factors are based on datasets that assume unpolarized incident irradiation. That means the average responsivity value between both measured polarization states is used. Figure 4.21 already shows an example on the maximum effect of polarization onto the angular-dependent spectral responsivity for a single wavelength and at a specific azimuth angle φ . To study the impact of angular losses due

to polarized or partly polarized incident diffuse radiance, a simple sensitivity analysis is presented. It includes a first estimation of the impact on the calculated angular losses of an encapsulated WPVS reference solar cell at two selected wavelengths, 450 nm and 1100 nm, determined with the modified f_2 model (based on CIE) using $f_{2,loss,diff}$.

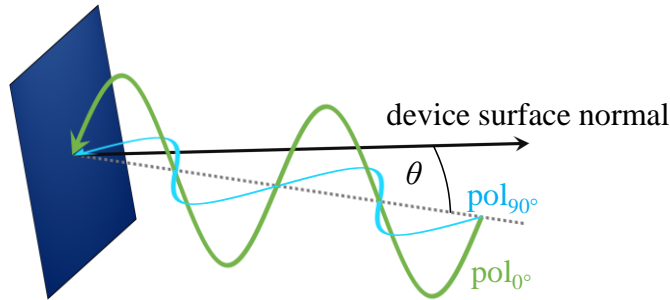


Figure 5.12: Schematic of linear polarized photons with a defined wavelength at a given angle of incidence θ related to the device's surface normal. The green colored wave illustrates photons, which provide a polarization state of 0° and the blue colored wave indicate those photons with a 90° polarization state.

Figure 5.12 shows an exemplary schematic illustration of the linear polarization of incident photons onto an inclined solar cell surface. In the following example, angular losses are determined for one specific azimuthal orientation φ of the diffuse incident radiance, which is assumed to be isotropic and polarized. A ratio between the amount of 0° polarized radiance, pol_{0° , and 90° polarized radiance, pol_{90° , is used to show the difference of losses due to polarization:

$$\Delta f_{2,loss,diff}(\lambda) = \left(pol_{0^\circ} \cdot f_{2,loss,diff,0^\circ}(\lambda) + pol_{90^\circ} \cdot f_{2,loss,diff,90^\circ}(\lambda) \right) - f_{2,loss,diff,unpol}(\lambda) \quad (5.8)$$

with $pol_{0^\circ} + pol_{90^\circ} = 1$

The resulting differences $\Delta f_{2,loss,diff}$ are plotted in Figure 5.13 as a function of the ratio representing the amount of 0° polarization for each of the exemplary wavelengths. The difference at 50 % amount of 0° polarization represents the case for unpolarized light. For other ratios, it shows a strong wavelength dependency and differences of up to 2 % in the angular loss assigned to the diffuse radiance at 450 nm (black line with blue shaded area). This sensitivity analysis represents specific irradiation conditions to estimate a maximum impact of polarization onto the angular losses. For realistic conditions, polarization dependencies usually remain unconsidered and may provide a more complex spatial distribution due to Rayleigh scattering in the Earth's atmosphere.

Based on this simple sensitivity analysis, a first estimate of the impact of polarized sky radiance on typical global angular losses, including the angular loss assigned to the direct irradiance, is in the range of approximately 10^{-4} and thus considered to be negligible for the most scenarios in this study.

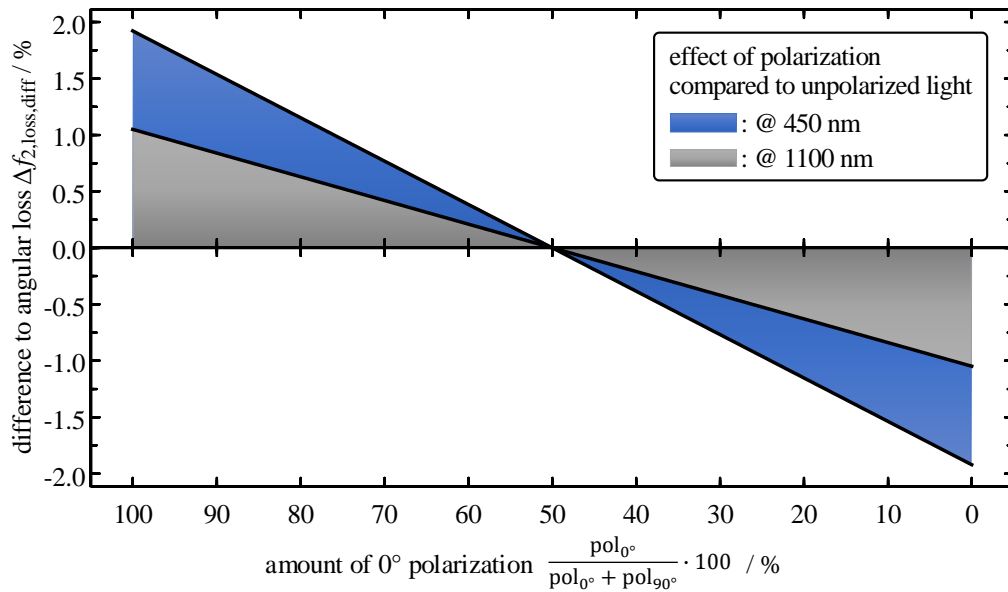


Figure 5.13: Polarization dependent difference of the encapsulated WPVS reference devices angular loss $\Delta f_{2,\text{loss,diff}}$ for two selected wavelengths. The black line enveloping the blue shaded area indicates the differences at 450 nm, while the black line enveloping the grey shaded area shows the effect at a wavelength of 1100 nm.

6. The propagation of measurement uncertainties assigned to the angular-dependent responsivity measurement procedure presented in Chapter 4 is performed by using a Monte Carlo method. This study demonstrates the impact on angular losses measurement uncertainty when using the modified f_2 model (based on CIE) and the simplified MR model (IEC). Correlated input quantities related to uncertainties of the non-linearity of the electrical current measurement, the angular non-uniformity of the rotation volume, the thickness of the solar cell and an alignment offset of the AOI θ to the optical axis are considered in this analysis. All other contributions to the uncertainty described in Section 4.2 are treated as uncorrelated input quantities. The global angular loss of the encapsulated device under the global horizontal conditions used in Subsection 5.2.3 is $1.20 \% \pm 0.02 \%$ with an assigned expanded uncertainty U ($k=2$) determined by using the modified f_2 model (based on CIE). The global angular loss determined with the simplified MR model (IEC) results in $1.543 \% \pm 0.007 \%$.

It becomes apparent, that the value of the uncertainty is dependent from the model which is used, with the consequence, that the uncertainties of the global angular loss calculated with the simplified MR model (IEC) is three times smaller than this determined with the modified f_2 model (based on CIE). The angular loss coefficient a_r , used by the simplified MR model is insufficient to propagate measurement uncertainties related to the experimental procedure appropriately through the angular loss model. In conclusion, mathematical errors of the fitting procedure should be considered when determining measurement uncertainties of angular losses in combination with the simplified MR model proposed in the IEC standard for PV energy rating (IEC 61853-3, 2018). Therefore, the author suggests examining the residuals between the angular

transmission function $\tau(\theta)$ described by the coefficient a_r and the actual measured values to estimate the uncertainty of the fitting procedure.

5.2.5. Summary

A comparison of three different approaches for the computation of angular losses of two different types of WPVS reference solar cells highlights, that differences in the calculated global angular loss can be in the range of the angular loss itself. The losses determined with the simplified MR model proposed by the energy rating standard IEC 61853 series provide the largest differences compared to the modified f_2 model (based on CIE) and the proposed model, assuming an isotropic diffuse radiance, while the latter two models are in better agreement. A sensitivity analysis was performed to determine systematic deviations contributing to the uncertainty of the angular loss. Assumptions and simplifications made for different models are discussed to bring their contributions to uncertainty into relation to the measurement uncertainties originating from the experimental setup and the calculation procedure. The use of a Levenberg-Marquardt fitting algorithm together with the simplified MR model results in deviations of the global angular loss of the encapsulated WPVS solar cell compared to the original measured values in the range of 10^{-3} related to the solar cells short-circuit current output. The comparison emphasizes that the largest difference in the angular losses arises between the isotropic and anisotropic approaches. The anisotropic approach considers two effects as superposition, azimuthal asymmetry of the solar cell and the diffuse radiance's anisotropy. The analysis revealed differences of up to one percent in case of the encapsulated WPVS solar cell and differences of several percent for the IR-filtered solar cell arising from the simplifications made regarding the azimuthal symmetry and the sky radiance's isotropy.

A variation of the angular resolution in the modified f_2 model (based on CIE) used for the determination of angular losses exposed systematic effects contributing to the total uncertainty of the global angular losses in the range of 10^{-5} related to the solar cells total current output under global horizontal sunlight, when reducing the step width from 5° to 1° .

A simple comparison of different polarization conditions of the incident diffuse spectral radiance onto the encapsulated device revealed differences of up to 2 %, compared to unpolarized incident radiance. In relation to the global angular loss of a solar cells total short-circuit current output under global horizontal sunlight, a maximum effect in the range of 10^{-4} is estimated for the investigated example.

An investigation on how the measurement uncertainty of the angular-dependent spectral responsivity $u(s(\theta))$ propagates through the state-of-the-art angular loss models was performed. It turns out that their contribution to the uncertainty of the global angular loss is in the range of 10^{-4} and 10^{-5} for the modified f_2 model (based on CIE) and the simplified MR model (IEC), respectively. Compared to the total differences between the models arising from the previously discussed assumptions and simplifications, which represent the dominant limitations, this measurement uncertainty is rather insignificant.

5.3. Effect of diurnal variations of the irradiation conditions on the spectral-angular mismatch

The last section of this chapter includes a study on the diurnal variation of the irradiation conditions for an ideal clear sky day at the first equinox of the year: March the 20th of 2017. This parameter variation is focused on the impact of diurnal changes on the spectral and spectral-angular losses of the three previously investigated reference solar cells compared to an ideal pyranometer. An ideal pyranometer implies that this irradiance sensor would have an angular-dependent responsivity following the cosine of the AOI θ and that the instrument provides azimuthal symmetry. Additionally, an ideal pyranometer is not spectrally selective. The losses are calculated for a single day in accordance with the energy rating standard (IEC 61853-3, 2018) but using timesteps of 20 minutes instead of 60 minutes intervals. To emphasize the differences between the alternative models used for the computation of spectral-angular losses, the results obtained by using the IEC procedure are compared with the modified f_2 model (based on CIE) applied before in the previous section and the novel metric developed in this work.

The simulation of the irradiation conditions of this idealized scenario is performed using libRadtran with input parameters as described in Chapter 3 and contains a fixed device installation located at the ground level of PTB's site in Braunschweig (coordinates: N 52.291923°; E 10.460539°). The devices studied here provide an orientation of $\theta' = 37^\circ$ tilted towards the south ($\varphi' = 180^\circ$) and a spectral ground albedo of light soil is assumed (see Figure 5.14).

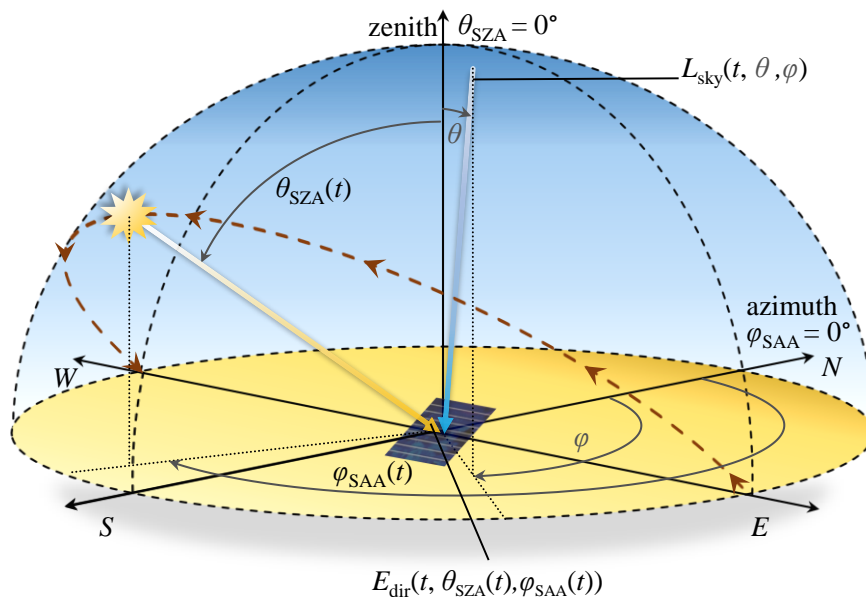


Figure 5.14: Angle of incidence dependence of the solar irradiation inclined on a tilted PV device. The dashed brown curve shows the diurnal variation of the solar position, and accordingly, the varying direct irradiance. Changes in the sky radiance L_{sky} and the varying spectrum are not shown in this schematic for reasons of clarity.

The resulting simulated spectral radiances and direct spectral irradiances include 36 different datasets from dawn till dusk of this day at approximately 05:40 (5:40 a.m.) and 17:20 (5:20 p.m.). Both times are in Coordinated Universal Time (UTC) format.

For using these multidimensional datasets with the state-of-the-art models, the global in-plane irradiances E_{glo} and spectral irradiances $E_{\lambda,\text{glo}}(\lambda)$ are derived within the investigated wavelength range from 300 nm – 1200 nm. The following subsection treats the variation of the global spectral irradiance independent from the solar cell technology, and in a second subsection, the technology-dependent spectral-angular irradiance losses for three different WPVS solar cells are investigated. Then a discussion on the differences found between the calculation approaches is presented with focus on assumptions and simplifications made by these models. Finally, the impact of spectral and angular losses on the available solar energy for that day is shown and discussed. A summary concludes this section that is dedicated to the thematic context of PV module energy rating.

5.3.1. Variation of the global spectral irradiance

The simulation of the global spectral irradiance is described in Sections 3.3 and 3.5. For each calculated timestep till noon, the global spectral irradiance onto the tilted device surface (in-plane) is shown in Figure 5.15, top. The diagram clearly shows the dependence of the solar spectrum to the time of the day and thus to the airmass AM decreasing till noon. In Figure 5.15, bottom, the relative change of the normalized spectrum is displayed qualitatively as a color contour. It shows a spectral shift from lower photon energies (orange color) to higher photon energies on average (purple color).

To obtain a more quantitative value of the diurnal change in the composition of the spectrum, the average photon energy parameter APE (see Section 2.1) is used as function of the time of the day. Note that the APE value usually includes the complete spectral range from zero to infinity wavelength. Because the spectra are simulated only for a specific wavelength region, the APE parameter is computed in accordance with Equation (2.2), but with limited integral limits ranging from 300 nm to 1200 nm. Figure 5.16 indicates an increase of the $APE_{300-1200\text{ nm}}(t)$ value with a maximum at the local solar noon. During dawn and dusk (before 06:00 and after 17:00 o'clock UTC) the APE value strongly increases because the direct irradiance follows the cosine of the angle of incidence of the direct sunlight inclined on the devices surface. Even if the direct sunlight has a rather red spectrum at dawn and dusk, the absolute direct irradiance approaches zero; and with that the more bluish diffuse irradiance of the sky dominates the APE parameter. The APE of the AM1.5G reference spectrum that is given in (IEC 60904-3 Edition 2, 2008) is illustrated as a grey line in Figure 5.16. The $APE_{300-1200\text{ nm}}(t)$ function of the simulated spectra approaches the $APE_{300-1200\text{ nm}}(\text{AM1.5G})$ very close between 10:00 and 13:00 o'clock UTC. Therefore, a spectral mismatch or spectral loss minimum for PV devices can be expected within this interval compared to reference conditions.

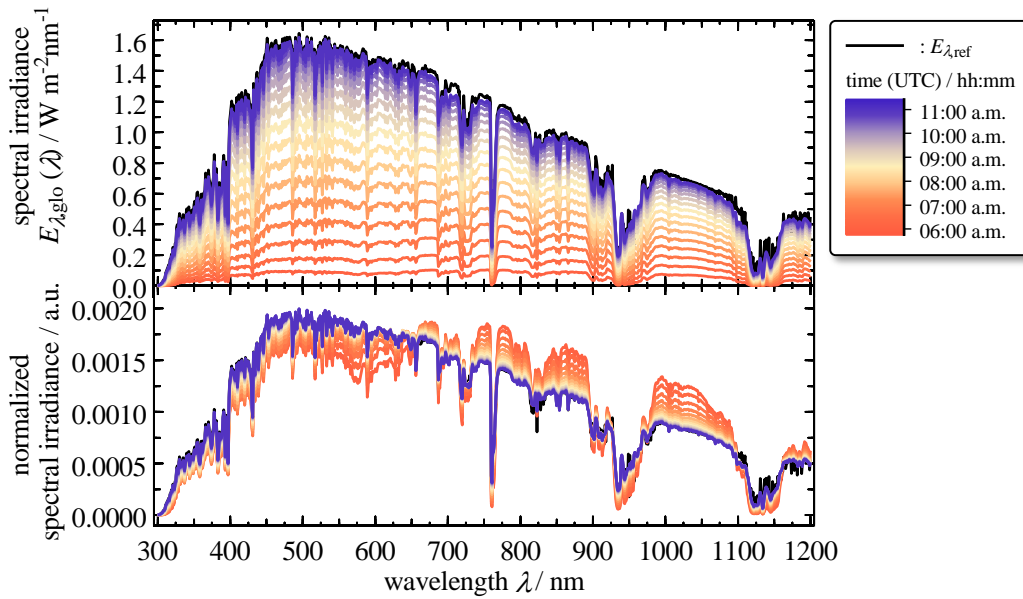


Figure 5.15: Diurnal variation of the global in-plane spectral irradiance $E_{\lambda, \text{glo}}(\lambda)$ calculated using libRadtran. The set of colored curves visualizes the change of the spectral irradiance from dawn till noon of March 20th, 2017 (first equinox of the year). The different spectra are representing a scenario under clear sky conditions and show the spectral irradiance within an interval of 20 minutes inclined on a $\theta^\circ = 37^\circ$ tilted surface towards the south. The top graph shows the spectral irradiances on absolute scale, while the bottom graph displays the normalized spectra with focus on the relative change. The values are normalized to the individual broadband irradiance E_{glo} within 300 nm to 1200 nm. The black curve represents the reference spectral irradiance $E_{\lambda, \text{ref}}(\lambda)$. For reasons of clarity the spectra from noon till dusk are not displayed.

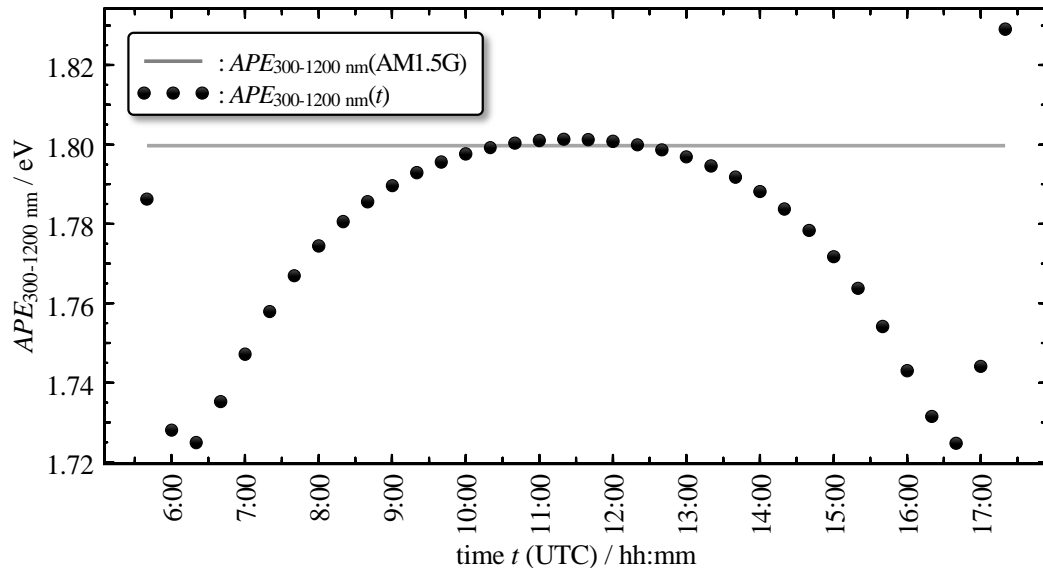


Figure 5.16: Average photon energy $APE_{300-1200 \text{ nm}}$ within a wavelength range from 300 nm - 1200 nm as a function of the time of the day on March 20th, 2017 (black circles). The grey line shows the $APE_{300-1200 \text{ nm}}$ value of the AM1.5G reference spectral irradiance within the same wavelength range.

5.3.2. Calculation of spectral and spectral-angular losses

While the *APE* value is a device and technology independent measure that indicates when a spectral loss or mismatch occurs, it is additionally important to quantify the spectral loss itself for individual devices. Hence, this subsection focuses on the calculation of the diurnal change of the spectral correction factor $C_S(t)$ based on the procedure proposed by the IEC standard (IEC 61853-3, 2018). The procedure corrects for angular losses first to obtain an effective irradiance onto the device before the spectral correction factor C_S is determined. To emphasize the importance of the correct order in the application of the calculation of the two different loss mechanisms (due to spectral and angular effects), the spectral correction factors $C_S(t)$ are additionally calculated without a prior AOI correction. This uncorrected spectral correction factor is labeled as $C_{S, \text{without AOI correction}}(t)$ and is calculated in accordance with the following equation:

$$C_{S, \text{without AOI correction}}(t) = \frac{\int_{300 \text{ nm}}^{1200 \text{ nm}} E_{\lambda, \text{ref}}(\lambda) d\lambda \int_{300 \text{ nm}}^{1200 \text{ nm}} s(\lambda) \cdot E_{\lambda, \text{glo}}(\lambda, t) d\lambda}{\int_{300 \text{ nm}}^{1200 \text{ nm}} E_{\lambda, \text{glo}}(\lambda, t) d\lambda \int_{300 \text{ nm}}^{1200 \text{ nm}} s(\lambda) \cdot E_{\lambda, \text{ref}}(\lambda) d\lambda} \quad (5.9)$$

Again, the angular loss determination for both, the modified f_2 model (based on CIE) and the simplified MR model (IEC), is based on angular-dependent responsivity datasets which are converted from spectrally resolved to AM1.5G-weighted broadband datasets. The conversion is applied for each of the seven measured azimuthal orientations to obtain an average angular-dependent responsivity. Figure 5.17 shows the differently obtained spectral correction factors for two different WPVS reference solar cells as a function of the time of the day. The resulting C_S factors obtained for the encapsulated device are shown in the top diagram with blue curves and those obtained for the IR-filtered device are shown in the bottom diagram with red curves. The triangles pointing downwards connected by dashed lines represent the spectral correction factors $C_S(t)$ using the IEC models AOI correction. Because the diffuse and direct spectral irradiances, $E_{\lambda, \text{diff}}(\lambda)$, and $E_{\lambda, \text{dir}}(\lambda)$, are included separately for each time step in the simulated libRadtran datasets, an individual AOI correction is applied for each spectrum to obtain the global AOI corrected effective in-plane spectral irradiance:

$$E_{\lambda, \text{glo, corr, AOI}}(\lambda, t) = E_{\lambda, \text{diff, corr, AOI}}(\lambda, t) + E_{\lambda, \text{dir, corr, AOI}}(\lambda, t) \quad (5.10)$$

The calculated $C_S(t)$ curves which include a prior AOI correction using the modified f_2 model (based on CIE) are indicated as upward pointing triangles connected by dotted lines in Figure 5.17. Again, they are obtained by using Equation (5.10) and Equation (2.26). The circles, connected by continues lines, represent the factors $C_{S, \text{without AOI correction}}(t)$ which are not including a correction of an effective in-plane irradiance onto the individual PV device.

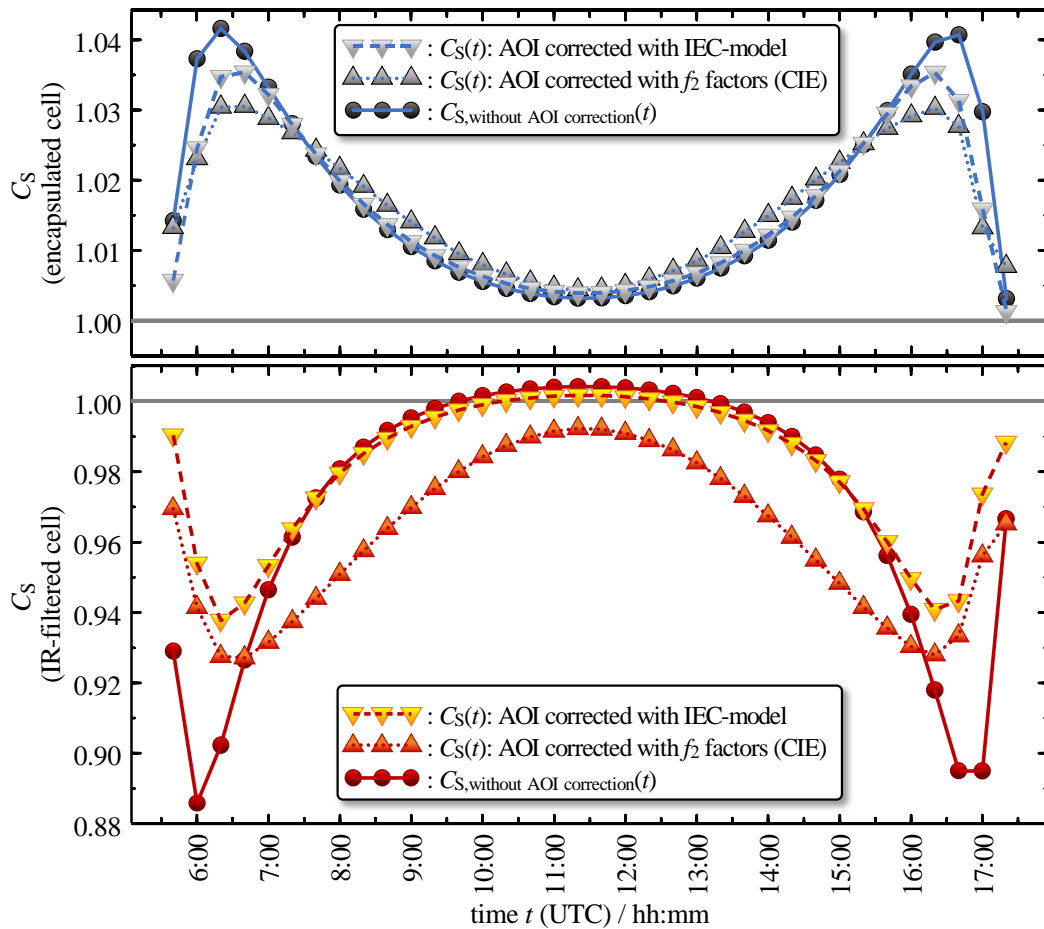


Figure 5.17: Spectral correction factors of two different WPVS solar cells as a function of the time of the day on March 20th, 2017. The top diagram with blue curves includes spectral correction factors for the encapsulated reference device, the bottom diagram includes red curves showing these factors for the IR-filtered device. Three differently obtained spectral correction factors are calculated: The triangles pointing downwards (connected by dashed lines) indicate C_s factors which include a prior AOI correction of the diffuse and direct spectral irradiance using the IEC model; the triangles pointing upwards (connected by dotted lines) indicate C_s factors including a prior AOI correction by applying the modified f_2 model (based on CIE), and the circles (connected by continuous lines) indicate C_s factors without any AOI correction.

As discussed in Subsection 5.2.3, the simplified MR model (IEC) overestimates the angular losses of the encapsulated device and underestimates them for the IR-filtered device. For the encapsulated device, the difference between the $C_s(t)$ factors, obtained with the MR models AOI correction and those obtained with the modified f_2 models AOI correction, ranges from 0.2 % to 0.5 %. These differences increase for the IR-filtered device to values ranging from 1 % to 3 %, dependent on the time of the day. In comparison to the $C_{S, \text{without AOI correction}}(t)$ factors determined in accordance with Equation (5.9), the $C_s(t)$ factors obtained with the simplified MR models AOI correction provide interestingly low differences of their loss values in the time between 07:30 and 15:30 UTC.

Consequently, the deviations between the angular losses determined by the different AOI correction models have significant impact on the calculated spectral correction factor C_s .

This leads to the conclusion, that the simplified MR model proposed in the IEC standard (IEC 61853-3, 2018) should be revised to consider the relationship between the correction factors for spectral and angular losses and their uncertainties more accurately.

While the state-of-the-art procedures proposed in the IEC standard require a strict separation of the angle of incidence and the spectral effects for the calculation of the spectral-angular loss, the model proposed in this work allows to consider these quantities as coupled effects. In addition to that, the proposed model accounts for azimuth-dependent differences in the angular-dependent responsivity, which can have a significant impact on the calculation of angular losses. To compare the different models spectral-angular losses, they are calculated and investigated for three different solar cells under varying irradiation conditions (see Figures 5.18 and 5.19). Figure 5.18, top, indicates the diurnal variation of the global in-plane irradiance $E_{\text{glo}}(t)$ as yellow diamonds connected by a black line. For March the 20th, 2017, the total amount of available solar energy irradiating a surface in this specific orientation is 5.698 kWh m⁻² under ideal clear-sky conditions.

The middle diagram in Figure 5.18 shows three differently obtained relative spectral-angular losses for an encapsulated WPVS solar cell. The orange-, blue- and green-colored bars indicate the values determined by using the modified f_2 model (based on CIE), the model proposed in this work and the IEC model, respectively. Figure 5.18 bottom displays the absolute irradiance losses due to spectral and angular effects in W m⁻². This has a more relevant informative value in terms of PV energy rating. For this encapsulated device, the absolute irradiance losses maxima of approximately 10 W m⁻² are apparent nearly one hour after sunrise and one hour before sunset. The absolute losses reveal that the values determined using the IEC model deviate mostly between 09:00 and 14:00 o'clock and show a definite overestimation of the loss compared to the modified f_2 model (based on CIE) and the model proposed in this work. The expanded uncertainties indicated as error bars of the datasets in the middle and bottom diagrams in Figure 5.18 show the impact of the azimuthal asymmetry. It considers the standard deviation of the losses determined for each azimuthal orientation individually. Note that these expanded uncertainties do not contain the individual uncertainty contributed by the experimental measurement setup. The goal of this analysis is to elaborate that systematic differences are originating from the procedures and assumptions used by the different models. No uncertainties are assigned to the datasets determined with the model proposed in this work, because it already considers the asymmetric shape of the measured angular-dependent responsivity datasets presented in Chapter 4.

Further analysis shows that most of the data determined with the proposed model and the modified f_2 model (based on CIE) is consistent within the expanded uncertainty contributed by azimuthal asymmetry. That is not the case for the data obtained by using the IEC model. It is considerable that the expanded uncertainty of the IEC model's data is much smaller than this of the data obtained with the modified f_2 model (based on CIE). This corresponds to the observation made in Subsection 5.2.3. The effect of azimuthal asymmetries is not properly reflected by means of the angular loss coefficient a_r used in the IEC model. Interestingly, during the course of the day the resulting losses show no obvious trend in their deviations

from each other. Moreover, single outliers can be found in the dataset obtained by using the model proposed in this work. Most likely, they can be attributed to the azimuthal asymmetry or to interpolation artefacts which are discussed in Subsection 5.2.4.

During the morning hours from 07:40 to 09:40 o'clock and in the afternoon from 12:40 to 14:40 o'clock the absolute irradiance losses of the encapsulated device due to spectral and angular effects provide negative values. This means that angular effects can be considered as an optical gain for the irradiation conditions at these times and that they overcompensate the impact due to the spectral effects investigated in Figure 5.17, top. The optical gain obviously originates from the "super cosine" effect that was previously observed for the encapsulated solar cell (see Figure 4.8, middle).

Figure 5.19 shows the spectral-angular losses similarly to Figure 5.18, but for the IR-filtered device (top diagram) and the non-encapsulated device (bottom diagram) determined by using the three discussed models. The irradiance losses for the IR-filtered device contain maxima between 07:00 and 08:00 o'clock and between 14:40 and 15:40 o'clock UTC. Dependent on the model used for the calculation, the maximum irradiance loss values due to spectral-angular effects for the investigated day deviate between 33 W m^{-2} and 48 W m^{-2} . The values calculated by using the modified f_2 model (based on CIE) show the largest deviations of up to 25 W m^{-2} compared to the values obtained by using the IEC model. With a few exceptions, the differently calculated spectral-angular losses of the IR-filtered device are not consistent within the expanded uncertainty contributed by the azimuthal asymmetry indicated as error bars. One reason of these strong deviation for the IR-filtered device is most likely attributed to the strong coupling of spectral- and angular-dependent responsivities, which are not considered by the state-of-the-art models (modified CIE and IEC model). A second reason of the strong deviation can be attributed to the assumption that the diffuse irradiance is isotropic, which is investigated and discussed in more detail in Subsection 5.1.5. Solely the model proposed in this work considers the anisotropic distribution of the diffuse irradiance, which can change considerably during the course of the day.

Deviations between the absolute irradiance losses determined by the modified f_2 (based on CIE) and the IEC models, both using an individual spectral correction factor, are also apparent for the non-encapsulated device (Figure 5.19, bottom). The values determined by using the model proposed by this work (blue circles) show a more dispersed distribution, which reflects the fact that this WPVS solar cell provides a distinct azimuthal asymmetry in its angular-dependent responsivity (see Figure 4.10). The state-of-the-art models' losses indicate a smoother and more symmetrical trend in their diurnal variation because they are smoothed by prior averaging of the measured data. The error bars assigned to the values obtained by the modified f_2 model (based on CIE) show large expanded uncertainties of up to $\pm 10 \text{ W m}^{-2}$, which reflects the large effect due to the azimuthal asymmetry of the non-encapsulated device. As observed before, this effect due to asymmetries is not reflected accurately by the uncertainties propagating through the simplified MR model (IEC). The uncertainties assigned to the values obtained with the IEC model provide maximum values of approximately $\pm 3 \text{ W m}^{-2}$. Interestingly, in the time close to solar noon (between 10:20 to

12:20 o'clock UTC) all the three approaches show the lowest deviations in their absolute irradiance losses determined in this study.

While the analysis of the irradiance losses based on data with high temporal resolution reveals a complex diversity of the different models for the loss computation and therewith details for single times of the day, it is worth to determine the energy losses for an entire day. Therefore, the integral values of the absolute energy losses are determined in kWh m⁻² from the data presented in Figures 5.18 and 5.19. Subsequently, they are set into relation to the available solar energy. The results obtained for the three different approaches are summarized in Table 5.6. The assigned expanded uncertainties are again used to express the impact of neglecting the azimuthal asymmetry in the angular-dependent responsivity data of the devices.

While the energy losses of the encapsulated device vary from 0.3 % to 0.6 %, they are larger for the IR-filtered device (4.12 % to 6.83 %) and the non-encapsulated device (2.05 % to 3.8 %). As previously observed the resulting energy loss of the encapsulated device determined with the IEC model is overestimated in comparison to the losses obtained with the modified f_2 model (based on CIE) and the model proposed in this work. The absolute difference of the value obtained using the IEC model to the values of the other models is with 0.3 % as large as the spectral and angular effects themselves. As expected, the energy loss of the IR-filtered solar cell is underestimated when the IEC model is used. Absolute differences of approximately 1.5 % to the model proposed in this work and an approximate difference of 2.7 % to the modified f_2 model are reported. Just as the results of the IR-filtered device, the energy loss of the non-encapsulated device is underestimated by the IEC model compared to the two other approaches. The absolute differences to the model proposed here is approximately 0.9 % and 1.8 % to the modified f_2 model (based on CIE). An expanded uncertainty of ± 0.26 % is assigned to the energy loss value determined by using the modified f_2 , which reflects the impact of the azimuthal symmetry assumption for this device better than the uncertainty of the IEC model does with a value of ± 0.04 %.

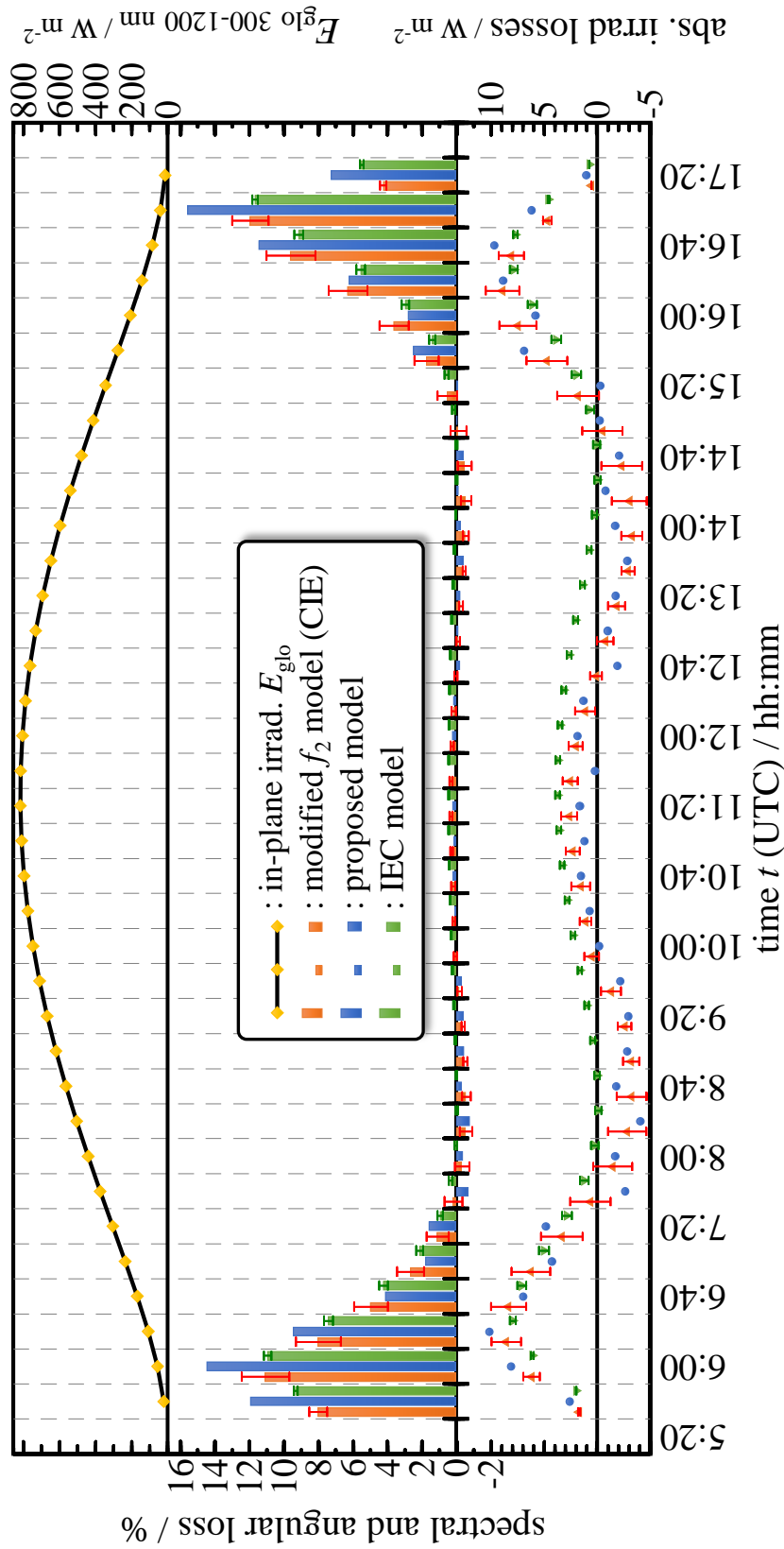


Figure 5.18: (Top) Diurnal variation of the global in-plane irradiance E_{glo} . (Middle) Relative spectral-angular loss of an encapsulated WPVS solar cell determined using three diverse models: The orange columns represent percentage values calculated using the modified f_2 model (based on CIE) to determine the angular losses, the blue columns represent percentage values calculated using the proposed model and the green columns represent percentage values calculated using the model proposed by the IEC standard 61853-3 (simplified MR model). (Bottom) Absolute irradiance losses in W m^{-2} for the encapsulated WPVS solar cell. The error bars in the middle and bottom diagram indicate the expanded uncertainty only due to azimuthal asymmetry, which are neglected when using the modified f_2 model (based on CIE) and the IEC model.

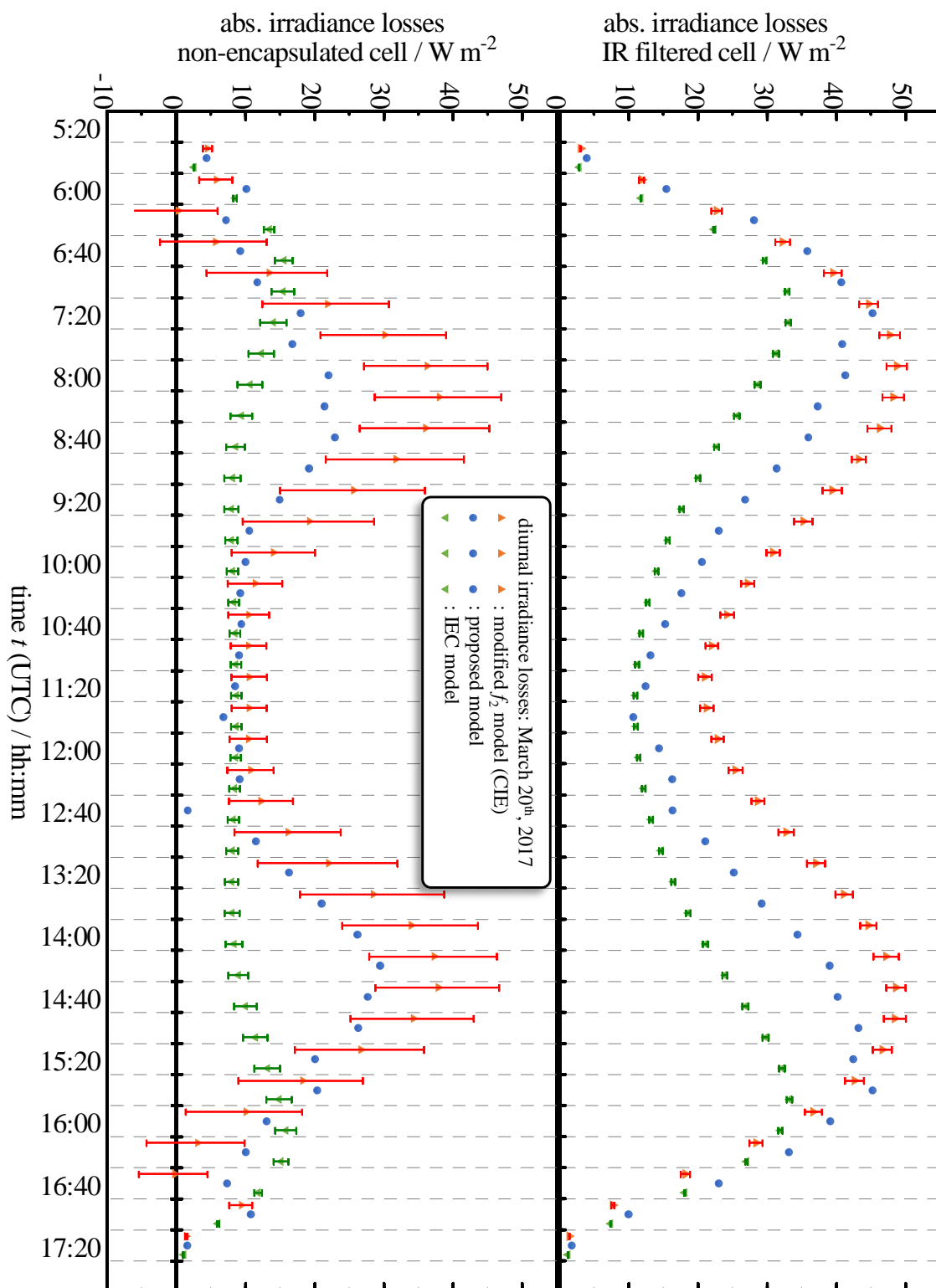


Figure 5.19: Spectral-angular irradiance losses in W m⁻² of an IR-filtered device (top) and a non-encapsulated device (bottom) calculated for March 20th, 2017 using three models.

Table 5.6: Average spectral-angular energy losses of three WPVS reference devices used as irradiance sensors compared to the case if the measurements are performed with an ideal pyranometer. Three different calculation approaches are compared under the simulated irradiation conditions for March 20th, 2017: The modified f_2 model, the model proposed in this work and the model proposed by the IEC energy rating standard 61853-3 (simplified MR model). The state-of-the-art models used here (modified CIE and IEC) are not considering azimuthal information on the devices' responsivities, therefore the standard deviation (given here as expanded uncertainty $k=2$) is calculated by determining the spectral-angular loss for each of the seven angular-dependent responsivities individually. The proposed model considers azimuthal resolved angular-dependent responsivities of the devices; therefore, no uncertainties are assigned.

PV device ↓	spectral-angular energy losses of reference solar cells compared to the available solar energy measured by an ideal pyranometer in % calculated with:		
	modified f_2 model (based on CIE) and spectral correction	proposed model	Simplified MR model and spectral correction (IEC)
encapsulated WPVS solar cell	0.33 % ± 0.05 %	0.30 %	0.60 % ± 0.01 %
IR-filtered WPVS solar cell	6.83 % ± 0.04 %	5.67 %	4.12% ± 0.01 %
non-encapsulated WPVS solar cell	3.80 % ± 0.26 %	2.94 %	2.05 ± 0.04 %

The results presented here don't show that one or another model follows a definite trend in their deviations. They show once again, that a general interpretation on the models' impact on the measurement uncertainty of the spectral-angular loss of the energy have to be made on case-by-case analysis'.

5.3.3. Summary and conclusion

While the first section of this chapter is focused on high-accuracy short-circuit current calibrations of PV devices under global sunlight with clear sky conditions, the second and third sections are focused on a study on spectral-angular losses for the determination of device-dependent effective irradiances. The state-of-the-art approaches investigated here - a simplified MR model (IEC), and a modified f_2 model (based on CIE) for the calculation of angular-dependent optical losses, which is essential for PV energy rating purposes - are studied in detail in the second section of this chapter. One exemplary clear sky irradiation condition on horizontally orientated devices and a defined Sun's position at $\theta_{SZA} = 50^\circ$ and $\varphi_{SAA} = 180^\circ$ is selected to perform parameter variations with focus on the uncertainties arising from assumptions and simplifications. In the third section, the irradiation conditions, dependent on the time of the day, are varied to study spectral and angular effects with focus on diurnal irradiance losses and average energy losses for an exemplary clear sky day.

First, the diurnal variation of the global in-plane spectral irradiance is presented within a wavelength range from 300 nm – 1200 nm to show the changes in the spectral composition from a solar cell technology-independent perspective. Therefore, the *APE* parameter is used within the designated wavelength range. Subsequently, the calculation approach of the spectral correction factor $C_s(t)$ is investigated in dependence of

1. the solar cells spectral responsivities,
2. the global in-plane spectral irradiance as function of the time of the day,
3. and the procedure applied first to correct the spectral irradiances for angular losses.

The resulting spectral correction factors $C_s(t)$ deviate between 0.2 % to 0.5 % in case of the encapsulated device and between 1 % to 3 % in case of the IR-filtered device. These large deviations lead to the conclusion that the determination of spectral-angular losses is strongly dependent on the model which is used for the angular loss correction procedure and consequently on the simplifications thereof.

A detailed analysis of the diurnal irradiance losses assigned to individual devices reveals large discrepancies of up to 25 W m^{-2} between the results of the different models for distinct times of the day, specifically in the morning and in the afternoon. However, by integrating the irradiance losses over the time of the day, energy losses are determined with differences ranging from less than 0.1 % (which is rather negligible) to approximately 2.7 %. The maximum deviations for each device are observed between the simplified MR model (IEC) and the modified f_2 model (based on CIE). The f_2 models result also deviates to the result of the model proposed by this work, with one exception: The encapsulated devices' energy loss. Here, the results of the modified f_2 model (based on CIE) provide very low deviations to the results obtained with the proposed model that accounts for anisotropic diffuse irradiance and azimuthal asymmetries. Thus, the modified f_2 model based on procedures defined in the CIE standard (ISO/CIE 19476, 2014) represents the more accurate simplified procedure for the spectral and angular loss determination, and thus for the energy rating of crystalline silicon PV modules.

Note that the energy losses studied here represent one exemplary day using simulated irradiation datasets under idealized clear sky conditions. Chapter 3 includes details on input parameters used and on simplifications made to obtain the simulated data. Additional outdoor field measurements should be performed to validate the models results, allowing to draw sophisticated conclusions on the individual models' quality and usability, that are based on long-term field measurements. To this end, extensive outdoor field measurements covering a variety of irradiation conditions, PV technologies and installation typologies would be required, supported by an enormous experimental effort for the instrumentation.

Because the simplified MR model (IEC) for the angular loss calculation is proposed in the IEC energy rating standard, the author recommends revising the approach carefully based on the observations presented here and based on a follow up validation study including high-accuracy long-term field experiments. More conclusions and thoughts on follow up research are discussed in depth in the following chapter.

6. Discussion and Outlook

The experimental results presented in Chapter 4 show the capabilities of an improved measurement setup for the high-accuracy characterization of PV devices. PTB's primary calibration facility covers now traceable measurements of PV devices responsivities under any relevant irradiation condition. Beside the temperature and irradiance dependence, the parameter space includes polarization-, spectral- and AOI-dependent properties of the incident irradiation. This multidimensional parameter space allows the calculation of PV device's short-circuit current under any relevant spectrum, directional distribution of the spectrum, and temperature condition. The new capabilities of the facility are now included as service in the portfolio of PTB's working group 4.52 "Solar Cells". The novelty of this method including the thorough evaluation on uncertainties has been presented in the PV research community and aroused interest of several researchers to discuss the thematic of AOI-dependent PV device measurements (Plag, et al., 2017a; 2017b; 2018a). An activity that emphasizes the relevance of the topic is driven by members of the Department of Photonics Engineering affiliated to the Technical University of Denmark: An international European interlaboratory comparison (round robin) of AOI-dependent measurements on large-area solar cells has been performed in 2018 with 8 participating renowned laboratories including the PTB. The results of this comparison are published in the conference proceeding (Riedel, et al., 2018). Only two participating laboratories, the Centre for Renewable Energy Systems Technology (CREST) affiliated to the Loughborough University, and the PTB show consistent results over the entire range of investigated AOI's within their assigned expanded uncertainties. The research leading to these results is not part of this thesis. It can be rather seen as follow-up activity stimulated by essential parts of this work that were published in advance.

Currently, the results of the round-robin are discussed in the technical committee 82, a standardization group of the IEC. Meanwhile also laboratories from overseas evinced interest to measure the set of samples that were already characterized by the participating European laboratories.

The work included in Chapter 3 and 5, covering the modeling of a spectral-angular mismatch and computational studies, is a first approach to include the multidimensional parameters into the calculation of the short-circuit current of PV devices and thus on the device's performance and energy yield. The results presented in Section 5.1 are selected to show the capability of a newly developed multidimensional metric to compute a spectral-angular mismatch for very specific cases. The example cases presented in Subsections 5.1.1 and 5.1.2 contain outdoor calibration scenarios close to the reference conditions defined in (IEC 60904-3 Edition 2, 2008). The results of different computational studies show that the spectral-angular mismatch systematically affects measurements taken under diffuse irradiance. This depends on the PV device's angular-dependent spectral responsivities and on the shape of the spectral radiance field of the individual irradiation condition. The angular

mismatches for these specific conditions can be larger than 1 %. Two additional scenarios that cover calibrations under global sunlight conditions with AM2, and a variation of the grounds spectral albedo show the significance of the coupling between spectral and directional effects. The resulting spectral-angular mismatches, that are in the percent range, become particularly significant since expanded measurement uncertainties for indoor laboratory calibrations of reference solar cells short-circuit current using only a direct beam are lower than 0.4 %. A draft for the revision of the IEC standard 60904-4 is currently under discussion. This standard contains procedures for calibrations of reference solar cells under natural sunlight and a budget of “typical uncertainty components ($k = 2$) of global sunlight method” where an expanded uncertainty of only 0.7 % is reported under neglect of angular mismatch effects (IEC draft 60904-4 Edition 3, 2018). Hence, there is an immediate need to discuss the findings of this thesis in the standardization group.

With the proposal to use a global solar reference spectral irradiance that contains no diffuse component (direct normal beam only), spectral and angular mismatch correction procedures for both indoor and outdoor measurements can be conducted with lower computational effort compared to a defined anisotropic reference angular distribution of the diffuse radiance. Meanwhile, this proposal has been discussed in the IEC standardization groups and the directional properties for the reference irradiance are included in a recent draft for the IEC standard that includes the reference spectrum (IEC draft 60904-3 Edition 4, 2018).

For the PV performance monitoring or energy yield prediction, the author assumes that, compared to the investigated clear sky conditions, the impact of the angular mismatch increases when the sky is dense overcast and therefore no direct irradiance is apparent. Scenarios that differ from those of clear sky conditions have not been investigated in this work. But with the metric proposed in Chapter 3, a method is developed that enables further investigation of complex diffuse irradiation scenarios that can lead to a spectral-angular mismatch between two PV devices referring to reference conditions.

The high variability of realistic outdoor conditions and the large number of possible PV system configurations provide a wide range of individual parameter sets that can be examined using the metric proposed to study their impact on the spectral-angular mismatch factor. The spectral-angular mismatch depends on individual spectral irradiance and radiance conditions, as well as on the PV devices used as the reference and the device under test. Hence, the mismatch cannot be quantified for general or typical cases. The individual radiance condition acts as input quantity for the multidimensional model and it has its own uncertainty contributing to the mismatch’s uncertainty. The studies in this work are based on simulated spectral sky radiance distributions, which do not necessarily represent real outdoor measurement conditions. Hence, future studies should investigate realistic and traceable spectral sky radiance measurements, polarization of the sky radiance and ground reflectance in the environment close to the measurement site. Even though, Subsection 5.1.5 includes a thorough sensitivity analysis on the assumptions and on possible simplifications of the model proposed in this work, the impact of the measurement uncertainties

determined in the experimental part of this work on the output quantity of the novel model has not been investigated completely.

A comprehensive uncertainty analysis should be carried out to evaluate the propagation of input parameters' measurement uncertainties using the proposed model. Additionally, the impact of simplifications on the mismatch by assuming a Lambertian spectral albedo should be carefully checked against realistic spatially-varying bidirectional reflectance distribution functions, and on the neglected polarization of the sky radiance. In the first attempt in this work, the impact of the albedo simplification on the spectral-angular mismatch is estimated to be rather small, because the contribution to the mismatch originating from the ground-reflected radiance is significantly lower than the contribution originating from the sky. Note that this may change if the device has a steeper tilt or if objects located at the horizon are considered, which is commonly the case for building-integrated photovoltaics (BIPV). The possible impact of polarized irradiance was estimated in Subsection 5.2.4 in a first attempt to assess how this assumption affects the output short-circuit current of a PV device.

A comparison of outdoor measurements, that are subject to future research, with the traceable indoor measurements presented in this work and performed at a high spectral and angular resolution with low uncertainties is suggested for a validation of the modeling approach proposed in this thesis. A comprehensive analysis of uncertainty propagation using the proposed model marks an essential step for the experimental validation. In addition, detailed simulation parameter studies, following the idea of example calculations shown in Subsections 5.1.3 and 5.1.4, using many differing libRadtran spectral radiance datasets should be performed to investigate the sensitivity of the metric to specific radiation fields, including overcast skies and broken clouds, or to more complex ground reflection properties, such as shading objects at the horizon line.

By means of the sensitivity analysis discussed in Subsection 5.1.5, individual contributions that are dependent on the mismatch are identified. Simplifications made in the angular mismatch calculation approaches can lead to differences of more than 0.6 % between the individual spectral-angular mismatch correction factors. In this case the use of such simplifications increases the uncertainty of the spectral-angular mismatch correction factor. In practice, extensive spectral and angular characterization of individual PV devices is appropriate only for high-accuracy calibration. For other applications, the multidimensional model could be simplified by neglecting the spectral quantities in the first step and in the second step by assuming isotropic sky radiance distributions, as demonstrated in Subsection 5.1.5. The comprehensive analysis of spectral-angular mismatch uncertainty for several typical irradiation scenarios will allow the effect of approximations and simplifications on the model to be studied in the future.

A second conclusion of this work is that the angular losses calculated for the energy rating of PV modules strongly depend on the model that is used. The results presented in Section 5.2 reveal differences in the range of the angular losses themselves for the state-of-the-art models: modified f_2 model (based on CIE) and simplified MR model (IEC). Although the discussion of the uncertainties considers several investigated contributions such as interpolation errors, limitations of mathematical models, polarization effects, finite angular

resolution, azimuthal asymmetry, and the measurement uncertainty of the PV devices responsivity. The most dominant source of uncertainty using these simplified models is related to the assumption of isotropic sky radiance instead of anisotropic conditions. The effect of angular losses can be corrected on the one hand, but on the other hand, in some cases, the correction's uncertainty is in the range of the correction itself. The novel approach proposed by this thesis allows to overcome this shortcoming.

Section 5.3 includes an investigation over the period of an entire day on the spectral-angular losses of PV devices that are present at outdoor operating conditions, compared to an ideal pyranometer, as purposed by the general idea of PV energy rating. It turns out, that the calculated total spectral-angular energy loss strongly depends on the model that is used. Particularly, for the state-of-the-art models it was found that differences in the angular losses that are calculated in the first step, significantly affect the resulting spectral losses calculated in the second step. Again, the results of the three models were compared, and the differences between the models are approximately half of the loss itself. A maximum difference of 2.7 % was found for one example. Because the scenario investigated here represents only the variations of a single ideal sunny day, no general conclusion under realistic conditions considering cloudy skies can be drawn. The uncertainty of the solar energy loss attributed to spectral-angular losses can be different for the energy rating covering all kinds of conditions of a full year. The purpose of this analysis is to demonstrate that the new proposed model can be also used to study and discuss the uncertainty of current energy rating procedures for PV modules.

The results found in this thesis enable and motivate further sensitivity analysis and comprehensive parameter studies of the spectral-angular losses affecting measurements of the PV device performance. Possible subjects for follow-up research topics include:

- Based on the analysis on diurnal variations of a clear sky day that is already performed in this work, annual variations in irradiance conditions, and the consideration of clouds and varying sky conditions that impact the energy rating of PV modules can be investigated with the proposed model, if spectral radiance data are available.
- The investigation on the spectral ground reflectance's impact on the mismatch discussed in Subsection 5.1.4 is performed for monofacial PV devices. The impact of this effect is estimated to be larger for bifacial PV devices. The model proposed in this work is ready to perform investigations on these effects in the field of emerging bifacial PV module technologies, and hence an investigation of suitable reference conditions therefore.
- Moreover, in the field of BIPV, the metric proposed can be used to study an expected increase of the angular mismatch due to larger tilt angles and reflections from surrounding objects.

- In this work non-linearity effects of the PV devices related to changing irradiances are neglected to keep the focus on the impact of spectral and angular effects. Subsequent steps in the procedure of the energy rating standards can be used to determine the impact of low light conditions on the energy yield. Additionally, the proposed model could be enhanced by considering irradiance non-linearity and temperature effects, that are vital for the determination of performance and energy rating parameters.
- The proposed model can be expanded to consider the polarization dependence of incident spectral sky radiance to study the polarization effects on the mismatch more quantitatively. Although the effect on the PV devices investigated in this work seem to be rather negligible, it cannot be concluded that polarization can be neglected for general cases as a contribution to the uncertainty. The samples investigated in this work are made of mono crystalline silicon. It remains unclear whether other texturization or encapsulation techniques and other solar cell technologies (e.g. thin film, or multijunction devices) may provide significantly larger polarization dependencies. Thorough analysis and outdoor measurements are required to determine these effects.
- Finally, indoor measurement conditions under simulated sunlight with different radiance fields such as large area LED-based solar simulators can be characterized, and the impact of the directional properties of the light source on high-accuracy measurements can be evaluated and corrected.

In addition to further PV applications, the model presented in this thesis can be used in other fields of solar radiometry or photometry. The proposal allows the limitations of simplified models to be overcome in the procedures such as defined in the IEC energy rating standard regarding angular losses of PV devices. The detailed mathematical description of spectral and directional properties solar irradiance and detectors responsivity allows to improve the traceability of solar cell calibrations under diffuse light sources. Related measurement uncertainties for PV device performance measurements and for PV energy ratings can be estimated more accurately. By considering the spectral-angular mismatch, the total measurement uncertainty for PV performance measurements under diffuse light sources decreases. The findings of this work shall stimulate the discussion on that topic and the metric developed here provides an appropriate tool for the improvement of PV metrology.

7. Summary

One achievement of this thesis is the development of a multidimensional model for the determination of the spectral-angular mismatch. It quantifies the effect of diffuse sunlight (natural or artificial) and of not direct normal incident sunlight on the electrical current output of PV devices. The procedure developed in this work allows the compensation of the spectral-angular mismatch by using it as correction factor, enabling comparisons with measurements taken under normal incidence only using a reference spectral irradiance. The multidimensional model supplements existing state-of-the-art modelling approaches to study the impact of simplifying assumptions made in the description of PV performance measurements.

A second achievement of this thesis is the enhancement of a laser-based calibration facility at PTB for high-accuracy short-circuit current and spectral responsivity calibrations of reference solar cells and industrial sized cells with and without encapsulation. As a result of a thorough validation and comprehensive uncertainty analysis, PTB offers a novel metrological service: The characterization of the polarization and AOI-dependent spectral responsivity of PV devices with sizes ranging from reference solar cells to mini modules. The thoroughly investigated uncertainty analysis, presented in Chapter 4, includes a step by step description on the establishment of an individual uncertainty budget. This work, together with the previously published article (Plag, et al., 2017b), provide a best practice guide for the evaluation of the uncertainty of AOI-facilities for the research community.

A variety of computational studies on the determination of the spectral-angular mismatch correction factors are presented. It demonstrates the impact of this effect on high-accuracy measurements taken under global sunlight. Devices providing a better matching angular-dependent responsivity show a lower sensitivity of the angular mismatch with significant changes in the apparent radiance field.

The study shows that the error due to the spectral-angular mismatch can be up to 5.8 %, and due to the bare angular mismatch up to 1 %. A parameter variation of the device tilt and of the ground reflectance revealed that a change of the ground albedo affects the bare angular mismatch by up to 0.2 % for the measurement of an IR-filtered solar cell. If not considered, the mismatch effect impacts directly the corresponding short-circuit current measurement of the PV device taken under the global sunlight condition. Thus, leading to a large systematic error in the determination of the PV device performance.

The demanding effort for the procedure motivates a systematic comparison with procedures having lower requirements. A corresponding sensitivity analysis in this work reveals that simplified modeling approaches differ up to 0.64 % from the mismatch value obtained with the proposed multidimensional model. A reasonable tradeoff between effort and accuracy was identified by applying a separation of spectral- and angular-dependent quantities, allowing the determination of spectral mismatch and angular mismatch separately. The maximum discrepancy between this simplification and the multidimensional approach was

found to be -0.17 %, while the mismatch effect itself is 6 %. It can be concluded that the separation of the spectral and directional properties leads to a reasonable tradeoff if the sky radiance's anisotropy remains considered. With this simplification the effort decreases by approximately two orders of magnitude and additionally the procedures can be realized with less costly laboratory equipment.

A separate section of in this work includes a comparison of different procedures for the determination on angular losses (angular-dependent optical losses). Two existing approaches are compared against the novel approach proposed in this work. The first state-of-the-art approach is based on the Martin and Ruiz (MR) angular loss model, that is further simplified in the IEC 61853-3 standard for the purpose of PV module energy rating. The second approach is based on a procedure in the photometric standard CIE 19476 which was further modified in this work to describe the angular loss instead of a single quality index known in the field of photometry as f_2 . It was found that the differences in the angular losses vary in the range of a few percent, while the largest difference observed for the IR-filtered solar cell was almost 4 % for the global irradiance loss under the investigated irradiation scenario. It turns out that the IEC procedure based on the determination of an angular loss coefficient is not properly representing the measured angular-dependent responsivity values and their azimuthal asymmetry. A discussion of the procedures uncertainties identifies mathematical methods used in the model, simplifications, angular resolution, interpolation methods and polarization dependencies in addition to the measurement uncertainty assigned to the device characterization described in Chapter 4 as contributions to the total uncertainty of the angular loss. The most dominant contribution observed in this work can be attributed to differences caused by the mathematical model.

The evaluation on contributions to the uncertainty of this correction parameter enables a reduction of the PV device calibration uncertainty under global sunlight. In addition to global natural sunlight measurements, the approach can be also utilized for the evaluation of uncertainties of indoor laboratory measurements with diffuse solar simulators and for a wide range of radiometric and photometric applications, including the characterization of extended radiant sources. An exemplary energy rating scenario was studied in this work to identify the impact on the determination of the generated electricity of PV devices under reference climate profiles. This exemplary energy rating procedure focusses on one single day with clear sky conditions. The solar energy losses onto a tilted surface related to spectral and angular effects were determined using three different models. The observed differences in the energy losses of that particular day for the encapsulated device vary from 0.3 % to 0.6 %, for the IR-filtered device from 4.12 % to 6.83 %, and for the non-encapsulated device from 2.05 % to 3.8 %. It turns out that the assumption of azimuthal symmetry of the devices' angular-dependent responsivities contributes significantly to the observed deviations and thus to the uncertainty of the energy rating for asymmetric devices.

The findings of this thesis are important for ongoing standardization activities in the corresponding committee of the IEC. The publication of the experimental results in advance of this thesis has stimulated other European laboratories to perform an interlaboratory comparison of AOI-dependent measurements on solar cells. It has been successfully completed and the results are now under discussion in the IEC standardization group TC82.

Data availability

The spectral- and angular-dependent responsivity datasets of the three WPVS reference solar cells and one of the *uvspec* input files investigated in this thesis (Condition 1) can be obtained from the PTB Open Access Repository using the following weblink: <https://doi.org/10.7795/720.20180517> (Plag et al.,2018b).

List of publications

Research articles related to this thesis

Plag, F., Kröger, I., Riechelmann, S., & Winter, S. (2018a). Multidimensional model to correct PV device performance measurements taken under diffuse irradiation to reference conditions. *Solar Energy*, 174, 431-444. doi:10.1016/j.solener.2018.08.072

Plag, F., Kröger, I., Fey, T., Witt, F., & Winter, S. (2017b). Angular-dependent spectral responsivity—Traceable measurements on optical losses in PV devices. *Progress in Photovoltaics: Research and Applications*, 26, 565-578. doi:10.1002/pip.2957

Conference proceedings related to this thesis

Plag, F. & Winter, S. (2019), Procedures for angular mismatch correction – Development of an International Standard Proposal, Marseille: Presentation at the 35th European Photovoltaic Solar Energy Conference.

Riedel, N., Santamaria Lancia, A. A., Amdemeskel, M., Thorsteinsson, S., Poulsen, P. B., Plag, F., Kröger, I., Slooff, L. H., Jansen, M. J., Carr, A. J., Manshanden, P., Bliss, M., Betts, T. R., Petrina Jauregui, I., Ezquer Mayo, M., Balenzategui, J. L., Roldán, R., Krähling, U., Baarah, G., Iandolo, B., Davidsen, R. S., Thorseth, A., Dam-Hansen, C., & dos Reis Benatto, G. A. (2018). Interlaboratory Comparison of Methodologies for Measuring the Angle of Incidence Dependence of Solar Cells. (pp. 1034 – 1039). Brussels: Proceedings of the 35th European Photovoltaic Solar Energy Conference. doi:10.4229/35thEUPVSEC20182018-5BO.10.4

Pravettoni, M., Galleano, R., Zaaiman, W., Alvarez, D. A., Belluardo, G., Betts, T. R., Bogeat, J. A., Cole, I. R., Drobisch, A., Ferretti, N., Friedrich, D., Fucci, R., Gómez T. J., Graditi, G., Halwachs, M., Haverkamp, E., Minuto, A., Phinikarides, A., Plag, F., Rennhofer, M., Molinero, R. R., Riedel, N., Theristis, M., Thorseth, A., Timò, G., & Vilaplana, J. M. (2018). Spectroradiometry in PV: how inter-laboratory comparison may improve measurement accuracy. (pp. 2584 – 2589). Waikoloa: Proceedings of the 7th World Conference on Photovoltaic Energy Conversion. doi:10.1109/PVSC.2018.8547975

Plag, F., Riechelmann, S., Kröger, I., & Winter, S. (2017a). Spectral and Angular Correction - A Multidimensional Approach to Model Measurements under Outdoor Conditions. (pp. 1364 - 1369). Amsterdam: Proceedings of the 33rd European Photovoltaic Solar Energy Conference and Exhibition. doi:10.4229/EUPVSEC20172017-5BO.6.4

Kröger, I., Fey, T., Witt, F., Plag, F., & Winter, S. (2017). Spectral angular responsivity calibration facility at PTB. Presented at the 33rd European Photovoltaic Solar Energy Conference and Exhibition in Amsterdam.

Plag, F., Riechelmann, S., Kröger, I., & Winter, S. (2017) Multidimensional metric for computation of spectral and angular mismatch, Tokyo: Proceedings of NEWRAD 2017.

Riechelmann, S. & Plag, F. (2017). A Camera-Based Characterization Method for Solar Simulators. (pp. 1554 - 1556). Amsterdam: Proceedings of the 33rd European Photovoltaic Solar Energy Conference and Exhibition. doi:10.4229/EUPVSEC20172017-5BV.4.7

Other publications of the author

Galleano, R., Kröger, I., Plag, F., Winter, S., & Müllejans, H. (2018). Traceable spectral irradiance measurements in photovoltaics: Results of the PTB and JRC spectroradiometer comparison using different light sources, *Measurement*, 124, 549-559. doi:10.1016/j.measurement.2017.09.007

Plag, F., Haas, F., Ramspeck, K., & Winter, S. (2016). Measuring Uniformity under Simulated Sunlight. (pp. 2177 - 2183)., Munich: Proceedings of the 32nd European Photovoltaic Solar Energy Conference and Exhibition. doi:10.4229/EUPVSEC20162016-5BV.4.2

Kröger, I., Galleano, R., Plag, F., Müllejans, H., & Winter, S. (2016). Intercomparison of PTB and ESTI Spectroradiometers Using Simulated and Natural Sunlight. (pp. 2230 - 2233). Munich: Proceedings of the 32nd European Photovoltaic Solar Energy Conference and Exhibition. doi:10.4229/EUPVSEC20162016-5BV.4.20

Galleano, R., Zaiman, W., Alonso-Álvarez, D., Minuto, A., Ferretti, N., Fucci, R., Marzoli, M., Manni, L., Halwachs, M., Friederichs, M., Plag, F., Friedrich D., & Haverkamp, E. (2016). Preliminary Results of the Fifth International Spectroradiometer Comparison for Improved Solar Spectral Irradiance Measurements. (pp. 1465 - 1469). Munich: Proceedings of the 32nd European Photovoltaic Solar Energy Conference and Exhibition. doi:10.4229/EUPVSEC20162016-5AO.7.5

Galleano, R., Zaiman, W., Alonso-Álvarez, D., Minuto, A., Ferretti, N., Fucci, R., Marzoli, M., Manni, L., Halwachs, M., Friederichs, M., Plag, F., Friedrich D., & Haverkamp, E. (2016). Results of the Fifth International Spectroradiometer Comparison for Improved Solar Spectral Irradiance Measurements and Related Impact on Reference Solar Cell Calibration. *IEEE Journal of Photovoltaics*, 6, 6, 1587-1597. doi:10.1109/JPHOTOV.2016.2606698

Ramspeck, K., Plag, F., Haas, F., Winter, S., & Metz, A. (2015). Temperature Coefficients of Silicon Solar Cells. (pp. 799 - 803). Hamburg: Proceedings of the 31st European Photovoltaic Solar Energy Conference and Exhibition. doi:10.4229/EUPVSEC20152015-2BV.8.2

Winter, S., Fey, T., Kröger, I., & Plag, F. (2014). Traceable Wavelength Calibration of a Monochromator Using a Fourier Transform Spectroradiometer. (pp. 185 -187). Otaniemi: Proceedings of NEWRAD 2014.

Kröger, I., Plag, F., Fey, T., Witt, F., & Winter, S. (2014). Establishment of Wavelength Traceability of a DSR-Facility Using Array Spectroradiometers and a Fourier-Transform-Spectroradiometer. (pp. 3447 - 3451). Amsterdam: Proceedings of the

29th European Photovoltaic Solar Energy Conference and Exhibition.
doi:10.4229/EUPVSEC20142014-5DV.3.51

Plag, F. (2013). Bestimmung der Messmittelfähigkeit eines gepulsten Solarsimulators mit Kennlinienmessgerät für die Kalibrierung von Solarzellen. Masterarbeit: Universität Kassel.

Sperfeld, P., Dzafic, D., Plag, F., Haas, F., Kröber, C., Albert, H., Nevas, S., & Pape, S. (2012). Usability of compact array spectroradiometers for the traceable classification of pulsed solar simulators. (pp. 3060 – 3065) Frankfurt: Proceedings of the 27th European Photovoltaic Solar Energy Conference and Exhibition.
doi:10.4229/27thEUPVSEC2012-4CO.12.3

EU PVSEC Student Award:

Plag, F., Haas, F., Ramspeck, K., Nagel, H., Albert, H., Nevas, S., Sperfeld, P., Witt, F., & Winter, S. (2014). Comprehensive Analysis of a Pulsed Solar Simulator to Determine Measurement Uncertainty Components. (pp. 2435 – 2442). Amsterdam: Proceedings of the 29th European Photovoltaic Solar Energy Conference and Exhibition.
doi:10.4229/EUPVSEC20142014-5DO.9.2

References

- Ahn, S., Ahn, S., Yun, J., Lee, D., Winter, S., Igari, S., & Yoon, K. (2014). Establishment of a primary reference solar cell calibration technique in Korea: Methods, results and comparison with WPVS qualified laboratories. *Metrologia*, *51*, 139. doi:10.1088/0026-1394/51/3/139
- Al Husna, H. (2018). Characterisation of spectral and angular effects on photovoltaic modules for energy rating. PhD Thesis: Loughborough University.
- Anderson, G. P., Clough, S. A., Kneizys, F. X., Chetwynd, J. H., & Shettle, E. P. (1986). AFGL atmospheric constituent profiles (0-120km) AFGL-TR-86-0110. *Hanscom AFB, MA: Optical Physics Division, U.S. Air Force Geophysics Laboratory*.
- Andrews, R. W., & Pearce, J. M. (2013). The effect of spectral albedo on amorphous silicon and crystalline silicon solar photovoltaic device performance. *Solar Energy*, *91*, 233-241. doi:10.1016/j.solener.2013.01.030
- Balenzategui, J. L., & Chenlo, F. (2005). Measurement and analysis of angular response of bare and encapsulated silicon solar cells. *Solar Energy Materials and Solar Cells*, *86*, 53-83. doi:10.1016/j.solmat.2004.06.007
- Barbose, G., & Darghouth, N. (2018). *Tracking the Sun - Installed Price Trends for Distributed Photovoltaic Systems in the United States*. Retrieved Nov 2018, from http://www.iea-pvps.org/fileadmin/dam/public/report/statistics/IEA-PVPS_-_A_Snapshot_of_Global_PV_-_1992-2017.pdf
- Barnard, G. P. (1936). The dependence of sensitivity of the selenium-sulphur rectifier photoelectric cell on the obliquity of the incident light, and a method of compensation therefor. *Proceedings of the Physical Society*, *48*, 153. doi:10.1088/0959-5309/48/1/321
- Barnard, G. P. (1939). The spectral sensitivity of selenium rectifier photoelectric cells. *Proceedings of the Physical Society*, *51*, 222. doi:10.1088/0959-5309/51/2/302
- Beal, R. J., Potter, B. G., & Simmons, J. H. (2014). Angle of Incidence Effects on External Quantum Efficiency in Multicrystalline Silicon Photovoltaics. *IEEE Journal of Photovoltaics*, *4*, 1459-1464. doi:10.1109/JPHOTOV.2014.2350672
- Brennan, M. P., Abramase, A. L., Andrews, R. W., & Pearce, J. M. (2014). Effects of spectral albedo on solar photovoltaic devices. *Solar Energy Materials and Solar Cells*, *124*, 111-116. doi:10.1016/j.solmat.2014.01.046
- Bullrich, K., Bary, E., & Möller, F. (1952). Die Farbe des Himmels. *Geofisica pura e applicata*, *23*, 69-110. doi:10.1007/BF01992459

- Cox, M. G., & Siebert, B. R. (2006). The use of a Monte Carlo method for evaluating uncertainty and expanded uncertainty. *Metrologia*, *43*, S178. doi:10.1088/0026-1394/43/4/S03
- Dennler, G., Forberich, K., Scharber, M. C., Brabec, C. J., Tomiš, I., Hingerl, K., & Fromherz, T. (2007). Angle dependence of external and internal quantum efficiencies in bulk-heterojunction organic solar cells. *Journal of Applied Physics*, *102*, 054516. doi:10.1063/1.2777724
- Driesse, A., Zaaiman, W., Riley, D. S., Taylor, N., & Stein, J. S. (2015). Indoor and Outdoor Evaluation of Global Irradiance Sensors. (pp. 1704 - 1709). Hamburg: Proceedings of the 31st European Photovoltaic Solar Energy Conference and Exhibition. doi:10.4229/EUPVSEC20152015-5CO.5.3
- Emde, C., Buras, R., Meyer, B., & Blumthaler, M. (2010). The impact of aerosols on polarized sky radiance: model development, validation, and applications. *Atmos. Chem. Phys.*, *10*, 383-396. doi:10.5194/acp-10-383-2010
- Emde, C., Buras-Schnell, R., Kylling, A., Mayer, B., Gasteiger, J., Hamann, U., Kylling, J., Richter, B., Pause, C., Dowling, T., & Bugliaro, L. (2016). The libRadtran software package for radiative transfer calculations (version 2.0.1). *Geoscientific Model Development*, *9*, 1647-1672. doi:10.5194/gmd-9-1647-2016
- Emery, K. (2005). Chapter 16: Measurement and Characterization of Solar Cells and Modules. In A. Luque, & S. Hegedus, *Handbook of Photovoltaic Science and Engineering* (p. 701 ff). Wiley.
- Emery, K. A., & Osterwald, C. R. (1988). Chapter 4: Efficiency Measurements and Other Performance-Rating Methods. In T. J. Coutts, & J. D. Meakin, *Current Topics in Photovoltaics Vol. 3* (p. 326 ff). San Diego, CA: Academic Press Inc.
- Emery, K. A., & Osterwald, C. R. (1989). Solar cell calibration methods. *Solar Cells*, *27*, 445-453. doi:10.1016/0379-6787(89)90054-9
- Gál, J., Horváth, G., Meyer-Rochow, V. B., & Wehner, R. (2001). Polarization patterns of the summer sky and its neutral points measured by full-sky imaging polarimetry in Finnish Lapland north of the Arctic Circle. *Proc. R. Soc. Lond.*, *457*, 1385-1399. doi:10.1098/rspa.2000.0726
- Geisemeyer, I., Tucher, N., Müller, B., Steinkemper, H., Hohl-Ebinger, J., Schubert, M. C., & Warta, W. (2017). Angle Dependence of Solar Cells and Modules: The Role of Cell Texturization. *IEEE Journal of Photovoltaics*, *7*, 19-24. doi:10.1109/JPHOTOV.2016.2614120
- Gjessing, J., & Marstein, E. S. (2014). An Optical Model for Predicting the Quantum Efficiency of Solar Modules. *IEEE Journal of Photovoltaics*, *4*, 304-310. doi:10.1109/JPHOTOV.2013.2272877
-

- Glunz, S., & Würfel, U. (2014). Fundamentals of Solar Cells. University of Freiburg: Lecture material - Solar Energy Engineering.
- Goldstein, D. H. (2010). Chapter 2: Polarization in the Natural Environment - Polarized Light in the Atmosphere. In *Polarized Light 3rd Edition* (pp. 9-16). CRC Press.
- Goldstein, H. (1980). Chapter 4-4: The Euler Angles. In *Classical Mechanics 2nd Edition* (p. 143 ff). Reading, MA: Addison-Wesley.
- Goswami, D. Y., Kreith, F., & Kreidler, J. F. (2000a). Chapter 2: Fundamentals of Solar Radiation - The Physics of the Sun and its Energy Transport. In *Principles of Solar Engineering 2nd Edition* (p. 13 ff). Taylor & Francis.
- Goswami, D. Y., Kreith, F., & Kreidler, J. F. (2000b). Chapter 9: Photovoltaics. In *Principles of Solar Engineering 2nd Edition* (pp. 415-430). Taylor & Francis.
- Gueymard, C. A. (1987). An anisotropic solar irradiance model for tilted surfaces and its comparison with selected engineering algorithms. *Solar Energy*, 38, 367-386. doi:10.1016/0038-092X(87)90009-0
- Gueymard, C. A. (1995). SMARTS2 - Simple Model of the Atmospheric Radiative Transfer of Sunshine: Algorithms and Performance Assessment - FSEC-PF-270-95. *Florida Solar Energy Center*.
- Gueymard, C. A. (2017a). Cloud and albedo enhancement impacts on solar irradiance using high-frequency measurements from thermopile and photodiode radiometers. Part 1: Impacts on global horizontal irradiance. *Solar Energy*, 153, 755-765. doi:10.1016/j.solener.2017.05.004
- Gueymard, C. A. (2017b). Cloud and albedo enhancement impacts on solar irradiance using high-frequency measurements from thermopile and photodiode radiometers. Part 2: Performance of separation and transposition models for global tilted irradiance. *Solar Energy*, 153, 766-779. doi:10.1016/j.solener.2017.04.068
- Gueymard, C. A. (2018). A reevaluation of the solar constant based on a 42-year total solar irradiance time series and a reconciliation of spaceborne observations. *Solar Energy*, 168, 2-9. doi:10.1016/j.solener.2018.04.001
- Gueymard, C. A., Myers, D., & Emery, K. A. (2002). Proposed reference irradiance spectra for solar energy systems testing. *Solar Energy*, 73, 443-467. doi:10.1016/S0038-092X(03)00005-7
- Hay, J. E., & McKay, D. C. (1985). Estimating Solar Irradiance on Inclined Surfaces: A Review and Assessment of Methodologies. *International Journal of Solar Energy*, 3, 203-240. doi:10.1080/01425918508914395
- Heinämäki, A., & Guekos, G. (1987). Solar cell short-circuit current dependence on the angle of the incident radiation. *Solar Cells*, 20, 65-73. doi:10.1016/0379-6787(87)90022-6
-

- Hishikawa, Y., Igari, S., & Kato, H. (2003). Calibration and measurement of solar cells and modules by the solar simulator method in Japan. 2, pp. 1081-1084. Proceedings of the 3rd World Conference on Photovoltaic Energy Conversion. doi:10.1109/WCPEC.2003.1306100
- Honsberg, C., & Bowden, S. (2018a). *PVEducation.org*. Retrieved 10 2018, from <https://www.pveducation.org/>
- Honsberg, C., & Bowden, S. (2018b). *PVEducation.org*. Retrieved Oct 2018, from <https://www.pveducation.org/pvcdrom/solar-cell-operation/collection-probability>
- IEA, International Energy Agency. (2018). *Snapshot of Global Photovoltaic Markets (1992-2017); Report IEA PVPS T1-33:2018*. Retrieved Nov 2018, from http://www.iaepvps.org/fileadmin/dam/public/report/statistics/IEA-PVPS_-_A_Snapshot_of_Global_PV_-_1992-2017.pdf
- IEC 60891 Edition 2. (2009). Photovoltaic devices - Procedures for temperature and irradiance corrections to measured I-V characteristics. *International Electrotechnical Commission*.
- IEC 60904-1 Edition 2. (2006). Photovoltaic devices - Part 1: Measurement of photovoltaic current-voltage characteristics. *International Electrotechnical Commission*.
- IEC 60904-10 Edition 2. (2009). Photovoltaic devices - Part 10: Methods of linearity measurement. *International Electrotechnical Commission*.
- IEC 60904-2 Edition 2. (2007). Photovoltaic devices - Part 2: Requirements for photovoltaic reference devices. *International Electrotechnical Commission*.
- IEC 60904-3 Edition 2. (2008). Measurement principles for terrestrial photovoltaic (PV) solar devices with reference spectral irradiance data. *International Electrotechnical Commission*.
- IEC 60904-3 Edition 3. (2016). Photovoltaic devices - Part 3: Measurement principles for terrestrial photovoltaic (PV) solar devices with reference spectral irradiance data. *International Electrotechnical Commission*.
- IEC 60904-4. (2009). Photovoltaic devices - Part 4: Reference solar devices - Procedures for establishing calibration traceability. *International Electrotechnical Commission*.
- IEC 60904-7 Edition 3. (2008). Computation of the spectral mismatch correction for measurements of photovoltaic devices. *International Electrotechnical Commission*.
- IEC 60904-8 Edition 3. (2014). Photovoltaic devices - Part 8: Measurement of spectral responsivity of a photovoltaic (PV) device. *International Electrotechnical Commission*.
- IEC 60904-9 Edition 2. (2007). Photovoltaic devices - Part 9: Solar simulator performance requirements. *International Electrotechnical Commission*.
-

- IEC 61853-1. (2011). Photovoltaic (PV) module performance testing and energy rating – Part 1: Irradiance and temperature performance measurements and power rating. *International Electrotechnical Commission*.
- IEC 61853-2. (2016). Photovoltaic (PV) module performance testing and energy rating - Part 2: Spectral responsivity, incidence angle and module operating temperature measurements. *International Electrotechnical Commission*.
- IEC 61853-3. (2018). Photovoltaic (PV) module performance testing and energy rating – Part 3: Energy rating of PV modules. *International Electrotechnical Commission*.
- IEC 61853-4. (2018). Photovoltaic (PV) module performance testing and energy rating - Part 4: Standard reference climatic profiles. *International Electrotechnical Commission*.
- IEC draft 60904-3 Edition 4. (2018). Photovoltaic devices - Part 3: Measurement principles for terrestrial photovoltaic (PV) solar devices with reference spectral irradiance data. *International Electrotechnical Commission*.
- IEC draft 60904-4 Edition 3. (2018). Photovoltaic devices - Part 4: Reference solar devices - Procedures for establishing calibration traceability. *International Electrotechnical Commission*.
- Iqbal, M. (1983). Chapter 3: The Solar Constant and Its Spectral Distribution. In *An Introduction To Solar Radiation* (p. 48). Academic Press.
- ISO/CIE 19476. (2014). Characterization of the performance of illuminance meters and luminance meters. *International Organization for Standardization/International Commission on Illumination*.
- ISO/IEC 17043. (2010). Conformity assessment – General requirements for proficiency testing. *International Organization for Standardization/International Electrotechnical Commission*.
- Jardine, C. N., Gottschalg, R., Betts, T., & Infield, D. (2002). Influence of Spectral Effects on the Performance of Multijunction Amorphous Silicon Cells. In *Conference Proceedings*.
- JCGM 100. (2008). Evaluation of measurement data – Guide to the expression of uncertainty in measurement. *Joint Committee for Guides in Metrology*.
- JCGM 101. (2008). Evaluation of measurement data – Supplement 1 to the "Guide to the expression of uncertainty in measurement" – Propagation of distributions using a Monte Carlo method. *Joint Committee for Guides in Metrology*.
- JCGM 104. (2009). Evaluation of measurement data – An introduction to the "Guide to the expression of uncertainty in measurement" and related documents. *Joint Committee for Guides in Metrology*.
- JCGM 200 Edition 3. (2012). International vocabulary of metrology - Basic and general concepts and associated terms (VIM). *Joint Committee for Guides in Metrology*.
-

- John, J., Rajasekar, V., Tatapudi, S., & Tamizhmani, G. (2014). Angle of incidence effects on soiled PV modules. *9179*, pp. 9179-0D. San Diego: Proceedings of SPIE Solar Energy + Technology. doi:10.1117/12.2063351
- King, D. L., Boyson, W. E., & Kratochvill, J. A. (2004). *Photovoltaic Array Performance Model*. Albuquerque, NM and Livermore, CA: Sandia National Laboratory.
- King, D. L., Kratochvil, J. A., & Boyson, W. E. (1997). Measuring solar spectral and angle-of-incidence effects on photovoltaic modules and solar irradiance sensors. (pp. 1113-1116). Anaheim: Conference Record of the Twenty Sixth IEEE Photovoltaic Specialists Conference. doi:10.1109/PVSC.1997.654283
- Kopp, G., & Lean, J. L. (2011). A new, lower value of total solar irradiance: Evidence and climate significance. *Geophys. Res. Lett.*, *38*, L01706. doi:10.1029/2010GL045777
- Martin, N. (1999). Estudio de la influencia de la reflexión el ángulo de incidencia y la distribución espectral de la radiación solar en los generadores fotovoltaicos. Tesis doctoral, Escuela Técnica Superior de Ingenieros de Telecomunicación, Universidad Politécnica de Madrid.
- Martin, N., & Ruiz, J. M. (2001). Calculation of the PV modules angular losses under field conditions by means of an analytical model. *Solar Energy Materials and Solar Cells*, *70*, 25-38. doi:10.1016/S0927-0248(00)00408-6
- Martin, N., & Ruiz, J. M. (2002). A new model for PV modules angular losses under field conditions. *International Journal of Solar Energy*, *22*, 19-31. doi:10.1080/01425910212852
- Martin, N., & Ruiz, J. M. (2005). Annual angular reflection losses in PV modules. *Progress in Photovoltaics: Research and Applications*, *13*, 75-84. doi:10.1002/pip.585
- Mayer, B., & Kylling, A. (2005). Technical note: The libRadtran software package for radiative transfer calculations - description and examples of use. *Atmospheric Chemistry and Physics*, *5*, 1855-1877. doi:10.5194/acp-5-1855-2005
- Mayer, B., Kylling, A., Emde, C., Buras, R., Hamaa, U., Gasteiger, J., & Richter, B. (2015). libRadtran user's guide - Edition for libRadtran version 2.0., Retrieved March 2016, from www.libradtran.org.
- McEvoy, A., Markvart, T., & Castaner, L. (2012). Chapter 1: Principles of Solar Cell Operation. In *Practical Handbook of Photovoltaics - Fundamentals and Applications* (pp. 7-25). Academic Press.
- Metzdorf, J. (1987). Calibration of solar cells. 1: The differential spectral responsivity method. *Applied Optics*, *26*, 1701-1708. doi:10.1364/AO.26.001701
- Mialhe, P., Mouhamed, S., & Haydar, A. (1991). The solar cell output power dependence on the angle of incident radiation. *Renewable Energy*, *1*, 519-521. doi:10.1016/0960-1481(91)90065-W
-

- Michalsky, J. J., Harrison, L. C., & Berkheiser, W. E. (1995). Cosine response characteristics of some radiometric and photometric sensors. *Solar Energy*, *54*, 397-402. doi:10.1016/0038-092X(95)00017-L
- Mihaylov, B. (2016). Uncertainty Considerations in Photovoltaic Measurements. PhD Thesis: Loughborough University.
- Miyake, Y., Shimokawa, R., Nakanishi, Y., & Hamakawa, Y. (1987). Global radiation model and angular distribution of the diffuse irradiance. *Solar Cells*, *20*, 127-143. doi:10.1016/0379-6787(87)90037-8
- Müllejjans, H., Zaaïman, W., Dunlop, E. D., & Ossenbrink, H. A. (2005a). Calibration of photovoltaic reference cells by the global sunlight method. *Metrologia*, *42*, 360. doi:10.1088/0026-1394/42/5/004
- Müllejjans, H., Zaaïman, W., Merli, F., Dunlop, E. D., & Ossenbrink, H. A. (2005b). Comparison of traceable calibration methods for primary photovoltaic reference cells. *Progress in Photovoltaics: Research and Applications*, *13*, 661-671. doi:10.1002/pip.625
- Norton, M., Gracia Amillo, A., & Galleano, R. (2015). Comparison of solar spectral irradiance measurements using the average photon energy parameter. *Solar Energy*, *120*, 337-344.
- Osterwald, C. R., Anevsky, S., Bücher, K., Barua, A. K., Chaudhuri, P., Dubard, J., Emery, K., Hansen, B., King, D., Metzendorf, J., Nagamine, F., Shimokawa, R., Wang, Y. X., Wittchen, T., Zaaïman, W., Zastrow, A., & Zhang, J. (1999). The world photovoltaic scale: an international reference cell calibration program. *Progress in Photovoltaics: Research and Applications*, *7*, 287-297. doi:10.1002/(SICI)1099-159X(199907/08)7:4<287::AID-PIP259>3.0.CO;2-I
- Parretta, A., Sarno, A., Tortora, P., Yakubu, H., Maddalena, P., Zhao, J., & Wang, A. (1999). Angle-dependent reflectance measurements on photovoltaic materials and solar cells. *Optics Communications*, *172*, 139-151. doi:10.1016/S0030-4018(99)00561-1
- Perez, R., Ineichen, P., Seals, R., Michalsky, J., & Stewart, R. (1990). Modeling daylight availability and irradiance components from direct and global irradiance. *Solar Energy*, *44*, 271-289. doi:10.1016/0038-092X(90)90055-H
- Plag, F. (2013). Bestimmung der Messmittelfähigkeit eines gepulsten Solarsimulators mit Kennlinienmessgerät für die Kalibrierung von Solarzellen. Masterarbeit: Universität Kassel.
- Plag, F., Riechelmann, S., Kröger, I., & Winter, S. (2017a). Spectral and Angular Correction - A Multidimensional Approach to Model Measurements under Outdoor Conditions. (pp. 1364 - 1369). Amsterdam: Proceedings of the 33rd European Photovoltaic Solar Energy Conference and Exhibition. doi:10.4229/EUPVSEC20172017-5BO.6.4
-

- Plag, F., Kröger, I., Fey, T., Witt, F., & Winter, S. (2017b). Angular-dependent spectral responsivity—Traceable measurements on optical losses in PV devices. *Progress in Photovoltaics: Research and Applications*, 26, 565-578. doi:10.1002/pip.2957
- Plag, F., Kröger, I., Riechelmann, S., & Winter, S. (2018a). Multidimensional model to correct PV device performance measurements taken under diffuse irradiation to reference conditions. *Solar Energy*, 174, 431-444. doi:10.1016/j.solener.2018.08.072
- Plag, F., Riechelmann, S., Kröger, I., & Winter, S. (2018b). Datasets for Multidimensional model to correct PV device performance measurements taken under diffuse irradiation to reference conditions. doi:10.7795/720.20180517
- Potter, B. G., Hansen, C. W., Simmons J., H., & King, B. (2015). Incidence-angle dependent external quantum efficiency: Laboratory characterization and use in irradiance-to-power modeling. (pp. 1-4). New Orleans: IEEE 42nd Photovoltaic Specialist Conference (PVSC). doi:10.1109/PVSC.2015.7355998
- PTB Working Group 4.52 - Website. (2018). Services of the Working Group "Solar Cells". Retrieved Aug 2018, from <https://www.ptb.de/cms/en/ptb/fachabteilungen/abt4/fb-45/ag-452.html>
- Reiners, N. (2018). Angle and Spectral Dependence of the Internal and External Quantum Efficiency of Solar Modules. PhD Thesis: University of Luxembourg.
- Riedel, N., Santamaria Lancia, A. A., Amdemeskel, M., Thorsteinsson, S., Poulsen, P. B., Plag, F., Kröger, I., Slooff, L. H., Jansen, M. J., Carr, A. J., Manshanden, P., Bliss, M., Betts, T. R., Petrina Jauregui, I., Ezquer Mayo, M., Balenzategui, J. L., Roldán, R., Krähling, U., Baarah, G., Iandolo, B., Davidsen, R. S., Thorseth, A., Dam-Hansen, C., & dos Reis Benatto, G. A. (2018). Interlaboratory Comparison of Methodologies for Measuring the Angle of Incidence Dependence of Solar Cells. Brussels: Proceedings of the 35th European Photovoltaic Solar Energy Conference. doi:10.4229/35thEUPVSEC20182018-5BO.10.4
- Schinke, C., Vogt, M. R., & Bothe, K. (2018). Optical Modeling of Photovoltaic Modules with Ray Tracing Simulations. In M. F. Müller, *Photovoltaic Modeling Handbook* (pp. 27-91). Scrivener Publishing LLC.
- Schrempf, M. (2018). Development of methods to determine biologically-weighted UV exposure of humans in different environments. PhD Thesis: Leibniz University Hannover.
- Scientific Software Development. (2016). HYPRADATA 6.5 - Datenbank, Analysetool und Präsentationsprogramm für Messreihen. <http://www.ssd.de/hypradata/home.htm>. Retrieved Nov 2016.
- Seibert, G. (1968). Solar cell output as a function of angle of incidence for both unpolarized and linear polarized light. *Energy Conversion*, 8, 121-123. doi:10.1016/0013-7480(68)90113-7
-

- Shettle, E. P. (1989). Models of aerosols, clouds, and precipitation for atmospheric propagation studies. (pp. 15-1 to 15-13). Paris: AGARD Conference Proceedings No 454: Atmospheric propagation in the UV, visible, IR and mm-region and related system aspects.
- Shimokawa, R., Miyake, Y., Nakanishi, Y., Kuwano, Y., & Hamakawa, Y. (1986). Possible Errors due to Deviation from the Cosine Response in the Reference Cell Calibration under Global Irradiance. *Japanese Journal of Applied Physics*, 25, L102. doi:10.1143/JJAP.25.L102
- Shimokawa, R., Nagamine, F., Miyake, Y., Fujisawa, K., & Hamakawa, Y. (1987). Japanese Indoor Calibration Method for the Reference Solar Cell and Comparison with the Outdoor Calibration. *Japanese Journal of Applied Physics*, 26, 86. doi:10.1143/JJAP.26.86
- Smeets, M., Smirnov, V., Bittkau, K., Meier, M., Cariu, R., Rau, U., & Paetzold, U. W. (2015). Angular dependence of light trapping in nanophotonic thin-film solar cells. *Opt. Express*, 23, A1575-A1588. doi:10.1364/OE.23.0A1575
- Stamnes, K., Tsay, S.-C., Wiscombe, W., & Jayaweera, K. (1988). Numerically stable algorithm for discrete-ordinate-method radiative transfer in multiple scattering and emitting layered media. *Applied Optics*, 27, 2502-2509. doi:10.1364/AO.27.002502
- Stant, L. T., Aaen, P. H., & Ridler, N. M. (2016). Comparing methods for evaluating measurement uncertainty given in the JCGM 'Evaluation of Measurement Data' documents. *Measurement*, 94, 847-851.
- Theocharous, E. (2008). Absolute linearity characterization of lock-in amplifiers. *Applied Optics*, 47, 1090-1096. doi:10.1364/AO.47.001090
- Treble, F. C. (1965). Chapter 36 - Solar Cell Performance Measurement. In D. H. Collins (Ed.), *Batteries 2* (pp. 503-520). Pergamon. doi:10.1016/B978-1-4831-6705-3.50041-1
- Ulbrich, C. (2011). Spectral and directional dependence of light-trapping in solar cells. PhD Thesis: RWTH Aachen University.
- Walker, J. (1996). Colour Rendering of Spectra. Retrieved March 2017, from <https://www.fourmilab.ch/documents/specrend/>
- Winter, S. (2003). Analyse und Verbesserung der rückführbaren Kalibrierung von Solarzellen. PhD Thesis: TU Braunschweig.
- Winter, S., Fey, T., Kröger, I., Friedrich, D., Ladner, K., Ortel, B., Pendsa, S., & Witt, F. (2014). Design, realization and uncertainty analysis of a laser-based primary calibration facility for solar cells at PTB. *Measurement*, 51, 457-463. doi:10.1016/j.measurement.2013.12.001
- Winter, S., Friedrich, D., & Gerloff, T. (2010). Effect of the Angle Dependence of Solar Cells on the Results of Indoor and Outdoor Calibrations. (pp. 4304 - 4306). Valencia:
-

Proceedings of the 25th European Photovoltaic Solar Energy Conference and Exhibition / 5th World Conference on Photovoltaic Energy Conversion. doi:10.4229/25thEUPVSEC2010-4AV.3.97

Winter, S., Wittchen, T., & Metzdorf, J. (2000). Primary Reference Cell Calibration at the PTB Based on an Improved DSR Facility. 3, pp. 2198-2201. Glasgow: Proceedings of the 16th European Photovoltaic Solar Energy Conference.

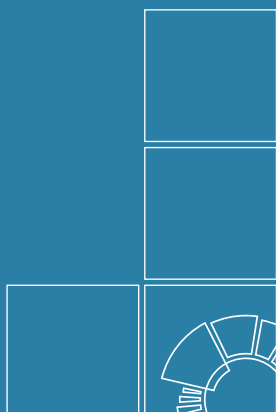
Witt, F., Kröger, I., Fey, T., Friedrich, D., & Winter, S. (2013). Front Glassing Influence on the Primary Calibration of WPVS Reference Solar Cells. (pp. 3485 - 3487). Paris: Proceedings of the 28th European Photovoltaic Solar Energy Conference . doi:10.4229/28thEUPVSEC2013-4AV.6.40

Zhang, J., Watanabe, K., Yoshino, J., Kobayashi, T., Hishikawa, Y., & Doi, T. (2018). Physical process and statistical properties of solar irradiance enhancement observed under clouds. *Japanese Journal of Applied Physics*, 57, 08RG11. doi:10.7567/JJAP.57.08RG11

Acknowledgement/Danksagung

Gerne möchte ich mich bei Prof. Stefan Kück für die Betreuung des Arbeitsthemas, den wertvollen fachlichen Austausch, die richtungsweisenden Gespräche mit Ihm, sowohl als Vorgesetzten, als auch als geschätzten Kollegen bedanken. Ferner geht mein Dank an Prof. Andreas Waag für die Tätigkeit als Zweitgutachter, sowie die fachliche Beratung bei der strategischen Planung der Dissertation. Besonders bedanke ich mich bei Dr. Stefan Winter für das Ermöglichen und die Begleitung meiner fachlichen Tätigkeiten. Die unzähligen fachlichen Diskussionen mit Ihm, seinen Ansporn und das gemeinsame Feilen an visionären Ideen stellen einen unschätzbaren Wert für meine berufliche Entwicklung in den vergangenen Jahren dar. Meinem Mentor und Captain Dr. Ingo Kröger möchte ich für die Einarbeitung im Labor und die hilfreichen Gespräche zu Kurskorrekturen bei diesem und anderen Vorhaben danken. Dr. Stefan Riechelmann danke ich für die programmiertechnische Inspiration und die fruchtbaren Diskussionen rund um die Modellierungsansätze, sowie für die Versorgungsleistungen mit Keksen. Die Unterstützung der KollegInnen und Ehemaligen der PTB Arbeitsgruppen 4.52 und 4.53 möchte ich hier besonders erwähnen. Danke Dr. Florian Witt, Wolfgang Jöckel, Dr. Thomas Fey, Dietrich Schlüssel, Stefan Pendsa, Dirk Friedrich, Bernhard Ortel, Antje Schweitzer, Shashi Bhushan, Larissa Meyer, Tom Schulze-Bubert, Kai Michels, Marius Bagus, Wiebke Brandes, Malte Schneeberg, Felix Duwe, Rouven Krake, Dr. Hendrik Sträter, Clarissa Hädrich, Nadja Jordan, Ute Krüger und Thomas Wittchen. Gerne möchte ich auch Dr. Peter Sperfeld meinen Dank ausdrücken, der eine wertvolle Inspirationsquelle für meine Entscheidung einen metrologischen Werdegang einzuschlagen gewesen ist. Ferner danke ich den KollegInnen aus den Fachbereichen 4.1 und 4.5 der PTB für die tolle Zusammenarbeit und die angenehmen Gespräche bei Kaffee und Kuchen, sowie für die spannenden Betriebsausflüge und -feiern. Ein spezieller Dank geht auch an Yvonne Geckeler-Zimber, die mir besonders bei Navigationsproblemen durch die Formularsammlung der Behörde, und bei anderen bürokratischen Untiefen die richtige Richtung gewiesen hat. Bei Dr. Michael Kazda möchte ich mich für die großartige Unterstützung bei Gesprächen in schwierigen Zeiten, die wertvolle Kritik an meinen Präsentationen und Schriften, für die humorvolle Aufmunterung und für die angenehmen Treffen bei Eiskaffee und Streuselkuchen bedanken. Bei Judith Krakowski und dem Team der Graduiertenschule B-IGSM möchte ich mich für die Planung und Betreuung der äußerst vielseitigen Veranstaltungen, Ausflügen sowie Teambuildingmaßnahmen bedanken. Bernd Warnke danke ich für die technische Unterstützung diese Zeilen über die Druckmaschine zu Papier zu bringen. Für den anregenden internationalen wissenschaftlichen Austausch bedanke ich mich insbesondere bei Dr. Blagovest Mihaylov, Dr. Harald Mülleijans, Roberto Galleano, Wim Zaaiman, Dr. Elena Salis, Dr. Diego Pavanello und Esma Musić. Meinen Freunden, meiner Familie und besonders meiner Freundin Eva Waldmann danke ich für die außerordentliche Geduld, fortwährende Unterstützung und Motivation während der vergangenen Jahre.

Parts of this work/project has received funding from the EMPIR program co-financed by the Participating States and from the European Union's Horizon 2020 research and innovation program.



Herausgeber:

Physikalisch-Technische Bundesanstalt
ISNI: 0000 0001 2186 1887

Presse und Öffentlichkeitsarbeit

Bundesallee 100
38116 Braunschweig

Telefon: (05 31) 592-93 21
Telefax: (05 31) 592-92 92
www.ptb.de

Vertrieb:

Fachverlag NW in der
Carl Schünemann Verlag GmbH

Zweite Schlachtpforte 7
28195 Bremen

Telefon: (04 21) 369 03-0
Telefax: (04 21) 369 03-63
www.schuenemann-verlag.de